Atmospheric Peroxy Radical Chemistry Studied by Infrared Kinetic Spectroscopy

Thesis by
Aileen Oyama Hui

In Partial Fulfillment of the Requirements for the
Degree of
Doctor of Philosophy

CALIFORNIA INSTITUTE OF TECHNOLOGY
Pasadena, California

2019
Defended November 29, 2018

Aileen Oyama Hui
ORCID: 0000-0003-4217-2698

ACKNOWLEDGEMENTS

During my time at Caltech and JPL, I have had the privilege of working alongside numerous talented people, and I am extremely humbled to be surrounded by countless intelligent and inspiring minds. There have been so many people who have touched my life in profound ways and have been instrumental in my success in various aspects of my PhD experience. While I take pride in my accomplishments, my success would not have been possible without the support of my mentors, colleagues, friends, and family. To quote Sir Isaac Newton, "If I have seen further than others, it is by standing upon the shoulders of giants." More than any technical skill and knowledge I have gained from my time at Caltech, I value the relationships that I have made and the experiences I have had with these wonderful people.

First and foremost, I would like to thank my advisors, Mitchio Okumura and Stanley Sander, who have guided me through not only their intellect and expertise, but also their unwavering support. I feel very fortunate to have not one, but two very kind advisors who always provided encouragement and belief in my success. I would also like to thank my committee members, Tom Miller, Geoff Blake, and Rudy Marcus, for challenging me to always aim higher so that I could reach my full potential.

I have received several fellowships during my time at Caltech that have helped pay for my stipend and travel to conferences. I'm honored to have received the International Journal of Chemical Kinetics Fellowship in 2015, which funded my travel to the 33rd International Symposium on Free Radicals, where I gave a talk on my work on acetonylperoxy reactions. I also received two fellowships, the NASA Graduate Student Researchers Program (GSRP) and the NASA Earth and Space Science Fellowship (NESSF), which have funded several years of my PhD work.

I am grateful for my predecessors, Aaron Noell and Lance Christensen, who both helped me get started with the IRKS apparatus and answered all of my questions. Their expertise and knowledge about this complicated and temperamental apparatus have helped me so much, and they have played a big part in guiding me towards becoming a good scientist. The work carried out in this thesis would not have been possible without the collaboration with Siamak Forouhar and the Microdevices Lab (MDL) at JPL, who manufactured our IR lasers. I especially want to thank Mathieu Fradet, who was responsible for the fabrication of our mid-infrared (MIR) laser. Mathieu was so patient with me and gave me lots of advice for implementing this new laser into our existing apparatus. Thanks to Lance, Mathieu, and Ryan Briggs

so much for letting me borrow their Pyrocams so many times and for so long! I don't know how I could have aligned the MIR without these fancy cameras.

I am fortunate for being given the opportunity to work with Professor Fred Grieman and his Pomona students, especially Emily Darby, Julia Dohner, Julia Cowen, and Sara Murphy. Fred is a very kind and supportive person who really cares about his students. I always enjoyed working and brainstorming with him. Working with his students during the summers and parts of the school year was also a great learning opportunity for me to mentor younger students. All of Fred's Pomona students were very hard-working, and I feel lucky that I got to work with such bright students with great futures ahead of them.

I was also able to work alongside so many experts at the Jet Propulsion Laboratory (JPL), including everyone in the kinetics and photochemistry group. I especially want to thank Fred Winiberg, my office-mate at JPL, who was always really fun to talk to and also gave me lots of good advice and ideas when I got stuck on experiments or data analysis. I also learned a lot working with him on the NO + β-hydroxyethylperoxy (β-HEP) chemistry at the Advanced Light Source (ALS) at the Lawrence Berkeley National Laboratory (LBNL) in collaboration with David Osborne and Rebecca Caravan from the Sandia National Laboratories (SNL). I really appreciate all of them for teaching me how to operate the MPIMS instrument to do some interesting chemistry at the synchrotron. Xu Zhang has also helped me several times when I needed to collect the IR spectra of CH_3OH and CH_3CHO in the gas phase with her FTIR spectrometer. She was always patient and willing to teach me about FTIR spectroscopy and her instrument, as well as the projects she was working on at the time. I really enjoyed having lunch together and having good conversations! I would also like to thank Carl Percival for always being so supportive. Fred, Xu, and Carl all read and gave me some great feedback on my props for my Props Exam. Their kind words of encouragement and scientific feedback played a big part in my success.

Dave Natzic at JPL often helped me build things on the fly in his machine shop, and I also really value his friendship. He never refused to help me, no matter how busy he was, and there are so many things with the IRKS apparatus that would not have worked without his help. He was also someone I felt comfortable talking to, and I will really miss having lunch with him. I got a lot of help from Kyle Bayes with various things at JPL, such as finding impurities in the old NO cylinder that I was using with his mass spectrometer and helping me get set up to calibrate my Baratrons. His extensive knowledge of everything in the lab (and elsewhere) will

forever inspire me. All of my excimer issues where resolved by Frank Cipolla, who was the only good part about our excimer not working. Having the chance to talk and catch up with him was definitely the silver lining of our excimer ailments. He was also always generous with his time and consulted with me for long periods of time over the phone to talk me through diagnosing the laser.

I feel lucky to have had access to some great administrative assistants, both at JPL and Caltech, who have helped me, from placing orders for various lab equipment, to getting travel reimbursements: Elisha Okawa and Monica Brito at Caltech and Xuan Sabouchi, Simon Flores, Kyle Thornburg, and Laura Fisher at JPL. I am also grateful for the quality and accessibility of the mental health services that were available to me. The staff at the Caltech Counseling Center and Evelyn Novello have been so instrumental in maintaining my sanity throughout my time in graduate school.

My success would not have been possible without the encouragement and support from both previous and current members of the Okumura group, including Kana Takematsu, Thinh Bui, Leah Dodson, Linhan Shen, Joey Messinger, Gautam Stroscio, Doug Ober, and Greg Jones. I value the advice I have received from everyone in my group, and I wish the present graduate students the best during the rest of their time at Caltech. Thanks especially to Joey, who has kindly offered to read and give me comments on a few chapters of this thesis and ran some last-minute Gaussian calculations for me. I'll also always appreciate him for answering a lot of my questions about Cavity Ringdown Spectroscopy when I was writing my props for my Props Exam, and more importantly, telling me whenever there was free food available on campus.

I have also made some amazing friends within the Okumura group, particularly Laura Mertens, Elizabeth Lunny, and Matt Smarte. Their intelligence, kindness, and friendship will continue to inspire me for the rest of my life. Laura has been a really good friend and has always been so supportive of me, especially during trying times in my graduate school career. I miss having tea at Chado, and I'll always remember the fun Thanksgiving we had one year. Even though she had graduated from Caltech over a year ago, she read and gave me feedback on all of my props for my Props Exam. Elizabeth is one of the most generous and supportive people I have ever met and has been an amazing friend. She always gave me good advice and a reality check every time I was stressing out and blowing things out of proportion. I'll admit, I'll probably miss having the giant exercise ball kicked at me. I feel very privileged to have been able to work closely with Matt while we were at the ALS, where he was a project leader on several projects. I truly admire and respect his work ethic, attention

to detail, and simply just his intelligence. I am also so grateful for his time and advice while I was preparing for my Props Exam. He gave me some really amazing feedback on my props and spent at least an hour with me going through my talk in great detail, both of which were immensely helpful and played a big part in making my exam a success. Aside from being a great colleague, Matt has also been a great friend, who encouraged me and gave me confidence in my abilities when I doubted myself. I'll really miss the weekly ramen dinners with Elizabeth and Matt!

I truly appreciate the support and guidance I have received from my other amazing friends outside of the Okumura group. I especially want to thank my best friend from college, Daphne Che, who has helped me through some of the toughest times. Heather McCaig and Artemis Ailianou, who are Caltech PhD graduates, have also been pillars for me, and I am so thankful for their friendship. On top of being great friends, they have given me tons of great advice about my professional career. They were also a part of the ballet and dance community that I became involved with. Ballet has always been a big part of my life ever since I was a child, and I feel fortunate that I have been able to continue pursue dancing during my time at Caltech. Zoe Keijser, Daniel Tran, Cynara Woolner, Tiffany Hsu, Vincent Cheong, Donna Mo, Yadi Younse, Beth Trussell, Janis Chodas, Barbara Bennett Lai, Kellene Adachi, Holly Boruck, Oksana Sandefur, Marlena Brown, and Kathy Bubash are some of the people in this community who have supported my pursuit of a PhD in various ways. I would like to thank the Caltech Ballet Club as well as my dance and fitness instructors and mentors: Kathy Braidhill, Preston Li, Helga de Kansky, Richard Bradley, Lawrence Blake, Michael Cornell, Melissa Waters, and Leigh Purtill. I would like to thank Cynthia Young and the Pasadena Dance Theatre (PDT) not only for giving me the opportunity to be a part of the professional company but for creating this community of people that I grew so close to. Dancing in a professional company, while also maintaining a full workload at Caltech was not easy, but was extremely fulfilling. I take pride in being a part of PDT's production of *The Nutcracker* and my experiences have empowered me and given me the courage to take on many challenges.

My family, especially Mom, Dad, and my brother Takeshi, always provided unwavering emotional support and belief in me every step of the way no matter what I pursued in my life. Finally, I want to thank my boyfriend and best friend Matt Tramel, who has shared the stress of my last few years at Caltech. I am forever grateful for his patience and his unconditional belief in me. He stood by me throughout this entire journey and gave me the confidence that I never thought I had. He has filled

my life with so many wonderful experiences and opened my eyes to a much bigger, more colorful world.

To every one of you that I have mentioned as well as others whom I may have unwittingly neglected to name, I am so thankful for having you in my life. You have all enriched my life in so many ways and I hope to one day inspire in others what you have inspired in me.

ABSTRACT

My thesis work used laboratory studies to characterize gas phase organic peroxy radical (RO_2) reactions that are relevant to atmospheric chemistry. RO_2 chemistry plays a central role in atmospheric science, as these radicals control the oxidative capacity of the atmosphere and are key intermediates in the cycling of ozone in the troposphere in regions where levels of nitrogen oxides ($NO_x \equiv NO + NO_2$) are high. In more remote regions of the Earth where NO_x concentrations are low, RO_2 loss is dominated by reaction with hydroperoxy (HO_2) and other peroxy radicals, leading to removal of reactive radicals from the troposphere. However, for certain species of RO_2, reaction with HO_2 can also propagate radical chemistry by recycling hydroxyl (OH) radicals, a primary oxidant in the atmosphere. Both HO_2 and OH radicals play important roles in atmospheric oxidation reactions. Accurate characterization of various RO_2 reactions that contribute to consuming and recycling HO_x ($HO_x \equiv HO_2 + OH$) are instrumental for understanding the effects of atmospheric composition on climate forcing, air quality, and the global ozone budget.

The main body of my work focused on studying the self reactions of HO_2 and RO_2 as well as their cross reactions ($HO_2 + RO_2$) using a time-resolved experimental technique called Infrared Kinetic Spectroscopy (IRKS), which combines infrared (IR) and ultraviolet (UV) absorption spectroscopy. Perfect isolation of one specific reaction is generally difficult or impossible due to radical recycling and secondary chemistry, which leads to numerous reactions occurring simultaneously. Thus, although laboratory studies provide controlled environments to study these reactions, the accuracy of the results are highly dependent on the experiment's selectivity and sensitivity to specific transient species. In this work, a new mid-IR (MIR) laser was implemented into the existing apparatus for measuring OH radicals. In addition to UV absorption spectroscopy, the IRKS apparatus was equipped for selective detection of HO_2 and OH radicals in the near-IR (NIR) and MIR, respectively.

The kinetics and product yields of a reaction are two important factors for assessing the impact of these reactions on the atmosphere. IRKS was used to study the kinetics of the self reactions of acetylperoxy ($CH_3C(O)O_2$) and acetonylperoxy ($CH_3C(O)CH_2O_2$), as well as their reactions with HO_2. The OH and O_3 yields from the reaction of $HO_2 + CH_3C(O)O_2$ were also measured, providing the first parametrization of the temperature dependence of the OH product channel. The temperature dependence of the HO_2 self reaction kinetics was re-investigated to resolve discrepancies in the results previously reported in the literature. Furthermore,

this work identified and characterized rate enhancement effects on the HO_2 self reaction by the adducts of HO_2 formed from the reaction of HO_2 with methanol (CH_3OH), acetaldehyde (CH_3CHO), and acetone ($CH_3C(O)CH_3$), which were used as radical precursors for HO_2, $CH_3C(O)O_2$, and $CH_3C(O)CH_2O_2$, respectively.

Finally, the improved sensitivity of the IRKS apparatus enabled the investigation of fast reaction kinetics. The rate constants of Cl atoms with CH_3OH and CH_3CHO were measured over a wide range of temperatures. The results were consistent with previously reported values in the literature and additionally validated assumptions that had been made regarding the temperature independence of these reactions. The temperature and pressure dependences of the OH yield from the reaction of CH_3CO with O_2 were also studied to resolve current discrepancies in the literature. The yield of HO_2 from this reaction was also directly measured for the first time.

TABLE OF CONTENTS

LIST OF FIGURES

Chapter 2

Chapter 3

Chapter 4

Chapter 5

Chapter 6

Chapter 7

LIST OF TABLES

Chapter 2

Chapter 3

Chapter 4

Chapter 5

Chapter 6

Chapter 7

Chapter 1

INTRODUCTION

1.1 Motivation

The beginning of the Industrial Revolution in the mid-eighteenth century marks one of the major turning points in history. The tremendous progress in technology and manufacturing is clearly manifested in many aspects of our lives today. However, the advantages of industrialization have also been accompanied by detrimental effects to the environment. One of the many prominent environmental effects of anthropogenic activity is the dramatic increase in global temperatures in the past few decades, leading to rising sea levels and extreme weather patterns. The reality of climate change has undoubtedly prompted serious concerns and the need for advancements in atmospheric and environmental science has never been more apparent.

A major goal in the field of atmospheric science is the development of atmospheric models to combat current environmental challenges, such as global warming, stratospheric ozone depletion, and air pollution. Constructing such models requires both field and laboratory studies to develop a comprehensive understanding of the fundamental chemistry that occurs in the Earth's atmosphere. Observational records compiled from field measurements provide a database of long-term changes in atmospheric composition and climate forcing, serving to measure the accuracy of current models. Meanwhile, laboratory experiments provide controlled environments to study specific reactions that occur in the atmosphere. Results from laboratory studies provide evidence that can either support or challenge existing models, as well as create building blocks for developing better representations of the Earth's atmosphere. The collective effort of laboratory and field studies helps improve the predictive capabilities of current atmospheric models and develops strategies to mitigate climate change.

1.2 Scientific background

The most general description of the Earth's atmosphere divides it into layers that are distinguished by their vertical temperature profiles [1]. Most of the chemistry that impacts our weather and climate occurs in the two lowest layers of the atmosphere, where the gas density is the highest. The lowest layer is known as the troposphere, which extends from the Earth's surface to ~10 km altitude. Within the troposphere,

the average temperature decreases with height and is characterized by turbulent mixing. The stratosphere is the region above the troposphere and extends to ~50 km altitude. In the stratosphere, absorption of high frequency solar ultraviolet (UV) radiation by O_3 releases heat and results in a positive temperature profile with altitude.

An important chemical process that occurs in the Earth's upper troposphere/lower stratosphere (UTLS) is O_3 catalysis. Combined with the discovery of tropospheric O_3 as one of the major contributors to photochemical smog [2, 3], the observation of the polar stratospheric O_3 hole [4] sparked further interest in understanding the major chemical pathways of O_3 in the atmosphere. The presence of an O_3 layer in the stratosphere is crucial for sustaining life on Earth. O_3 absorbs high frequency UV light and prevents harmful solar radiation from reaching the Earth's surface. On the other hand, tropospheric O_3 production is undesired because of the toxic effect of O_3 on human health. Oxidative processes that impact the global O_3 budget are therefore useful markers for assessing the reactivity of the atmosphere and the implications for the environment.

The chemical pathways of O_3 in both the troposphere and the stratosphere involve odd oxygen ($O_3 + O(^3P)$) and nitrogen oxides ($NO_x \equiv NO + NO_2$), but the ultimate fate of O_3 is vastly different in each region: odd oxygen and NO_x promote O_3 production in the troposphere while promoting O_3 destruction in the stratosphere [5]. Although there are some natural sources of NO_x, large concentrations of NO_x are emitted from vehicle exhausts as well as other combustion processes. Thus, an understanding of these reaction mechanisms is important for evaluating appropriate global emission standards and regulations.

The Chapman mechanism describes stratospheric O_3 originating from the photolysis of oxygen molecules (O_2) by low wavelength ($\lambda < 240$ nm) solar radiation (R1) to produce oxygen atoms in their ground electronic state, $O(^3P)$, which combines with O_2 to generate O_3 (R2)

$$O_2 \xrightarrow{h\nu\ (\lambda < 240\ \text{nm})} 2\,O(^3P) \tag{R1}$$

$$O(^3P) + O_2 \xrightarrow{M} O_3 \tag{R2}$$

where M is a third body inert molecule that aids in dissipating excess energy as heat. The subsequent loss of O_3 by reaction with $O(^3P)$ (R3) leads to a null cycle.

$$O_3 + O(^3P) \longrightarrow 2\,O_2 \tag{R3}$$

The steady-state concentration of O_3 depends on the production and loss rates of R1 - R3, as well as additional reactions that consume or produce O_3.

The production of O_3 in the troposphere is described by a different mechanism because UV radiation of wavelengths shorter than $\lambda < 300$ nm do not penetrate into the troposphere due to absorbance of lower wavelength UV light by stratospheric O_3. Tropospheric O_3 production occurs primarily through the photodissociation of nitrogen dioxide (NO_2) to form $O(^3P)$ (R4), which rapidly combines with O_2 (R2) to produce O_3.

$$NO_2 \xrightarrow{h\nu} NO + O(^3P) \tag{R4}$$

A null cycle occurs if nitric oxide (NO), the co-product of R4, regenerates NO_2 by consuming O_3 (R5).

$$O_3 + NO \longrightarrow NO_2 + O_2 \tag{R5}$$

Peroxy radicals (RO_2) unbalance the null cycle by recycling NO_2 without consuming O_3 via oxidation of NO (R6), and thus play an important role in the production of tropospheric O_3.

$$RO_2 + NO \longrightarrow NO_2 + RO \tag{R6}$$

RO_2 radicals are produced from the oxidation of hydrocarbons (RH) by hydroxyl radicals (OH), which are primary oxidants in the atmosphere:

$$OH + RH \longrightarrow R\cdot + H_2O \tag{R7}$$

$$R\cdot + O_2 \xrightarrow{M} RO_2 \tag{R8}$$

While anthropogenic and biogenic sources contribute to RH emissions, the initial formation of OH in the troposphere occurs through photolysis of O_3 taking place in a narrow spectral region spanning 300 - 320 nm, generating the excited atomic oxygen, $O(^1D)$ (R9). OH is produced from the subsequent reaction of $O(^1D)$ with water vapor, H_2O (R10).

$$O_3 \xrightarrow{h\nu} O_2 + O(^1D) \tag{R9}$$

$$O(^1D) + H_2O \longrightarrow 2\,OH \tag{R10}$$

Because most high frequency light in the UV is filtered out by stratospheric O_3 and the solar flux is therefore low in the troposphere, the production of $O(^1D)$ via

R9 is slow. Thus, the sustained levels of OH in the troposphere are attributed to the recycling of OH through NO_x chemistry. For example, the alkoxy radical (RO) co-product from R6 combines with O_2 to form hydroperoxy radicals, HO_2 (R11). HO_2 is the other dominant oxidant in the atmosphere and recycles OH by reaction with NO (R12).

$$RO + O_2 \longrightarrow R^{'}CHO + HO_2 \quad \text{(R11)}$$

$$HO_2 + NO \longrightarrow OH + NO_2 \quad \text{(R12)}$$

However, studies have shown that tropospheric O_3 production via oxidation of RH was not enough to account for the O_3 concentration obtained from observational measurements [6]. Further investigations have revealed that the modeled O_3 was limited by NO_x emissions [7], demonstrating the importance of understanding the chemistry occurring under low NO_x conditions in order to mitigate pollution and improve air quality.

1.3 Summary of thesis work

The range of experimental techniques that are available for characterizing reactions of peroxy radicals continues to expand, advance, and push the limits of technological progress. The collection of results obtained using various techniques carried out by independent studies provides confidence in forming conclusions about these reactions, which are difficult to study due to the complexity of the chemical systems. The work described in this thesis was carried out using the Infrared Kinetics Spectroscopy (IRKS) apparatus, which enabled sensitive detection of various radical species in real-time. The experimental methods and procedures are described in detail in Chapter 2, which also summarizes the characterizations and calibrations of the main components of the apparatus, including a new laser that was implemented for detecting OH radicals.

This thesis describes laboratory investigations of key radical reactions that occur in low-NO_x atmospheres. Under these conditions, the dominant loss of RO_2 is in reactions with HO_2, which has several possible product channels depending on the specific RO_2 radical (R13).

$$HO_2 + RO_2 \longrightarrow ROOH + O_2 \quad \text{(R13a)}$$

$$\longrightarrow ROH + O_3 \quad \text{(R13b)}$$

$$\longrightarrow OH + RO + O_2 \quad \text{(R13c)}$$

Until recently, $HO_2 + RO_2$ reactions were thought to be exclusively chain terminating, leading only to the formation of stable products via R13a or R13b. However, more recent laboratory and theoretical studies have shown evidence that, for some RO_2 radicals, the reaction can also form OH radicals through a third channel (R13c), which has important implications for assessing the oxidative capacity of the atmosphere. Isolating $HO_2 + RO_2$ reactions in the laboratory is often difficult or impossible due to competing secondary chemistry, such as the self reactions of HO_2 and RO_2. In the atmosphere, the HO_2 self reaction (R14) plays a key role in radical termination by producing hydrogen peroxide (H_2O_2), which is scavenged by aerosols and serves as a temporary reservoir for HO_x.

$$HO_2 + HO_2 \xrightarrow{M} H_2O_2 + O_2 \qquad \text{(R14)}$$

Although comparatively less significant in the atmosphere due to low radical density, the self reactions of RO_2 are the major sources of interference in laboratory studies, necessitating the characterization of these reactions. My thesis work investigated the three main reactions: the self reaction of HO_2 and the cross reactions of HO_2 with $CH_3C(O)O_2$ and with $CH_3C(O)CH_2O_2$. The work carried out for each system also included characterization of the major interfering secondary reactions (i.e., RO_2 self reactions), as well as inherently coupled reactions, such as initial radical generation mechanisms.

Investigation of the kinetics and product yields of the $HO_2 + CH_3C(O)O_2$ reaction is the subject of Chapter 4. $CH_3C(O)O_2$ radicals are key intermediates formed from the oxidation of VOCs and play important roles in the recycling of OH radicals in remote atmospheres. In addition to UV absorbance measurements of various reactant and product species, IRKS enabled sensitive and selective detection of HO_2 in the NIR and OH the MIR. Using the time-resolved data obtained using all three detection probes, we determined the yields of OH and O_3, as well as the overall rate constant of the $HO_2 + CH_3C(O)O_2$ reaction. Implementation of a direct OH detection technique also expanded the scope for studying $CH_3C(O)O_2$ reactions. Chapter 5 details the work done to investigate the pressure dependence of the yield of OH from the reaction of $CH_3C(O) + O_2$.

In this work, radicals were generated by photolysis of Cl_2 to produce Cl radicals, which reacted with radical precursors and formed peroxy radicals in the presence of O_2. The relative amount of HO_2 and RO_2 radicals that were produced depended on the rate constants of the reactions of Cl with the radical precursors. As a prerequisite for studying the $HO_2 + CH_3C(O)O_2$ reaction, the rate constants of the reaction of Cl

with CH_3OH and with CH_3CHO were measured in the work described in Chapter 6.

In the laboratory, the self reaction of HO_2 was further complicated by rate enhancement by radical adducts formed from the reaction of HO_2 with the radical precursors, such as CH_3OH and CH_3CHO. Chapter 3 describes the determination of the temperature-dependent HO_2 self reaction rate constant and the rate enhancement effects by the $HO_2 \cdot CH_3OH$ and $HO_2 \cdot CH_3CHO$ adducts. The equilibrium constants of the reaction of HO_2 with CH_3OH and CH_3CHO were also measured. The rate enhancement of the HO_2 self reaction by $HO_2 \cdot CH_3C(O)CH_3$ is presented in Chapter 7 as part of the work on investigating the kinetics of the HO_2 + $CH_3C(O)CH_2O_2$ reaction. Chapter 7 also includes determination of the UV absorption cross-section of $CH_3C(O)CH_2O_2$ and the rate constant of the $CH_3C(O)CH_2O_2$ self reaction.

References

[1] Seinfeld, J. H.; Pandis, S. N., *Atmospheric Chemistry and Physics: From Air Pollution to Climate Change*, 3rd ed.; John Wiley & Sons, Inc.: Hoboken, New Jersey, 2016.

[2] Haagen-Smit, A. J. Chemistry and Physiology of Los Angeles Smog. *Industrial & Engineering Chemistry* **1952**, *44*, 1342–1346.

[3] Haagen-Smit, A. J.; Bradley, C. E.; Fox, M. M. Ozone Formation in Photochemical Oxidation of Organic Substances. *Industrial & Engineering Chemistry* **1953**, *45*, 2086–2089.

[4] Farman, J. C.; Gardiner, B. G.; Shanklin, J. D. Large Losses of Total Ozone in Antarctica Reveal Seasonal ClOx/NOx Interaction. *Nature* **1985**, *315*, 207–210.

[5] Jacob, D. J., *Introduction to Atmospheric Chemistry*; Princeton University Press: 1999.

[6] Tyndall, G. S.; Cox, R. A.; Granier, C.; Lesclaux, R.; Moortgat, G. K.; Pilling, M. J.; Ravishankara, A. R.; Wallington, T. J. Atmospheric Chemistry of Small Organic Peroxy Radicals. *Journal of Geophysical Research: Atmospheres* **2001**, *106*, 12157–12182.

[7] Chameides, W. L.; Fehsenfeld, F.; Rodgers, M. O.; Cardelino, C.; Martinez, J.; Parrish, D.; Lonneman, W.; Lawson, D. R.; Rasmussen, R. A.; Zimmerman, P.; Greenberg, J.; Mlddleton, P.; Wang, T. Ozone Precursor Relationships in the Ambient Atmosphere. *Journal of Geophysical Research: Atmospheres* **1992**, *97*, 6037–6055.

Chapter 2

EXPERIMENTAL METHODS

2.1 Introduction

Infrared Kinetics Spectroscopy (IRKS) is an extremely sensitive technique that employs simultaneous infrared (IR) wavelength modulation spectroscopy (WMS) and ultraviolet (UV) direct absorption spectroscopy in a temperature-controlled pulsed laser photolysis flow cell. Although UV absorption techniques benefit from the large absorption cross-sections of peroxy radicals in this spectral region, spectral overlap of various species precludes specific detection of reactive radicals, which can introduce systematic errors. In addition to UV absorption spectroscopy, IRKS uses IR heterodyne WMS to achieve selective and sensitive real-time detection of HO_2 and OH radicals in the near-IR (NIR) and mid-IR (MIR), respectively. The combination of IR path length amplification using multi-pass optics and WMS enables sensitivities on the order of 10^{10} to 10^{11} molecule cm^{-3}.

The main part of the apparatus was constructed by Dr. Lance Christensen before I began my research and has been described previously in his papers and thesis [1, 2]. Furthermore, Dr. Aaron Noell has carried out extensive characterization of the instrument, which is detailed in his thesis [3]. This chapter describes my own contributions to the IRKS apparatus, which includes the implementation of a new MIR diode laser for the detection of OH radicals as well as significant improvements that were made to the instrument sensitivity. The last section of this chapter also describes characterization of two additional lasers that ultimately could not be implemented into the IRKS apparatus for their intended purposes due to limitations in their sensitivity. The general schematic of the IRKS apparatus is shown in Figure 2.1.

2.2 Flow cell

The Pyrex cell measured a total length of 175 cm with an inner diameter of ~5 cm and was supported by two aluminum boxes, which were connected to either ends of the cell via O-ring seals. The entire box-cell-box volume was enclosed by wedged CaF_2 windows attached to the boxes and the total window-to-window length of the cell was 208 cm [2]. The cell was jacketed to allow for temperature control using liquid nitrogen-chilled methanol as the coolant, and an insulated cover encased the

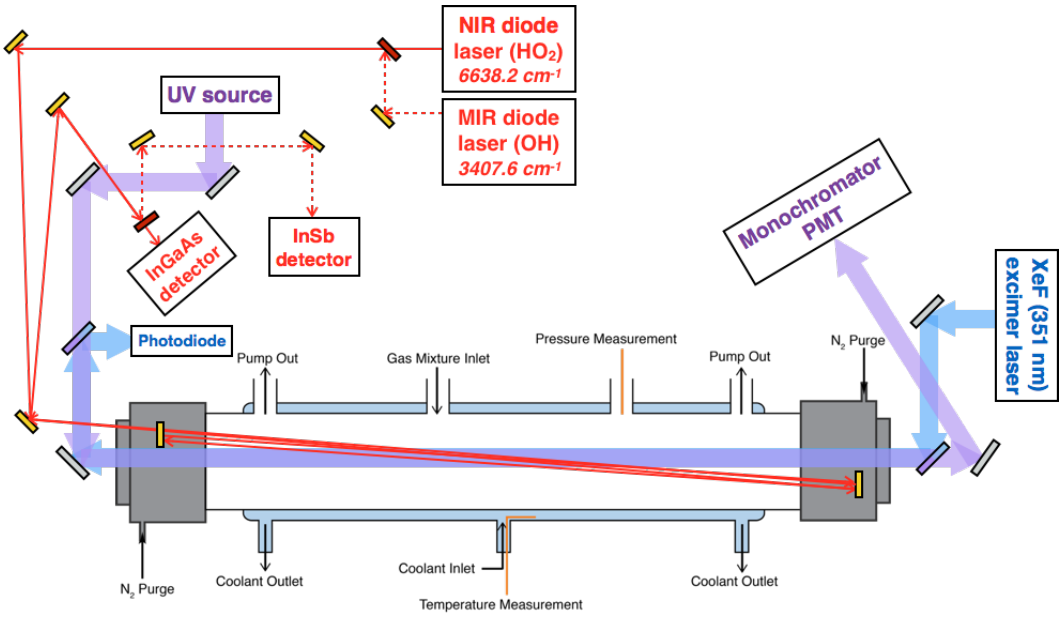

Figure 2.1: Schematic of the IRKS apparatus. A pre-cooled gas mixture entered the temperature-controlled Pyrex flow tube, where radicals were generated by pulsed excimer laser photolysis (beam path shown in blue). Three independent absorption probe beams were used to temporally monitor the reactant and product species: NIR and MIR light (solid and dashed red lines) from two diode lasers were coupled to multi-pass Herriott optics and broadband UV light made a single-pass through the reaction cell (purple). Flip mirrors were used (red rectangles) to switch between the two IR lasers.

entire length of the jacketed region. The temperature inside the reaction cell was measured by a calibrated type T thermocouple (Omega) that was inserted into the jacket of the cell and in contact with the coolant. The pressure inside the cell was measured by a calibrated absolute capacitance manometer (MKS-220CA 1000 Torr, accuracy: 0.15% of reading).

Known concentrations of precursor gases were introduced into the cell using calibrated flow controllers (MKS 1149, 1147, GE50, and GM50 series). Vapors from condensed-phase precursors (e.g., CH_3OH, H_2O, CH_3CHO, $CH_3C(O)CH_3$) were introduced into the cell by flowing N_2 gas through glass bubblers containing the liquid compounds, held inside temperature-controlled baths. The bubbler pressures and temperatures were measured with calibrated absolute capacitance manometers (MKS-220CA 1000 Torr) and type T thermocouples (Omega), respectively, and the concentrations were calculated from the vapor pressures using the Antoine equation.

The reagent gases were pre-mixed and pre-cooled in a meter-long jacketed tube prior to entering the main reaction cell through an off-center inlet port and were

pumped out via two exit ports on either sides of the cell. The distance between the centers of the exit ports was 138 nm. Room temperature dry nitrogen purge gas flowed through both aluminum chambers to confine the reagent gases to the temperature-controlled region. The purge gas also served to protect the Herriott mirrors housed inside the aluminum boxes from corrosion from caustic gases such as Cl_2 and from condensation at lower temperatures. The optimum gas flow conditions for confining the reactant gas between the two exit ports were determined by previous measurements performed by Dr. Aaron Noell [3]. Experiments were typically conducted using purge gas flows that were 100% of the total flow. During non-operation, the flow cell was held under vacuum using a scroll pump (Edwards nXDS15i) in order to protect the Herriott mirrors from deterioration by outgassing caustic chemicals adsorbed on the walls of the cell.

2.2.1 Path length and temperature profile

At low temperatures, the room temperature purge gas flowing through the aluminum chambers prevented condensation of water on the Herriott mirrors; however, this protective measure also introduced temperature gradients in the flow cell. Characterization of the path length was explored at the beginning of my thesis work in collaboration with Dr. Aaron Noell and Professor Fred Grieman. The reactant path length as well as the length and locations of the mixing regions between the purge and reactant gas flow were determined by measuring the temperature profile of the gas along the length of the cell using a T-type thermocouple probe attached to the end of a long stainless steel rod. The temperature probe was inserted into the cell through a flange mounted at one end of the cell to allow controlled movement of the probe along the entire length of the cell, while simultaneously providing sufficient seal to maintain constant pressure inside the cell. The temperature at various points along the length of the cell was recorded at a total pressure of 100 Torr and 300 Torr (10 s residence time) with the main gas at 213 K and the purge gas at room temperature (Figure 2.2). The purge gas was flowed at 100% of the total flow of the reagent gas. All thermocouples were calibrated with a precision platinum resistance thermometer (Omega RTD HH376 PT).

As shown in Figure 2.2, while the cell temperature continued to decrease beyond ~10 cm past the first pump-out port (TC_{probe} position = 0 cm), the temperature remained low until past the second pump-out port (TC_{probe} position = 138 cm). One possible explanation is that because the reagent gas inlet port was not centered with respect to the pump-out ports, the gas near the left side of the cell was slightly

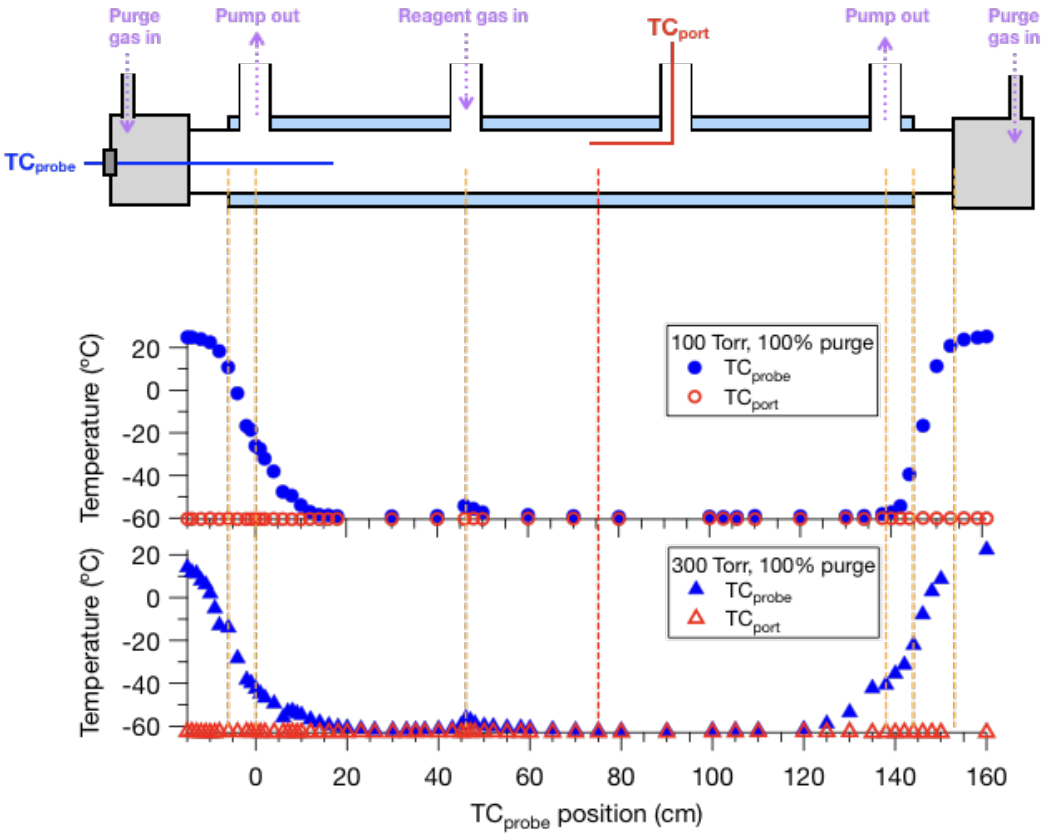

Figure 2.2: Temperature profiles of the cell at P=100 Torr (top panel) and at P=300 Torr (bottom panel) measured by the movable thermocouple probe (TC_{probe}: blue markers). The temperature readings by the stationary thermocouple (TC_{port}: red markers), located at ~13 cm from the edge of the port (marked by red dashed line), are plotted as a function of the probe position indicating that the temperature of the cell remained constant during the experiment. Dashed lines are shown with the schematic of the flow cell to visually map the location of TC_{probe} inside the flow cell where the temperature measurements were taken.

warmer than the right side. The gas was pre-cooled prior to entering the cell except in the small section where the pre-cooling glassware joins to the cell. This was likely causing some heat transfer, which is demonstrated by the small rise in temperature (~3-5°C) located at TC_{probe} position = 46 cm. The deviation in temperature at this position was not considered to be a significant source of error.

The total path length, including the entire mixing region, was ~160 cm at 100 Torr and ~170 cm at 300 Torr. While the path length between the midpoints of the mixing region was ~150 cm for both 100 Torr and 300 Torr, the mixing region extended over a wider volume at 300 Torr: comparing the temperature gradients on the right side of the cell, the length of the mixing region was ~10 cm at 100 Torr and ~30 cm at 300 Torr. As mentioned in Dr. Noell's thesis, these results confirmed

suspicions that the rate constants of the HO_2 and RO_2 self-reactions measured at higher pressures by the IRKS apparatus were unreliable due to the presence of mixing regions in the cell that caused large concentration gradients. The flow conditions that most reliably contained the reagent gas were concluded to be 100 Torr, 10 s residence time, and 100 % purge. Under these conditions, the absorbance of Cl_2 at 320 nm ($\sigma = 2.37 \times 10^{-19}$ cm^2) gave a path length of 143 ± 4 cm. For the kinetics experiments conducted for this thesis, a path length of 147 ± 10 cm was used (an average of the path lengths determined from Cl_2 absorption and from the temperature profile experiments).

The temperature profile measurements also revealed that temperature reading by TC_{probe} depended on how well the thermocouple was positioned in the cell. Due to the lack of coolant flowing in the port through which the thermocouple entered the cell, the thermocouple had to be threaded sufficiently far from the port to get an accurate measurement of the temperature of the gas inside the cell. For example, the temperature readings by TC_{port} when it was positioned 1 cm away from the edge of the port were 10°C warmer than the readings by TC_{probe}. At the same time, care had to be taken to ensure that the thermocouple tip was not touching the wall of the cell or blocking any of the optical paths of the IR, UV, and excimer beams. Due to the physical challenges of getting TC_{port} placed in the correct position, a separate thermocouple was placed inside the jacket of the cell for measuring the cell for all kinetics experiments conducted in this thesis. This thermocouple was in contact with the coolant and was calibrated against the temperature measured by TC_{port}. During calibration, TC_{port} was positioned ~13 cm away from the edge of the port (as in Figure 2.2), where it was clear that TC_{port} was correctly measuring the cell temperature since its temperature readings matched the TC_{probe} readings.

2.3 Photolysis source

Pulsed 351 nm light (pulse width: 20 ns) from a XeF excimer (Lambda Physik Compex 301) operating in the constant energy mode (typically 200 mJ/pulse to 280 mJ/pulse) initiated the radical chemistry by photolyzing Cl_2 molecules in the reagent gas mixture. Dichroic mirrors designed to reflect 351 nm but transmit all other UV wavelengths were used to direct the excimer beam through the length of the flow cell. The excimer beam passed through rectangular apertures (width: 2 cm, length: 2 cm) before entering and after exciting the cell. The divergence of the rectangular profile of the excimer pulse was shown to only cause a small decrease in the power that the effects could be neglected [2]. At the end of the path, the photolysis beam hit a

photodiode, which informed the data acquisition program that an excimer pulse was fired. The laser typically operated at repetition rates to allow for one gas residence time to pass every two excimer pulses; i.e., a 0.2 Hz repetition rate was used for experiments at 100 Torr, which were generally run with a 10 s residence time.

The average excimer pulse energies (50 shot average) at five different high voltage (HV) settings were measured and logged daily prior to data collection to keep a diagnostic record of the laser performance and to determine if a new excimer fill was needed. In constant energy mode, the excimer laser will adjust HV to maintain the user-defined energy; therefore, the laser was always set to the pulse energy measured at the lowest HV (22 kV) to ensure that the same excimer energy was supplied to all the experimental runs conducted on that day. During data collection, the excimer laser operated in the charge-on-demand (COD) mode to minimize the amount of time that the HV was applied to the thyratron, which acts as an active switch to discharge the storage capacitors; i.e., the storage capacitors are only charged upon receiving a trigger signal. Operation in this mode introduced a jitter of 2.5 μs (compared to 2 ns) but significantly minimized pick-up of the electromagnetic field (EMF) noise by the NIR and MIR channels, manifested as large spikes in the detected signals that were observed even when the excimer light was blocked.

2.3.1 Photolysis rate

Experiments were conducted to demonstrate that for reactant flows with a residence time of 10 s, increasing the photolysis rate from 0.1 Hz to 0.2 Hz resulted in no discernible differences in the observed kinetics traces. Therefore, experiments could be conducted twice as fast compared to previous standard operations, enabling more data points to be acquired. Figure 2.3 shows the NIR and UV traces from two different chemical systems using various photolysis rates. Figure 2.3(a) shows that both the NIR and UV (225 nm) data from the HO_2 self-reaction appear unchanged when the photolysis rate is increased from 0.1 to 0.6 Hz. This is not surprising since a large fraction of the reactive molecules would have either reacted away or diffused out of the photolysis volume before the second excimer pulse.

In the case of the $CH_3C(O)CH_2O_2$ self-reaction, the NIR data reveals sensitivity to the photolysis rate, unlike the UV (310 nm) data (Figure 2.3(b)). In the NIR data, although no differences are observed at longer kinetics times (> 3 ms), the fast time-scale formation kinetics appear to substantially deviate from the data collected at 0.1 Hz for photolysis rates greater than 0.5 Hz. Since some of the work in this thesis monitored reactions occurring on the microsecond timescale, a conservative

photolysis rate of 0.2 Hz was chosen to minimize interferences in the kinetics traces.

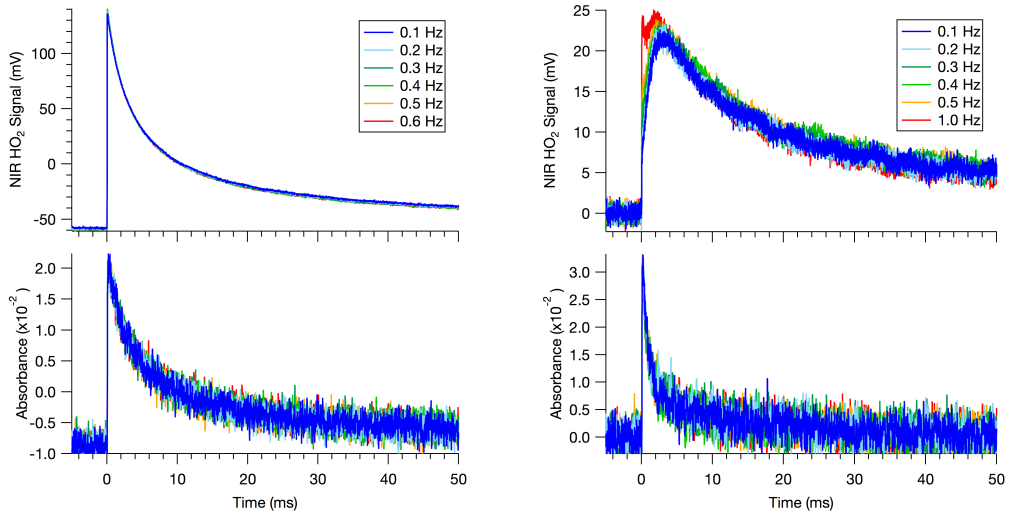

(a) NIR HO_2 (top panel) and 225 nm UV absorbance (bottom panel) signals from the HO_2 self-reaction. $[Cl_2] = 4.5 \times 10^{15}$ molecule cm^{-3}; $[CH_3OH] = 4.2 \times 10^{15}$ molecule cm^{-3}; $[Cl]_0 = 7 \times 10^{13}$ molecule cm^{-3}.

(b) NIR HO_2 (top panel) and 310 nm UV absorbance (bottom panel) signals from the $CH_3C(O)CH_2O_2$ self-reaction. $[Cl_2] = 7.9 \times 10^{15}$ molecule cm^{-3}; $[CH_3C(O)CH_3] = 2.2 \times 10^{16}$ molecule cm^{-3}; $[Cl]_0 = 1.8 \times 10^{14}$ molecule cm^{-3}.

Figure 2.3: NIR HO_2 and UV signals from the (a) HO_2 + HO_2 and (b) $CH_3C(O)CH_2O_2 + CH_3C(O)CH_2O_2$ self reactions taken at T = 298 K, P = 100 Torr, and at various excimer repetition rates. Each trace is an average from 50 excimer shots with sampling rate = 200 kHz and bandwidth = 30 kHz.

2.4 UV detection

Broadband UV light source was co-aligned with and counter-propagated the excimer beam and made one pass through the cell. The UV light passed through the same rectangular apertures used for the excimer beam to ensure that the two beams were co-aligned and that only light that sampled the photolysis volume entered the monochromator. The transmitted UV light passed through a monochromator (Acton Research Corporation Spectra Pro-300i) placed in front of a photomultiplier tube (PMT) for wavelength-specific detection. The high voltage supplied to the PMT was typically between 500 and 580 V. The monochromator was calibrated against atomic emission lines from Hg, Cd, and Zn penray lamps. Baffles were placed on both ends of the flow cell .

2.4.1 Comparison of UV sources

For the experiments outlined in Chapter 7, the UV source was a deuterium (D_2) lamp 150 W, Hamamatsu L1314). For the experiments outlined in Chapters 3 - 6, the D_2 lamp was replaced by a fiber-coupled laser driven light source (LDLS) purchased from Energetiq (EQ-99X-FC-S-UV-10-NA), which provided substantially better stability, power, collimation, as well as longer lamp lifetimes. UV light was coupled into a UV optical fiber (NA = 0.22) with core size of 230 μm and length of 1 m (spectral range: 190 nm - 900 nm). The fiber output was collimated with a UV-enhanced aluminum reflective collimator (240 - 450 nm, Thorlabs RC08SMA-F01).

Figure 2.4 compares the raw UV absorbance signals from the HO_2 self-reaction at λ = 220 nm collected using the D_2 lamp and LDLS under identical experimental conditions (pressure, temperature, flows, etc.) and monochromator slit width (200 μs). The high voltage supplied to the PMT was 580 V when using the D_2 lamp and was lowered to 510 V when using the LDLS to prevent saturation of the PMT. The SNR of the LDLS was over a factor of 3 times higher than that of the D_2 lamp. The RMS noise of the UV absorbance signals taken with the D_2 lamp and the LDLS at a bandwidth of 100 kHz were $\sim 1.9 \times 10^{-1}$ and $\sim 6.5 \times 10^{-2}$, respectively (in absorbance units, normalized to one excimer laser shot). Using a SNR of 2, the minimum detectable absorbance per $Hz^{-1/2}$ (mdA $Hz^{-1/2}$) was mdA $\sim 1.2 \times 10^{-3}$ $Hz^{-1/2}$ for the D_2 lamp and mdA $\sim 4.1 \times 10^{-4}$ $Hz^{-1/2}$ for the LDLS.

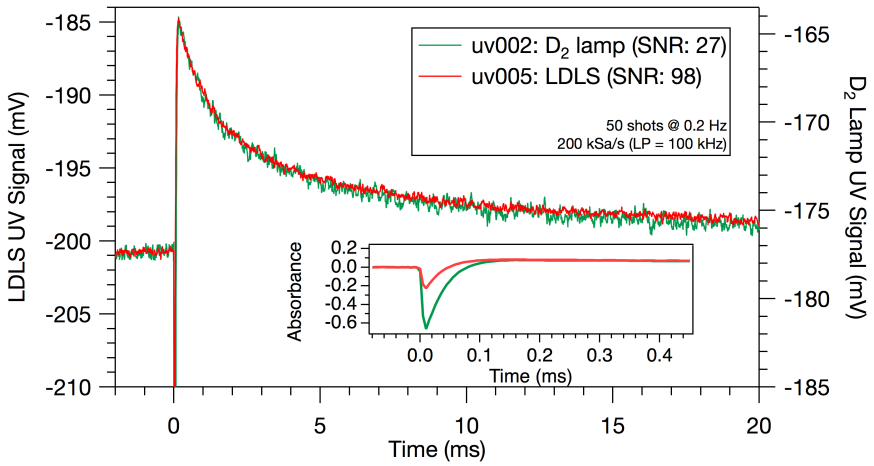

Figure 2.4: Comparison of UV absorbance signals from the HO_2 self reaction ($[HO_2]_0 = 1.6 \times 10^{14}$ molecule cm^{-3}) at 220 nm collected using a D_2 lamp (green) and a LDLS (red). Inset shows a zoomed-in view of the two traces plotted in absorbance units to demonstrate the effect of PMT saturation on the UV signals at t = 0 (photolysis time). T = 294 K; P = 100 Torr.

The inset in Figure 2.4 also shows a spike in the UV signal observed at t=0 due to scattered excimer light being reflected into the monochromator and saturating the PMT. It was verified that the spike disappeared when the excimer light was blocked. As a result, the UV signals were deemed unreliable before 150 μs in most of the UV data that were acquired. Although the signal from the LDLS shows improved PMT recovery time compared to the signal from the D_2 lamp, the observed difference is likely more due to differences in the alignment of the UV light through the monochromator as opposed to the source of the UV light. This can be corroborated by the fact that changes in the PMT recovery time were observed when the UV beam alignment was slightly altered while using the same UV source. A second dichroic was placed near the entrance of the monochromator but could not completely eliminate PMT saturation. As shown in Figure 2.5, the spike in the signal was observed to be more prevalent at lower wavelengths due to less effective filtering of the 351 nm light by the dichroic mirrors (CVI Laser Optics, part number: Y3-0725-45P). Although the absorption cross-section of HO_2 is larger at 220 nm ($\sigma_{220\,\mathrm{nm}} = 3.41 \times 10^{-18}$ cm^2) than at 225 nm ($\sigma_{225\,\mathrm{nm}} = 2.88 \times 10^{-18}$ cm^2), 225 nm was ultimately chosen for HO_2 measurements in the UV since the rise time of the UV signal at 220 nm was almost a factor of 10 times longer than the signal at 225 nm.

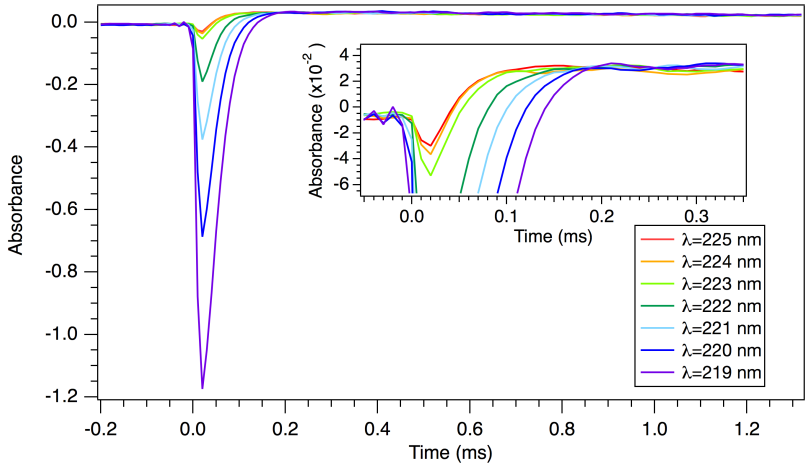

Figure 2.5: Dependence of the PMT recovery time on the UV wavelength. UV signals from the HO_2 self-reaction were taken using the D_2 lamp at T = 298 K, P = 100 Torr, and at varying wavelengths. Inset shows a zoomed-in view of the signals near t = 0 when the excimer laser was fired.

2.4.2 UV signal from LDLS: 42 kHz noise

The UV signals obtained using the LDLS exhibited coherent 42 kHz oscillations that could not be minimized with signal averaging (Figure 2.6). This was due to the

diode laser that heats the Xenon plasma in the lamp being modulated at this frequency to prevent mode-hopping. The typical peak-to-peak amplitude of the oscillation was about 0.5 V_{pp} and is observed in data collected using higher sampling rates and larger low-pass filter bandwidth (> 30 kHz). However, this did not introduce any systematic errors since most of the UV data were analyzed on millisecond timescales and therefore could be numerically filtered (42 kHz notch filter) using the IGOR Pro data analysis software without altering the kinetics profile.

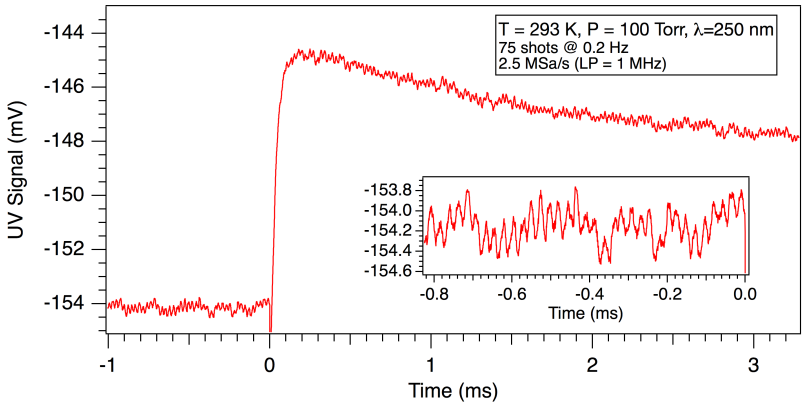

Figure 2.6: Raw UV signal at 250 nm from the HO_2 + $CH_3C(O)O_2$ experiments. Inset shows zoomed-in signal of pre-photolysis baseline to demonstrate 42 kHz noise.

2.5 IR detection

Two continuous-wave (CW) distributed feedback (DFB) lasers, both manufactured by the Microdevices Laboratory (MDL) group at the Jet Propulsion Laboratory (JPL), were used for the NIR and MIR detection of HO_2 and OH radicals, respectively. The NIR laser (3 mW) probed the first overtone of the OH stretch of HO_2 ($2\nu_1$: 6638.2 cm^{-1}), and MIR laser (6 mW) monitored OH radicals by probing the fundamental vibrational transition (ν_1, $P(3.5)f$: 3407.6 cm^{-1}). The frequency tuning range of each laser (NIR: ~6627 $cm^{-1}$to 6641 cm^{-1}, MIR: ~3446 $cm^{-1}$to 3457 cm^{-1}) was limited by the minimum and maximum input current of the lasers, as well as by the maximum temperature at which the diode lasers could be held. The laser frequencies were tuned to the absorption lines by adjusting the injection current provided by the low-noise current supply (ILX Lightwave, Model: LDC-3714 for NIR and Model: LDC-3724 for MIR). The frequency of the NIR laser was calibrated with a wavemeter and the calibration curve shown in Figure 2.7 demonstrates a relatively linear response in the region from 30 mA to 50 mA. This calibration curve was used only as a general guide to convert the laser input current to frequency due

to long-term drift (~several months) in the frequency calibration. The frequency calibration curve for the MIR laser was provided by the MDL group upon delivery and is included in **Fradet2016**.

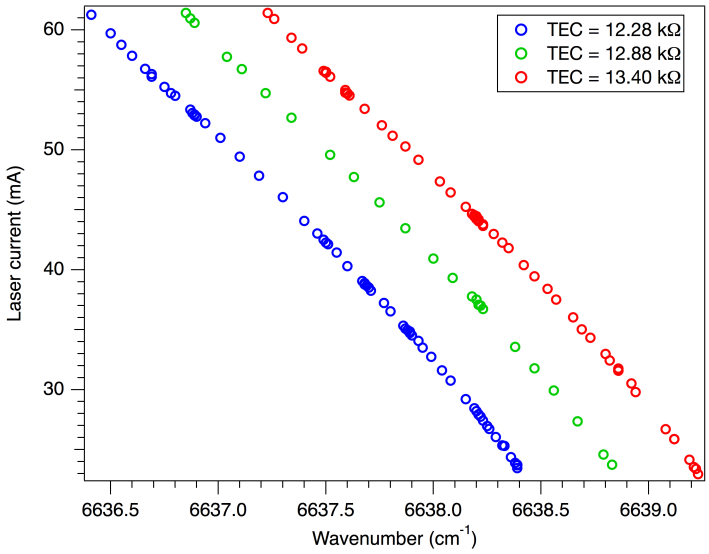

Figure 2.7: Frequency calibration of NIR laser.

2.5.1 Herriott cell

Light from the NIR and MIR lasers was coupled into a Herriott-type optical cavity to configure a multi-pass transit of the IR probes. The lasers were co-aligned with respect to each other and thus shared identical optical paths within the Herriott cell and probed the same photolysis volume. This essentially eliminated systematic error introduced by differences in diffusion effects in different regions of the flow cell. Flip mirrors were used to switch between the two IR lasers and their corresponding detectors.

Two halves of a 2-inch diameter gold-coated spherical mirror (radius of curvature: 2032 mm, substrate: Pyrex), each housed inside either one of the purged aluminum boxes, formed a Herriott cell that folded the IR optical path. The top half of the spherical mirror (i.e., "input mirror") had a 0.125-inch hole to allow the IR beam to enter and exit the optical cavity. The two mirrors were positioned slightly off-axis relative to each other to allow the photolysis and UV beams to pass above and below the back and input Herriott mirrors, respectively. Indium gallium arsenide (InGaAs, New Focus 1811) and indium antimonide (InSb, Infrared Associates IS-0.25) photodiode detectors were used to detect the transmitted NIR and MIR light,

respectively. The InGaAs detector had a built-in preamplifier, and the InSb detector was used with a variable gain high speed current amplifier (Femto DHPCA-100).

The distance between the Herriott mirrors dictated the total number of passes that could be obtained. A mirror separation of about 182 cm was used to achieve 30 passes, which corresponded to an estimated effective path length of 2700 cm. A Helium-Neon (HeNe) laser coaligned to the IR beams was used to visually aid in the optical alignment of the IR lasers. An elliptical spot pattern, characteristic for spherical mirrors, was observed once the mirrors were properly aligned [4]. Alignment was optimized to ensure sufficient separation between each spot to avoid overlap.

2.5.2 Wavelength Modulation and 2f detection electronics

WMS is a very sensitive detection scheme that has widespread applications in time-resolved kinetic experiments. The basic principle behind any modulation technique is the heterodyning, or mixing, of two frequencies to create new frequencies, which are called sidebands. This technique enables operation at higher frequency regimes that are less limited by frequency-dependent noise, such as $1/f$ noise, or pink noise. In fact, shot noise-limited detection sensitivity can often be achieved with WMS.

For the IRKS apparatus, the wavelength of each diode laser was modulated by superimposing an alternating current (AC) component on the direct current (DC) diode injection current. The resulting laser output was modulated in frequency, which translated to an amplitude modulation in the detected absorption. Thus, in the presence of an absorber, the intensity of the laser signal was modulated as the laser was tuned on and off the absorption feature of the absorber. The 2f signal was detected at twice the modulation frequency using sensitive phase- and frequency-dependent electronics. There are two main advantages of using 2f detection. Firstly, the 2nd harmonic component is detected, and this signal is proportional to the 2nd derivative of the absorption line shape; therefore, the wavelength-modulated spectra are symmetric. Secondly, noise from residual amplitude modulation (RAM) is much lower compared to 1f detection. Higher harmonics achieve further suppression of RAM-noise but suffer from reduced peak signal levels. Using 2f detection achieves low RAM while maintaining sufficiently high signal levels.

A schematic of the electronics configuration that was used during the work of this thesis is shown in Figure 2.8, and the detection electronics and components specific to the NIR and MIR lasers are summarized in Table 2.1. Details on how

these specifications were determined will be described in Section 2.5.2.1 and Section 2.5.2.2. A 2 V_{pp}, 6.8 MHz sine wave from an external radio frequency (RF) function generator (Agilent 33120A) was first sent to a power splitter, where one of the output signals was attenuated, isolated (7 MHz), and low-pass filtered before combining with the DC diode laser current at a bias-tee. The other output of the power splitter was frequency-doubled, 90° phase shifted relative to the original signal, and bandpass-filtered (13.6 MHz) before reaching the local oscillator (LO) of the mixer. The voltage-controlled phase shifter enabled adjustment of the demodulation phase angle between the initial modulation signal and the detected signal. The phase shifter also corrected for any shift resulting from the intrinsic time delay of each IC.

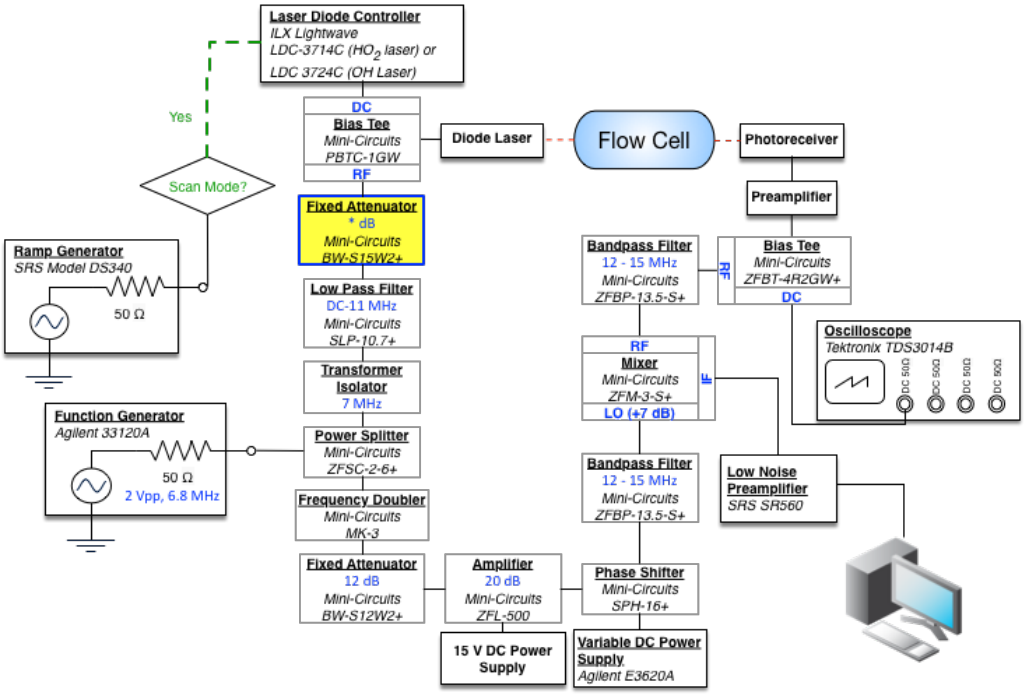

Figure 2.8: Generalized schematic of wavelength modulation (WM) electronics for NIR and MIR lasers. Highlighted attenuator controlled the modulation depth. Optimum value for * was 7 dB and 10 dB for MIR and NIR lasers, respectively.

The DC component of the absorption signal detected by the photoreceiver was removed by a bias-tee and was monitored on an oscilloscope. Meanwhile, the AC component was passed through a bandpass filter (13.6 MHz) prior to demodulation by the mixer, which was referenced to the LO frequency. At the beginning of my thesis work, it was determined that insufficient power (≈800 mV_{pp}) was being delivered to the +7 dB LO, which required an input power of 1.41 V_{pp}. Major improvements

Table 2.1: Specifications of WM electronics, photodiode detectors, and preamplifiers used for 2f detection of NIR and MIR signals.

	NIR	MIR
WM electronics		
Carrier signal attenuation (dB)	10	7
phase shifter voltage (V)	2.63	1.53
Detector	New Focus 1811	Infrared Associates IS-0.25
Material	InGaAs	InSb
Diameter (mm)	0.3	0.25
Preamplifier	Built-in	Femto DHPCA-100
Transimpedance Gain (V/A)	4×10^4	variable, set to 1×10^4 (high speed)
Bandwidth (MHz)	125 MHz	80 MHz
Output Impedance (Ω)	50	50

to the SNR of the demodulated signal were achieved by resolving this issue. The output of the mixer was loss-pass filtered and amplified (Stanford Research Systems SR560) before being sent to the computer. The low-pass filter also determined the overall response time of the spectrometer. For spectroscopy experiments, a sawtooth signal from an external ramp generator (Stanford Research Systems DS340) was applied to the laser injection current to sweep the laser frequency (operation in this configuration will be referred to herein as "scan mode").

Significant improvements were made to the electronics scheme that was first designed and constructed by Dr. Lance Christensen. Specifically, attenuators and amplifiers were strategically added and/or removed to ensure that for each IC, the damage threshold was not being exceeded and that the minimum input power requirement was being met. Improved shielding from EMF pick-up noise was also achieved by using shielded SMA and BNC cables for all connections, minimizing cable lengths, and enclosing the IC components in a die cast aluminum box.

Figure 2.9 compares the 2f signals of the NIR laser operating in scan mode, using the old (specifications found in Dr. Christensen's thesis) and new WM electronics configuration (Figure 2.8) under otherwise identical experimental conditions (e.g. same flows, pressures, laser alignment, etc). The laser frequency was swept across an absorption line of acetylene (C_2H_2) at 6636.89 cm^{-1} (line strength: 1.457×10^{-22} cm^{-1}/(molecule·cm^{-2}) [5]), which lies within the tuning range of the laser (Figure 2.7). The spike in the signal observed at the beginning of the sweep (from 0 to 0.4 ms) is an artificial signal that was always observed when an external ramp signal was applied through the current power supply.

The new electronics configuration resulted in an improvement of over a factor

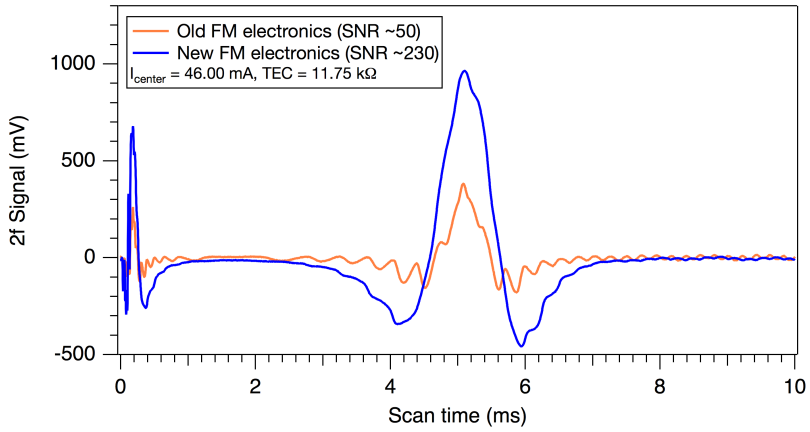

Figure 2.9: Comparison of the 2f signal of a C_2H_2 absorption line using the old and new electronics configuration. $[C_2H_2] = 8 \times 10^{15}$ molecule cm^{-3}; P = 70 Torr (N_2 bath gas), T = 296 K.

of 4 in the signal-to-noise ratio (SNR) and additionally minimized the level of ringing observed in the signal, which was likely due to etalon effects within the Herriott cell. The SNR was calculated by dividing the peak signal by the baseline noise. Improvement in laser alignment through the Herriott cell resulted in further enhancement of the SNR, as discussed in detail in the "IR alignment" subsection. The same configuration of the electronics shown in Figure 2.8 was used for both the NIR and MIR lasers, but the phase shifter voltage and the modulation depth had to be optimized separately for each laser to obtain the maximum 2f signal. The voltage applied to the phase shifter controlled the phase angle between the carrier and the detected 2f signals, while the modulation depth was determined by the level of attenuation to the carrier signal amplitude (highlighted in Figure 2.8).

To inspect the influence of these two parameters on the 2f absorption line shapes and determine their optimum values, a spectrum analyzer was first used to monitor the amplitudes of the 2f sidebands. However, the observed frequency spectra proved nontrivial to analyze because modulating the diode injection current to modulate the optical frequency also resulted in modulating the optical laser power output. As a result, frequency modulation was always accompanied by some residual amplitude modulation.

The optimum phase angle and modulation depth were therefore determined using an alternative, more empirical approach. The laser frequencies were swept across the HO_2 (NIR laser) or OH (MIR laser) line by operating in "scan mode," as will be described in the following sections. The phase angle and modulation depth were systematically adjusted until the best 2f lineshapes were obtained.

2.5.2.1 NIR: HO_2 spectroscopy

For HO_2 detection with the NIR laser, HO_2 was produced by photolyzing gas mixtures containing Cl_2, CH_3OH, O_2, and N_2: photolysis of Cl_2 generates Cl atoms, which react with CH_3OH to form HO_2 in the presence of O_2. Figure 2.10 shows the 2f HO_2 signals for various phase angles (only three shown for clarity) and demonstrates that a phase shifter voltage of 2.63 V yielded the maximum peak signal. It was verified that pre-photolysis signal yielded no absorbance signal. The maximum 2f HO_2 signal was also achieved when the attenuation to the carrier signal was 10 dB.

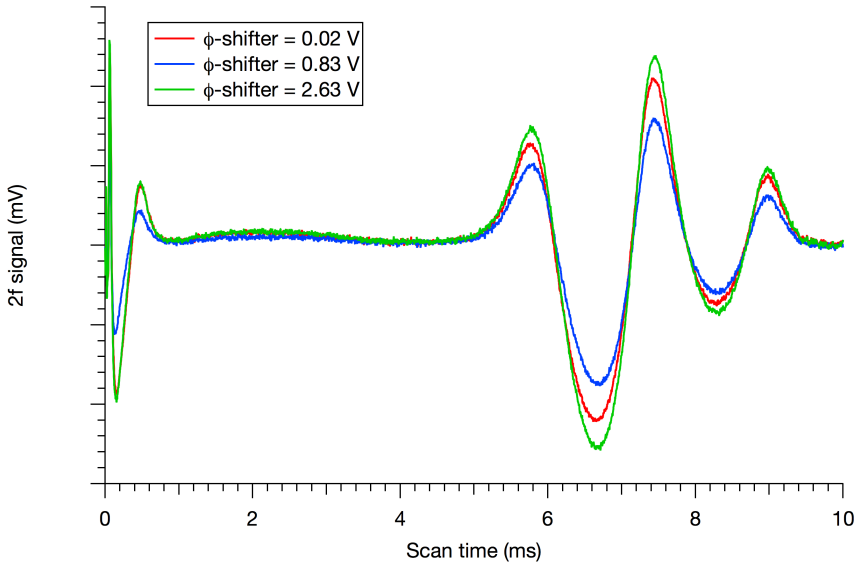

Figure 2.10: 2f HO_2 signals with the laser in scan mode obtained using various values of phase (ϕ) shifter voltages under otherwise identical experimental conditions. Each trace shown is an average of 25 excimer shots and was obtained from the HO_2 self reaction. T = 298 K; P = 100 Torr; concentrations (molecule cm^{-3}): $[Cl_2] = 5.2 \times 10^{15}$; $[CH_3OH] = 3.8 \times 10^{15}$.

2.5.2.2 MIR: OH spectroscopy

OH detection with the MIR was verified by reaction of HO_2 with NO, which is a known source of OH. The maximum OH signal was obtained when a voltage of 1.53 V or higher was applied to the phase shifter (Figure 2.11(a)). Figure 2.11(b) shows the 2f OH signal for various modulation depths. As shown, the 2f lineshape narrows with decreasing modulation depths (i.e., increasing attenuation to the carrier signal) at the expense of decreased amplitude. Figure 2.12 shows the corresponding kinetics traces of OH from HO_2 + NO at each modulation depth with the laser tuned and "parked" (i.e., external ramp signal removed) to the center of the OH absorption line.

The best signal-to-noise was achieved when the attenuation to the carrier signal was between 6 and 7 dB. Since the 2f line shape is narrower with lower modulation depths, 7 dB was ultimately chosen to better avoid potential interferences from unknown absorbers as well as from pressure-broadening.

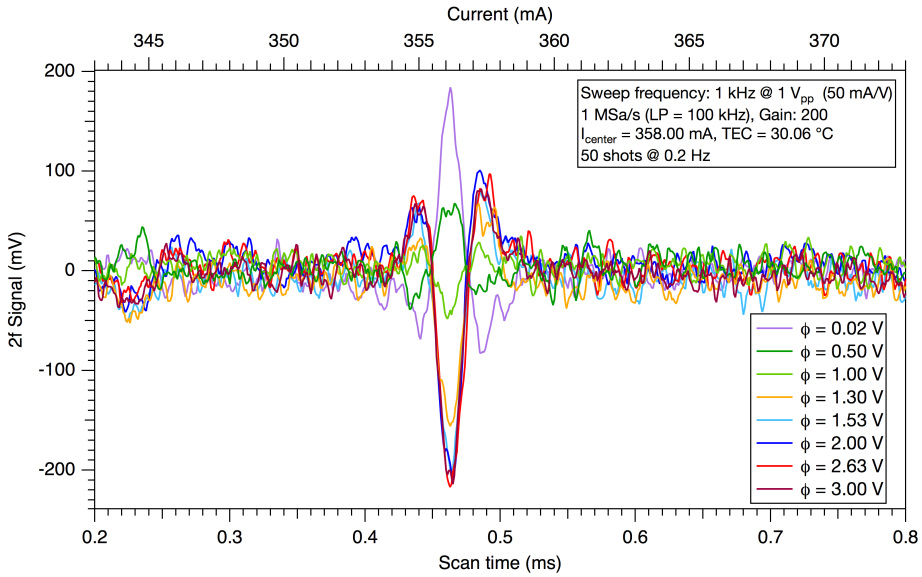

(a) Varying phase angles with fixed modulation depth (attenuation to modulation carrier signal = 10 dB). The baseline has been adjusted to 0 mV for easier comparison.

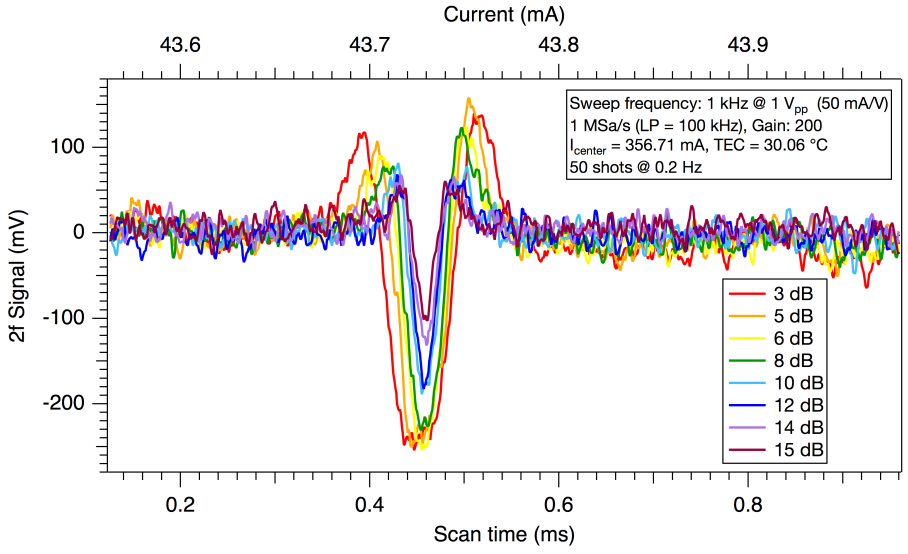

(b) Varying modulation depths with fixed ϕ-shifter voltage = 1.53 V.

Figure 2.11: Frequency sweeps of 2f OH signals obtained using various modulation depths (a) and phase angles (b) under otherwise identical experimental conditions: T = 294 K; P = 100 Torr; $[Cl_2] = 3 \times 10^{15}$ molecule cm^{-3}; $[CH_3OH] = 3.9 \times 10^{15}$ molecule cm^{-3}; $[NO] = 1.2 \times 10^{15}$ molecule cm^{-3}.

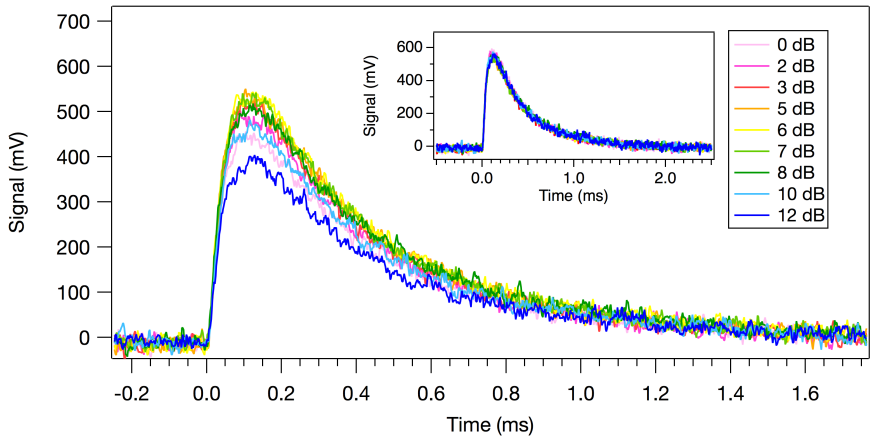

Figure 2.12: 2f OH signal (average of 50 excimer shots) from HO_2 + NO using various modulation depths, but otherwise identical experimental conditions. ϕ-shifter voltage = 1.53 V; T = 294 K; P = 100 Torr; $[Cl_2] = 3 \times 10^{15}$ molecule cm^{-3}; $[CH_3OH] = 3.9 \times 10^{15}$ molecule cm^{-3}; $[NO] = 1.2 \times 10^{15}$ molecule cm^{-3}. Inset shows all data sets scaled to the same maximum to demonstrate that the observed decay rates were identical.

To ensure that that the OH detection in this spectral region would not suffer from interference from other absorbing species, spectral line lists of several molecules were compiled from the HITRAN and PNNL databases, and FTIR spectra of several compounds were also collected with the help of Dr. Xu Zhang using the Nicolet 6700 FTIR spectrometer. The top panel of Figure 2.13 shows good agreement between the measured and literature FTIR spectra of CH_3OH and CH_3CHO, and shows negligible interference to the OH lines in this spectral region. The bottom panel of Figure 2.13 shows the spectral line positions of OH and other species with O−H stretching transitions obtained from HITRAN. The 3407.6 cm^{-1} line of the OH doublet was chosen due to the lack of spectral interference from the weak lines belonging to HO_2, which is revealed in the zoomed-in perspective shown in the inset.

The peak 2f signal from the HO_2 + NO reaction as well as from the HO_2 self-reaction (i.e., [NO] = 0) was measured at various values of the laser injection current. The top panel in Figure 2.14 shows the OH (blue) and HO_2 (red) lines from data collected on the same day. As shown, a weak HO_2 line is observed in the vicinity of one of the OH lines (3407.99 cm^{-1}) from the HO_2 self-reaction data (red triangles), consistent with an HO_2 line at 3408.01 cm^{-1} as listed in the HITRAN database [5]. The kinetics traces of the MIR signals at these laser frequencies were identical to those collected using the NIR laser (tuned to the HO_2 overtone) under identical conditions, verifying that the MIR signals corresponded to HO_2 absorption (Figure 2.15). The other OH line located at 3406.71 cm^{-1} had no spectral interference from

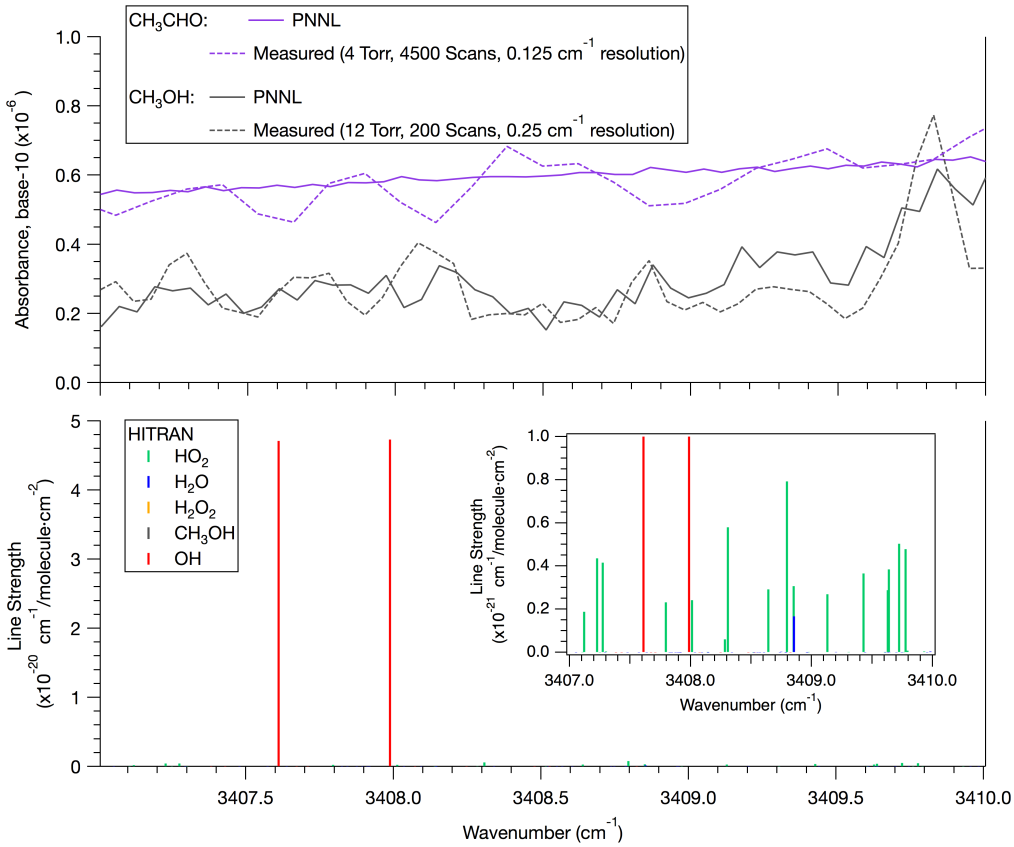

Figure 2.13: OH stretch lines of various relevant species. Top panel compares the measured FTIR spectra of CH_3OH and CH_3CHO (dashed lines) with those from the PNNL database (solid lines). Note that the measured spectra has been scaled for clarity. Bottom panel shows spectral line positions of OH near 3407 cm^{-1} and other species with O–H stretching transitions. The zoomed-in perspective shown in the inset shows the presence of several weak transitions belonging to HO_2 and H_2O in the vicinity of the OH lines.

HO_2 and was therefore chosen for detecting OH.

The MIR laser frequency calibration tended to vary slightly day-to-day. The bottom panel shows data points from the HO_2 self-reaction collected on two different days with varying phase angles. The data represented by the orange and green markers were collected on the same day using different phase angles; as shown, the phase angle had no effect on the frequency calibration. However, comparing either of these data points to the red markers, which were data collected on a different day, shows a shift in the frequency calibration; therefore, the laser frequency was re-tuned to the OH line daily by sweeping the laser current and maximizing the peak OH signal during the calibration runs using HO_2 + NO.

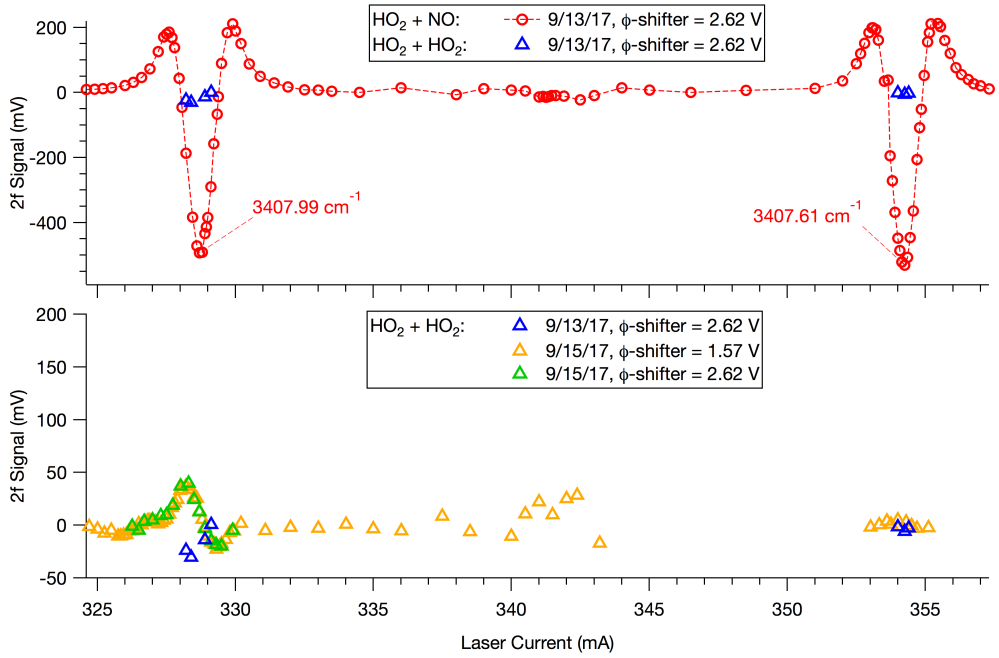

Figure 2.14: 2f signals of OH and HO_2 lines obtained using the MIR laser. T = 294 K; P = 100 Torr; $[Cl_2] = 2.2 \times 10^{15}$ molecule cm^{-3}; $[CH_3OH] = 3.8 \times 10^{15}$ molecule cm^{-3}; [NO] = 1.5×10^{15} molecule cm^{-3} (red), [NO] = 0 (blue, orange, and green).

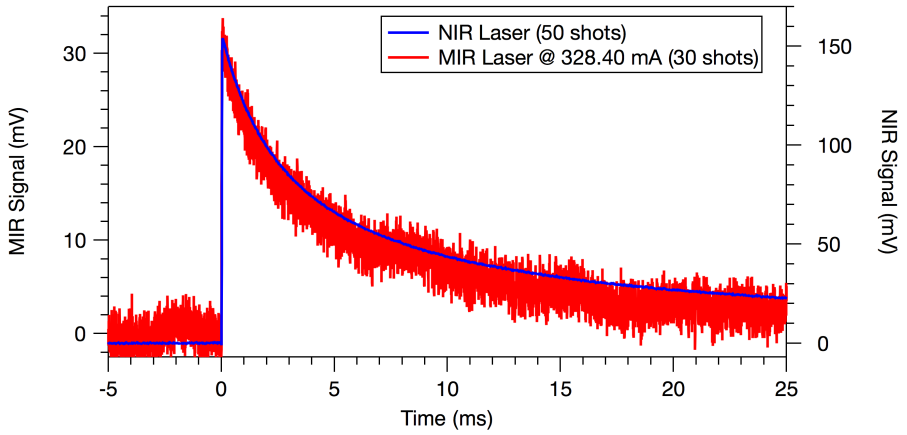

Figure 2.15: 2f signals of HO_2 from the HO_2 self-reaction obtained using the NIR and MIR lasers. T = 294 K; P = 100 Torr; $[Cl_2] = 2.2 \times 10^{15}$ molecule cm^{-3}; $[CH_3OH] = 3.8 \times 10^{15}$ molecule cm^{-3}.

2.5.3 IR calibration and sensitivities

Since WM spectroscopy (WMS) only measures the relative changes in concentration, both the NIR and MIR lasers required calibration to obtain absolute concentrations. The NIR laser was calibrated against the UV absorption cross-

section of HO_2 at 225 nm ($\sigma_{HO_2}(\lambda = 225\ \text{nm}) = 2.88 \times 10^{-18}\ \text{cm}^2\ \text{molecule}^{-1}$ [6]) by simultaneously measuring the NIR and UV decay signals when HO_2 was the only peroxy radical present. Despite a different geometric overlap, the IR and UV probe beams should capture the same physical processes at relatively short timescales (< 20 ms); i.e., before diffusion becomes a significant loss process. The MIR laser was then calibrated against the HO_2 laser by titration with NO, which produces a known amount of OH radicals provided that the HO_2 and NO concentrations are known. Calibration of both lasers was highly sensitive to the optical alignment and varied day-to-day. Therefore, these calibrations were repeated on a daily basis.

The calibration changed daily as it is highly dependent on the alignment of each laser. The flip mirror that was used to switch between the NIR and MIR lasers caused small changes in alignment and was found to change the calibration factor by more than 10%. Therefore, for experiments utilizing both the HO_2 and OH lasers (Chapter 4 and onwards), the following protocol was implemented to avoid any movement of optics in between the calibration and experimental runs using the same laser:

1. Optimize NIR alignment
2. HO_2 laser calibration
3. Switch to MIR laser and optimize MIR alignment
4. OH laser calibration
5. Run experiments with MIR laser for OH detection
6. Switch to NIR laser for HO_2 detection and repeat all experiments conducted in Step #5

This procedure minimized uncertainties in the calibration factors since the flip mirrors were only used to guide the OH beam into the HO_2 laser path and not vice versa.

2.5.3.1 HO_2 laser calibration

Since both the absorption cross-section of HO_2 in the UV and the kinetics of the HO_2 self-reaction are well-characterized, the 2f signal of the NIR laser was converted to an absolute scale by simultaneously fitting both the NIR and UV ($\lambda = 225$ nm) traces with a bi-molecular decay using the kinetics modeling program, FACSIMILE. UV absorbance by both HO_2 and H_2O_2 ($\sigma_{H_2O_2}(\lambda = 225\ \text{nm}) = 2.17 \times 10^{-19}\ \text{cm}^2$ molecule^{-1} [6]) were included in the model. Figure 2.16 shows an example of the NIR and UV kinetics traces. The NIR signal in mV, S_{NIR}, is directly proportional to the HO_2 concentration:

$$[HO_2] = V_{M,HO_2} \times S_{NIR} \tag{2.1}$$

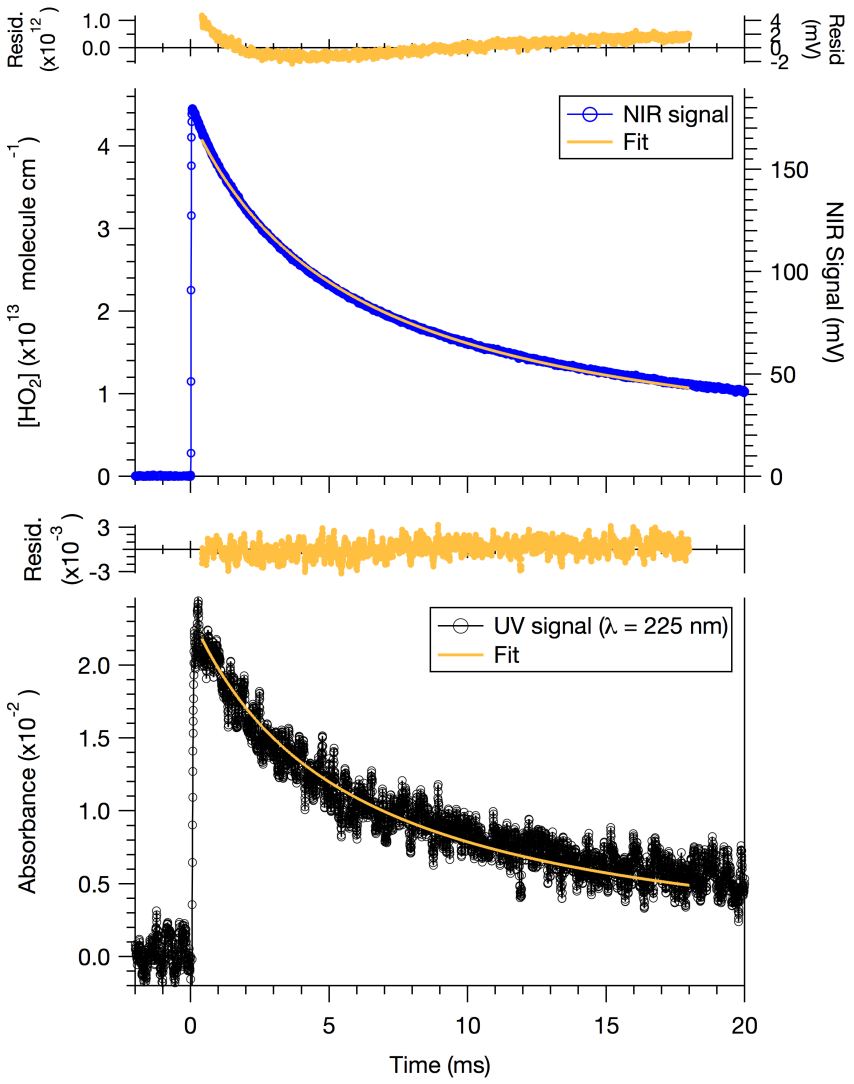

Figure 2.16: Calibration of the NIR laser against UV absorption at 225 nm using HO_2 self-reaction kinetics at T = 296 K and P = 100 Torr. Fits to data and residuals are shown in green. $[Cl]_0 = 4.4 \times 10^{13}$ molecule cm^{-3}.

where the voltage multiplier, V_{M,HO_2}, is the calibration factor. To demonstrate that this was a robust method of calibrating the NIR laser, V_{M,HO_2} was calculated from data collected (on the same day) using various concentrations of Cl_2, the radical precursor. As expected, the values of V_{M,HO_2} were independent of the Cl_2 concentration.

It should be noted, however, that changes in V_{M,HO_2} were sometimes observed over the course of the day, although this was not always the case. On the days that V_{M,HO_2} did change, V_{M,HO_2} always appeared to get smaller (i.e., to have better sensitivity) over time. Comparison of the corresponding UV signals were identical,

indicating that the changes in V_{M,HO_2} were not due to changes in the chemistry, but due to changes in the IR alignment. This may have been caused by slight changes in the mirror positions as the mounts expanded and compressed with changes in temperature inside the flow cell. On days when experiments were conducted at low temperatures, there was no way to determine the V_{M,HO_2} at the end of the day because the cell could not actively be brought back to room temperature. The procedure for recalibrating the HO_2 laser in this case was to scale the peak IR signal of the $HO_2 + HO_2$ reaction collected at low temperature to that of the data obtained at room temperature using the same Cl_2 concentrations. The corresponding UV data from the room and low-temperature runs were compared to verify that no changes in the initial radical concentration were observed.

Other unknown factors also contributed to changes in V_{M,HO_2}: for example, changes in V_{M,HO_2} were also observed over the course of the day independently of temperature, although this was not always the case. V_{M,HO_2} appeared to change more rapidly soon after the diode laser was first switched on, and eventually reached a constant value after about 3 hours. Therefore, the laser was switched on several hours prior to collecting data to allow sufficient warm-up time.

2.5.3.2 OH laser calibration

The FM signal from the OH laser was calibrated to an absolute scale from the kinetics traces of HO_2 and OH from the reaction of HO_2 + NO, which produces OH with unity yield (R1).

$$HO_2 + NO \longrightarrow OH + NO_2 \tag{R1}$$

The MIR 2f signal in mV, S_{MIR}, is directly proportional to the OH concentration:

$$[OH] = V_{M,OH} \times S_{MIR} \tag{2.2}$$

where the voltage multiplier, $V_{M,OH}$, is the calibration factor for the MIR laser.

The MIR calibration runs were carried out immediately after the $HO_2 + HO_2$ NIR calibration runs. Excess amounts of NO and CH_3OH relative to the initial radical concentration were used: typical concentrations of NO and CH_3OH were [NO]~1×10^{15} molecule cm^{-3} and [CH_3OH] ~5×10^{15} molecule cm^{-3}. The primary loss processes of OH were reactions with NO (R2) and with CH_3OH (R3).

$$OH + NO \xrightarrow{M} HONO \tag{R2}$$

$$OH + CH_3OH \longrightarrow CH_2OH + H_2O \quad \text{(R3a)}$$
$$\longrightarrow CH_3O + H_2O \quad \text{(R3b)}$$

From the second-order rate constant of R3 (k_3(298 K) = 9.1×10^{-13} cm^3 molecule^{-1} s^{-1}) and the effective second-order rate constant of R2 at P = 100 Torr (k_2(298 K, 100 Torr) = 1.8×10^{-12} cm^3 molecule^{-1} s^{-1}) [6], the approximate lifetime of OH was ~700 μs.

Since the rate constant of this reaction is known (k_1(298 K) = 8.0×10^{-12} cm^3 molecule^{-1} s^{-1} [6]), and all the loss processes of OH are well-characterized, the absolute OH concentration could be determined from the formation and subsequent decay of the OH signal, provided that the initial radical concentrations are known. The initial radical concentration, $[Cl]_0$, was assumed to be the same as that obtained from the HO_2 self-reaction runs when the same $[Cl_2]$ was used. Since the OH decays rapidly via R2 and R3, the two lowest initial radical concentrations ($[Cl]_0 \sim (5-7) \times 10^{13}$ molecule cm^{-3}) were used in order to accurately model the peak OH signal. The sampling rate was also increased to 2.5 MHz capture a sufficient number of data points. Figure 2.17 shows an example of the NIR and MIR signals from the HO_2 + NO reaction.

2.5.4 IR alignment

The sensitivity of the IR lasers was highly dependent on the initial alignment. It has been found previously that the HO_2 signal suffers from a baseline shift post-photolysis [3], and the same was observed for the OH signal. The degree to which the baseline shifted depended heavily on the alignment of the lasers. Figure 2.18 shows the NIR direct absorption (D.A.) and 2f signals of HO_2 from the HO_2 self-reaction taken before (red traces) and after (blue traces) adjustments to the NIR laser alignment. As shown, the quality of the D.A. signal and baseline is extremely sensitive to the alignment. For the corresponding 2f signals, the baseline problem is not observed and the qualitative kinetics features remain uncompromised; however, the sensitivity is enhanced with improved alignment as evidenced by the differences in the SNR of the observed signals.

Further improvements to the IR laser alignment were achieved by refined collimation and spatial filtering of the IR beam prior to entering the Herriott cell. In addition to having a good baseline in the observed signal, two additional criteria for good alignment were established: minimal ringing in the observed signals and good

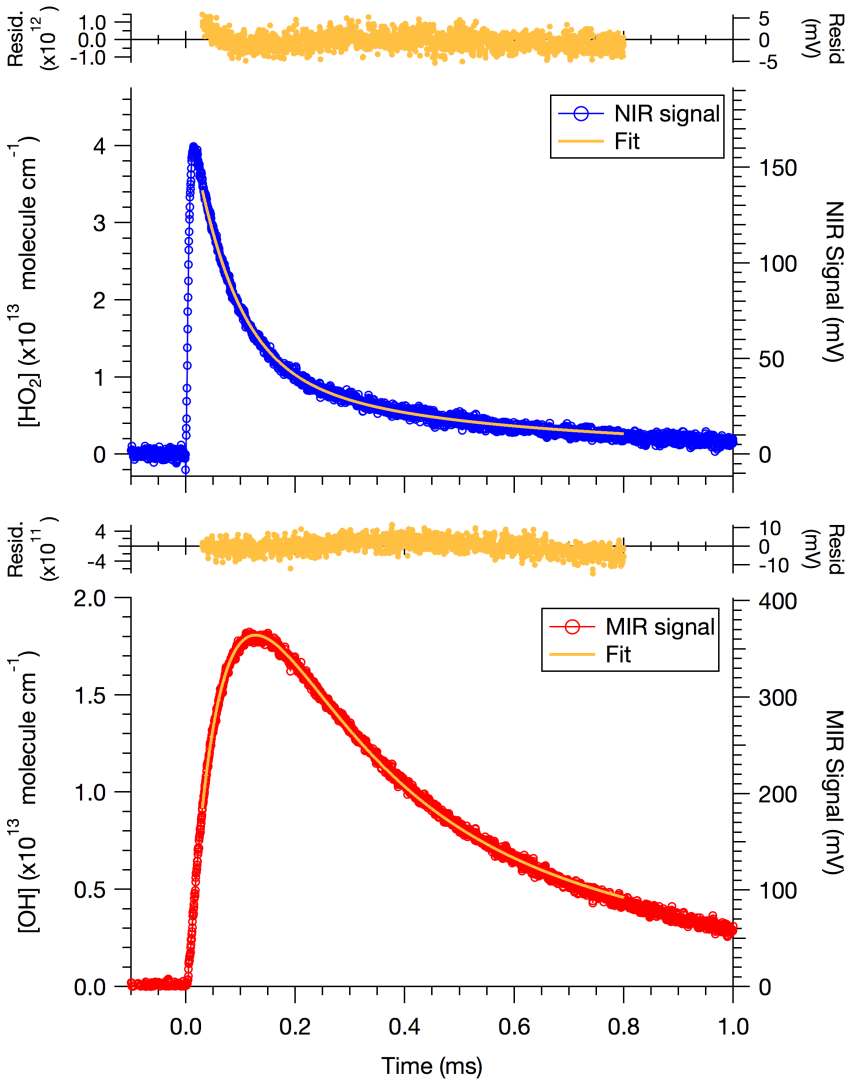

Figure 2.17: Calibration of the MIR laser against NIR laser using HO_2 + NO kinetics at T = 296 K and P = 100 Torr. Fits to data and residuals are shown in green. $[Cl]_0 = 4.4 \times 10^{13}$ molecule cm^{-3}.

agreement in the kinetics decay between the D.A. and 2f signals. Figure 2.19 shows examples of the D.A. and 2f signals in the NIR (Figure 2.19(a)) and MIR (Figure 2.19(b)) from what was considered good alignment.

For the HO_2 laser, a small shift in the baseline of the 2f signal after photolysis made a negligible difference in the kinetics, since the amount of HO_2 produced in our experiments was large and displaced far from the baseline. Furthermore, with the exception of the HO_2 + NO calibration runs, the HO_2 lifetime was typically a lot longer (> 2 ms) in most of our experiments, and the HO_2 kinetics profile rarely decayed all the way to zero. Therefore, any baseline shift was not apparent unless

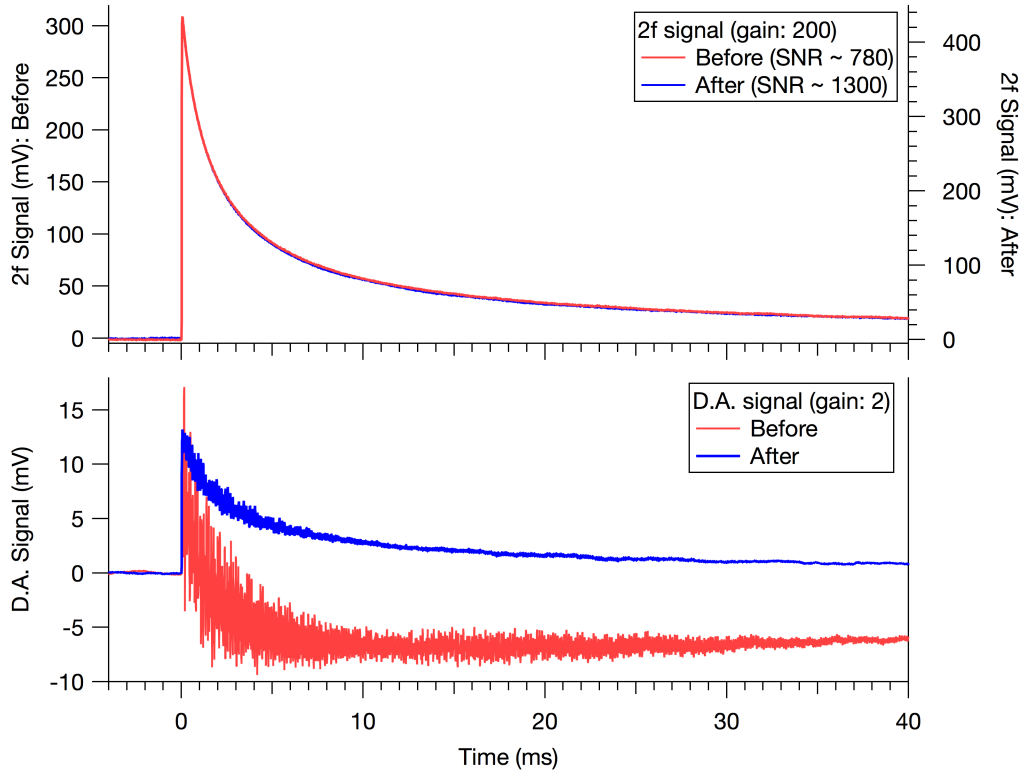

Figure 2.18: D.A. (bottom) and 2f signals (top) from the HO_2 self-reaction under identical experimental conditions: $[CH_3OH] = 4.1 \times 10^{15}$ molecule cm^{-3}, $[Cl_2] = 5.9 \times 10^{15}$ molecule cm^{-3}; T = 297 K; P = 100 Torr; sampling rate: 200 kHz, low-pass filter: 30 kHz. Red and blue traces are signals taken before and after, respectively, adjustments were made to the NIR laser alignment. Traces of the same color were taken using identical laser alignment.

the HO_2 decayed very rapidly or the pre- and post-excimer pulse NIR signal was observed with no radicals present.

Alignment of the OH laser was much more difficult because the baseline of the post-trigger signal had to be accurate. The OH kinetics profile was a lot closer to the baseline due to the much smaller amount of OH present in the cell in addition to the fast decay of OH (< 2 ms). This meant that any changes in the baseline post-photolysis made a big difference in the fitted yields of OH. Figure 2.20 shows some example OH 2f signals obtained from the HO_2 + $CH_3C(O)O_2$ experiments. Some data had a noisy baseline before and after photolysis with a low-frequency component in the noise (top trace). These data had to be thrown out, as the true baseline could not be established. For other data, the post-photolysis baseline clearly represented the true baseline (bottom three traces) and was thus used instead of the pre-photolysis baseline.

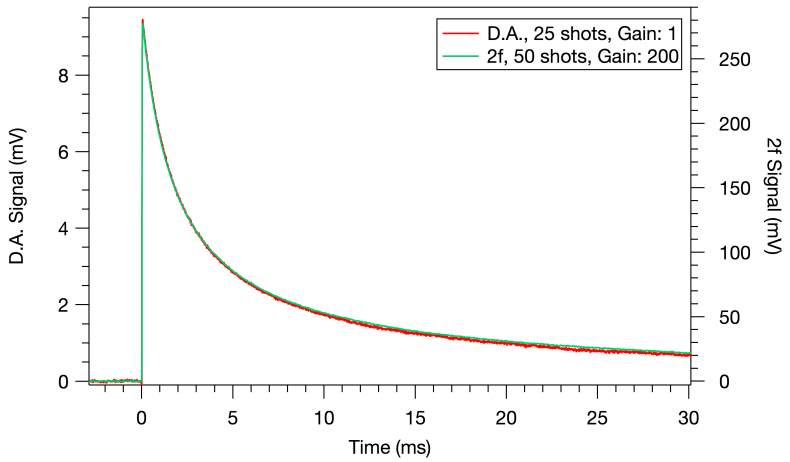

(a) HO_2 signal from HO_2 + HO_2 at T = 294 K and P = 100 Torr. $[CH_3OH] = 3.9 \times 10^{15}$ molecule cm^{-3}, $[Cl_2] = 4.6 \times 10^{15}$ molecule cm^{-3}.

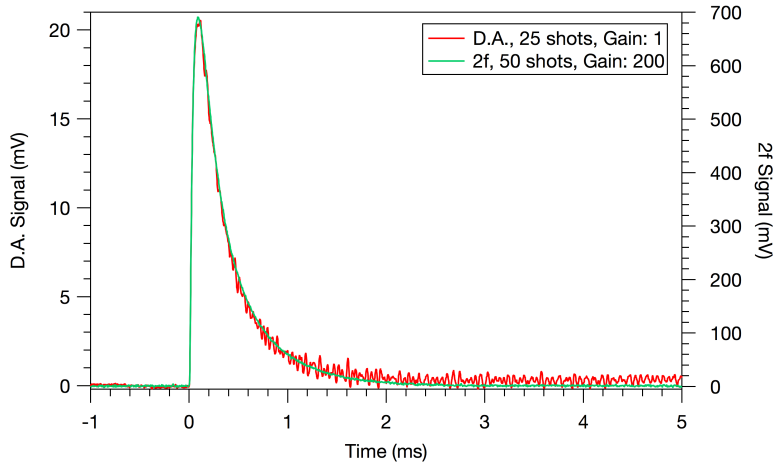

(b) OH signal from HO_2 + NO at T = 294 K and P = 100 Torr. $[CH_3OH] = 3.9 \times 10^{15}$ molecule cm^{-3}, $[Cl_2] = 6.1 \times 10^{15}$ molecule cm^{-3}, $[NO] = 1.4 \times 10^{15}$ molecule cm^{-3}.

Figure 2.19: Examples of D.A. (red) and 2f (green) signals from well-aligned NIR (a) and MIR (b) lasers.

The best way to optimize both the HO_2 and OH alignment was to first monitor the D.A. signals of both the HO_2 and OH traces using HO_2 + NO. Using this reaction, the presence of a baseline shift in the HO_2 D.A. signal could be monitored since the HO_2 decay from reaction with NO is fast. Furthermore, although the frequency calibration of the HO_2 laser remained relatively constant over several months, the OH laser frequency calibration appeared to shift day-to-day; therefore, this procedure also served as a way to tune the OH laser frequency to the OH line, which is more difficult than using the 2f signal due to the more complex 2f lineshape. The alignment

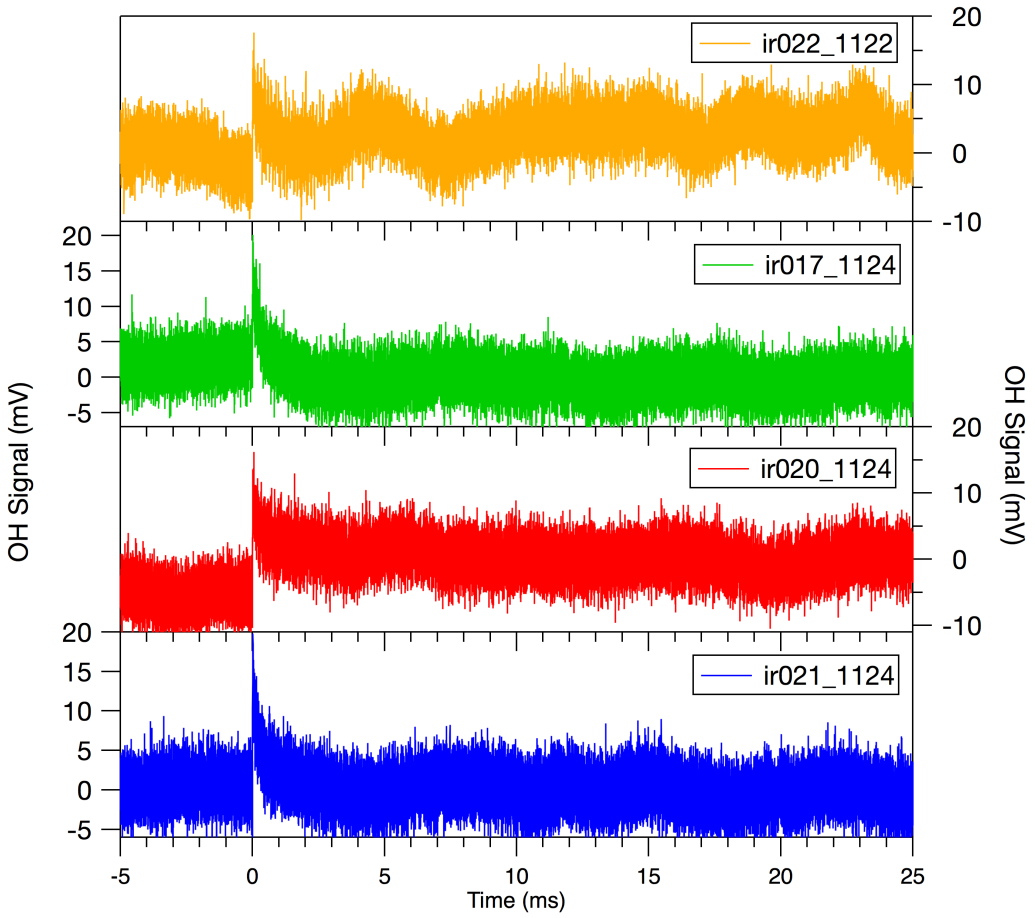

Figure 2.20: Examples of OH signals from the HO_2 + $CH_3C(O)O_2$ reaction. Sampling rate: 2.5 MHz; low-pass filter: 1 MHz.The top trace is an example of an ill-defined baseline, while the bottom three traces exhibit clear baselines (albeit with a shift after photolysis at t = 0 ms). Signals similar to the bottom three traces were still considered good data and the post-photolysis baseline was used, starting at kinetic times much later than the OH decay appeared to have completed; i.e., starting from 10 ms.

of the lasers was adjusted until the post-photolysis baseline closely matched the pre-trigger baseline, while also minimizing ringing in the IR signal.

The main sources of noise in the OH laser appeared to be alignment and proper grounding of the Femto pre-amplifier. Although various designs of grounding and shielding were tested, the performance in the SNR appeared to vary day-to-day. Capacitive conductance of the shielded BNC cable connecting the InSb detector to the FM detection electronics was also observed, and large noise from ground-loops could only be removed if the cable was in physical contact with the laser table.

2.5.4.1 Sensitivity

V_{M,HO_2} and $V_{M,OH}$ were also diagnostic tools for comparing the sensitivities of the NIR and MIR lasers, respectively. For the NIR laser, V_{M,HO_2} was typically $\sim 2.5 \times 10^{11}$ molecule cm^{-3} mV^{-1}. The root-mean-square (RMS) noise of the NIR laser taken with a 30 kHz bandwidth was approximately 2 mV (normalized to one excimer laser shot), which gave a noise-equivalent HO_2 concentration per Hz$^{-1/2}$ (NEC_{HO_2} Hz$^{-1/2}$) of $\sim 2.9 \times 10^9$ molecule cm^{-3} Hz$^{-1/2}$. $V_{M,OH}$ for the MIR laser was typically $\sim 5 \times 10^{10}$ molecule cm^{-3} mV^{-1}. The root-mean-square (RMS) noise of the MIR laser taken with a 1 MHz bandwidth was ~10 mV (normalized to one excimer laser shot), which gave a noise-equivalent OH concentration per Hz$^{-1/2}$ (NEC_{OH} Hz$^{-1/2}$) of $\sim 5.0 \times 10^8$ molecule cm^{-3} Hz$^{-1/2}$. The mdA Hz$^{-1/2}$ of the NIR and MIR lasers (mdA_{NIR} Hz$^{-1/2}$ and mdA_{MIR} Hz$^{-1/2}$, respectively) using SNR = 2, an estimated NIR path length of 2700 cm [2], and estimated absorption cross-sections σ_{HO_2} $\sim 4 \times 10^{-20}$ [2] cm^2 and σ_{OH} $\sim 2 \times 10^{-18}$ cm^2 (calculated from [5] line parameters assuming a Lorentzian profile), were mdA_{NIR} $\sim 6.2 \times 10^{-7}$ Hz$^{-1/2}$ and mdA_{MIR} $\sim 5.4 \times 10^{-6}$ Hz$^{-1/2}$ (normalized to one excimer laser shot). Data taken with the NIR laser was typically signal-averaged for 40 to 50 excimer laser shots, while data taken with the MIR laser was usually signal-averaged for 75 to 85 excimer laser shots. Table 2.2 compares the sensitivities of the IR probes and UV probes.

Table 2.2: Comparison of the minimum detectable absorbance per Hz$^{-1/2}$ (mdA Hz$^{-1/2}$) for the IR and UV probes, normalized to one excimer laser shot.

Source	mdA Hz$^{-1/2}$
UV (D_2 lamp)	1.2×10^{-3}
UV (LDLS)	4.1×10^{-4}
NIR (6638.2 cm^{-1})	6.2×10^{-7}
MIR (3407.8 cm^{-1})	6.5×10^{-6}

It should be noted that further improvement on the OH sensitivity is expected in future work using the IRKS apparatus. The coatings on the Herriott mirrors at the time of data collection for this thesis were optimized for NIR reflectivity and had limited MIR reflectivity. Therefore, further optimization of the optics is expected to maximize the OH sensitivity and lower the detection limit of the MIR probe. At the time of this writing, the Herriott mirrors have been recoated to maximize reflectivity in both the NIR and MIR with an average reflectivity R > 97% for the range ~3390 cm^{-1} to 6667 cm^{-1}. Additional testing of the newly coated mirrors will be carried out in the future.

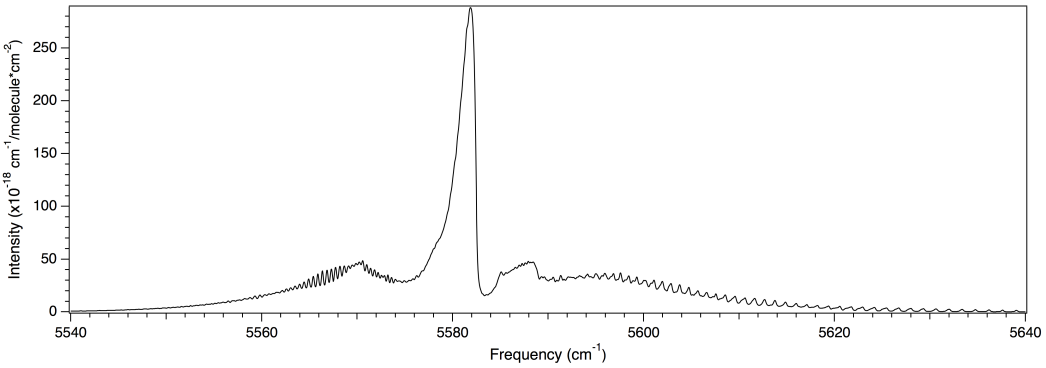

Figure 2.21: Simulated spectrum (unresolved, with added 0.3 cm^{-1} linewidth) of the trans conformer of $CH_3C(O)O_2$ showing the strong Q branch. Rotational constants from Zalyubovsky et al. [7] were used for the simulations.

2.6 Additional diode lasers

This section describes two additional DFB lasers that extensively characterized but were unfortunately not implemented into the IRKS apparatus due to limited sensitivity and performance. Nonetheless, extensive characterization of both lasers were carried out and the following information may be useful in the future for other applications.

2.6.1 5583.5 cm^{-1} laser

A 1791 nm (5583.5 cm^{-1}) DFB laser (Nanoplus) was purchased with the intent of detecting $CH_3C(O)O_2$ radicals for the studies on the HO_2 + $CH_3C(O)O_2$ reaction. The spectrum of the $\tilde{A}^2A'$–$\tilde{X}^2A''$ electronic transition of the $CH_3C(O)O_2$ radical has been measured previously by Zalyubovsky et al. [7]. Using the reported rotational constants and origin of 5582.5(5) cm^{-1}, the rotational spectrum of $CH_3C(O)O_2$ has been simulated using the PGOPHER program. Figure 2.21 shows the unresolved Q branch of the trans conformer of $CH_3C(O)O_2$ obtained from the simulation.

2.6.1.1 Frequency calibration

The frequency of the laser was calibrated against CH_4 and HO_2 which has known absorption lines in this spectral region [5]. The top panel in Figure 2.22 shows the direction absorption signals of the laser in scan mode with HO_2 or CH_4 present in the flow cell. The bottom panel in Figure 2.22 shows the corresponding absorption lines of CH_4 and HO_2 obtained from the HITRAN database. The middle panel shows the resolved rotational lines near the origin of the $\tilde{A}^2A'$–$\tilde{X}^2A''$ electronic transition of $CH_3C(O)O_2$.

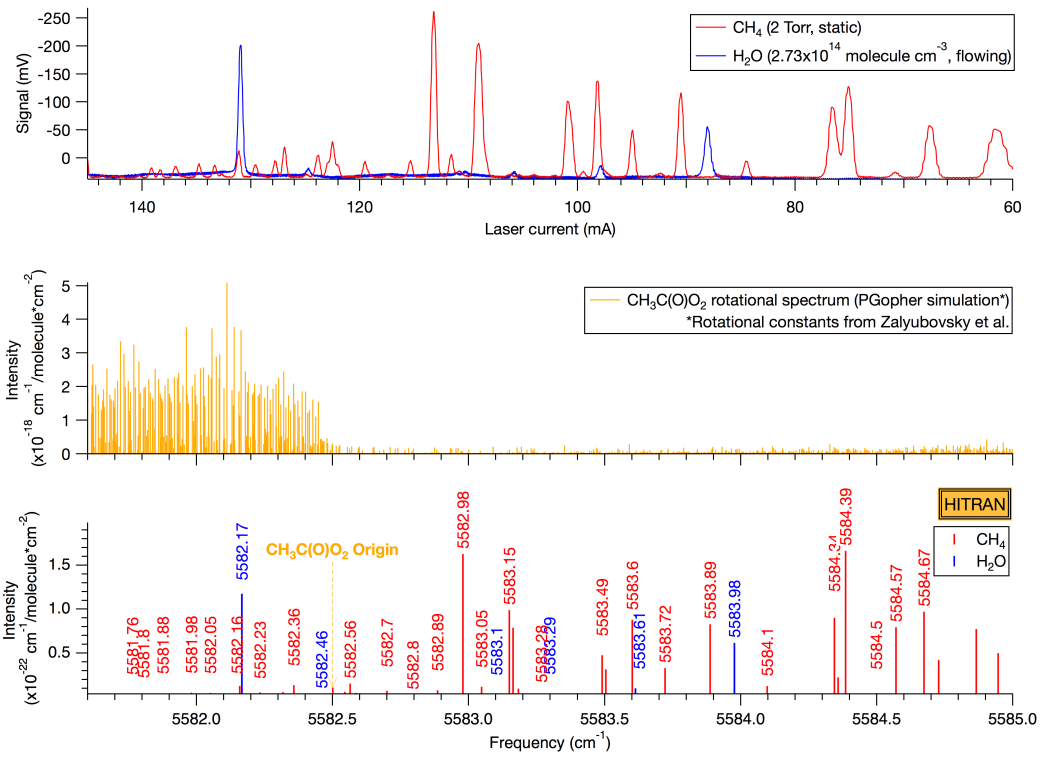

Figure 2.22: Direct absorption signal of RO_2 laser in scan mode (top panel). Ramp signal: 5.5 V_{pp}, 100 Hz. The lower two panels show the simulated rotational lines of $CH_3C(O)O_2$ using the rotational constants from Zalyubovsky et al. [7] (middle panel) and the spectral lines of CH_4 and H_2O from the HITRAN database (bottom panel).

Figure 2.23 shows the 5583.5 cm^{-1} laser injection current plotted against the absorption lines of CH_4 and HO_2. The data points near the expected region of the origin band of $CH_3C(O)O_2$ were fitted to a line to approximate the calibration curve for the laser (Equation 2.3):

$$\tilde{\nu} = -0.046I + 5588.2 \tag{2.3}$$

where $\tilde{\nu}$ is the wavenumber (cm^{-1}) and I is the laser current in mA.

The ramp signal to the laser current was then removed to operate the laser in park mode to locate and optimize the direct absorption signal of $CH_3C(O)O_2$. Photolysis of a reagent gas mixture containing $Cl_2/CH_3CHO/O_2/N_2$ at 351 nm was used to generate $CH_3C(O)O_2$ radicals (see Chapter 4 and/or Chapter 5 for more details on the radical generation chemistry). Using Equation 2.3 as a guide, the laser was tuned to the approximate region of the edge of the Q branch. The laser injection current was manually adjusted, and the time-resolved absorption signals were collected at

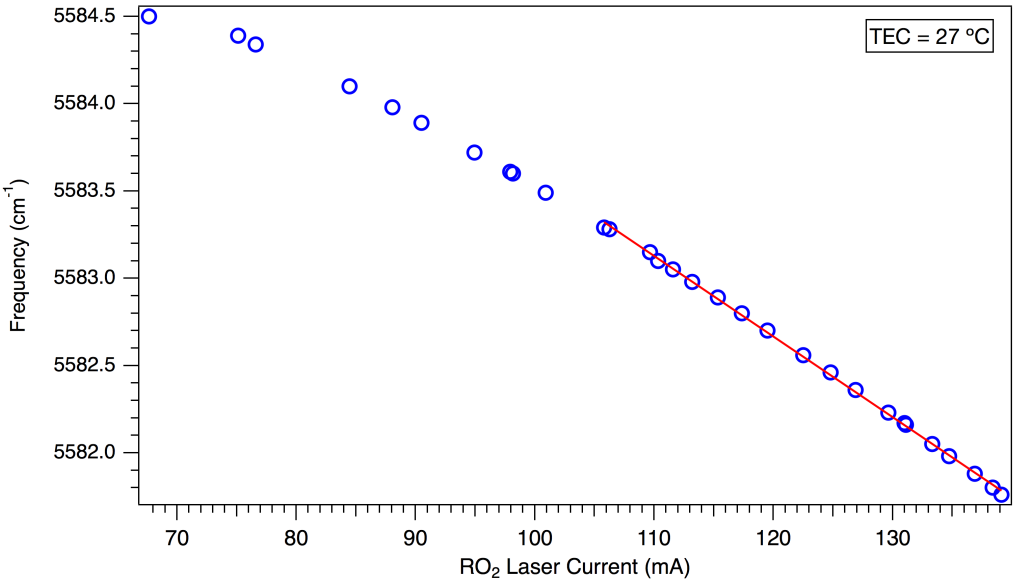

Figure 2.23: Frequency calibration of the 5583.5 cm^{-1} laser using the absorption lines of CH_4 and HO_2. TEC for the diode laser was set to 27°C.

each current setting.

Figure 2.24 shows the time-resolved direct absorption signal obtained at various laser currents. Data from only four selected current settings are shown for clarity. The figure shows an increase in the absorption signal as the current is increased from 90 mA to 110 mA. Above 110 mA, no changes in the absorption signal were observed, suggesting that the band edge was centered between approximately 100 mA and 110 mA. No absorption signals were observed if either Cl_2 were removed from the cell or if the excimer laser light was blocked from entering the cell.

A high frequency "ringing" noise observed in the data was highly dependent on the quality of the laser beam alignment through the cell. Although various attempts were made to optimize the alignment, the noise could not completely be removed. Nonetheless, application of wavelength modulation was expected to resolve these issues, as was observed in the case of the NIR HO_2 and MIR OH lasers.

With the approximate band edge of $CH_3C(O)O_2$ located from the time-resolved direct absorption measurements, wavelength modulation was applied to the laser. The 2f signals of $CH_3C(O)O_2$ at three wavelengths near the band edge were collected for various phase shifter voltages and modulation depths.

The three panels in Figure 2.25 shows the 2f signals of $CH_3C(O)O_2$ obtained using three different laser currents (i.e., optical frequencies) near the band edge of $CH_3C(O)O_2$. At each current setting, data were collected using various modulation amplitudes, which were achieved by changing the level of attenuation to the carrier

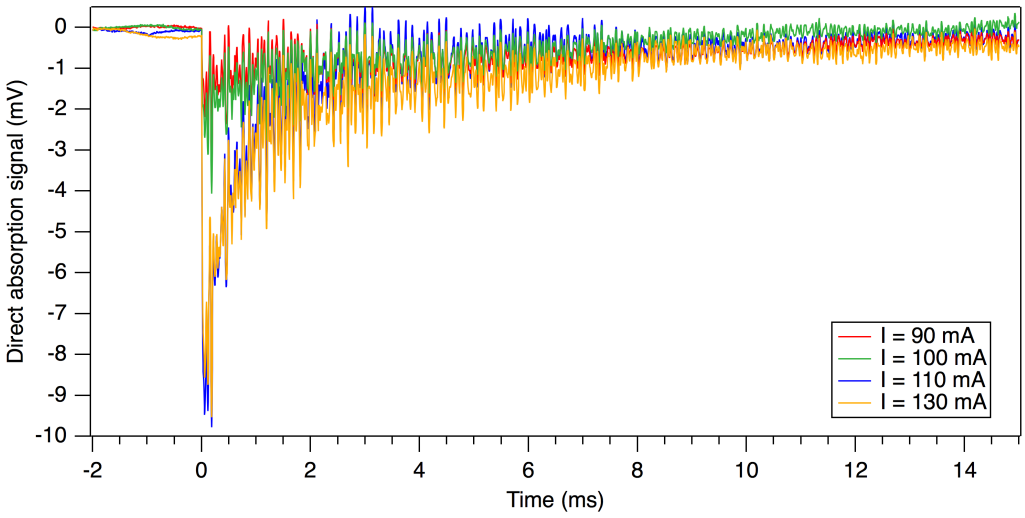

Figure 2.24: Direct absorption signals of $CH_3C(O)O_2$ using various laser injection currents (only four shown for clarity). Each trace was an average of 50 excimer shots and data was collected at a sampling rate of 200 kSa/s at a 30 kHz bandwidth. T = 298 K; P = 100 Torr; $[Cl_2] = 4.4 \times 10^{15}$ molecule cm^{-3}; $[CH_3CHO] = 9.3 \times 10^{15}$ molecule cm^{-3}.

signal. All other experimental conditions (e.g., flows, pressures, temperatures, excimer pulse energy, etc) were kept the same. Only three different modulation amplitudes are shown in the figure for clarity. The amplitude and frequency of the carrier signal were fixed at the same values as were used for the NIR HO_2 laser, and the phase shifter voltage was fixed at 0.83 V for this part of the experiment. From the figure, the peak 2f signals are obtained using the largest modulation depth (i.e., 0 dB attenuation to the carrier signal). However, application of wavelength modulation spectroscopy did not appear to completely remove the high frequency noise that was observed in the direct absorption signal.

To determine the optimum phase shifter voltage, data were collected for various phase shifter voltages using the maximum modulation depth (0 dB attenuation). Since the peak signal shown in Figure 2.25 was observed to occur beyond 110 mA, data was collected using laser currents ranging from 108 to 112 mA for this part of the experiment. All other experimental conditions were otherwise identical. Figure 2.26 shows the 2f signals of $CH_3C(O)O_2$ obtained at three different laser current settings using various phase shifter voltages (only three are shown for clarity). The data showed that the peak 2f signal was obtained using a phase shifter voltage of 0.76 V.

Using the optimum phase shifter voltage of 0.76 V and the maximum modulation depth (0 dB attenuation), the 2f signals of $CH_3C(O)O_2$ at various laser currents were

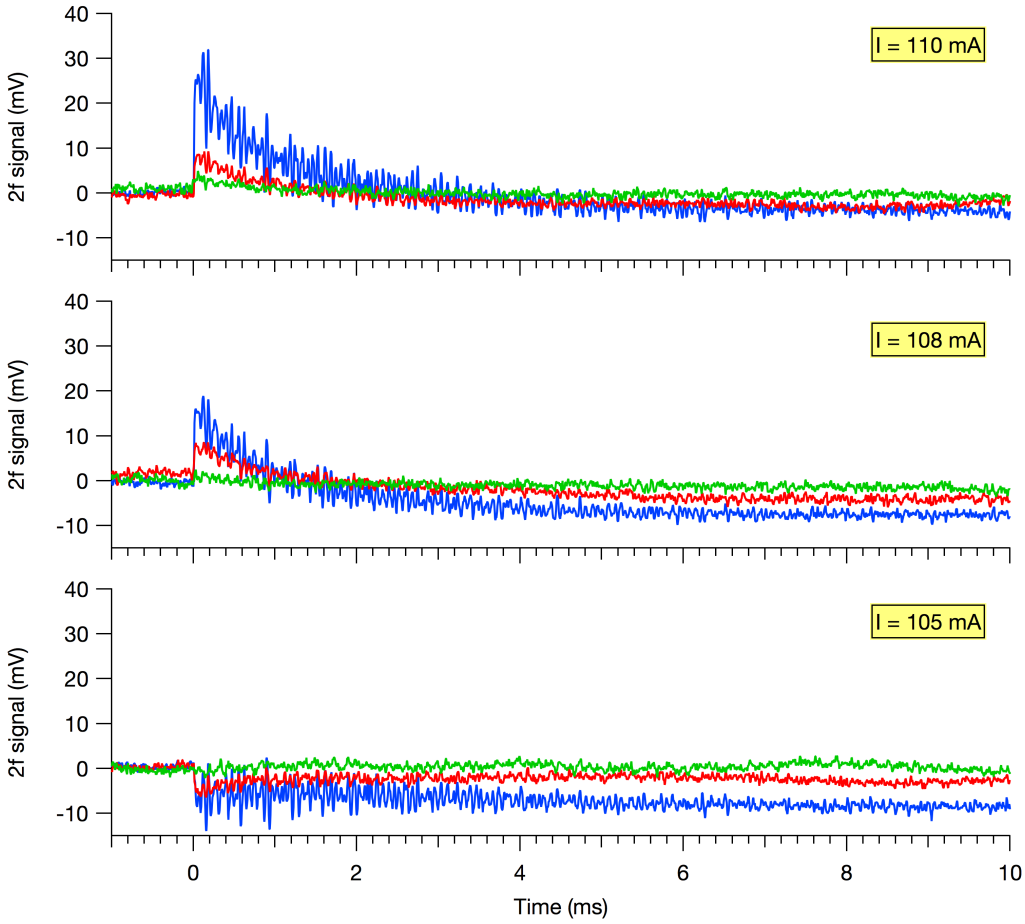

Figure 2.25: 2f signals of $CH_3C(O)O_2$ obtained at three laser currents (i.e., optical frequencies) near the band edge of $CH_3C(O)O_2$: 110 mA (top panel), 108 mA (middle panel) and 105 mA (bottom panel). Note that decreasing the current corresponds to increasing wavenumber cm^{-1}. For each current setting, data were collected for various levels of attenuation to the carrier signal: 0 dB (blue), 3 dB (red), and 10 dB (green). The phase shifter voltage was fixed at 0.83 V for all of the data shown here. Each trace was an average of 50 excimer shots and data was collected at a sampling rate of 200 kSa/s at a 30 kHz bandwidth. T = 298 K; P = 100 Torr; $[Cl_2] = 4.4 \times 10^{15}$ molecule cm^{-3}; $[CH_3CHO] = 7.2 \times 10^{15}$ molecule cm^{-3}.

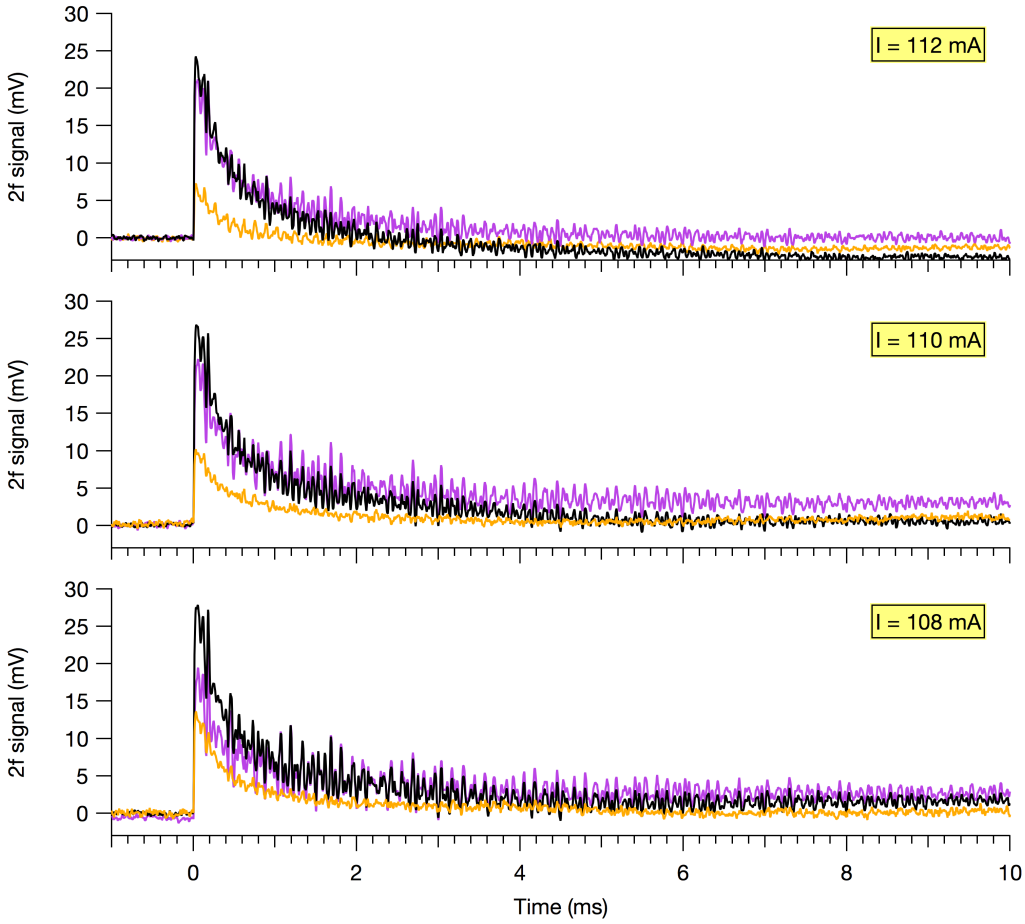

Figure 2.26: 2f signals of $CH_3C(O)O_2$ obtained at three laser currents (i.e., optical frequencies) near the band edge of $CH_3C(O)O_2$: 112 mA (top panel), 110 mA (middle panel) and 108 mA (bottom panel). Note that decreasing the current corresponds to increasing wavenumber cm^{-1}. For each current setting, data were collected for various phase shifter voltages: 0.0 V (orange), 0.76 V (black), and 1.0 V (purple). . The modulation depth was fixed using 0 dB attenuation to the carrier signal for all the data shown here. Each trace was an average of 50 excimer shots, and data was collected at a sampling rate of 200 kSa/s at a 30 kHz bandwidth. T = 298 K; P = 100 Torr; $[Cl_2] = 4.5 \times 10^{15}$ molecule cm^{-3}; $[CH_3CHO] = 7.2 \times 10^{15}$ molecule cm^{-3}.

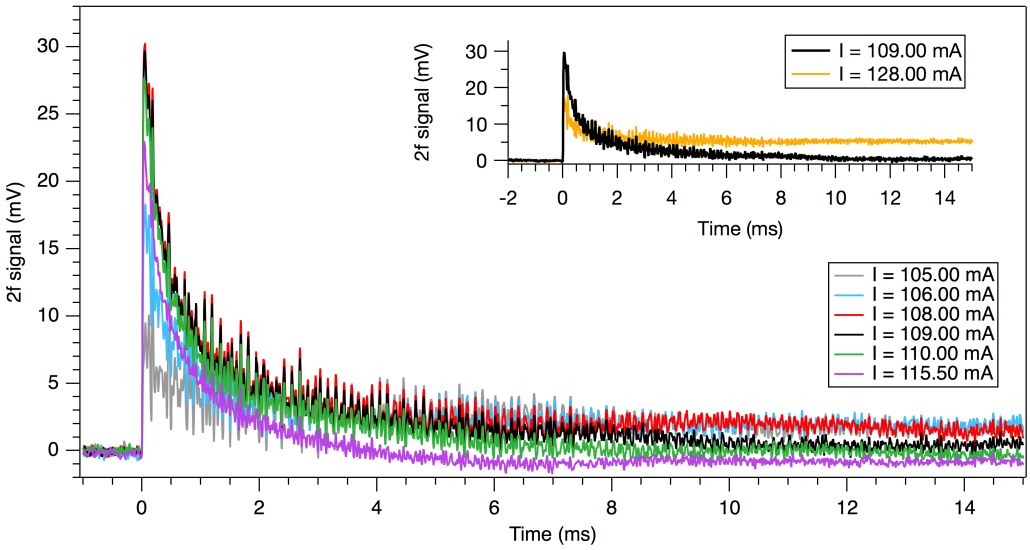

Figure 2.27: 2f signals of $CH_3C(O)O_2$ using various laser injection currents (only seven shown for clarity) with ϕ-shifter = 0.76 V and 0 dB attenuation to the carrier signal. The signal obtained using I = 128 mA displayed in the inset shows a constant absorption signal for t > 2 ms after photolysis. The signal obtained using I = 109 mA is also shown in the inset for comparison. Each trace was an average of 50 excimer shots, and data was collected at a sampling rate of 200 kSa/s at a 30 kHz bandwidth. T = 298 K; P = 100 Torr; $[Cl_2] = 4.5 \times 10^{15}$ molecule cm^{-3}; $[CH_3CHO] = 2.7 \times 10^{15}$ molecule cm^{-3}.

obtained to fine-tune the peak 2f signal. Figure 2.27 shows the time-resolved 2f signals of $CH_3C(O)O_2$ using laser currents in the range 105 -128 mA (only seven are shown for clarity). The maximum peak 2f signal was obtained with the laser current set to 108 mA or 109 mA. At the highest current setting (I = 128 mA), a persisting absorption signal was observed for t > 2 ms after photolysis. An absorption line of H_2O is located at 5582.17 cm^{-1} [5], and H_2O is a product of the oxidation of CH_3CHO by OH. As discussed in Chapter 5, OH is generated from the reaction of $CH_3CO + O_2$. However, the H_2O line strength ($\sim 10^{-22}$ cm^{-1}/molecule·cm^{-2} [5]) is orders of magnitude smaller than that of $CH_3C(O)O_2$ and the OH yield at 100 Torr was approximately 3%. Thus, the reaction of OH + CH_3CHO alone cannot fully explain the observed absorption signal if the signal were attributed to absorbance by H_2O; however, further investigation was beyond the scope of this work.

Although the optimum WM conditions were characterized for this laser, kinetics analysis of the data proved to be challenging due to inconsistent decay rates that were observed in different data sets even when all other experimental conditions were identical. These problems were specific to the 5583.5 cm^{-1} laser, as the corresponding data collected using the NIR HO_2 and MIR (3408 cm^{-1}) OH lasers

yielded consistent results.

Furthermore, the post-photolysis shift in the baseline that was observed for the 3408 cm^{-1} laser as described previously was also observed for the 5583.5 cm^{-1} laser, and was far more apparent and variable day-to-day. In addition, WM could not completely remove the high frequency noise that was observed. These problems may be due to the laser itself, or to the fact that wavelength modulation was applied across a band edge as opposed to across an absorption line.

Finally, we could not identify a robust method for calibrating the 2f signal of the 5583.5 cm^{-1} laser. The method that was used was the $CH_3C(O)O_2$ self reaction, with the initial radical concentration determined from a prior NIR HO_2 laser calibration run using the HO_2 self reaction. However, consistent values of the calibration factor could not be obtained due to the rapid and complex secondary chemistry, as discussed in Chapters 5 and 4.

2.6.2 3447 cm^{-1} laser

This laser was manufactured by the Microdevices Laboratory (MDL) at JPL and was originally intended to be used for measuring OH radicals; however, strong interference from several weak H_2O absorption lines resulted in insufficient sensitivity to OH radicals. The upper panel of Figure 2.28 compares the raw detected signal (with no wavelength modulation applied) at various laser injection currents measured with the cell in vacuum and with a small amount of H_2O vapor introduced into the flow cell. With the cell in vacuum, the figure exhibits several broad peaks near the expected absorption lines of OH (the lower panel in the figure shows the absorption lines of H_2O and OH obtained from the HITRAN database [5]). Observation of additional absorbance with the introduction of H_2O into the cell provided further verification that the observed peaks were the pressure-broadened absorption lines of H_2O in the ambient air, which attenuated more than 70% of the optical power.

A large portion of the laser beam path was purged by installing a series of PVC tubes that were sealed at the ends by thin PFA films, which were transparent in the MIR. A small but constant flow of dry N_2 gas was introduced into the network of PVC tubing to remove as much H_2O as possible from the laser beam path. Although the laser power almost doubled as a result, the improvement was still insufficient to provide the necessary sensitivity for detecting OH radicals accurately. Furthermore, working with this laser using the PVC tubing proved to be difficult due to the limited space on the optical table and the congested beam paths, which caused a part of the beam to be clipped. Additionally, any changes in the relative humidity in the room

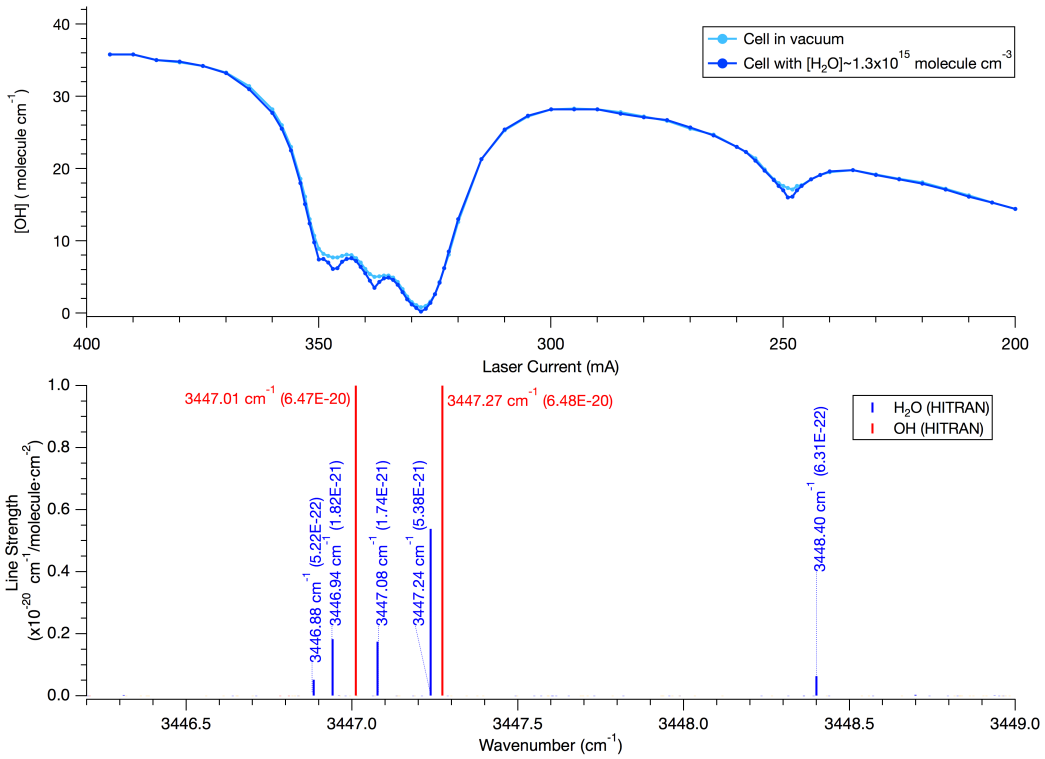

Figure 2.28: Top panel: raw detected signals of the 3447 cm^{-1} laser measured at various injection currents (i.e., optical frequency) with the cell under vacuum (light blue) and with a small amount of HO_2 introduced into the cell (dark blue). Lower panel: Absorption lines of H_2O and OH from the HITRAN database [5]. The numbers in parentheses for each line are the line intensities. Note that the OH line intensities are off the scale of the plot.

translated to a noisier 2f signal of OH.

The 3447.77 cm^{-1} OH line was more severely impacted by the adjacent H_2O absorption line, which attenuated more than 90% of the optical power of the laser without any of the beam path being purged by dry nitrogen. The other OH line at 3447.01 cm^{-1} was relatively more isolated from H_2O absorption lines, but suffered from an additional spectral interference by a previously unidentified weak HO_2 line. With only HO_2 present in the cell, a time-dependent absorption signal was observed and had an identical decay rate as the corresponding decay signal obtained using the NIR HO_2 laser. Although this HO_2 line was significantly weaker than the OH line, this spectral interference was problematic for the experimental studies on HO_2 + $CH_3C(O)O_2$ (Chapter 4), where the OH yield was small and HO_2 was in much higher excess.

The sensitivity of the 3447 cm^{-1} laser to OH radicals was more than one order of magnitude lower than the 3408 cm^{-1} laser, which was ultimately used for OH

detection: the NEC_{OH} $Hz^{-1/2}$ (normalized to one excimer shot) of the 3447 cm^{-1} laser was $\sim 1.4 \times 10^{10}$ molecule cm^{-3} $Hz^{-1/2}$. Using an estimated absorption cross-section of σ_{OH} $\sim 3 \times 10^{-18}$ cm^2 (calculated from [5] line parameters assuming a Lorentzian profile), this corresponded to a minimum detectable absorbance of mdA $\sim 2.2 \times 10^{-4}$ $Hz^{-1/2}$.

Because of insufficient sensitivity to OH radicals and spectral interference by other molecules, this laser could not be used for its initial intended purposes. However, the laser was later used in a separate project to measure absolute water vapor concentrations for work that was carried out at the Advanced Light Source (ALS) investigating the effects of water vapor on the kinetics of the β-hydroxyethylperoxy (β-HEP) self-reaction (project lead by graduate student Matt Smarte) and the reaction of β-HEP with NO (project lead by post-doc Fred Winiberg).

References

[1] Christensen, L. E.; Okumura, M.; Sander, S. P.; Friedl, R. R.; Miller, C. E.; Sloan, J. J. Measurements of the Rate Constant of HO2 + NO2 + N2 → HO2NO2 + N2 Using Near-Infrared Wavelength-Modulation Spectroscopy and UV-Visible Absorption Spectroscopy. *The Journal of Physical Chemistry A* **2004**, *108*, 80–91.

[2] Christensen, L. E. Laboratory Studies of Atmospherically Important Gas-Phase Peroxy Radical Reactions., Ph.D. Pasadena, CA: California Institute of Technology, 2002.

[3] Noell, A. C. Laboratory Studies of the Self and Cross Reactions of Atmospheric Peroxy Radicals., Ph.D. Pasadena, CA: California Institute of Technology, 2009.

[4] Herriott, D. R.; Schulte, H. J. Folded Optical Delay Lines. *Applied Optics* **1965**, *4*, 883–889.

[5] HITRAN on the Web. `http://hitran.org/`.

[6] Sander, S. P.; Abbat, J.; Barker, J.R.; Burkholder, J.B.; Huie, R.E.; Kolb, C.E.; Kurylo, M.J.; Wilmouth, D.M.; Orkin, V.L.; Wine, P.H. *Chemical Kinetics and Photochemical Data for Use in Atmospheric Studies, Evaluation No. 18*; Jet Propulsion Laboratory, Pasadena: JPL Publication 15-10, 2015.

[7] Zalyubovsky, S. J.; Glover, B. G.; Miller, T. A. Cavity Ringdown Spectroscopy of the $\tilde{A}$ - X Electronic Transition of the CH3C(O)O2 Radical. *The Journal of Physical Chemistry A* **2003**, *107*, 7704–7712.

Chapter 3

HYDROGEN-BONDED ADDUCTS OF HO_2 WITH CH_3OH AND WITH CH_3CHO: EQUILIBRIUM CONSTANTS AND RATE ENHANCEMENT EFFECTS ON THE HO_2 SELF REACTION

Abstract

Hydrogen-bonded adducts, or complexes, of HO_2 have been known to impact the kinetics of HO_2 reactions. In this work, the equilibrium constants for the adducts formed from the reaction of HO_2 with CH_3OH ($K_{c,M}$) and CH_3CHO ($K_{c,A}$) were determined over the temperature range T = 220 - 270 K and T = 230 - 280 K, respectively, at a total pressure of 100 Torr in N_2. The rapid loss of HO_2 from adduct formation was detected using infrared kinetic spectroscopy (IRKS), which employed NIR 2f wavelength modulation spectroscopy (WMS) for sensitive and selective detection of HO_2. The thermodynamics parameters for the complexation reactions were also determined from a van 't Hoff analysis of the data. The change in enthalpy and entropy for the association reaction of HO_2 with CH_3OH was $\Delta_r H^\circ_{250\text{ K}} = -28.1 \pm 0.4$ kJ mol^{-1} and $\Delta_r S^\circ_{250\text{ K}} = -64.9 \pm 1.6$ J mol^{-1}, respectively. For the association reaction of HO_2 with CH_3CHO, the thermodynamic parameters were $\Delta_r H^\circ_{255\text{ K}} = -15 \pm 2$ kJ mol^{-1} and $\Delta_r S^\circ_{255\text{ K}} = -14 \pm 9$ J mol^{-1}, respectively.

The impact of these hydrogen bonded adducts on the observed kinetics of the $HO_2 + HO_2$ reaction was also investigated. One of the motivating factors behind this work was to resolve discrepancies in the previously measured temperature dependence of the HO_2 self reaction rate constant, k_4. The results from this work were in good agreement with the current recommendations by the JPL data evaluation. Using the JPL recommended value for the termolecular rate constant, Arrhenius parameters for the bimolecular rate constant, $k_{4,bi}$ were determined to be $A_{4,bi} = (2.4^{+3.2}_{-1.9}) \times 10^{-13}$ cm^3 molecule^{-1} s^{-1} and $E/R_{4,bi} = -525 \pm 75$ K (1σ uncertainties).

The observed rate enhancement of the HO_2 self reaction by CH_3OH, characterized by the enhancement factor, k''_{4M}, was measured over the temperature range T = 230 - 320 K. The Arrhenius parameters were $A''_{4M} = (9.2^{+0.7}_{-0.6}) \times 10^{-36}$ cm^6 molecule^{-2} s^{-1} and $E/R''_{4M} = -4340 \pm 17$ K (1σ uncertainties). The rate enhancement factor by CH_3CHO, k''_{4A}, was determined over the temperature range T = 230 - 294 K. The Arrhenius parameters were $A''_{4,A} = (8.3^{+9.0}_{-7.3}) \times 10^{-34}$ cm^6 molecule^{-2} s^{-1} and $E/R''_{4,A} = -3600 \pm 540$ K (1σ uncertainties). The latter was important for accurate

characterization of the kinetics of the HO_2 + $CH_3C(O)O_2$ reaction, which is the subject of Chapter 4.

3.1 Introduction

The hydroperoxy (HO_2) radical plays a key role in oxidative processes in the atmosphere and influences tropospheric ozone (O_3) production. One of the motivating factors in laboratory atmospheric studies is to understand the photochemical production of O_3 in the troposphere; specifically, this entails the identification and characterization of the various sources and sinks of HO_2.

A common method for generating HO_2 in the laboratory is the photolysis of Cl_2 in the presence of CH_3OH and O_2:

$$Cl_2 + h\nu\,(351\,\text{nm}) \longrightarrow 2\,Cl \tag{R1}$$

$$Cl + CH_3OH \longrightarrow CH_2OH + HCl \tag{R2}$$

$$CH_2OH + O_2 \longrightarrow HO_2 + CH_2O \tag{R3}$$

This reaction mechanism is a simple and straightforward source of HO_2 since no other radicals are produced. Furthermore, the only subsequent reactive loss of HO_2 is through the self reaction (R4):

$$HO_2 + HO_2 \xrightarrow{M} H_2O_2 + O_2 \tag{R4}$$

R4 is an important sink for HO_x ($HO_x \equiv HO_2 + OH$) in the troposphere and is also the dominant source of stratospheric H_2O_2, which acts a temporary reservoir for HO_x. The overall rate constant of R4 (k_4) has been investigated by numerous studies over a wide range of temperatures and pressures (see list of references in the JPL data evaluation [1]), and the values are generally in good agreement for temperatures above and at room temperatures. However, at lower temperatures, Christensen et al. [2, 3] revealed that using CH_3OH as a HO_2 precursor faced complications, due to the formation of a reactive hydrogen-bonded adduct from the association reaction of HO_2 with CH_3OH. Furthermore, as mentioned in Chapter 4 of this thesis, experiments investigating the cross-reactions of HO_2 with acetylperoxy radicals ($CH_3C(O)O_2$) were also found to be affected by adducts formed from the reaction of HO_2 with acetaldehyde (CH_3CHO), which is the most widely used precursor for $CH_3C(O)O_2$ $CH_3C(O)O_2$ [4–12].

In general, the formation of the radical adduct of HO_2 with some molecule, X,

can be described by an equilibrium reaction:

$$HO_2 + X \underset{M}{\overset{M}{\rightleftharpoons}} HO_2 \cdot X \tag{R5}$$

The amount of radical adducts formed via R3.1 depend on the equilibrium constant, $K_{c,X}$:

$$K_{c,X} = \frac{[HO_2 \cdot X]_{eq}}{[HO_2]_{eq}[X]_{eq}} \tag{3.1}$$

These adducts impact the observed overall kinetics of HO_2 reactions. For example, the radical adducts undergo additional reactive losses via R6 and R7, resulting in an enhanced observed HO_2 self-reaction rate constant, $k_{4,obs}$:

$$HO_2 + HO_2 \cdot X \longrightarrow \text{products} \tag{R6}$$

$$HO_2 \cdot X + HO_2 \cdot X \longrightarrow \text{products} \tag{R7}$$

Hamilton [13] reported the first observation of the HO_2 self reaction rate enhancement by H_2O, which was later confirmed by other studies [14–18]. Similar rate enhancement effects by NH_3 [14, 17] and by CH_3OH [2, 19–21] were also revealed.

Christensen et al. [3] demonstrated that under high pressure and low radical concentrations, the equilibrium reaction of R5 for X = CH_3OH is established rapidly on a timescale much shorter than the HO_2 loss rate through R4, R6, and R7. Their work was additionally supported by the observation that HO_2 loss followed second-order behavior, even with rate enhancement. As a result, any unaccounted loss of HO_2 via R5 introduces systematic errors that propagate into the uncertainties of the rate constants of HO_2 reactions when CH_3OH is used as a radical precursor. Furthermore, since these complexes are more favored at low temperatures, the rate enhancement effect also has a temperature dependence that needs to be taken into account in temperature dependence studies. Thus, measuring the equilibrium constants of R5 is important for kinetics measurements involving HO_2.

In this work, experiments were carried out using the Infrared Kinetics Spectroscopy (IRKS) apparatus (Chapter 2), which employed simultaneous, time-resolved IR and UV absorption spectroscopy. All of the results presented in this chapter are based on HO_2 measurements using only the near-infrared (NIR) probe; i.e., the UV probe was only used for the purpose of calibrating the NIR laser. The first part of this chapter describes work carried out to measure the equilibrium constants of R5

for X = CH_3OH ($K_{c,M}$) and for X = CH_3CHO ($K_{c,A}$), where

$$K_{c,M} = \frac{[HO_2 \cdot CH_3OH]_{eq}}{[HO_2]_{eq}[CH_3OH]_{eq}} \tag{3.2}$$

and

$$K_{c,A} = \frac{[HO_2 \cdot CH_3CHO]_{eq}}{[HO_2]_{eq}[CH_3CHO]_{eq}} \tag{3.3}$$

$K_{c,M}$ and $K_{c,A}$ were measured at 100 Torr in N_2 over the temperature range T = 220 - 270 K and T = 230 - 280 K, respectively, and the thermodynamics of the equilibrium reactions are discussed. The measured values of $K_{c,M}$ are compared to those reported by Christensen et al. [3], who used a different data analysis method than the one used in this work.

The second part of this chapter presents results from the reinvestigation of the temperature dependence of R4 at 100 Torr in N_2 over the temperature range T = 230 - 320 K and the rate enhancement effect by CH_3OH (T = 230 - 320 K) and by CH_3CHO (T = 230 - 294 K). As mentioned previously, R4 has been widely studied, and its rate constant, k_4, is well-characterized at room temperature. However, the temperature dependence of k_4 at lower temperatures measured by Christensen et al. [2] using the IRKS apparatus appears to be in large disagreement with other previously reported values in the literature. For instance, at 222 K, there is a systematic discrepancy of ~20% between the values recommended by the current JPL data evaluation [1] and the results reported by Christensen et al. [2]. Since this work and that of Christensen et al. [2] used the same experimental apparatus, reinvestigation of the temperature dependence of k_4 was crucial for accurate kinetics measurements and for ruling out potential systematic errors caused by the instrument. Finally, the rate enhancement of R4 by CH_3CHO was also characterized, as it was important for accurate determination of the rate constant and product yields of the reaction of HO_2 + $CH_3C(O)O_2$, which is the subject of Chapter 4.

3.2 Experimental Methods

A detailed description of the experimental apparatus is given in Chapter 2; thus, only a brief summary of the details that pertain to this work will be given here. The kinetics experiments were conducted in a temperature-controlled, pulsed photolysis flow cell employing simultaneous NIR and UV absorption spectroscopy. Pulsed 351 nm light from a XeF excimer laser (Compex 301) initiated the radical chemistry by photolyzing Cl_2 molecules in the reagent gas mixture containing

either $Cl_2/N_2/O_2/CH_3OH$ or $Cl_2/N_2/O_2/CH_3OH/CH_3CHO$. The reaction cell was a jacketed, 5-cm diameter Pyrex cell measuring 175 nm in length. The temperature inside the cell was controlled by flowing either liquid nitrogen-cooled methanol (T < room temperature) or heated water (T > room temperature) through the jacket of the cell. The temperature was monitored with a type-T thermocouple (Omega), which was inserted into the jacket and was in contact with the temperature-controlling fluid.

The reagent gases were pre-mixed and pre-cooled in a jacketed Pyrex manifold prior to entering the cell. The gas flows were regulated by mass flow controllers (MKS Instruments), and the total flow rate was kept at approximately 2000 cm^3 (STP) min^{-1}, maintaining a total pressure of 100±2 Torr with a 10 s residence time inside the cell. A photolysis repetition rate of 0.2 Hz was used, allowing for two photolysis events to occur per residence time. Room temperature N_2 purge gas flowed from either end of the cell to confine the main gas flow to the temperature-controlled region. CH_3OH and CH_3CHO vapors were introduced to the cell by passing N_2 gas through glass bubblers holding the liquid compounds. The bubblers were placed inside temperature-controlled baths held at 0 °C (CH_3OH) and -25 °C (CH_3CHO). Absolute capacitance manometers (MKS Baratron) were used to measure the pressures inside the cell and the bubblers, and the concentrations of CH_3OH and CH_3CHO vapors were determined manometrically. Experiments were conducted using a wide range of reagent gas concentrations: $[CH_3OH] = (2.0-26)\times10^{15}$ molecule cm^{-3}, $[CH_3CHO] = (0-8.4)\times10^{15}$ molecule cm^{-3}, $[O_2] = (1.6-2.0)\times10^{18}$ molecule cm^{-3}; $[Cl_2] = (0.75-7.1)\times10^{15}$ molecule cm^{-3}. The total initial radical concentrations covered the range $[Cl]_0 = (0.20-2.2)\times10^{14}$ molecule cm^{-3}.

Broadband UV light from a laser-driven light source (Energetiq EQ-99XFC) was collimated and made a single pass through the cell, counter-propagating the photolysis beam, with an effective path length of 147 ± 10 cm. The transmitted light was focused and guided into a monochromator (Acton Research Corporation Spectra Pro-300i) coupled to a photomultiplier tube (PMT), where 225 nm light was detected. The slit width was typically set to ~130 μm.

NIR light from a 3 mW continuous wave (CW) distributed feedback (DFB) diode laser was used to monitor HO_2 by probing the ro-vibrational transitions associated with the O–H overtone stretch ($2\nu_1$) at 6638.2 cm^{-1}. A pair of spherical mirrors were used to configure a multipass Herriott resonator, in which the NIR light made 30 passes. Each mirror was housed inside the purged (with room temperature N_2 gas) aluminum boxes placed on either end of the reaction cell. The diode laser was wavelength modulated, and the detected signal was demodulated at twice the

modulation frequency (2f-heterodyne detection).

Because wavelength modulation spectroscopy (WMS) only measures the relative change in concentrations, the NIR data from IRKS experiments require daily calibration, which depends on the alignment of the laser. Since the UV absorption cross-section of HO_2 is known ($\sigma_{\lambda=225\text{ nm}} = 2.88 \times 10^{-18}$ cm^2 [22]) and the kinetic rate constant of HO_2 is well-characterized at room temperature [1], the NIR was calibrated against UV absorption at 225 nm by simultaneously measuring the NIR and UV signals when HO_2 was the only peroxy radical present. The calibration experiments were always conducted at room temperature at the beginning of the day. The NIR and UV signals were simultaneously fit with a kinetics model using the FACSIMILE software to obtain the calibration factor, V_{M,HO_2}, which places the NIR signal in mV, S_{NIR}, on an absolute scale:

$$[HO_2] = V_{M,HO_2} \times S_{NIR} \tag{3.4}$$

For this work, the UV data was used solely for calibrating the NIR signal, and the equilibrium constants and rate coefficients were not derived from kinetics traces measured with the UV probe.

3.3 Equilibrium constants for $HO_2 \cdot X$ adduct

The equilibrium constants of R5 for X = CH_3OH and CH_3CHO were determined at 100 Torr in N_2 over the temperature range 219.7 - 269.0 K for $K_{c,M}$ and 230.1 - 280.2 K for $K_{c,A}$. At each temperature, data were collected under numerous experimental conditions that varied in the relative amounts of CH_3OH and CH_3CHO, as well as in the total initial radical concentrations. $K_{c,M}$ was determined from experiments using a reagent gas mixture of $Cl_2/N_2/O_2/CH_3OH$, and $K_{c,A}$ was measured by adding CH_3CHO to the gas mixture. Experiments at T = 220 K were attempted for the determination of $K_{c,A}$; however, evidence of particle formation were observed, manifested as large absorbance signals in the NIR time traces at longer kinetics times when the signal would otherwise be expected to return to baseline. Thus, data at temperatures below 230 K for the $K_{c,A}$ experiments could not be used. The photo-induced nucleation of HO_2 has been previously investigated using the IRKS apparatus, as detailed in Dr. Aaron Noell's thesis [23]. The equilibrium constants at room temperature were not determined due to the low amount of complex that was formed.

The approach for measuring the equilibrium constants consisted of measuring the amount of complex that was formed for varying concentrations of CH_3OH and

CH_3CHO. This was achieved by measuring the loss of HO_2 in the first ~20-50 μs after photolysis using the NIR probe. The underlying assumption in this analysis is that the equilibrium between HO_2 and X is established almost instantaneously, which was substantiated by the observed rapid drop in the peak HO_2 signal with increasing concentrations of CH_3OH and CH_3CHO. Since the NIR only measures the amount of monomeric HO_2, the observed difference in the peak HO_2 signal with various concentrations of CH_3OH and CH_3CHO provided an indirect measurement of the total amount of complex that was formed.

For some species X_i, let $[HO_2 \cdot X_i]$ denote the concentration of the adduct $HO_2 \cdot Xi$ formed from the reaction of HO_2 with X_i. The total concentration of HO_2 bound in an adduct can be expressed in terms of $[HO_2]_0$, the total initial HO_2 concentration in the limit of $\sum_i [HO_2 \cdot X_i] = 0$:

$$[HO_2]_0 - [HO_2]_{eq} = \sum_i [HO_2 \cdot X_i]_{eq} \tag{3.5}$$

$$= [HO_2]_{eq} \sum_i K_{c,X_i} [X_i]_{eq} \tag{3.6}$$

where $[HO_2]_{eq}$ is the concentration of the free HO_2 in equilibrium with $\sum_i [HO_2 \cdot X_i]_{eq}$ and K_{c,X_i} is the equilibrium constant for species X_i, as given by Equation 3.1. Using the definition $\Delta[HO_2]_0 \equiv [HO_2]_0 - [HO_2]_{eq}$, we can write:

$$\frac{\Delta[HO_2]_0}{[HO_2]_{eq}} = \sum_i K_{c,X_i} [X_i]_{eq} \tag{3.7}$$

From Equation 3.7, K_{c,X_j} for the reaction of HO_2 with species X_j can be derived from the slope of $\Delta[HO_2]_0/[HO_2]_{eq}$ versus $[X_j]_{eq}$, provided that the concentrations of all other species $X_k \neq X_j$ are held constant.

$[HO_2]_{eq}$ was determined by fitting the NIR HO_2 signal with a biexponential function and extrapolating the fitted signal to t = 0 s (i.e., time when the excimer laser was fired). The data were fit from 0.02 ms to ~1-5 ms after photolysis using a nonlinear least-squares algorithm (Levenberg-Marquardt) built-in to the IGOR Pro software. The fitting range was adjusted to ensure that good fits were achieved near t = 0 s. $[HO_2]_0$ was determined from data collected when CH_3CHO was absent; more details will be given in the following subsections.

Using the values of K_{c,X_i} measured at the various temperatures, the thermodynamics of R5 for $X_i = CH_3OH$ and for $X_i = CH_3CHO$ were determined from the van 't Hoff equation, which relates the equilibrium constant to the standard change in

enthalpy ($\Delta_r H^\circ$) and entropy ($\Delta_r S^\circ$) of the reaction:

$$R \ln K_{\mathrm{p,X}_i}(T) = -\frac{\Delta_r H^\circ}{T} + \Delta_r S^\circ \tag{3.8}$$

where T is the temperature, $N_A = 6.022 \times 10^{23}$ molecules mol^{-1}, $R \equiv 8.314$ J mol^{-1} K^{-1}, and

$$K_{\mathrm{p,X}_i} \equiv \frac{N_A}{RT} K_{\mathrm{c,X}_i} \tag{3.9}$$

For the determination of the equilibrium constants, errors in the calibration of the NIR laser did not contribute to the overall error because V_{M,HO_2} cancels out in the mathematical expressions for $K_{c,M}$ and $K_{c,A}$. Systematic errors in the pressures, flows, and temperatures estimated the total uncertainties in [CH_3OH] and [CH_3CHO] to be ~2.5% and ~5%, respectively. The larger errors in [CH_3CHO] were attributed to larger uncertainties in the Antoine equation parameters that were used in the calculation of the CH_3CHO vapor pressure at the bubbler temperature that was used (T_{CH_3CHO} = -25°C). Due to the high vapor pressure of CH_3CHO, the bubbler temperature had to be set to a value below the range over which the CH_3CHO vapor pressures had been previously measured [24].

3.3.1 $HO_2 + CH_3OH \rightleftharpoons HO_2 \cdot CH_3OH$

In the absence of CH_3CHO, all of the initial Cl atoms formed from photolysis are converted to HO_2. The total initial HO_2 concentration is denoted as $[HO_2]_{0,M}$ and expressed as:

$$[HO_2]_{0,M} = [HO_2]_{eq} + [HO_2 \cdot CH_3OH]_{eq} = [Cl]_0, \tag{3.10}$$

where $[Cl]_0$ is the total initial radical concentration generated from the photolysis of Cl_2 and $[HO_2]_{eq}$ is the concentration of the free HO_2 in equilibrium with CH_3OH; i.e.,

$$HO_2 + CH_3OH \underset{M}{\overset{M}{\rightleftharpoons}} HO_2 \cdot CH_3OH, \tag{R8}$$

Figure 3.1 shows examples of the HO_2 decays obtained from the NIR signals at T = 248.4 K. Although the same radical concentrations were used in all six experimental runs shown in the figure, the data exhibit rapid drops in the peak HO_2 signal immediately after photolysis (t = 0 s). The amount of peak signal attenuation is positively correlated with [CH_3OH], supporting the hypothesis that equilibrium of

R8 is established rapidly (< 20 μs).

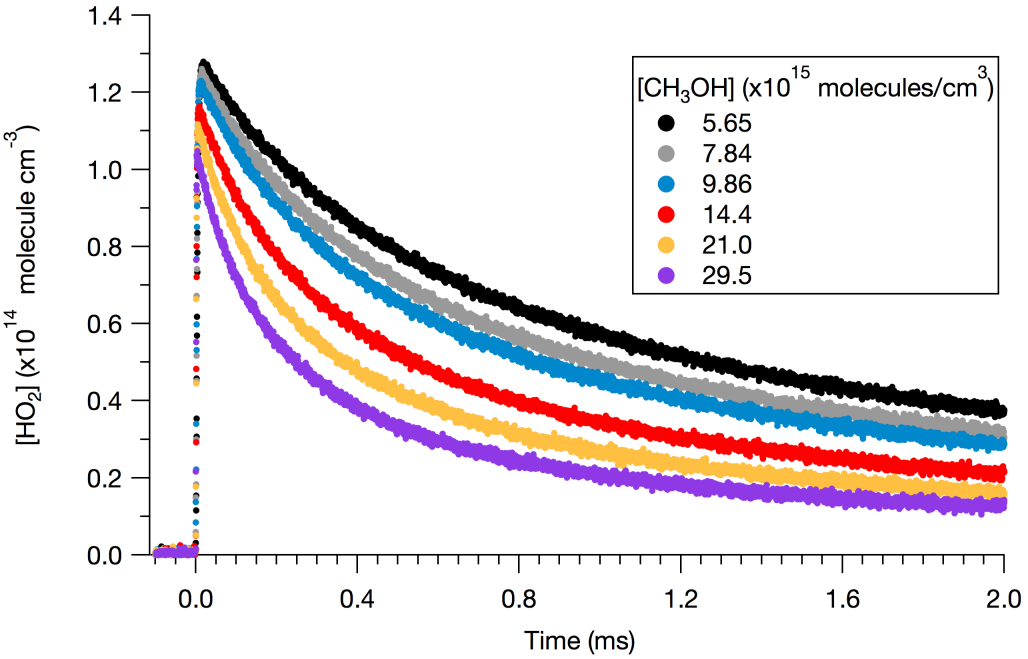

Figure 3.1: Example data of HO_2 decay curves at T = 248.4 K; P = 100 Torr; $[Cl_2]$=4.6 $\times$ 10^{15} molecule cm^{-3}.

Initially, data analysis using the method described by Dr. Lance Christensen [3, 25] was attempted. As described in his thesis and paper, the flat region in the first 50 μs of the data was used to determine $[HO_2]_{eq}$. In this work, however, a plateau in the HO_2 signal, even on this short timescale, was not always straightforward to define, particularly at the lowest temperature. Figure 3.2 shows several HO_2 signals obtained at T = 219.7 K and at T = 230.1 K. As shown in Figure 3.2(a), little change in $[HO_2]$ is observed between 20 to 50 μs, and an equilibrium concentration of HO_2 can easily be determined by taking the average signal in that time range. However, in Figure 3.2(b), a non-equilibrium state in which fast production of HO_2 via R2 and R3 is observed, followed by decay of HO_2 via R8, which is in competition with rapid loss of HO_2 via reaction with $HO_2 \cdot CH_3OH$.

It was also observed that this analysis method could not be used under all experimental conditions in the data where both CH_3OH and CH_3CHO were present due to additional loss processes of HO_2 competing with R5, which will be described in the following sections. Thus, to maintain consistency in the analysis of all data, $[HO_2]_{eq}$ was determined using the alternative approach described at the beginning of the Results section; i.e., a bi-exponential function was used to fit the NIR signal and the extrapolated value at t = 0 s was taken to be $[HO_2]_{eq}$. Uncertainties in the

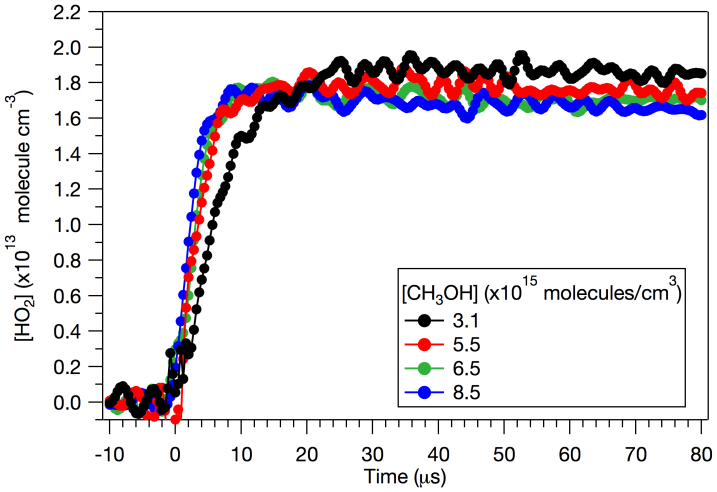

(a)

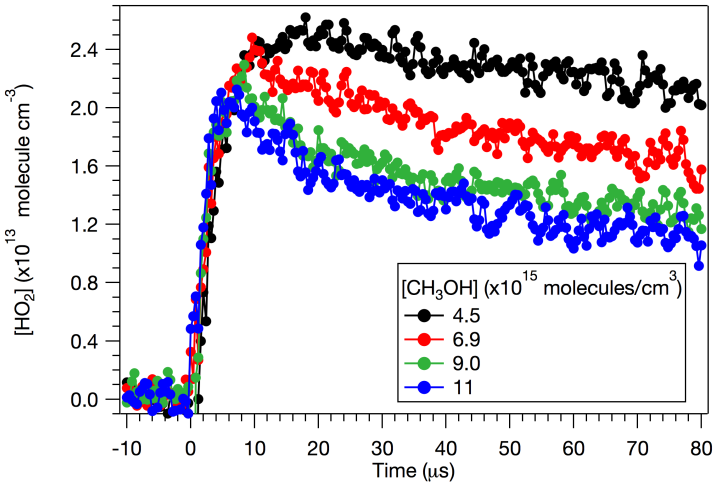

(b)

Figure 3.2: Examples HO_2 signals on the μs timescale at (a) T = 230.1 K ($[Cl]_0$=2.0 $\times$ 10^{13} molecule cm^{-3}) and (b) T = 219.7 K ($[Cl]_0$=4.2 $\times$ 10^{13} molecule cm^{-3}); P = 100 Torr in N_2.

measured values of $[HO_2]_{eq}$ included the random errors in the fits. Figure 3.3 shows examples of the fits to the HO_2 decay curves obtained at T = 269.0 K and at T = 219.7 K.

Using Equation 3.7, we have:

$$\frac{\Delta[HO_2]_0}{[HO_2]_{eq}} = K_{c,M}[CH_3OH] \tag{3.11}$$

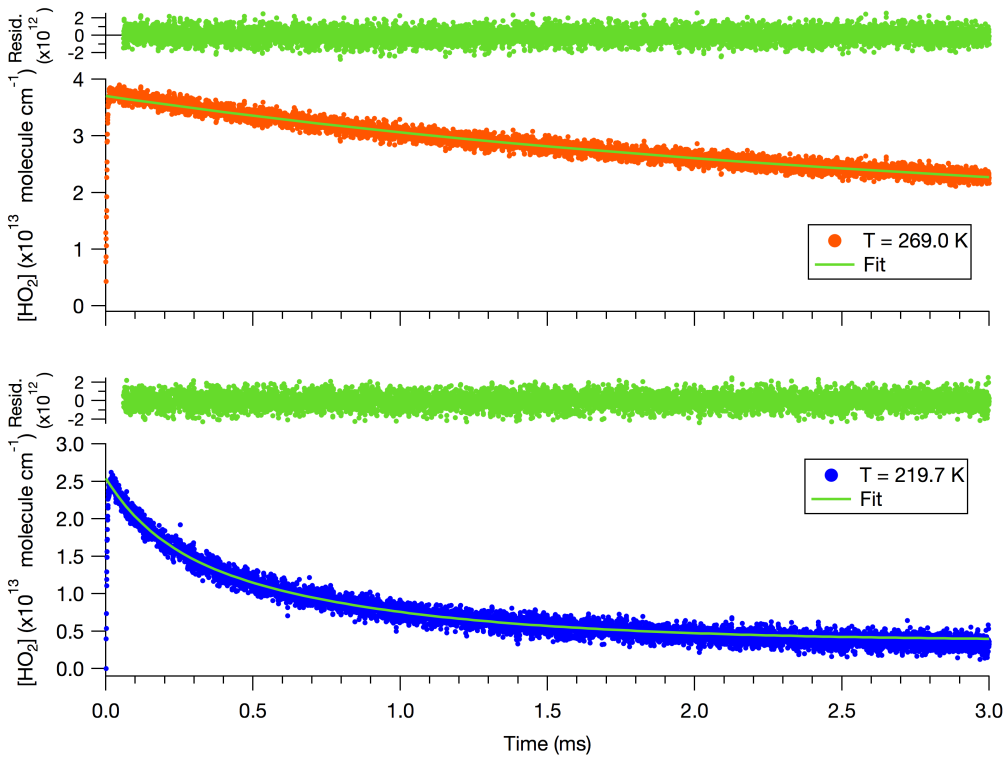

Figure 3.3: Example data of HO_2 decay curves obtained at T = 269.0 K (top panel) and at T = 219.7 K (bottom panel), with $[CH_3CHO]$ = 0; P = 100 Torr

where

$$\Delta[HO_2]_0 \equiv [HO_2]_{0,M} - [HO_2]_{eq} \tag{3.12}$$

$[HO_2]_{eq}$ for each run was determined by extrapolating the fitted HO_2 signal to t = 0 s, as described previously. To determine $[HO_2]_{0,M}$, Equation 3.6 was rearranged to give:

$$\frac{1}{[HO_2]_{eq}} = \frac{1}{[HO_2]_0} + \frac{K_{c,M}}{[HO_2]_0} \tag{3.13}$$

At each temperature, data were collected using varying concentrations of $[CH_3OH]$ for the same total initial radical concentration (i.e., same $[Cl_2]$ and excimer energy). Figure 3.4 shows a plot of $1/[HO_2]_{eq}$ versus $[CH_3OH]$, which was fit to a line to determine $[HO_2]_0$ from the y-intercept ($[CH_3OH]$ = 0).

At some temperatures, multiple data sets were collected using 2 - 3 different values of $[HO_2]_0$. All the data were put on a common scale by plotting $\Delta[HO_2]_0/[HO_2]_{eq}$ as a function of CH_3OH, as shown in Figure 3.5. $K_{c,M}$ at each temperature was derived from the slope of the weighted linear fit to the data. Table 3.1 lists the range of

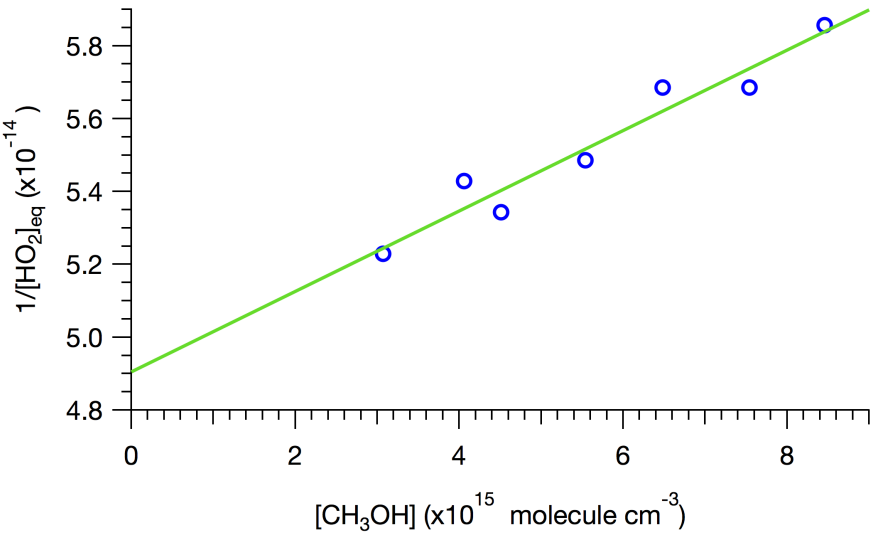

Figure 3.4: Plot of $1/[HO_2]_{eq}$ vs $[CH_3OH]$ at T = 230.2 K and P = 100 Torr. The data points (blue circles) were fit with a line using linear regression (green line) to determine $[HO_2]_0$ from the inverse of the y-intercept.

experimental conditions over which data were collected, as well as the values of $K_{c,M}$ that were determined. The data obtained at room temperature did not show evidence of complexation within experimental uncertainty; thus, $K_{c,M}$ was not determined at this temperature. Although Figure 3.5 shows some evidence of complexation at 280.5 K at high $[CH_3OH]$, the data at this temperature were also excluded in the van 't Hoff analysis because the measured value of $K_{c,M}$ at this temperature was highly uncertain due to the low amount of complex that was formed.

Table 3.1: Range of experimental conditions for determination of $K_{c,M}$ at 100 Torr.

T (K)	$[Cl_2]^a$	$[CH_3OH]^a$	$[Cl]_0{}^b$	# of experiments	$K_{c,M}{}^c$
280.5	1.5 - 4.5	7.6 - 26	3.7 - 10	16	-
269.0	1.5 - 4.5	2.6 - 26	3.9 - 10	18	4.73
259.9	1.6 - 4.5	3.4 - 23	3.7 - 9.3	12	6.28
248.4	4.5 - 7.1	5.7 - 3.0	14 - 20	10	11.0
239.9	4.5 - 7.1	4.4 - 10	15 - 21	8	16.9
229.2	0.75 - 1.5	2.7 - 20	2.1 - 5.2	17	33.6
219.7	1.5 - 4.5	2.6 - 11.0	4.2 - 8.1	10	100.4

[a]Units: 10^{15} molecule cm^{-3}
[b]Units: 10^{13} molecule cm^{-3}
[c]Units: 10^{-18} cm^3 $molecule^{-1}$

Figure 3.6 shows the van 't Hoff plot of $R \ln K_{p,M}$ versus 1/T. A weighted linear least-squares fit to the data yielded $\Delta_r H^\circ_{250\,K} = -28.1 \pm 0.4$ kJ mol^{-1} from the slope

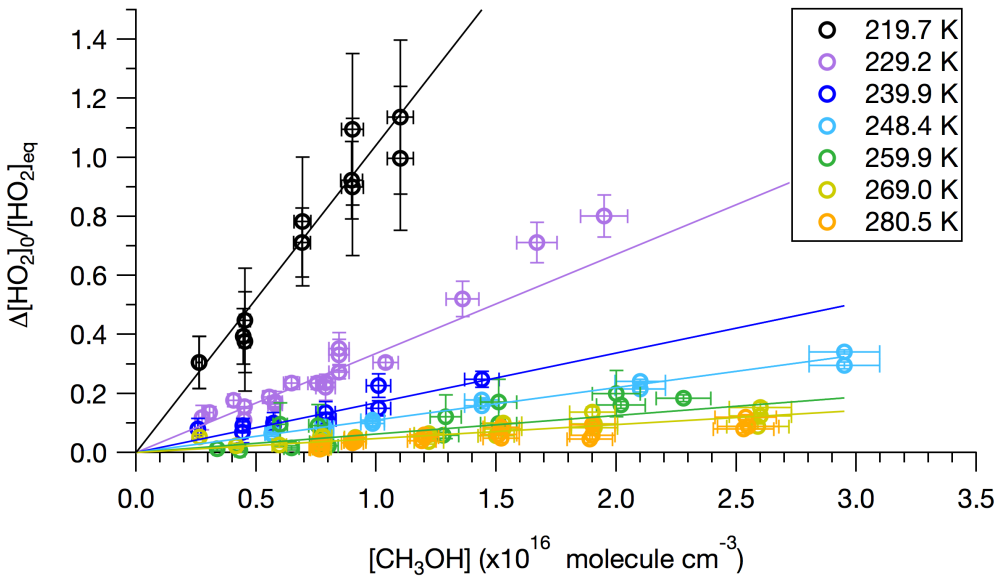

Figure 3.5: Plots of $\Delta[HO_2]_{0,M}/[HO_2]_{eq}$ versus $[CH_3OH]$ at various temperatures.

and $\Delta_r S^{\circ}_{250\,K} = -64.9 \pm 1.6$ J mol^{-1} from the y-intercept (1σ uncertainties), where T = 250 K was the midpoint of the temperature range.

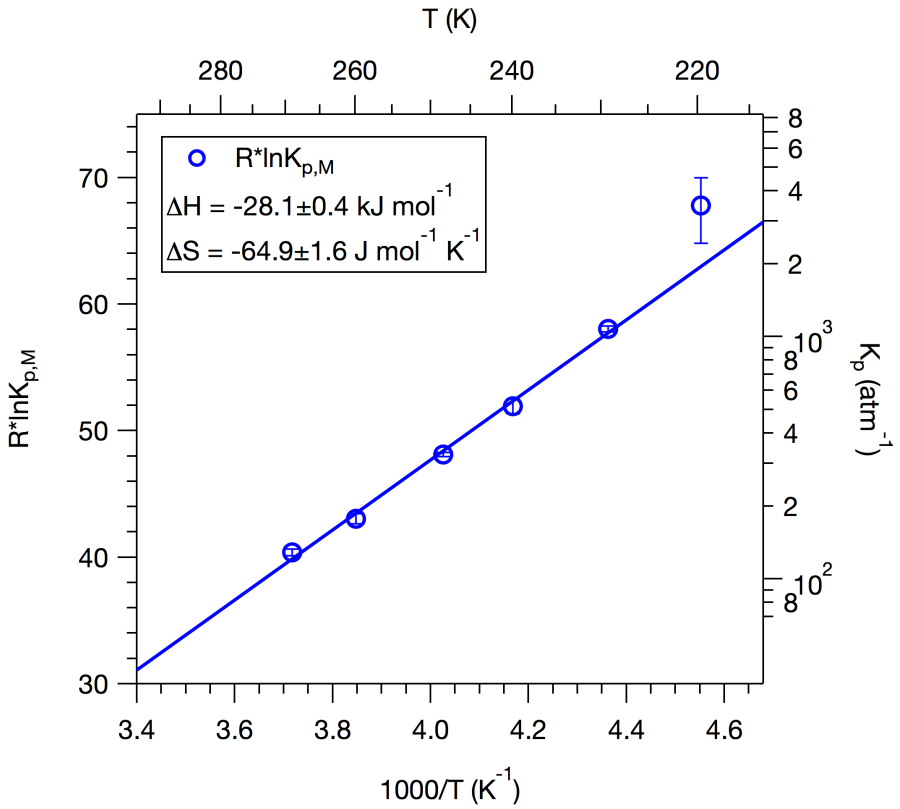

Figure 3.6: van 't Hoff plot of $R \ln K_{p,M}$ versus 1/T.

Bloss et al. [21] measured the equilibrium constant of $HO_2 \cdot CH_3OH$ formation at room temperature, reporting $K_{c,M} = 6.15 \times 10^{-19}$ cm^3 molecule^{-1}. Extrapolating the van 't Hoff plot from this work gives $K_{c,M} = 1.4 \times 10^{-18}$ cm^3 molecule^{-1}, which is greater than a factor of two larger. Table 3.2 also compares the thermodynamic parameters determined in this work to those reported by previous studies. The results from this work were inconsistent with those of Christensen et al. [3], who reported $\Delta_r H^\circ_{246\,K} = -37.4 \pm 4.8$ kJ mol^{-1} and $\Delta_r S^\circ_{246\,K} = -100 \pm 196$ J mol^{-1} from data collected in the range 231 K and 261 K, which agreed with the theoretical calculations performed in the same study. The disagreement between the results obtained in this work with those of Christensen et al. [3] remains unexplained since the same experimental technique was used. Possible sources for the discrepancy are the different analysis methods and the wider temperature range that was explored in this work. On the other hand, the value of the change in enthalpy measured in this work is in good agreement with the value reported by Andersson et al. [19], who reported a value of -25 ± 3 kJ mol^{-1} from kinetics analysis of time-resolved UV absorption data.

Table 3.2 also provides the thermodynamic parameters for other molecules that are known to form hydrogen-bonded complexes with HO_2. The stabilization energies of HO_2 adducts with H_2O, CH_3OH, and NH_3 are of similar magnitude with values similar to the energy of a typical hydrogen bond. This suggests that all three substrates undergo similar equilibrium mechanisms for adduct formation with HO_2. Previous works have concluded that the H atom on HO_2 bonds with the N atom on NH_3 [17, 19] and with the O atoms on CH_3OH [3] and H_2O (theoretical work by Aloisio and Francisco [26] suggests that the H atom on H_2O also bonds with the O atom on HO_2, forming a floppy, five-membered ring).

Table 3.2: Comparison of $\Delta_r H^\circ_T$ and $\Delta_r S^\circ_T$ for various complexes of HO_2.

Complex	T (K)	$\Delta_r H^\circ_T$ (kJ mol^{-1})	$\Delta_r S^\circ_T$ (J mol^{-1} K^{-1})	Ref
$HO_2 \cdot CH_3OH$	220 - 269	-28.1 ± 0.4	-65 ± 1.6	This work (experiment)
	231 - 261	-37.4 ± 4.8	-100 ± 19	Christensen et al. [3] (experiment)
	245	-36.8	-106	Christensen et al. [3] (CCSD(T)/6-311++G(3df,3pd))
	278 - 299	-25 ± 3		Andersson et al. [19] (experiment)
$HO_2 \cdot H_2O$	230 - 298	-36 ± 16	-85 ± 40	Aloisio and Francisco [27] (experiment)
$HO_2 \cdot NH_3$	290 - 400	-54 ± 6.3	-140 ± 21	Lii et al. [17] (experiment)

3.3.2 $HO_2 + CH_3CHO \rightleftharpoons HO_2 \cdot CH_3CHO$

With the addition of CH_3CHO, a fraction of the Cl atoms generated from photolysis is converted to $CH_3C(O)O_2$ from the reaction of Cl with CH_3CHO; i.e., in addition to R2, we have R9, followed by R10:

$$Cl + CH_3CHO \longrightarrow CH_3C(O) + HCl \tag{R9}$$

$$CH_3C(O) + O_2 \xrightarrow{M} CH_3C(O)O_2 \tag{R10a}$$
$$\longrightarrow OH \tag{R10b}$$
$$\longrightarrow HO_2 \tag{R10c}$$

Under the conditions of these experiments where O_2 is in excess, both HO_2 and $CH_3C(O)O_2$ are produced essentially instantaneously with yields close to unity. The yields of OH and HO_2 from R10 were measured in a separate set of experiments (Chapter 5) and were both found to be ~1-3% at 100 Torr in N_2 across all temperatures, which did not affect the analysis of this work. Therefore, the notation $[HO_2]_{0,A}$ is used to refer to the fraction of total initial Cl atoms that was converted to HO_2 in the presence of both CH_3OH and CH_3CHO, where

$$[HO_2]_{0,A} = \frac{k_2[CH_3OH]}{k_2[CH_3OH] + k_9[CH_3OH]}[Cl]_0 \tag{3.14}$$

The rate constants of R2 and R9 (k_2 and k_9, respectively) were measured previously (Chapter 6) and were both found to be temperature independent over the range T = 230 - 297 K with values of $k_2 = (5.45 \pm 0.37) \times 10^{-11}$ cm^3 molecule^{-1} s^{-1} and $k_9 = (8.00 \pm 1.27) \times 10^{-11}$ cm^3 molecule^{-1} s^{-1} (2σ uncertainties). These results are in excellent agreement with the recommendations by the current JPL and IUPAC data evaluations. $[Cl]_0$ was determined from the $[HO_2]_{eq}$ measured in the absence of CH_3CHO, which we will denote as $[HO_2]_{eq,M}$. $[Cl]_0$ was calculated by multiplying $[HO_2]_{eq,M}$ by the factor $(1 + K_{c,M}[CH_3OH])$, which corrects for the amount of HO_2 lost via complexation with CH_3OH.

With CH_3CHO present, we have R11 in addition to R8

$$HO_2 + CH_3CHO \underset{M}{\overset{M}{\rightleftharpoons}} HO_2 \cdot CH_3CHO \tag{R11}$$

Data were collected using various concentrations of CH_3CHO for fixed values of $[CH_3OH]$, $[Cl_2]$, and excimer energy. Figure 3.7 shows a subset of the data obtained

at T = 250.5 K. The black trace shows the HO_2 signal when $[CH_3CHO] = 0$. Upon addition of CH_3CHO, a large drop in signal is observed, attributed to the competitive loss of Cl via R9 in addition to HO_2 loss via R11 and R8.

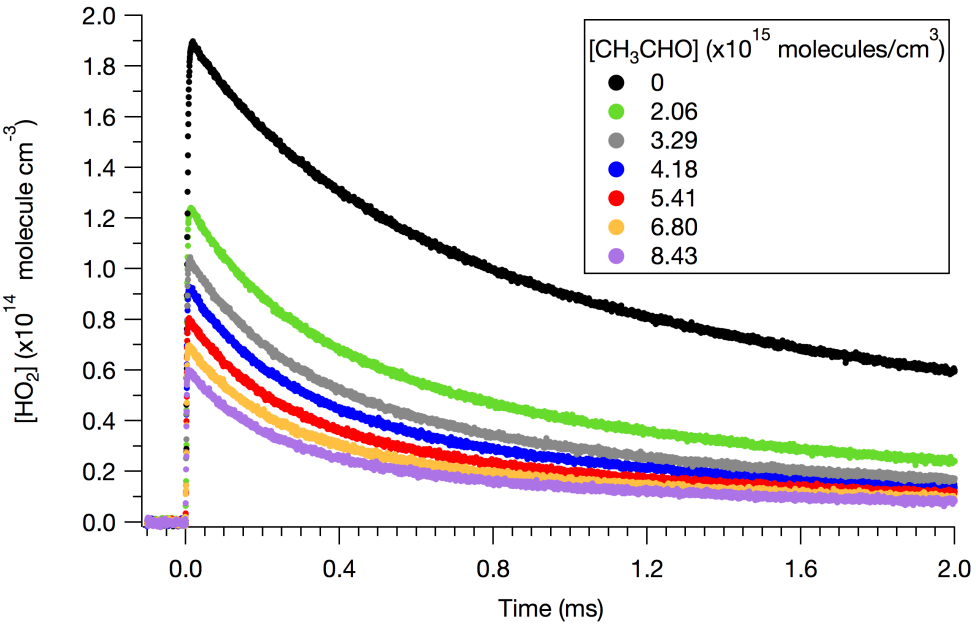

Figure 3.7: Example data of HO_2 decay curves collected using varying concentrations of CH_3CHO at T = 250.5 K and fixed $[CH_3OH] = 6.4 \times 10^{15}$ molecule cm^{-3}; P = 100 Torr; $[Cl_2]$=3.5×10^{15} molecule cm^{-3}.

$[HO_2]_{eq,A}$, defined as the equilibrium concentration of monomeric HO_2 in the presence of both CH_3OH and CH_3CHO, was determined by extrapolating the measured HO_2 signal to t = 0 s. Example fits to the data collected at two different temperatures are shown in Figure 3.8. From Equation 3.6, we have:

$$\frac{\Delta[HO_2]_0}{[HO_2]_{eq,A}} = K_{c,M}[CH_3OH] + K_{c,A}[CH_3CHO] \tag{3.15}$$

where

$$\Delta[HO_2]_0 \equiv [HO_2]_{0,A} - [HO_2]_{eq,A} \tag{3.16}$$

For some selected temperatures, data were collected using various fixed concentrations of CH_3OH and/or Cl_2; thus, all the data were put on a common scale by dividing Equation 3.15 by $[CH_3OH]$, which gives:

$$\frac{\Delta[HO_2]_0}{[CH_3OH][HO_2]_{eq,A}} = K_{c,M} + K_{c,A}\frac{[CH_3CHO]}{[CH_3OH]} \tag{3.17}$$

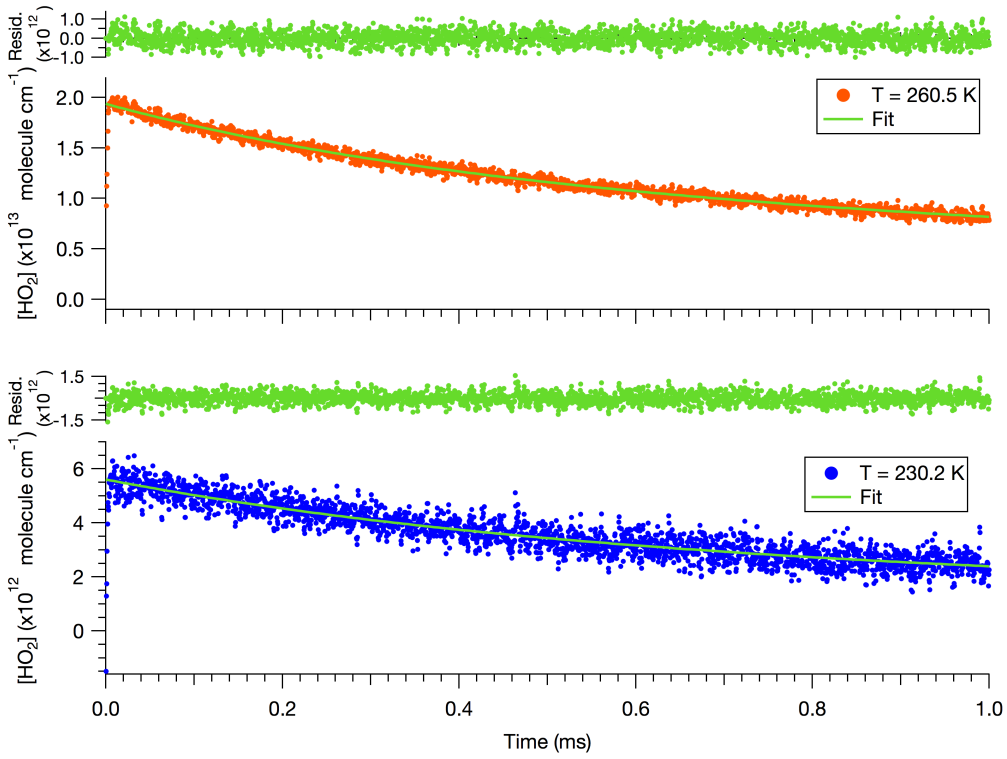

Figure 3.8: Example fits to HO_2 decay curves obtained at T = 260.5 K (top panel) and at T = 230.2 K (bottom panel) in the presence of both CH_3OH and CH_3CHO; P = 100 Torr. Residuals of fits are shown above each curve.

Table 3.3 lists all the experimental conditions over which data were collected.

Figure 3.9 shows a plot of $\Delta[HO_2]_{0,A}/([CH_3OH][HO_2]_{eq})$ versus $[CH_3CHO]/[CH_3OH]$ for all of the temperatures studied. $K_{c,A}$ at each temperature was determined from the slope of the weighted linear fit. The points at $[CH_3CHO] = 0$ were calculated from the values of $K_{c,M}$ measured when CH_3CHO was absent.

A weighted linear least-squares fit to the van 't Hoff plot of $R \ln K_{p,A}$ versus 1/T shown in Figure 3.10 yielded $\Delta_r H^\circ_{255\ K} = -15 \pm 2$ kJ mol^{-1} from the slope and $\Delta_r S^\circ_{255\ K} = -14 \pm 9$ J mol^{-1} from the y-intercept, where T = 255 K was the midpoint of the temperature range.

The $HO_2 + CH_3CHO$ association reaction proceeds without a barrier to form a weakly bound pre-reactive complex. Since the equilibrium constants were determined from the disappearance of HO_2, the product of the association reaction could not definitively be identified. However, previous experimental studies by Tomas et al. [6] demonstrated that the reaction proceeds to the isomerized peroxy radical, α-hydroxyethylperoxy ($CH_3CH(OH)O_2$), which was identified using UV absorption spectroscopy. These results were later supported by ab initio and master equation

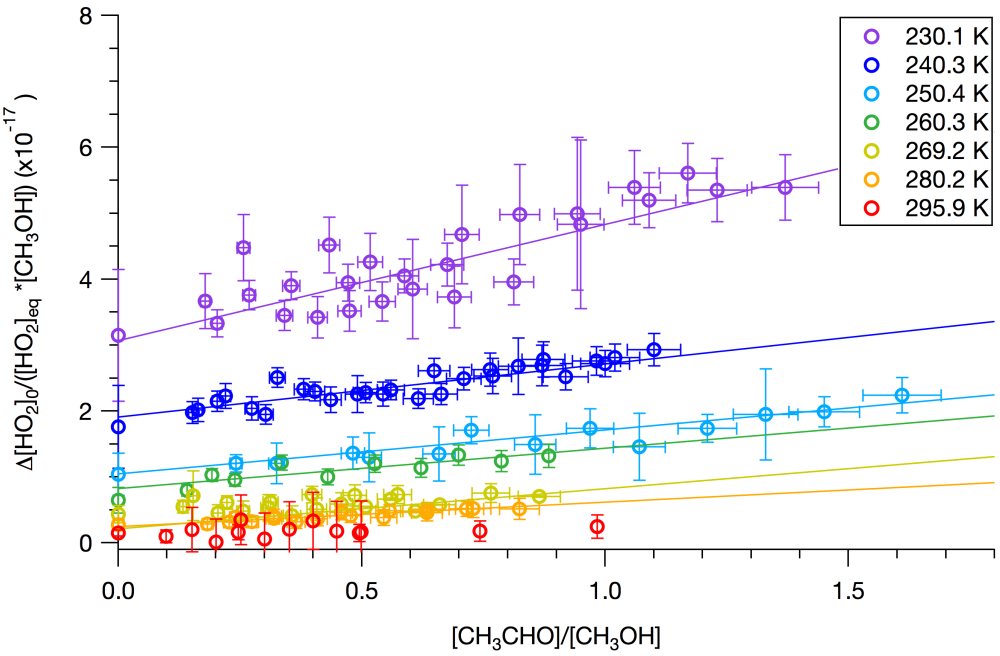

Figure 3.9: Plots of $\Delta[HO_2]_{0,A}/([CH_3OH][HO_2]_{eq})$ versus $[CH_3CHO]/[CH_3OH]$ at various temperatures.

Table 3.3: Range of experimental conditions used for the determination of $K_{c,A}$ at 100 Torr.

T (K)	$[Cl_2]^a$	$[CH_3OH]^a$	$[CH_3CHO]^a$	$[Cl]_0{}^b$	# of experiments	$K_{c,A}{}^c$
295.9	1.5 - 5.3	6.1 - 7.1	0.70 - 7.0	4.7 - 19	11	-
280.2	1.6	7.0 - 8.0	1.3 - 5.8	5.2	15	3.71
269.2	1.6	6.5 - 8.8	1.0 - 5.6	4.9 - 5.3	17	6.09
260.3	1.7	8.8	1.2 - 7.8	4.8	10	6.10
250.4	1.9 - 3.5	5.2 - 6.3	1.3 - 8.4	7.0 - 13	13	6.67
240.3	1.8	6.0 - 6.5	0.99 - 6.6	5.1	26	8.05
230.1	0.75	4.0 - 5.9	1.0 - 7.0	2.0	24	17.6

[a]Units: 10^{15} molecule cm^{-3}
[b]Units: 10^{13} molecule cm^{-3}
[c]Units: 10^{-18} cm^3 molecule^{-1}

calculations performed by theoretical studies [28–31]. The energy level diagram for the HO_2 + CH_3CHO reaction adapted from da Silva and Bozzelli [29] is shown in Figure 3.11. The HO_2 + CH_3CHO association reaction is barrierless and forms the weakly bound pre-reactive complex $HO_2 \cdot CH_3CHO$. Subsequent isomerization to $CH_3CH(OH)O_2$ proceeds via a submerged barrier and is thus expected to be rapid. Previous experimental studies [5, 6, 32] measured the equilibrium constant for the reaction of HO_2 + $CH_3CHO \rightleftharpoons CH_3CH(OH)O_2$ ($K_{c,A,isom}$) at temperatures at or above room temperature with values within a factor of two of $\sim 1.6 \times 10^{-17}$ cm^3

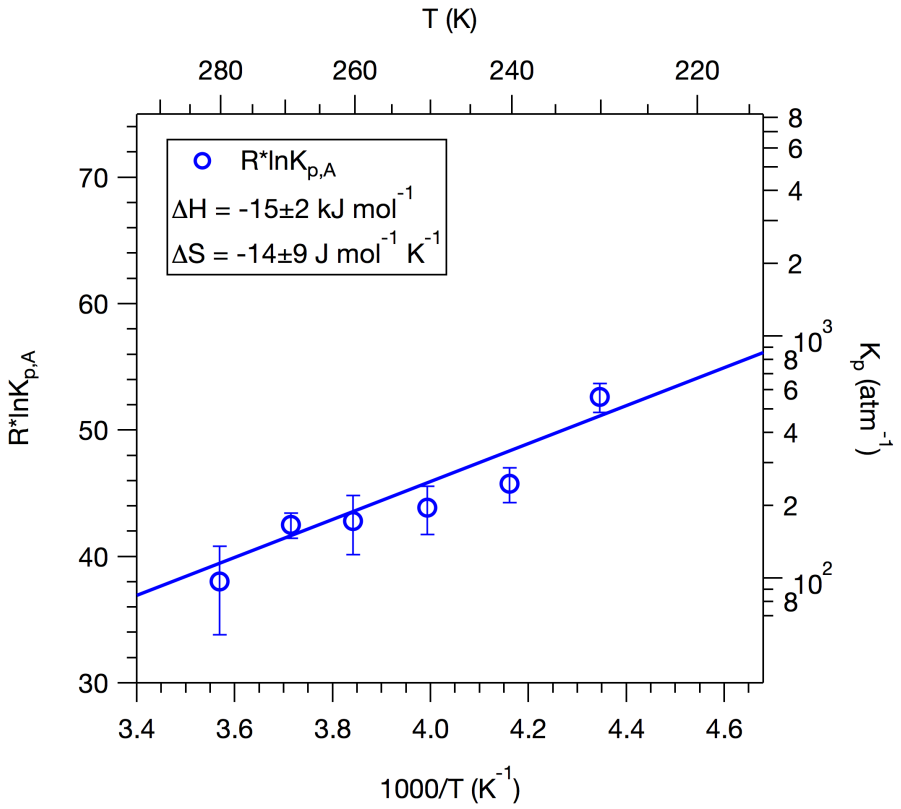

Figure 3.10: van 't Hoff plot of $R \ln K_{p,A}$ versus 1/T.

molecule^{-1}. Collisional stabilization of the complex was considered unimportant due to small barriers for dissociation and isomerization of the complex. Extrapolation of the van 't Hoff plot to T = 298 K gives $K_{c,A}$ ~3×10^{-18} cm^3 molecule^{-1}, which is smaller than the previously reported values of $K_{c,A,isom}$ by more than an order of magnitude. This is not surprising because of the low barrier for isomerization to $CH_3CH(OH)O_2$.

Table 3.4 compares the thermodynamic parameters for the HO_2 + CH_3CHO equilibrium reaction to the hydrogen-bonded complex, $HO_2 \cdot CH_3CHO$, and to the isomerized peroxy radical, $CH_3CH(OH)O_2$. The theoretical values were calculated from the standard enthalpies and entropies of formation of each species determined by da Silva et al. [30]. The values of $\Delta_r H^\circ_T$ and $\Delta_r S^\circ_T$ determined in this work are significantly different from the theoretical values. Comparison to other equilibrium reactions of HO_2 with carbonyl-containing compounds are also provided in Table 3.4 to evaluate the validity of these results.

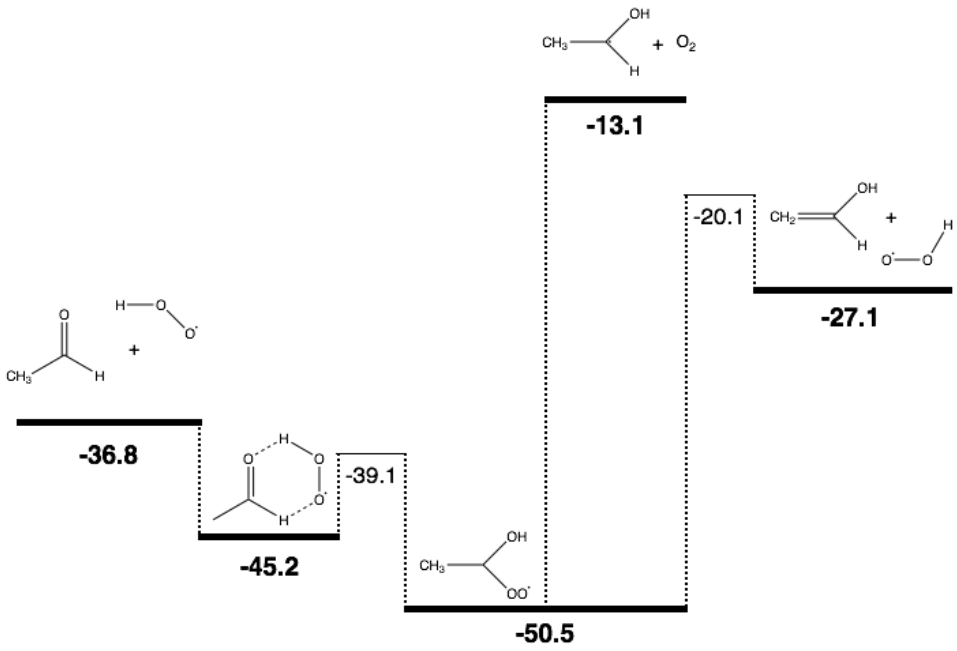

Figure 3.11: Energy level diagram of the HO_2 + CH_3CHO association reaction, adapted from da Silva and Bozzelli [29]. Energies are zero-point corrected and are in kcal mol^{-1}.

Table 3.4: Comparison of $\Delta_r H^\circ_T$ and $\Delta_r S^\circ_T$ for the reaction of HO_2 with various carbonyl compounds.

Reaction	T (K)	$\Delta_r H^\circ_T$ (kJ mol^{-1})	$\Delta_r S^\circ_T$ (J mol^{-1} K^{-1})	Ref
$HO_2 + CH_3CHO \rightleftharpoons HO_2 \cdot CH_3CHO$	230 - 280	−15 ± 2.0	−14 ± 9.0	This work (experiment)
	298	−35.2	−125	da Silva et al. [30] (DFT B3LYP/6-31G(d))
$HO_2 + CH_3CHO \rightleftharpoons CH_3CH(OH)O_2$	298 - 373	−64 ± 8	−157 ± 6	Tomas et al. [6] (experiment)
	298	−57.4	−145	da Silva et al. [30] (DFT B3LYP/6-31G(d))
$HO_2 + CH_2O \rightleftharpoons CH_2(OH)OO$	275 - 333	−68.0 ± 1.3	−146 ± 20	Veyret et al. [33] (experiment)
	292 - 306	−83	−201	Morajkar et al. [32] (experiment)[a]
$HO_2 + (CH_3)_2CO \rightleftharpoons HO_2 \cdot (CH_3)_2CO$	215 - 272	−35.4 ± 2.0	−88.2 ± 8.5	Grieman et al. [34] (experiment)
	245	−38.2	−126	Aloisio and Francisco [27][b] (DFT/B3LYP/6311++G(2df,3pd))
	245	−42.3	−135	Hermans et al. [28][b] (G2Mc//DFT/B3LYP/cc-pVTZ)

[a]Determined from van 't Hoff analysis of the reported equilibrium constants.
[b]Determined by Grieman et al. [34] using van 't Hoff analysis of the cited theoretical result.

The HO_2 adducts of CH_3CHO and CH_2O both form a six-membered ring, with the hydrogen of HO_2 bonding to the carbonyl oxygen and the aldehydic H bonding to the oxygen atom of HO_2 [28, 30]. The complex formed between HO_2 and CH_2O ($HO_2 \cdot CH_2O$) has been demonstrated experimentally to isomerize to form the hydroxymethylperoxy radical, $CH_2(OH)OO$ (HMP) [33], consistent with theoretical predictions [28]. Rapid isomerization of the $HO_2 \cdot CH_3CHO$ to form $CH_3CH(OH)O_2$ may explain the small values of $K_{c,A}$ that were observed. However, the small change in entropy for R11 that was measured in this work is difficult to rationalize based on the closed, ring-like structure of $HO_2 \cdot CH_3CHO$ that has been predicted theoretically.

For example, the experimentally measured equilibrium constants and thermodynamic parameters were concluded to be that of the $HO_2 + (CH_3)_2CO \rightleftharpoons HO_2 \cdot (CH_3)_2CO$ [34] based on thermodynamic assessment. The HO_2 adduct formed with acetone ($(CH_3)_2CO$), $HO_2 \cdot (CH_3)_2CO$, has been predicted to involve a $C{=}O\cdots HO_2$ hydrogen bond with [26] or without [28, 35] additional bonding between the oxygen atom of HO_2 and the methyl hydrogens on $(CH_3)_2CO$. The decrease in entropy that was measured experimentally and that was predicted for both conformers was significantly larger than that measured for $HO_2 \cdot CH_3CHO$ formation.

The results were likely influenced by systematic errors associated with the experimental conditions. The quoted errors for $\Delta_r H^\circ_{255\,K}$ (kJ mol^{-1}) and $\Delta_r S^\circ_{255\,K}$ (J mol^{-1} K^{-1}) do not take into account these errors, which are difficult to quantify. For the $K_{c,A}$ experiments, the loss of HO_2 by the equilibrium reaction was small and effectively reduced the sensitivity of the HO_2 time profiles for $K_{c,A}$. The range of $[CH_3CHO]$ over which data were collected were limited by the need to minimize competing secondary chemistry. Since k_9 is larger than k_2, $[CH_3OH]$ had to be large to ensure that enough HO_2 radicals were generated such that the $CH_3C(O)O_2$ self-reaction did not dominate. However, $[CH_3OH]$ also had to be sufficiently low to minimize the subsequent loss of HO_2 with the adducts formed with CH_3OH and CH_3CHO, which will be discussed in more detail in the next section. As a result, only low concentrations of $HO_2 \cdot CH_3CHO$ were being measured, which could not be avoided due to limitations placed by the complicated secondary chemistry.

3.4 Kinetics of $HO_2 + HO_2$

The $HO_2 + HO_2$ reaction proceeds via a tetroxide intermediate and has both bimolecular and termolecular pathways[36, 37]. The overall rate constant is pressure-

dependent and is expressed as a sum of two terms:

$$k_4 = k_{4,\mathrm{bi}} + k_{4,\mathrm{ter}}[\mathrm{M}], \tag{3.18}$$

where $k_{4,\mathrm{bi}}$ is the pressure-independent bimolecular rate constant and $k_{4,\mathrm{ter}}$ is the pressure-dependent termolecular rate constant. The reported values of k_4 from this work were obtained at a total pressure of 100 Torr in N_2. Values of $k_{4,\mathrm{bi}}$ were obtained using the JPL recommended value of $2.1 \times 10^{-33}[\mathrm{M}] \exp(920/T)$.

3.4.1 Rate enhancement of R4 by CH_3OH

The hydrogen-bonded complex of HO_2 with CH_3OH impacts the rate of the HO_2 self-reaction through a chaperone mechanism, i.e.,

$$\mathrm{HO_2 + HO_2 \cdot CH_3OH \longrightarrow H_2O_2 + O_2 + CH_3OH} \tag{R12}$$

At high concentrations of CH_3OH, the adducts undergo additional loss via the self reaction:

$$\mathrm{HO_2 \cdot CH_3OH + HO_2 \cdot CH_3OH \longrightarrow products} \tag{R13}$$

In the absence of CH_3CHO, the rate law of HO_2 is expressed as:

$$\frac{d[\mathrm{HO_2}]}{dt} = -2k_4[\mathrm{HO_2}]^2 - k_{12}[\mathrm{HO_2}][\mathrm{HO_2 \cdot CH_3OH}] \tag{3.19}$$

Assuming that the equilibrium in R8 is established rapidly relative to the timescales of R12, we use Equation 3.2 to get:

$$\frac{d[\mathrm{HO_2}]}{dt} = -(2k_4 + k_{12}K_{\mathrm{c,M}}[\mathrm{CH_3OH}])[\mathrm{HO_2}]^2 \tag{3.20}$$

$$= -2k_{4\mathrm{obs,M}}[\mathrm{HO_2}]^2 \tag{3.21}$$

where

$$k_{4\mathrm{obs,M}} = k_4 + \frac{k_{12}K_{\mathrm{c,M}}}{2}[\mathrm{CH_3OH}] \tag{3.22}$$

and k_4 is the rate constant for R4 in the limit of $[CH_3OH] = 0$. Thus, the observed second-order rate constant is linear in $[CH_3OH]$ with a proportionality constant given by the rate enhancement factor, $k''_{4,\mathrm{M}}$:

$$k_{4\mathrm{obs,M}} = k_4 + k''_{4,\mathrm{M}}[\mathrm{CH_3OH}] \tag{3.23}$$

where

$$k''_{4,\mathrm{M}} \equiv \frac{k_{12}K_{\mathrm{c,M}}}{2} \tag{3.24}$$

Figure 3.12 shows a plot of $k_{4\mathrm{obs,M}}$ versus [CH_3OH] for each temperature studied. Linear regression of the data points, weighted by the uncertainties in [CH_3OH] (~5%) and the fitted values of $k_{4\mathrm{obs,M}}$ (random error ~1-3%), were performed to obtain k_4 and $k''_{4\mathrm{M}}$ from the y-intercepts and slopes, respectively. Note that the data taken at T = 229.1 K deviated from linearity and was not well-described by Equation 3.23. Table 3.5 summarizes the experimental conditions over which the data were collected and lists the fitted values of k_4 and $k''_{4\mathrm{M}}$ at each temperature.

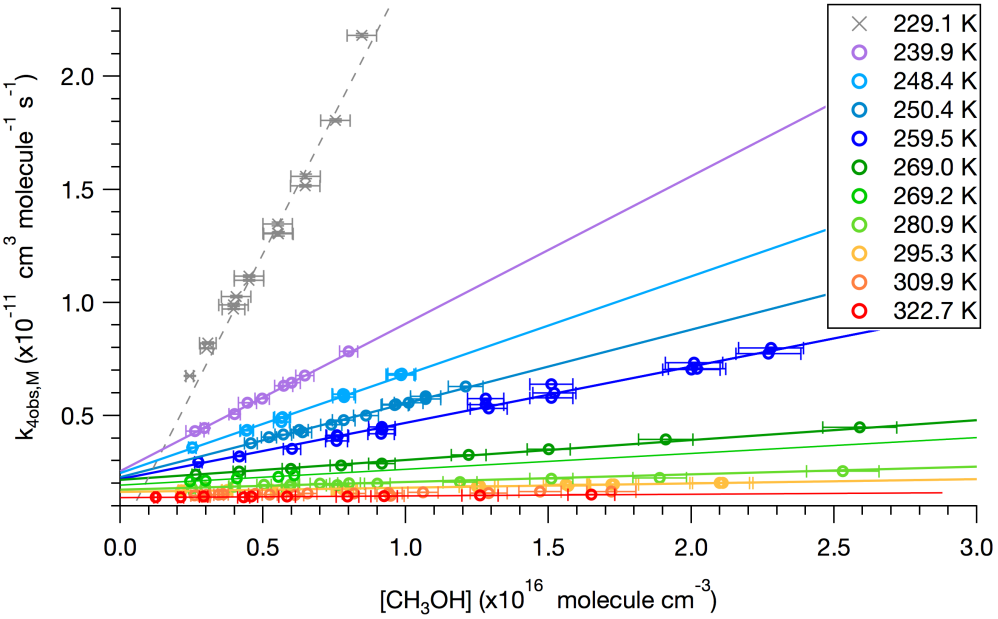

Figure 3.12: Plot of $k_{4\mathrm{obs,M}}$ as a function of [CH_3OH].

The Arrhenius plot of $k''_{4\mathrm{M}}$ is shown in Figure 3.13. At 100 Torr in N_2, the Arrhenius parameters for $k''_{4\mathrm{M}}$ were $A''_{4\mathrm{M}} = (9.2^{+0.7}_{-0.6}) \times 10^{-36}$ cm^6 molecule^{-2} s^{-1} and $E/R''_{4\mathrm{M}} = -4340 \pm 17$ K. Since Christensen et al. [2] used the UV data instead of the NIR data to measure the observed HO_2 self reaction rate constant, a direct comparison with the values of $k''_{4\mathrm{M}}$ measured in this work is not possible because the NIR and UV inherently observe different decay rates. The NIR measures HO_2 by probing the overtone of the O−H stretch. Since the H atom participates in hydrogen-bonding to form the complex, the frequency of the overtone transition of HO_2 bound in the complex is thought to be shifted sufficiently away from that of the free (i.e., monomeric) HO_2, such that the NIR probes only HO_2, and not $HO_2 \cdot X$. In

Table 3.5: Range of experimental conditions for determination of k_4 and $k''_{4,M}$ at 100 Torr.

T (K)	$[Cl_2]^a$	$[CH_3OH]^a$	$[Cl]_0{}^b$	# of experiments	$k_4{}^c$	$k''_{4,M}{}^d$
322.7	4.5 - 8.2	2.1 - 17	10 - 17	8	1.37	0.75
309.9	4.6 - 8.6	3.0 - 15	10 - 20	14	1.42	1.59
295.3	4.5 - 7.1	2.1 - 21	11 - 22	26	1.61	1.91
280.9	1.6 - 4.5	2.5 - 25	5.1 -10	13	1.72	3.40
269.2	1.6	2.5 - 6.1	5.2	5	1.92	7.00
269.0	4.5	2.6 - 26	10	7	1.92	8.84
259.5	1.6 - 4.5	2.7 - 23	3.7 - 9.3	18	2.18	25.0
250.4	1.9 - 5.3	4.6 - 12	7.2 - 18	12	2.28	32.7
248.4	4.6 - 7.1	2.5 - 9.9	14 - 20	11	2.46	43.5
240.1	1.8 - 4.5	3.0 - 9.9	4.9 - 15	7	2.53	65.2
229.1	0.75 - 1.9	2.4 - 8.5	2.0 - 4.0	13	-	-

[a]Units: 10^{15} molecule cm^{-3}
[b]Units: 10^{13} molecule cm^{-3}
[c]Units: 10^{-12} cm^3 molecule^{-1} s^{-1}
[d]Units: 10^{-29} cm^6 molecule^{-2} s^{-1}

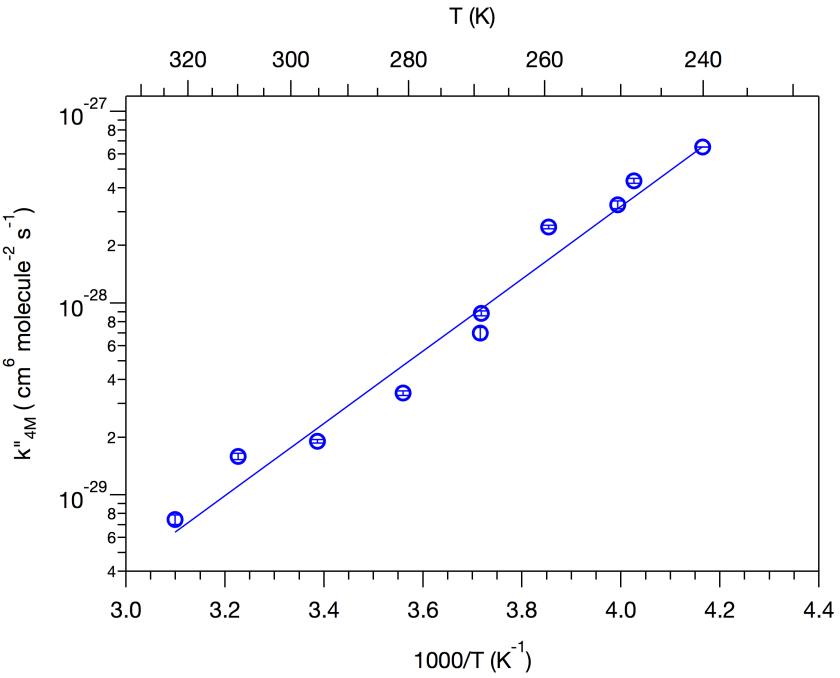

Figure 3.13: Arrhenius plot of k''_{4M}, shown with the weighted linear fit (blue line) to the data points (blue circles).

contrast, the UV presumably measures absorbance by both HO_2 and $HO_2 \cdot X$ since the UV probes the $B \leftarrow X$ transition of the electron on the non-bonding O atom, which does not participate in hydrogen bonding; i.e., HO_2 and $HO_2 \cdot X$ are likely to have similar absorption cross-sections. As a result, the NIR and UV probes begin to

observe different rate constants at lower temperatures due to the presence of $HO_2 \cdot X$. Since the total amount of HO_2 radicals is not observed in the NIR, the NIR probe observes a faster apparent decay rate than would be observed in the UV.

However, k_{12} can be used as an indirect comparison. The UV kinetics for sufficiently low [CH_3OH] ($K_{c,M}[CH_3OH] \ll 1$) were described by a second-order rate law with an effective rate constant given by

$$k_{4obs,M(UV)} = k_4 + (k_{12} - 2k_4)K_{c,M}[CH_3OH] \tag{3.25}$$

$$= k_4 + k''_{4,M(UV)} \tag{3.26}$$

where

$$k''_{4,M(UV)} \equiv (k_{12} - 2k_4)K_{c,M} \tag{3.27}$$

The Arrhenius plot of k_{12} determined from Equation 3.24 using the thermodynamic parameters as presented in the previous section is shown in Figure 3.14. The Arrhenius parameters were obtained from the weighted linear fit to the data: $A = (3.8^{+16}_{-0.9})\times10^{-13}$ cm^3 molecule^{-1} s^{-1} and $E/R = -1270 \pm 360$ K (1σ uncertainties). The uncertainties include errors in $K_{c,M}$ and $k''_{4,M(IR)}$. Figure 3.14 also compares the results to the values of k_{12} determined from Equation 3.27, which were calculated using the values of $K_{c,M}$ from the thermodynamic parameters reported in [3]. $k''_{4,M(UV)}$ was also calculated using the corresponding Arrhenius parameters reported in the same paper. The values appear to be in agreement within uncertainty for T > 260 K, but begin to deviate at lower temperatures. The observed difference may be explained by discrepancies in the measured values of $K_{c,M}$ as well as in k_4, which were used to calculate k_{12} from $k''_{4,M(UV)}$.

3.4.2 Temperature dependence of k_4

The Arrhenius plot of k_4 at 100 Torr is shown in Figure 3.15. A weighted linear fit to the data yielded the Arrhenius parameters: $A = (2.2 \pm 0.2)\times10^{-13}$ cm^3 molecule^{-1} s^{-1} and $E/R = -580 \pm 3$ K (1σ uncertainties). Using the JPL recommended value of 2.1×10^{-33}[M] exp $(920/T)$, the Arrhenius parameters for $k_{4,bi}$ were determined to be $A = (2.4^{+3.2}_{-1.9}) \times 10^{-13}$ cm^3 molecule^{-1} s^{-1} and $E/R = -525 \pm 75$ K. Comparison of the Arrhenius parameters are listed in Table 3.6. It should be noted that the value of $k_{4,ter}$ used by Christensen et al. [2] was from an older JPL data evaluation (JPL00-3), which was quoted as 1.7×10^{-33}[M] exp $(1000/T)$.

The results show good agreement with the JPL recommended values [1], but

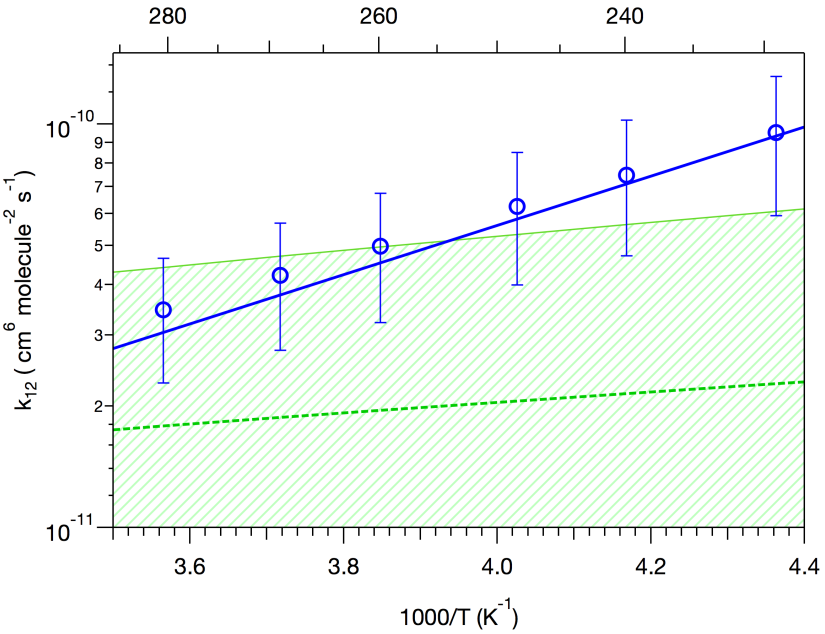

Figure 3.14: Arrhenius plot of k_{12}, shown with the linear fit (blue line) to the data points (blue circles). Values calculated from Christensen et al. [3] (green dashed line) with uncertainty bounds (1σ) are shown for comparison.

Table 3.6: Comparison of Arrhenius parameters for k_4. Quoted uncertainties from this work are 1σ; Christensen et al. [2] are 2σ. Note that $k_{4,ter}$ used by Christensen et al. [2] was slightly different from that in the current JPL data evaluation.

Ref.	T range (K)	$A_{4,100\ \mathrm{Torr}}{}^a$	$E/R_{4,100\ \mathrm{Torr}}$ (K)	$A_{4,bi}{}^a$	$E/R_{4,bi}$ (K)
This work	240.1 - 322.7	2.2 ± 0.2	-580 ± 3	$2.4^{+3.2}_{-1.9}$	-525 ± 75
[2]	222 - 295	8.8 ± 0.9	-210 ± 26	15 ± 2	-19 ± 31
[1]	222 - 500	2.6	-533	3.0	-460

[a] Units: 10^{-13} cm^3 molecule^{-1} s^{-1}

are inconsistent with the results from Christensen et al. [2], even though the same apparatus was used. It should be noted, however, that while this work was based only on the NIR data, the work in Christensen et al. [2] was based on the UV data, using the assumption that the cross-sections of HO_2 and $HO_2 \cdot CH_3OH$ are the same. One possible explanation for the discrepancy between the values reported by Christensen et al. [2] and those measured in this work is that the peak UV absorption cross-section of $HO_2 \cdot CH_3OH$ may be shifted away from that of HO_2, such that the cross-sections of the monomer and adduct at a given wavelength are no longer the same. The results presented here were not subject to systematic errors associated with uncertainties in the UV absorption cross-sections of HO_2, $HO_2 \cdot CH_3OH$, and H_2O_2, except in the

calibration of the NIR, which was done at room temperature where contribution of $HO_2 \cdot CH_3OH$ to the total absorbance was negligible.

Another possible explanation for the discrepancy is based on Dr. Aaron Noell's investigation of the purge effects on the observed rate constants measured by the UV and the NIR probes [23]. His work was motivated by the discrepancies in the pressure dependence of k_4 measured by the NIR and by the UV. This was attributed to the mixing regions on either end of the flow cell influencing the kinetics probed by the UV. As described in Chapter 2 of this thesis, temperature profile measurements showed a temperature gradient of length ~10 cm on either side of the cell, resulting from the mixing of the room temperature N_2 purge gas and the cold main reagent gas flow. This has two main implications on the measured kinetics. Firstly, the effective UV path length is not well-defined since the UV beam overlaps with the excimer beam and probes the entire length of the cell, including the mixing regions. Secondly, in the mixing regions, UV probes warmer gas, which reacts more slowly. Consequently, the observed rate coefficient in the UV would be underestimated at lower temperatures, which is consistent with the deviation seen in Figure 3.15. On the other hand, the NIR probe was less sensitive to purge effects due to the off-axis geometry of the NIR beam. This is expected since the majority of the overlap between the NIR beam and the excimer laser occurs towards the center of the reaction cell.

3.4.3 Rate enhancement of R4 by CH_3CHO

With CH_3CHO present, we have R14 and R15 in addition to R12 and R13:

$$HO_2 + HO_2 \cdot CH_3CHO \longrightarrow \text{products} \tag{R14}$$

$$HO_2 \cdot CH_3CHO + HO_2 \cdot CH_3CHO \longrightarrow \text{products} \tag{R15}$$

Assuming that fast equilibrium of HO_2 with CH_3OH and CH_3CHO is established via R8 and R11, respectively, the rate law for HO_2 can be written as:

$$\frac{d[HO_2]}{dt} = -(2k_4 + k_{12}K_{c,M}[CH_3OH] + k_{14}K_{c,A}[CH_3OH])[HO_2]^2 \tag{3.28}$$

$$= -2k_{4obs,A}[HO_2]^2 \tag{3.29}$$

where

$$k_{4obs,A} = k_4 + \frac{k_{12}K_{c,M}}{2}[CH_3OH] + \frac{k_{14}K_{c,A}}{2}[CH_3CHO] \tag{3.30}$$

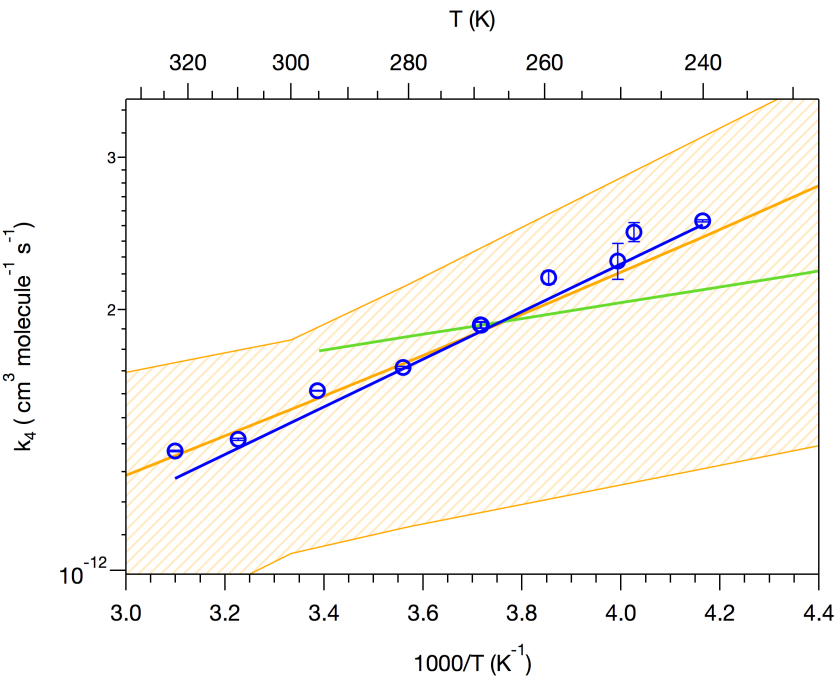

Figure 3.15: Arrhenius plot of k_4 at 100 Torr. Data points (blue circles) and fit (blue line) from this work are compared to the values from the current JPL data evaluation [1] (orange line) and from Christensen et al. [2] (green line). The orange shaded area denotes the uncertainty bounds on the JPL recommendations calculated from the uncertainty factors [1].

The observed bimolecular rate constant can be described by Equation 3.31:

$$k_{4\text{obs,A}} = k_4 + k''_{4,\text{M}}[\text{CH}_3\text{OH}] + k''_{4,\text{A}}[\text{CH}_3\text{CHO}] \tag{3.31}$$

where

$$k''_{4,\text{A}} = \frac{k_{14}K_{\text{c,A}}}{2} \tag{3.32}$$

From Equation 3.31, it follows that for a fixed [CH_3OH], $k_{4\text{obs,A}}$ is linear in [CH_3CHO] with a proportionality constant given by the rate enhancement factor, $k''_{4,\text{A}}$. $k_{4\text{obs,A}}$ was measured using varying concentrations of CH_3CHO at a fixed [CH_3OH]; however, data analysis was not as straightforward due to competing HO_2 + $CH_3C(O)O_2$ chemistry which could not be avoided:

$$\text{HO}_2 + \text{CH}_3\text{C(O)O}_2 \longrightarrow \text{CH}_3\text{C(O)OOH} + \text{O}_2 \tag{R16a}$$

$$\longrightarrow \text{CH}_3\text{C(O)OH} + \text{O}_3 \tag{R16b}$$

$$\longrightarrow \text{OH} + \text{CH}_3\text{C(O)O} + \text{O}_2 \tag{R16c}$$

Therefore, measurement of $k_{4obs,A}$ required the use of a complex chemical model and was inherently coupled with the determination of the rate constant of R16, which is described in detail in Chapter 4. Briefly, $k_{4obs,A}$ was determined by fitting the data with a kinetics model using the kinetics modeling software, FACSIMILE [38]. All fitted values of $k_{4obs,A}$ shown in the figures and tables in the following sections were determined from Monte Carlo analysis as described in Chapter 4. Data were collected under three general concentration conditions to investigate the rate enhancement effect by CH_3OH and CH_3CHO:

1. Varying both [CH_3OH] and [CH_3CHO] while keeping the [CH_3OH]:[CH_3CHO] ratio constant
2. Varying [CH_3OH] for a fixed [CH_3CHO]
3. Varying [CH_3CHO] for a fixed [CH_3OH]

As was the case for the $K_{c,A}$ experiments, the range of [CH_3CHO] over which data could be collected to investigate $k_{4obs,A}$ was limited by competing secondary chemistry. As mentioned previously, [CH_3OH] had to be large to ensure that enough HO_2 radicals were generated to minimize the $CH_3C(O)O_2$ self-reaction, but also sufficiently low to minimize the subsequent loss of HO_2 with the adducts formed with CH_3OH.

3.4.3.1 Varying [CH_3OH] and [CH_3CHO] with fixed [CH_3OH]:[CH_3CHO]

The fitted values of $k_{4obs,A}$ are plotted versus [CH_3OH]:[CH_3CHO] in Figure 3.16(a). The plotted data is limited to three temperatures for clarity. The figure shows that for a given value of [CH_3OH]:[CH_3CHO], the measured values of $k_{4obs,A}$ varied as much as 60-100% at T = 228.9 K. In comparison, the measured values of k_{16} were observed to be invariant of [CH_3OH]:[CH_3CHO]. Figure 3.16(b) shows a plot of the values of k_{16} versus [CH_3OH]:[CH_3CHO] for the same three temperatures, demonstrating that k_{16} is not enhanced by CH_3OH or by CH_3CHO.

Since $[CH_3OH]/[CH_3CHO] \propto [HO_2]_0/[CH_3CHO]_0$, the differences in the observed values of $k_{4obs,A}$ for a fixed value of [CH_3OH]:[CH_3CHO] could not be attributed to systematic errors in the secondary chemistry represented by the kinetics model. Rather, the values of $k_{4obs,A}$ appear to depend on both [CH_3OH] and [CH_3CHO], which will be demonstrated in more detail in the following sections.

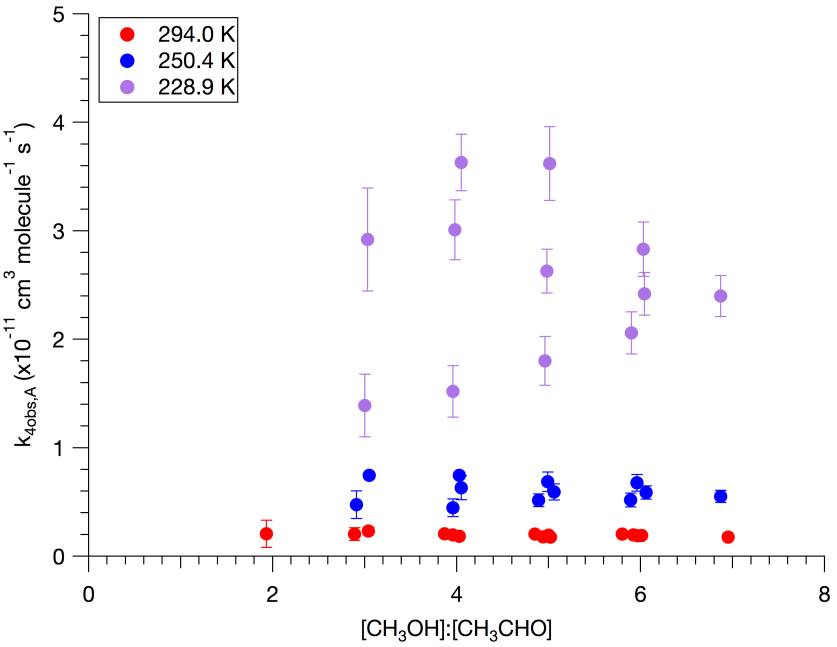

(a)

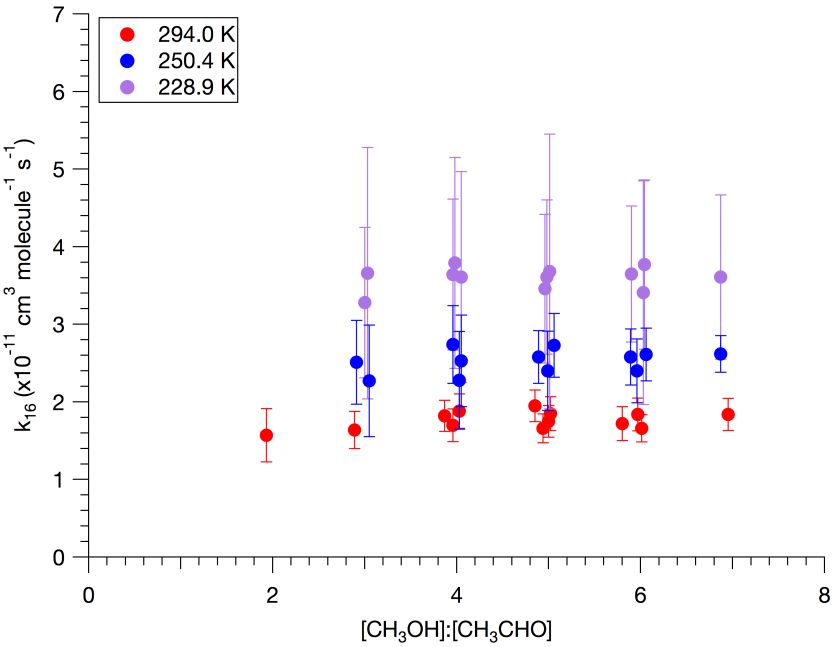

(b)

Figure 3.16: Plot of (a) $k_{4\text{obs,A}}$ and (b) k_{16} (shown with 1σ error bars) versus [CH_3OH]:[CH_3CHO] for three temperatures: 228.9 K (purple), 250.4 K (blue), and 294.0 K (red); data from other temperatures are excluded for clarity.

3.4.3.2 Varying [CH_3OH] for a fixed [CH_3CHO]

Figure 3.12 shows the values of $k_{4obs,A}$ determined at each temperature plotted as a function of [CH_3OH] from data sets collected using a fixed [CH_3CHO]. As expected, $k_{4obs,A}$ is observed to increase linearly with [CH_3OH], with stronger rate enhancement at lower temperatures. From Equation 3.31, values of $k''_{4,M}$ at each temperature were obtained from the slopes of the weighted linear fits to the plots of $k_{4obs,A}$ vs [CH_3OH]. Table 3.7 compares the measured values of $k''_{4,M}$ to the calculated values based on results from the work described in Section 3.4.1, showing generally good agreement within experimental uncertainty with the exception of the T = 228.9 K data, which were more susceptible to systematic error due to larger interference from secondary chemistry.

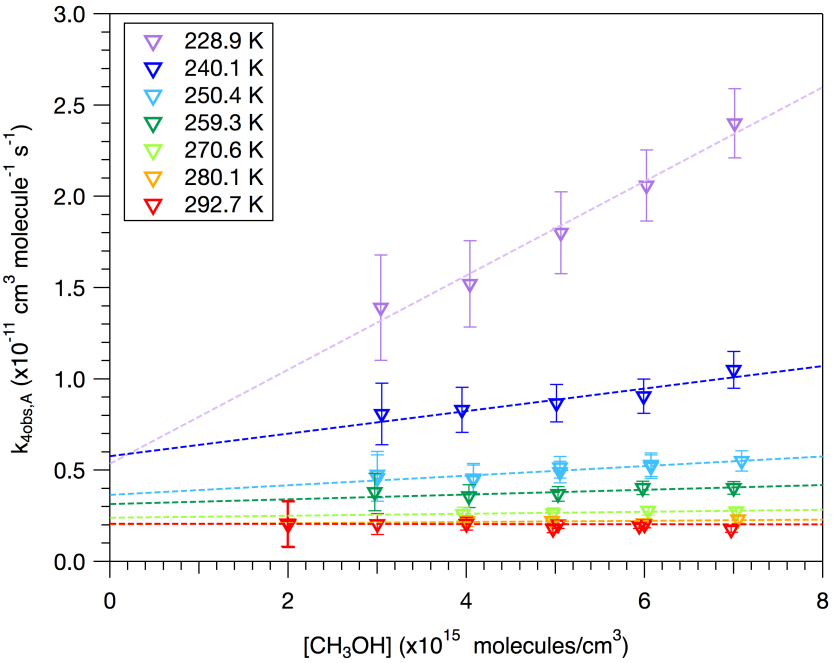

Figure 3.17: Values of $k_{4obs,A}$ (shown with 1σ error bars) measured using varying [CH_3OH] with fixed [CH_3CHO] = 1.0×10^{15} molecule cm^{-3}.

Table 3.7 also shows that the values of $k_{4obs,A}$ extrapolated to [CH_3OH] = 0 were consistently higher than the values of k_4 calculated using the Arrhenius parameters determined in Section 3.4.2, suggesting that $k''_{4,A} \neq 0$. As mentioned in Chapter 4, acceptable fits of the kinetics time traces to the kinetics model could only be attained by constraining $k_{4obs,A}$, which was always evaluated to be higher than the values calculated from Equation 3.23.

Table 3.7: Comparison of the slopes and intercepts of $k_{4obs,A}$ versus [CH_3OH] (1σ uncertainties) to values of $k''_{4,M}$ and k_4 calculated using the Arrhenius parameters determined from results in Section 3.4.1 and Section 3.4.2, respectively.

T (K)	Slope[a]	$k''_{4,M}$ [a]	Intercept[b]	k_4 [b]
280.1	3.3 ± 11	4.9	2.0 ± 0.63	1.8
270.6	5.4 ± 13	8.5	2.4 ± 0.76	1.9
259.3	13 ± 18	17	3.1 ± 1.1	2.1
250.4	26 ± 20	31	3.6 ± 1.1	2.2
240.1	62 ± 40	65	5.8 ± 2.2	2.5
228.9	260 ± 22	160	5.4 ± 1.1	2.8

[a]Units: 10^{-28} cm^6 $molecule^{-2}$ s^{-1}
[b]Units: 10^{-12} cm^3 $molecule^{-1}$ s^{-1}

3.4.3.3 Varying [CH_3CHO] for a fixed [CH_3OH]

Values of $k_{4obs,A}$ obtained at each temperature from data sets using a fixed [CH_3OH] are plotted versus [CH_3CHO] in Figure 3.18. The figure demonstrates that $k_{4obs,A}$ linearly increases with [CH_3CHO] and that stronger enhancement effects are observed at lower temperatures, further providing evidence that $k_{4obs,A}$ is enhanced by [CH_3CHO].

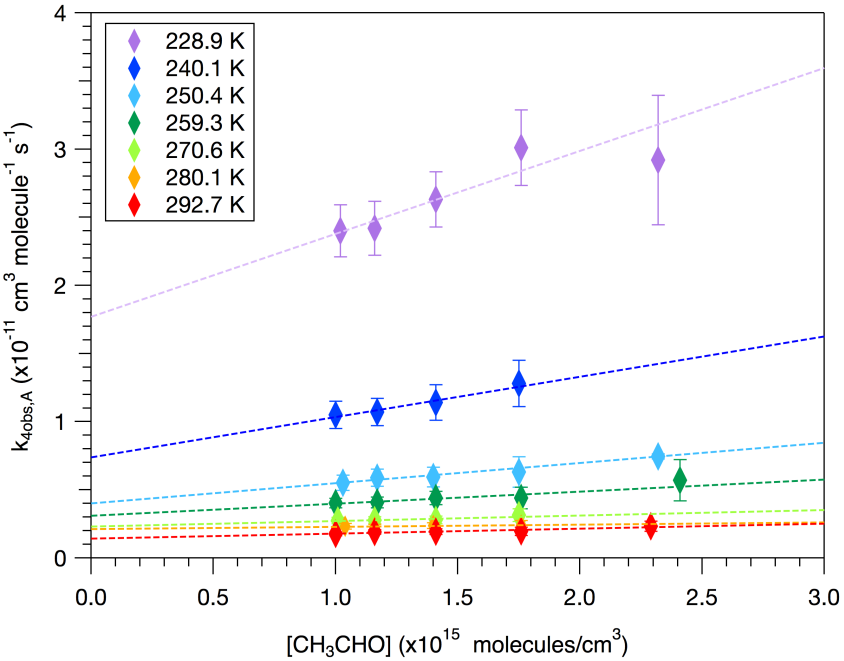

Figure 3.18: Values of $k_{4obs,A}$ (shown with 1σ error bars) measured using varying [CH_3CHO] with fixed [CH_3OH] = 7.0×10^{15} molecule cm^{-3}.

Table 3.8 summarizes the experimental conditions and the fitted values of $k_{4obs,A}$

and $k''_{4,A}$. The Arrhenius parameters for $k''_{4,A}$ were determined from the unweighted

Table 3.8: Range of experimental conditions for determination of $k''_{4,A}$ at 100 Torr.

T (K)	$[Cl_2]^a$	$[CH_3OH]^a$	$[CH_3CHO]^a$	$[Cl]_0{}^b$	# of experiments	$k''_{4,A}{}^c$
292.7	2.3	7.0 - 8.8	1.0 - 2.3	8.7	8	3.6 ± 2.7
280.1	3.8	7.0 - 8.8	1.0 - 2.2	13	7	1.6 ± 5.0
270.6	3.8	7.0 - 8.8	1.0 - 2.2	13	7	4.0 ± 6.3
259.3	3.0 - 3.8	7.0 - 8.8	1.0 - 2.9	11 - 13	10	8.8 ± 7.8
250.4	3.8	7.0 - 8.8	1.0 - 2.3	8.3	8	15 ± 3.7
240.1	2.3 - 3.8	7.0 - 8.8	1.0 - 2.2	5.7 - 9.1	9	30 ± 25
228.9	2.4 - 3.8	7.0 - 8.8	1.0 - 2.3	5.6 - 8.7	10	61 ± 32

[a]Units: 10^{15} molecule cm^{-3}
[b]Units: 10^{13} molecule cm^{-3}
[c]Units: 10^{-28} cm^6 molecule^{-2} s^{-1}

linear fit to the Arrhenius plot, shown in Figure 3.19. A weighted fit was not possible because the otherwise observable temperature dependence was concealed by the large error bars on the measured values of $k''_{4,A}$. At 100 Torr in N_2, the Arrhenius parameters were $A''_{4,A} = (8.3^{+9.0}_{-7.3}) \times 10^{-34}$ cm^6 molecule^{-2} s^{-1} and $E/R''_{4,A} = -3600 \pm 540$ K (1σ uncertainties). The uncertainties include systematic errors in the rate constants of the secondary reactions in the kinetics model that were used to determine $k_{4,obs}$. These errors were determined from Monte Carlo simulations, which are described in detail in Chapter 4. The results show a clear enhancement effect by CH_3CHO that is approximately an order of magnitude larger than that by CH_3OH. A slightly smaller temperature dependence was observed for $k''_{4,A}$, albeit inconclusively due to the large uncertainties.

3.5 Conclusion

The equilibrium constants of the reaction of HO_2 with CH_3OH and CH_3CHO were measured at 100 Torr in N_2 over the temperature range T = 220 - 296 K and T = 230 - 296 K, respectively, using NIR WMS in a pulsed photolysis flow cell. The thermodynamic parameters for the formation of the adducts were determined using van 't Hoff analysis and were compared to previous experimental and theoretical results as well as to the thermodynamics of the formation of other related, analogous adducts. Large systematic errors were suspected for the measured thermodynamic parameters of R11 due to the limited range of experimental conditions; thus, a more thorough reinvestigation of this reaction may be warranted in the future.

The temperature dependence of the HO_2 self-reaction rate constant was also reinvestigated at 100 Torr over the temperature range T = 230 - 320 K. The results

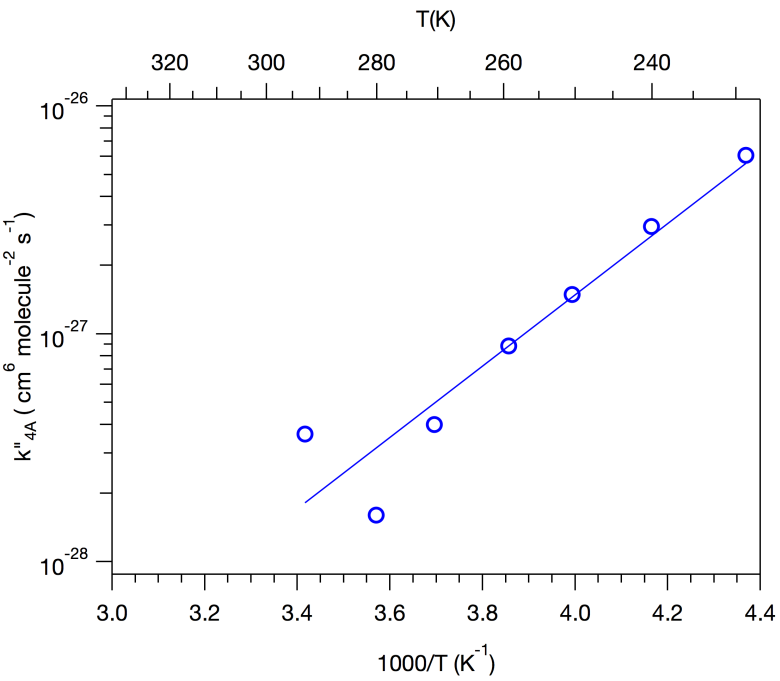

Figure 3.19: Arrhenius plot of k''_{4A}, shown with the unweighted linear fit (blue line) to the data points (blue circles).

were in good agreement with the JPL recommended values. Discrepancies with the values reported by Christensen et al. [2] are suggested to be due to purge effects in the mixing regions of the flow cell that were affecting the rate constant observed by the UV probe. The rate enhancement of the HO_2 self reaction by CH_3OH and CH_3CHO was characterized at 100 Torr over the temperature range T = 230 - 320 K and T = 230 - 294 K, respectively. Time-dependent NIR HO_2 signals were analyzed using pseudo-second order kinetics. The observed HO_2 rate constants were found to increase linearly with $[CH_3OH]$ and $[CH_3CHO]$ under the experimental conditions of this work. Both rate enhancement effects were negatively dependent on temperature and the rate enhancement by CH_3CHO was revealed to be approximately an order of magnitude larger than the rate enhancement by CH_3OH. The results from this work demonstrate the importance of including these additional loss processes of HO_2 for accurate characterization of the kinetics of HO_2 reactions at low temperatures.

References

[1] Sander, S. P.; Abbat, J.; Barker, J.R.; Burkholder, J.B.; Huie, R.E.; Kolb, C.E.; Kurylo, M.J.; Wilmouth, D.M.; Orkin, V.L.; Wine, P.H. *Chemical Kinetics and Photochemical Data for Use in Atmospheric Studies, Evaluation No. 18*; Jet Propulsion Laboratory, Pasadena: JPL Publication 15-10, 2015.

[2] Christensen, L. E.; Okumura, M.; Sander, S. P.; Salawitch, R. J.; Toon, G. C.; Sen, B.; Blavier, J.-F.; Jucks, K. W. Kinetics of HO2 + HO2 → H2O2 + O2: Implications for Stratospheric H2O2. *Geophysical Research Letters* **2002**, *29*, 13–1.

[3] Christensen, L. E.; Okumura, M.; Hansen, J. C.; Sander, S. P.; Francisco, J. S. Experimental and Ab Initio Study of the HO2CH3OH Complex: Thermodynamics and Kinetics of Formation. *J. Phys. Chem. A* **2006**, *110*, 6948–6959.

[4] Moortgat, G.; Veyret, B.; Lesclaux, R. Absorption Spectrum and Kinetics of Reactions of the Acetylperoxy Radical. **1989**, *93*, 2362–2368.

[5] Crawford, M. A.; Wallington, T. J.; Szente, J. J.; Maricq, M. M.; Francisco, J. S. Kinetics and Mechanism of the Acetylperoxy + HO2 Reaction. *The Journal of Physical Chemistry A* **1999**, *103*, 365–378.

[6] Tomas, A.; Villenave, E.; Lesclaux, R. Reactions of the HO2 Radical with CH3CHO and CH3C(O)O2 in the Gas Phase. *The Journal of Physical Chemistry A* **2001**, *105*, 3505–3514.

[7] Le Crâne, J.-P.; Rayez, M.-T.; Rayez, J.-C.; Villenave, E. A Reinvestigation of the Kinetics and the Mechanism of the CH3C(O)O2 + HO2 Reaction Using Both Experimental and Theoretical Approaches. *Physical Chemistry Chemical Physics* **2006**, *8*, 2163–2171.

[8] Jenkin, M. E.; Hurley, M. D.; Wallington, T. J. Investigation of the Radical Product Channel of the CH3C(O)O2 + HO2 Reaction in the Gas Phase. *Physical Chemistry Chemical Physics* **2007**, *9*, 3149–3162.

[9] Dillon, T. J.; Crowley, J. N. Direct Detection of OH Formation in the Reactions of HO2 with CH3C(O)O2 and Other Substituted Peroxy Radicals. *Atmospheric Chemistry and Physics* **2008**, *8*, 4877–4889.

[10] Groß, C. B. M.; Dillon, T. J.; Schuster, G.; Lelieveld, J.; Crowley, J. N. Direct Kinetic Study of OH and O3 Formation in the Reaction of CH3C(O)O2 with HO2. *The Journal of Physical Chemistry A* **2014**, *118*, 974–985.

[11] Winiberg, F. A. F.; Dillon, T. J.; Orr, S. C.; Groß, C. B. M.; Bejan, I.; Brumby, C. A.; Evans, M. J.; Smith, S. C.; Heard, D. E.; Seakins, P. W. Direct Measurements of OH and Other Product Yields from the HO2 + CH3C(O)O2 Reaction. *Atmos. Chem. Phys.* **2016**, *16*, 4023–4042.

[12] Hui, A. O.; Fradet, M.; Okumura, M.; Sander, S. P. Temperature Dependence of the Kinetics and Product Yields of the HO2 + CH3C(O)O2 Reaction by Direct Detection of OH and HO2 Radicals Using 2f-IR Wavelength Modulation Spectroscopy., Manuscript in preparation, Manuscript in preparation, 2018.

[13] Hamilton, E. J. Water Vapor Dependence of the Kinetics of the Self-reaction of HO2 in the Gas Phase. *The Journal of Chemical Physics* **1975**, *63*, 3682–3683.

[14] Hamilton, E. J.; Lii, R.-R. The Dependence on H2O and on NH3 of the Kinetics of the Self-Reaction of HO2 in the Gas-Phase Formation of HO2·H2O and HO2·NH3 Complexes. *International Journal of Chemical Kinetics* **1977**, *9*, 875–885.

[15] DeMore, W. B. Reaction of Hydroperoxo Radicals with Ozone and the Effect of Water Vapor on Hydroperoxo Kinetics. *The Journal of Physical Chemistry* **1979**, *83*, 1113–1118.

[16] Cox, R. A.; Burrows, J. P. Kinetics and Mechanism of the Disproportionation of Hydroperoxyl Radical in the Gas Phase. *The Journal of Physical Chemistry* **1979**, *83*, 2560–2568.

[17] Lii, R.-R.; Gorse, R. A.; Sauer, M. C.; Gordon, S. Temperature Dependence of the Gas-Phase Self-Reaction of Hydroperoxo Radicals in the Presence of Ammonia. *The Journal of Physical Chemistry* **1980**, *84*, 813–817.

[18] Kircher, C. C.; Sander, S. P. Kinetics and Mechanism of HO2 and DO2 Disproportionation. *J. Phys. Chem* **1983**, *88*, 2081–2091.

[19] Andersson, B. Y.; Cox, R. A.; Jenkin, M. E. The Effect of Methanol on the Self Reaction of HO2 Radicals. *International Journal of Chemical Kinetics* **1988**, *20*, 283–295.

[20] Clegg, S. M.; Abbatt, J. P. D. Oxidation of SO2 by H2O2 on Ice Surfaces at 228 K: A Sink for SO2 in Ice Clouds. *Atmos. Chem. Phys.* **2001**, *1*, 73–78.

[21] Bloss, W. J.; Rowley, D. M.; Cox, R. A.; Jones, R. L. Rate Coefficient for the BrO + HO2 Reaction at 298 K. *Physical Chemistry Chemical Physics* **2002**, *4*, 3639–3647.

[22] Keller-Rudek, H.; Moortgat, G. K.; Sander, R.; Sörensen, R. The MPI-Mainz UV/VIS Spectral Atlas of Gaseous Molecules of Atmospheric Interest. *Earth System Science Data* **2013**, *5*, 365–373.

[23] Noell, A. C. Laboratory Studies of the Self and Cross Reactions of Atmospheric Peroxy Radicals., Ph.D. Pasadena, CA: California Institute of Technology, 2009.

[24] Shuzo, O. Computer Aided Data Book of Vapor Pressure. `http://e-data.jp/vpcal2/e/`.

[25] Christensen, L. E. Laboratory Studies of Atmospherically Important Gas-Phase Peroxy Radical Reactions., Ph.D. Pasadena, CA: California Institute of Technology, 2002.

[26] Aloisio, S.; Francisco, J. S. Existence of a Hydroperoxy and Water (HO2·H2O) Radical Complex. *The Journal of Physical Chemistry A* **1998**, *102*, 1899–1902.

[27] Aloisio, S.; Francisco, J. S. Complexes of Hydroxyl and Hydroperoxyl Radical with Formaldehyde, Acetaldehyde, and Acetone. *The Journal of Physical Chemistry A* **2000**, *104*, 3211–3224.

[28] Hermans, I.; Müller, J.-F.; Nguyen, T. L.; Jacobs, P. A.; Peeters, J. Kinetics of -Hydroxy-Alkylperoxyl Radicals in Oxidation Processes. HO2•-Initiated Oxidation of Ketones/Aldehydes near the Tropopause. *The Journal of Physical Chemistry A* **2005**, *109*, 4303–4311.

[29] Da Silva, G.; Bozzelli, J. W. Role of the -Hydroxyethylperoxy Radical in the Reactions of Acetaldehyde and Vinyl Alcohol with HO2. *Chemical Physics Letters* **2009**, *483*, 25–29.

[30] Da Silva, G.; Bozzelli, J. W.; Liang, L.; Farrell, J. T. Ethanol Oxidation: Kinetics of the -Hydroxyethyl Radical + O2 Reaction. *The Journal of Physical Chemistry A* **2009**, *113*, 8923–8933.

[31] Farnia, S.; Vahedpour, M.; Abedi, M.; Farrokhpour, H. Theoretical Study on the Mechanism and Kinetics of Acetaldehyde and Hydroperoxyl Radical: An Important Atmospheric Reaction. *Chemical Physics Letters* **2013**, *583*, 190–197.

[32] Morajkar, P.; Schoemaecker, C.; Okumura, M.; Fittschen, C. Direct Measurement of the Equilibrium Constants of the Reaction of Formaldehyde and Acetaldehyde with HO2 Radicals. *International Journal of Chemical Kinetics* **2014**, *46*, 245–259.

[33] Veyret, B.; Lesclaux, R.; Rayez, M. T.; Rayez, J. C.; Cox, R. A.; Moortgat, G. K. Kinetics and Mechanism of the Photo-Oxidation of Formaldehyde. 1. Flash Photolysis Study. *The Journal of Physical Chemistry* **1989**, *93*, 2368–2374.

[34] Grieman, F. J.; Noell, A. C.; Davis-Van Atta, C.; Okumura, M.; Sander, S. P. Determination of Equilibrium Constants for the Reaction Between Acetone and HO2 Using Infrared Kinetic Spectroscopy. *The Journal of Physical Chemistry A* **2011**, *115*, 10527–10538.

[35] Cours, T.; Canneaux, S.; Bohr, F. Features of the Potential Energy Surface for the Reaction of HO2 Radical with Acetone. *International Journal of Quantum Chemistry* **2006**, *107*, 1344–1354.

[36] Patrick, R.; Barker, J. R.; Golden, D. M. Computational Study of the Hydroperoxo + Hydroperoxo and Hydroperoxo-d + Hydroperoxo-d Reactions. *The Journal of Physical Chemistry* **1984**, *88*, 128–136.

[37] Mozurkewich, M.; Benson, S. W. Self-Reaction of HO2 and DO2: Negative Temperature Dependence and Pressure Effects. *International Journal of Chemical Kinetics* **1985**, *17*, 787–807.

[38] *FACSIMILE* version 4.1.41 [computer software]; Faringdon, Oxon, UK, 2003.

Chapter 4

TEMPERATURE DEPENDENCE STUDY OF THE KINETICS AND PRODUCT YIELDS OF THE HO_2 + $CH_3C(O)O_2$ REACTION BY DIRECT DETECTION OF OH AND HO_2 RADICALS USING 2F-IR WAVELENGTH MODULATION SPECTROSCOPY

Abstract

The HO_2 + $CH_3C(O)O_2$ reaction consists of three product channels: $CH_3C(O)OOH$ + O_2 (R1a), $CH_3C(O)OH$ + O_3 (R1b), and OH + $CH_3C(O)O$ + O_2 (R1c). The overall rate constant (k_1) and product yields (α_{1a}, α_{1b}, and α_{1c}) were determined over the atmospherically-relevant temperature range of 230 - 294 K at 100 Torr in N_2. Time resolved kinetics measurements were performed in a pulsed laser photolysis experiment in a slow flow cell employing simultaneous infrared (IR) and ultraviolet (UV) absorption spectroscopy. HO_2 and $CH_3C(O)O_2$ were formed by Cl-atom reactions with CH_3OH and CH_3CHO, respectively. Heterodyne near- and mid-infrared (NIR and MIR) wavelength modulation spectroscopy (WMS) was employed to selectively detect HO_2 and OH radicals. Ultraviolet absorption at 225 nm and 250 nm was used to detect various peroxy radicals as well as ozone (O_3). These experimental techniques enabled direct measurements of α_{1c} and α_{1b} via time-resolved spectroscopic detection in the MIR and the UV, respectively. At each temperature, experiments were performed at various ratios of initial HO_2 and $CH_3C(O)O_2$ concentrations to quantify the secondary chemistry. The Arrhenius expression was found to be $k_1(T) = 1.38^{+1.17}_{-0.63} \times 10^{-12} \exp[(730 \pm 170)/T]$ cm^3 molecule^{-1} s^{-1}. α_{1a} was temperature-independent while α_{1b} and α_{1c} increased and decreased, respectively, with increasing temperatures. These trends are consistent with the current recommendation by the IUPAC data evaluation [1]. Hydrogen-bonded adducts of HO_2 with the precursors, $HO_2 \cdot CH_3OH$ and $HO_2 \cdot CH_3CHO$, played a role at lower temperatures; as part of this work, kinetics of the adducts were also measured.

4.1 Introduction

Organic peroxy radicals (RO_2), important intermediates in the Earth's atmosphere, are formed from the oxidation of volatile organic compounds (VOCs). RO_2 plays a key role in the tropospheric HO_x ($HO_x \equiv HO_2$ + OH) cycle and its chemistry influences the formation of tropospheric O_3 and other secondary pollutants. In

polluted regions (i.e. high $NO_x \equiv NO + NO_2$), the predominant sink for RO_2 is reaction with NO, which primarily propagates radical chemistry by recycling NO_2 and OH radicals. During the day, NO_2 photolysis produces O_3, which is the primary constituent of photochemical smog. In remote regions of the atmosphere where NO_x concentrations are low, the primary loss processes for RO_2 are reaction with HO_2 and with other RO_2 radicals.

Reactions of RO_2 with HO_2 are of particular interest because the product distribution depends on the structure of the R group. Although $HO_2 + RO_2$ reactions were initially thought to be radical terminating processes, more recent studies have shown that for some more complex peroxy radicals, the reaction can also produce OH radicals via a radical propagating channel, effectively sustaining the oxidative capacity of the atmosphere.

$$\begin{aligned} HO_2 + RO_2 &\longrightarrow ROOH + O_2 \\ &\longrightarrow ROH + O_3 \\ &\longrightarrow OH + RO + O_2 \end{aligned}$$

$HO_2 + RO_2$ reactions that have an OH recycling channel are of atmospheric importance because they contribute to higher OH concentrations in VOC-rich regions. There is currently disagreement between modeled and observed OH levels over remote, forested regions of the Earth. Results from various field campaigns have demonstrated that in these regions, the level of the discrepancy appears to be positively correlated with concentrations of isoprene, which is an abundant chemically active biogenic compound [2–6]. While this discrepancy could be due to possible missing sources of OH in current atmospheric models, instrument-dependent artifacts in the OH measurements, or a combination of both, a full picture of the radical chemistry in VOC-rich atmospheres requires further laboratory experiments.

One significant oxidation product of isoprene is the acetylperoxy radical, $CH_3C(O)O_2$. Hasson et al. [7] found that the reaction of $CH_3C(O)O_2$ with HO_2 includes an OH product channel:

$$\begin{aligned} HO_2 + CH_3C(O)O_2 &\longrightarrow CH_3C(O)OOH + O_2 && \text{(R1a)} \\ &\longrightarrow CH_3C(O)OH + O_3 && \text{(R1b)} \\ &\longrightarrow OH + CH_3C(O)O + O_2 && \text{(R1c)} \end{aligned}$$

$CH_3C(O)O_2$ plays an important role in tropospheric chemistry because they are also

formed from the photooxidation of a large variety of higher carbonyl compounds such as acetaldehyde, acetone, and other VOCs that are abundant in the atmosphere. Although this reaction may not fully resolve the OH discrepancy between the models and observations, this reaction still serves as an important benchmark system to study OH regeneration from HO_2 + RO_2 reactions in low NO_x environments.

R1 has been the subject of a number of experimental studies and was initially thought to be exclusively radical terminating, based on end-product studies of stable products [8, 9]. Hasson et al. [7] first observed the OH product channel. Subsequently, two independent quantum chemistry calculations [10, 11] suggested that R1 proceeds via one of two mechanisms: 1) hydrogen transfer on a triplet surface to form $CH_3C(O)OOH$ + O_2 (R1a) or 2) formation of a hydrotetroxide (ROOOOH) intermediate followed by decomposition on a singlet surface to form either $CH_3C(O)OH$ + O_3 (R1b) or OH + $CH_3C(O)O$ + O_2 (R1c). The potential energy surfaces from both studies showed that R1c was less exothermic than R1b. A simplified energy level diagram of R1 modified from Hasson et al. [10] is shown in Figure 4.1. The figure demonstrates the differences in the energies calculated by Hasson et al. [10] and Le Crâne et al. [11]. Le Crâne et al. [11] cited the low exothermicity of R1c relative to R1b to explain the < 0.1 yield of OH that was reported experimentally. However, Hasson et al. [10] performed master equation calculations which found that R1c is a significant product channel proceeding via a chemically activated $HO_2 \cdot CH_3C(O)O_2$ adduct.

Since these revelations, both indirect [11, 12] and direct [13–15] measurements of OH radicals from R1c have been made. Table 4.1 summarizes the experimental techniques employed by previous laboratory studies of R1. Although a majority of these experimental studies reports a significant OH yield from R1 and support Hasson et al. [10]'s postulate, there are discrepancies in the reported values. Chamber-type studies of this reaction produced valuable data in identifying and quantifying the stable species [7–9, 12, 15]; however, extracting accurate kinetics information from these studies is limited by the uncertainties in the rate coefficients of the secondary chemistry. Furthermore, with the exception of Winiberg et al. [15], these studies also lacked direct sensitivity to reactive radical species. Meanwhile, many of the pulsed photolysis experiments of the title reaction have used UV absorption techniques, which can detect peroxy radicals with good sensitivity due to the large absorption cross-sections. However, there is significant spectral overlap among the peroxy radicals, as well as with product species generated from unavoidable secondary chemistry. The spectral overlap necessitates deconvolution of the observed UV

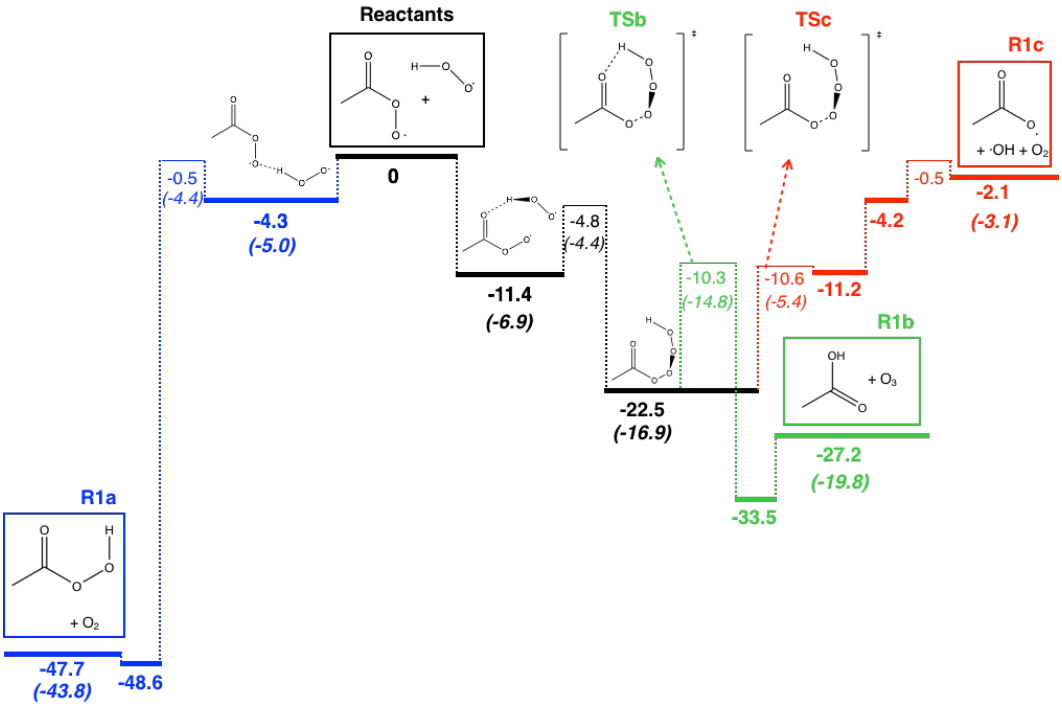

Figure 4.1: Simplified energy level diagram (energies in kcal mol^{-1}) of the HO_2 + $CH_3C(O)O_2$ reaction, modified from Hasson et al. [10]. Energies in parenthesis, if provided, were taken from Le Crâne et al. [11]. All other energies were taken from Hasson et al. [10]. The triplet surface is shown in blue. The two product channels on the singlet surface are shown in red (R1c) and green (R1b). The part of the singlet surface that is common to R1c and R1b is shown in black.

spectrum, which introduces additional systematic errors. Previous studies of this reaction utilizing laser-induced fluorescence (LIF) provided an extremely sensitive way of detecting OH radicals directly; however, no studies have yet used techniques that directly and selectively measure both OH and HO_2.

Table 4.1: Summary of previous HO_2 + $CH_3C(O)O_2$ studies and their sensitivities to key chemical species (R = $CH_3C(O)$). FP = flash photolysis; PLP = pulsed laser photolysis; UVAS = UV absorption spectroscopy; HPLC = high performance liquid chromatography; FTIR = Fourier Transform infrared spectroscopy; LIF = laser induced fluorescence.

Ref.	Method	T (K)	P (Torr)	HO_2	RO_2	OH	ROOH	O_3	ROH
Niki et al. [8] [a]	FTIR	298	700				Direct	Direct	Direct
Moortgat et al. [16] [b]	FP/UVAS	253 - 368	600 - 650	UV	UV			UV	
Horie and Moortgat [9] [c]	FTIR	263 - 333	730 - 770			Direct	Direct	Direct	
Crawford et al. [17] [b]	PLP/IR/UVAS	269 - 363	50	Direct	UV			UV	
Tomas et al. [18] [b]	FP/UVAS	273 - 403	760	UV	UV			UV	
Hasson et al. [7] [b]	UVP/FTIR/HPLC	298	800				Direct		Direct
Le Crâne et al. [11] [b]	FP/UVAS	298	760	UV	UV			UV	
Jenkin et al. [12] [b]	UVP/FTIR	296	700			Indirect	Direct		Direct
Dillon and Crowley [13] [b]	PLP/LIF	298	75 - 529			Direct			
Groß et al. [14] [b]	PLP/LIF/UVAS	298	100 - 500	UV	UV	Direct		UV	
Winiberg et al. [15] [b]	UVP/FTIR/LIF	293	750	Indirect		Direct	Direct	Direct	Direct
This work [b]	PLP/IR/UVAS	230 - 294	100	Direct	UV	Direct		UV	

[a] Reagent gases: Cl_2 /CH_2O/CH_3CHO/O_2 /N_2
[b] Reagent gases: Cl_2 /CH_3OH/CH_3CHO/O_2 /N_2
[c] Reagent gases: $CH_3C(O)C(O)CH_3$ /O_2 /Ar

In addition, there are no temperature dependence studies of R1c, which are needed in modeling studies of the upper troposphere. For example, the only experimental temperature dependence studies of both the kinetics and branching ratios of R1 assumed that the reaction was exclusively radical terminating [16–18], which may have led to an underestimation of the reported overall rate constant, k_1. It is also important to note that temperature dependence studies using CH_3OH and CH_3CHO as precursors for HO_2 and $CH_3C(O)O_2$, respectively, may not have fully accounted for the formation of hydrogen-bonded adducts involving HO_2 and the radical precursors. The radical adducts, $HO_2 \cdot CH_3OH$ and $HO_2 \cdot CH_3CHO$, react at enhanced rates with HO_2, leading to a faster observed HO_2 decay rate. Rate enhancement of the HO_2 self reaction by these adducts contributes to the total loss rate of HO_2 and becomes more significant at low temperatures, where adduct formation is more favored [19–21]. The reactions of the adducts must be considered in order to measure k_1 correctly.

In the present work, we used Infrared Kinetic Spectroscopy (IRKS) for sensitive and selective detection of several radical species. IRKS combines detection in the IR and UV to simultaneously monitor multiple species in real time. We determined the overall rate constant, k_1, and the product yields, α_{1a}, α_{1b}, and α_{1c}, where

$$\alpha_{1a} = k_{1a}/k_1 \qquad \alpha_{1b} = k_{1b}/k_1 \qquad \alpha_{1c} = k_{1c}/k_1 \tag{4.1}$$

and

$$k_1 = k_{1a} + k_{1b} + k_{1c} \tag{4.2}$$

In the near-IR (NIR) and mid-IR (MIR), we used a high resolution heterodyne technique, wavelength modulation spectroscopy (WMS), to selectively detect HO_2 and OH radicals, respectively. We generated HO_2 and $CH_3C(O)O_2$ radicals by pulsed laser photolysis (PLP), and measured the decay of HO_2 in the NIR, and the formation and subsequent decay of OH in the MIR. Direct detection of HO_2 in the NIR and OH in the MIR allowed for accurate determination of k_1 and direct measurements of α_{1c}. Although traditional LIF techniques offer superior sensitivity to OH radicals, an advantage of IRKS is that the OH and HO_2 probes follow identical optical paths, removing biases that would otherwise be introduced from differences in diffusion, path lengths, etc., that result from probing different regions of the photolysis volume. In addition to NIR and MIR WMS, we also employed direct absorption spectroscopy in the UV to monitor the time dependence of various reactant and product species.

Specifically, two wavelengths (λ = 225 nm and λ = 250 nm) were chosen to detect the peroxy radicals and O_3. Measurement of O_3 enabled direct determination of α_{1b}. Finally, α_{1a} was not measured directly, but was determined from the measured values of k_1, α_{1b}, and α_{1c}.

This study measured k_1, α_{1a}, α_{1b}, and α_{1c} over the temperature range of 230 - 296 K at 100 Torr. At each temperature, experiments were conducted over a wide range of experimental conditions that varied in total and relative initial radical concentrations of HO_2 and $CH_3C(O)O_2$. This work reports the first experimental temperature dependence measurements of α_{1c} and also extends to lower temperatures the range of temperatures over which k_1 has been previously measured. We also present kinetics measurements of the adducts of HO_2 formed from the reaction of HO_2 with the radical precursors, CH_3OH and CH_3CHO.

4.2 Experimental Methods

4.2.1 Overview of IRKS

The IRKS apparatus consisted of a temperature-controlled pulsed laser photolysis flow cell coupled to simultaneous spectroscopic detection in the UV and in the NIR or MIR (Figure 4.2). This technique has been used for studying the kinetics of various peroxy radicals and has been described in detail previously [22–24]. For this work, an additional diode laser operating in the MIR was introduced to the apparatus to enable direct detection of OH radicals. Back-to-back experiments were carried out, alternating between two diode lasers operating in the NIR and in the MIR. Gas temperatures, pressures, and flows were carefully monitored to ensure that the experimental conditions were identical for the two IR measurements. Pulsed 351 nm light (~250 mJ/pulse) from a XeF excimer laser (Compex 301) was directed coaxially through the flow cell to initiate the chemistry by photolyzing Cl_2 molecules in gas mixtures of $Cl_2/N_2/O_2/CH_3OH/CH_3CHO$. The photolysis beam cross-section was 2 cm x 1 cm.

4.2.2 Flow cell and precursor gases

Kinetics experiments were conducted in a jacketed Pyrex cell of length 175 cm and diameter 5 cm. The temperature inside the cell was controlled by flowing liquid nitrogen-cooled methanol circulating through the jacket of the cell and was measured with a type T thermocouple (Omega). Reagent gases were pre-mixed and pre-cooled in a Pyrex manifold prior to entering the cell. Room temperature N_2 purge gas flowed from the aluminum chambers on either end of the cell towards the gas pump-out ports

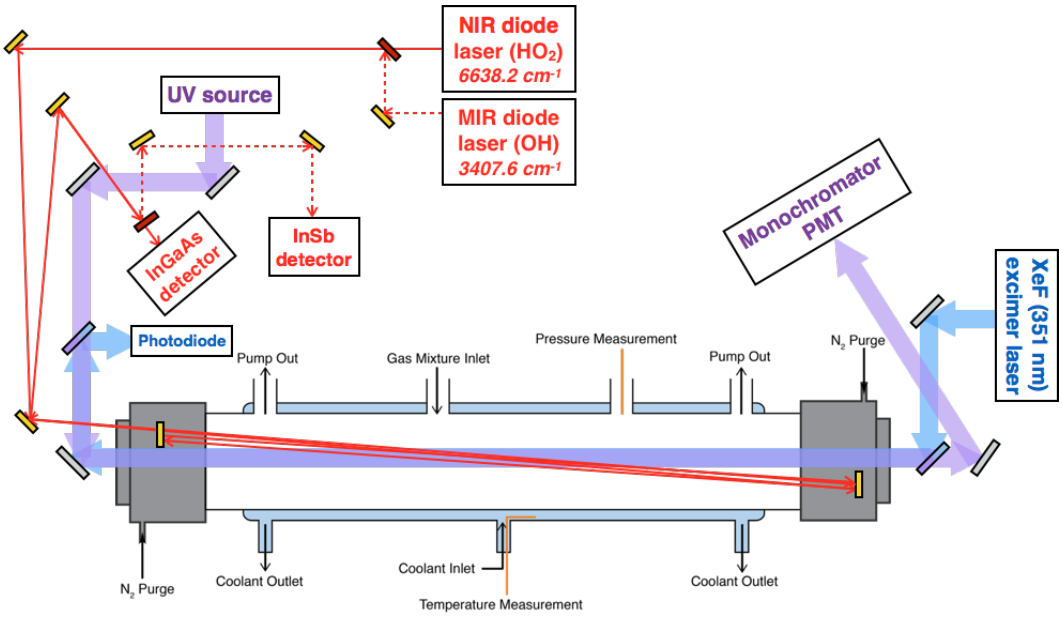

Figure 4.2: Schematic of the IRKS apparatus. A pre-cooled gas mixture entered the temperature-controlled Pyrex flow tube, where radicals were generated by pulsed excimer laser photolysis (beam path shown in blue). Three independent absorption probe beams were used to temporally monitor the reactant and product species: NIR and MIR light (solid and dashed red lines) from two diode lasers were coupled to multi-pass Herriott optics and broadband UV light made a single-pass through the reaction cell (purple). Flip mirrors were used (red rectangles) to switch between the two IR lasers.

to confine the main gas flow to the temperature-controlled region and to protect the Herriott mirrors that formed the multi-pass optical cavity for the IR probes. The gas flows were regulated by mass flow controllers (MKS Instruments) and the total flow rate was kept at approximately 2000 cm^3 (STP) min^{-1}, maintaining a 10 s residence time inside the flow cell at a total pressure of 100 ± 2 Torr. A photolysis repetition rate of 0.2 Hz was used, resulting in two photolysis events occurring per residence time. Decreasing the repetition rate to 0.1 Hz made no difference in the kinetics traces. CH_3OH and CH_3CHO were introduced into the cell by flowing N_2 through glass bubblers containing the liquid compounds, held inside temperature-controlled baths. The pressures in the reaction cell and bubblers were measured by absolute capacitance pressure gauges (MKS Baratron), and the concentrations of CH_3OH and CH_3CHO vapors were determined manometrically. Typical concentrations of the reagents were: $[CH_3OH] = (2.0 - 8.8) \times 10^{15}$ molecule cm^{-3}, $[CH_3CHO] = (1.0 - 2.9) \times 10^{15}$ molecule cm^{-3}, $[O_2] = (1.6 - 2.0) \times 10^{18}$ molecule cm^{-3}, and $[Cl_2] = (2.3 - 3.8) \times 10^{15}$ molecule cm^{-3}. Total initial radical concentrations were

typically $[Cl]_0 = (0.6 - 1.3) \times 10^{14}$ molecule cm^{-3}. More details of the experimental conditions are provided in the Supplementary Materials.

4.2.3 UV probe

Collimated broadband UV light from a laser-driven light source (Energetiq EQ-99XFC) was coaligned with and counter-propagated the excimer beam, making a single pass through the cell with an effective path length of 147 ± 10 cm. A monochromator (Acton Research Corporation Spectra Pro-300i) coupled to a photomultiplier tube (PMT) was used for wavelength-specific detection of the transmitted light. The slit width was typically set to 130 μm. The monochromator was calibrated against atomic emission lines from Hg, Cd, and Zn penray lamps. Baffles were placed on both ends of the flow cell to ensure that only light that sampled the photolysis volume entered the monochromator.

Using only the UV absorption signal to characterize R1 introduces systematic errors due to spectral interference of various RO_2 and product species (Figure 4.3). However, simultaneous fits of the NIR, MIR, and UV signals placed additional constraints on the multi-parameter fits. UV signals at 225 nm and 250 nm were collected back-to-back, each obtained simultaneously with either the NIR or MIR signal.

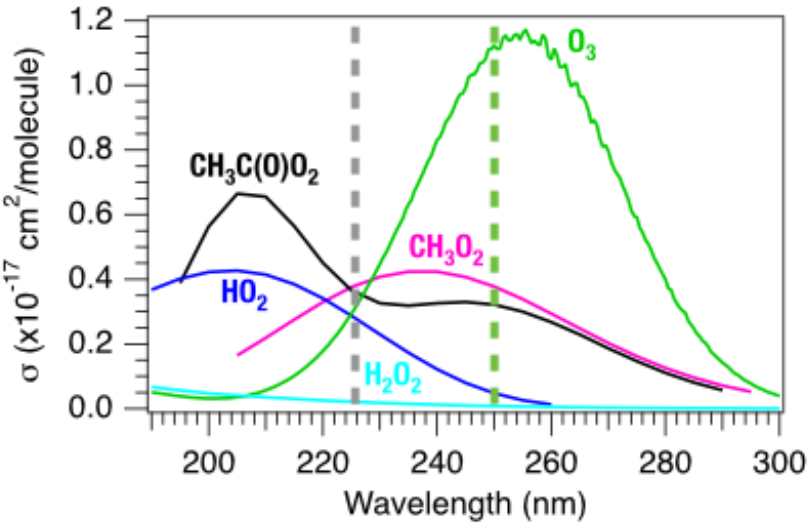

Figure 4.3: UV absorption cross-sections of major reactant and product species generated in the present work [25]. Dashed lines indicate the wavelengths selected in this work.

Sensitivity of the UV data to various peroxy radicals could be achieved by

taking advantage of the differences in the UV absorption cross-sections at these two wavelengths (Table 4.2). At 250 nm, absorption by O_3 dominates the total absorbance signal since the absorption cross-section of O_3 is at least a factor of ~3 times higher than those of other absorbing species. On the other hand, the 225 nm signal includes absorption by HO_2, CH_3O_2, and $CH_3C(O)O_2$. While the UV absorption cross-sections of CH_3O_2 at 225 nm and 250 nm are nearly identical, the cross-sections of $CH_3C(O)O_2$ are slightly different at the two wavelengths. Contribution of HO_2 to the total absorbance could be subtracted using the NIR data; therefore, simultaneous analysis of the NIR data with the two UV absorbance signals provided information about the relative concentration of $CH_3C(O)O_2$ to CH_3O_2.

Table 4.2: UV absorption cross-sections from [26] (units: 10^{-20} cm^2). Uncertainties for HO_2, $CH_3C(O)O_2$, and CH_3O_2 were calculated from [27]. All other uncertainties were taken from [26].

Species	$\sigma_{\lambda=225\text{ nm}}$	$\sigma_{\lambda=250\text{ nm}}$
HO_2	288 ± 20	48.0 ± 4.6
H_2O_2	21.7 ± 1.1	8.3 ± 0.4
$CH_3C(O)O_2$	366 ± 23	322 ± 23
$CH_3C(O)$	1120	68
CH_3O_2	376 ± 27	378 ± 27
O_3	322 ± 6	1100 ± 22

4.2.4 IR probes

Two continuous-wave (CW) distributed feedback (DFB) lasers operating in the NIR (3 mW) and MIR (10 mW), both manufactured by the Microdevices Laboratory (MDL) at the Jet Propulsion Laboratory (JPL), were used for selective detection of HO_2 and OH radicals, respectively. The NIR laser has been used in previous works and a detailed description can be found elsewhere [22]. The MIR laser was developed specifically for the experiments described in this work. In order to target the OH absorption line near 2.935 μm, a newly developed GaSb-based diode laser structure that was designed and grown at the National Research Council of Canada (NRC) was used. The targeted wavelength is reached slightly above room temperature, corresponding to over 10 mW of optical output power, and a side-mode suppression ratio greater than 25 dB. The architecture and details of the performance of this device is provided in Fradet et al. [28].

Experiments with the NIR and MIR probes were carried out back-to-back, using flip mirrors to switch between the two diode lasers and the corresponding detectors. Both the NIR and MIR beams were focused, collimated, and spatially filtered prior

to entering the cell. Protected gold Herriott mirrors placed on either ends of the cell folded the optical paths of the IR beams, enabling 30 passes inside the cell to amplify the path length to approximately 2700 cm. InGaAs (New Focus 1811) and InSb (Infrared Associates IS-0.25) photodiode detectors were used to detect the transmitted NIR and MIR light, respectively.

Both IR lasers were wavelength modulated at 6.8 MHz by using an external function generator to modulate the injection current. 2f-heterodyne detection was implemented by demodulating the detected signal at 13.6 MHz. The demodulated signal was amplified by a factor of 200. For a typical experimental run, the demodulated HO_2 and OH signals were collected at a sampling rate of 2.5 MHz at a bandwidth of 1 MHz, and averaged for 40 and 75 excimer laser shots, respectively. Since WMS only measures the relative changes in concentration, the NIR and MIR lasers were calibrated daily to obtain absolute concentrations of HO_2 and OH, respectively. The calibration procedure for each laser is described in detail below.

4.2.4.1 NIR calibration

The NIR laser probed the first overtone of the OH stretch of HO_2 ($2\nu_1$: 6638.2 cm^{-1}, $\sigma_{HO_2} \sim 4 \times 10^{-20}$ cm^2 [22]). The NIR signal was calibrated against UV absorption at λ= 225 nm by measuring the NIR and UV decay signals simultaneously when HO_2 was the only peroxy radical present (Figure 4.4(a)). Despite a different geometric overlap due to the off-axis orientation of the Herriott mirrors, the IR and UV probe beams should capture the same physical processes at relatively short timescales (< 20 ms); i.e. before diffusion becomes a significant loss process. At the beginning of every experiment, the kinetics traces from the HO_2 self reaction were collected at three different initial radical concentrations at room temperature. The IR and UV traces were simultaneously fit to a bimolecular decay with the kinetics modeling program, FACSIMILE [29], to obtain the calibration factor, V_{M,HO_2}, which relates the IR signal in mV (S_{HO_2}) to the absolute HO_2 concentration:

$$[HO_2] = S_{HO_2} \times V_{M,HO_2} \tag{4.3}$$

The fitted values of V_{M,HO_2} from the kinetics traces obtained from the three initial radical concentrations agreed within 5%. The systematic residuals in the NIR HO_2 signal in Figure 4.4(a) were attributed to the off-axis geometry of the NIR beam, which passes in and out of the photolysis volume, as well as the rise time of the detection electronics. On an absolute basis, the systematic residuals were small (2%)

and did not affect the data analysis. The noise-equivalent concentration per $Hz^{-1/2}$ (NEC $Hz^{-1/2}$) of HO_2 normalized to one excimer shot was 2.9×10^9 molecule cm^{-3} $Hz^{-1/2}$. Under the typical sampling rate of 2.5 MHz and 1 MHz bandwidth, the NEC of HO_2 was $\sim 7.3 \times 10^{10}$ molecule cm^{-3} (40 shots).

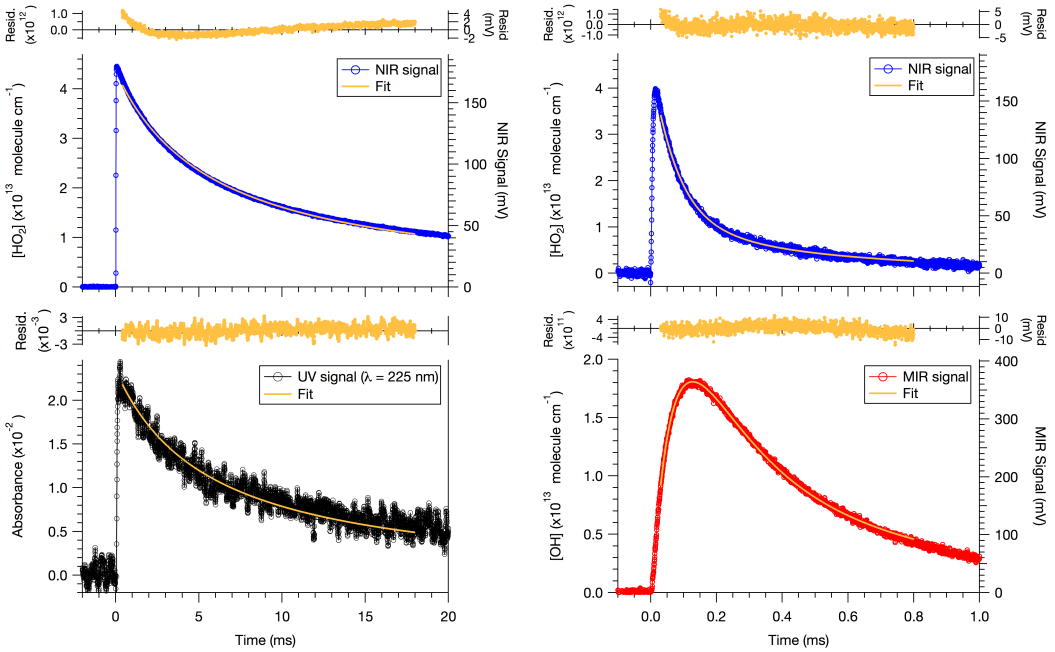

(a) NIR signal (top panel) and UV absorbance signal at $\lambda = 225$ nm (bottom panel) with fitted curves (orange traces) from the $HO_2 + HO_2$ reaction for NIR (HO_2) calibration.

(b) NIR (top panel) and MIR (bottom panel) signals from the HO_2 + NO reaction with fitted curves (orange traces) for MIR (OH) calibration. [NO] = 1.2×10^{15} molecule cm^{-3}.

Figure 4.4: Calibration of the 2f (a) NIR and (b) MIR signals. Residuals of the fits are shown above the data curves. T = 294 K; P = 100 Torr; $[Cl]_0 = 4.4 \times 10^{13}$ molecule cm^{-3}; $[CH_3OH] = 4.5 \times 10^{15}$ molecule cm^{-3}.

4.2.4.2 MIR calibration

The MIR laser monitored OH radicals by probing the fundamental vibrational transition (ν_1, $P(3.5)f$: 3407.6 cm^{-1}, $\sigma_{OH} \sim 2 \times 10^{-18}$ cm^2 [30]). This line corresponds to one of two doublets; Figure 4.5 shows the spectrum of the two OH lines obtained by scanning the optical frequency of the laser and measuring the 2f signal from the reaction of HO_2 with NO. Within experimental uncertainty, HO_2 + NO produces OH with a yield of unity. The line centered at 3407.6 cm^{-1} was chosen, which is free from interferences by HO_2 and H_2O.

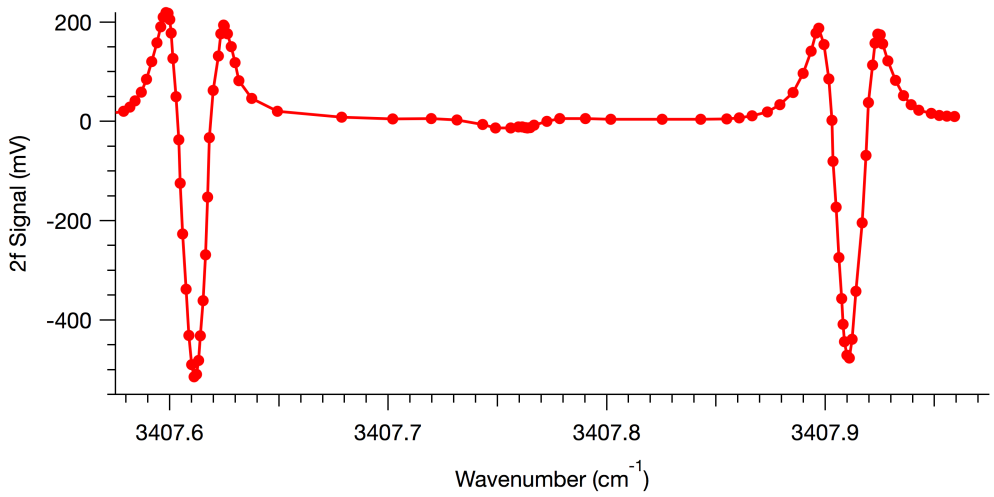

Figure 4.5: 2f signals of the MIR laser scanned across the OH doublets, obtained from the HO_2 + NO. The small dips between the OH lines are the weak absorption lines of HO_2.

The laser signal was calibrated by titrating HO_2 with NO and measuring the kinetics traces of HO_2 and OH from the reaction of HO_2 + NO (Figure 4.4(b)) immediately after the HO_2 self reaction calibration runs. Since the rate constant of this reaction is well-known and all the loss processes of OH are well-characterized, the absolute OH concentration could be determined from the formation and subsequent decay of the OH signal, provided that the initial radical concentrations are known. The initial radical concentrations were assumed to be the same as the HO_2 calibration runs since the same Cl_2 concentrations and excimer energy were used. The OH decays rapidly from reaction with NO and with CH_3OH; therefore, the two lowest initial radical concentrations were used for the HO_2 + NO calibrations in order to accurately capture the peak of the OH signal. The HO_2 and OH decays were simultaneously fit with a kinetics model using FACSIMILE [29] to determine calibration factor, $V_{M,OH}$, which scales the OH laser signal (S_{OH}) to absolute OH concentrations:

$$[OH] = S_{OH} \times V_{M,OH} \tag{4.4}$$

The NEC $Hz^{-1/2}$ of OH normalized to one excimer shot was 5.0×10^8 molecule cm^{-3} $Hz^{-1/2}$. Under the typical sampling rate of 2.5 MHz and 1 MHz bandwidth, the NEC of OH was 6.7×10^9 molecule cm^{-3} (75 shots). It should be noted that further improvement in the OH sensitivity is attainable in future work using the IRKS apparatus. Due to limited MIR reflectivity of the coatings on the Herriott mirrors, maximum sensitivity was not yet realized; thus, optimization of the optics is

expected to significantly lower the detection limit of the MIR probe.

The uncertainties in the calibration factors for each laser were determined from Monte Carlo analysis (see Error Analysis). The estimated systematic errors of V_{M,HO_2} and $V_{M,OH}$ were ~10% and 15%, respectively.

4.3 Results

4.3.1 Overview

Experiments were carried out at a total pressure of P = 100 Torr at seven temperatures in the range T = 230 - 294 K. At each temperature, data were collected under 10 - 15 different experimental conditions that varied in precursor and radical concentrations. For each experimental condition, we averaged 40 excimer laser shots probing in the NIR and λ = 250 nm, and 75 shots probing in the MIR and λ = 225 nm.

Photolysis of Cl_2 generated Cl atoms (R2):

$$Cl_2 + h\nu\,(351\,nm) \longrightarrow 2\,Cl \qquad \text{(R2)}$$

In the presence of O_2, the reaction of the Cl atoms with excess amounts of CH_3OH and CH_3CHO instantaneously (< 20 μs) produced HO_2 (R3 and R4) and $CH_3C(O)O_2$ (R5 and R6a) with yields very close to unity.

$$Cl + CH_3OH \longrightarrow CH_2OH + HCl \qquad \text{(R3)}$$

$$CH_2OH + O_2 \longrightarrow HO_2 + CH_2O \qquad \text{(R4)}$$

$$Cl + CH_3CHO \longrightarrow CH_3C(O) + HCl \qquad \text{(R5)}$$

$$CH_3C(O) + O_2 \xrightarrow{M} CH_3C(O)O_2 \qquad \text{(R6a)}$$

$$\longrightarrow OH \qquad \text{(R6b)}$$

$$\longrightarrow HO_2 \qquad \text{(R6c)}$$

The yields of OH and HO_2 from R6 (α_{6b} and α_{6c}, respectively) were determined from prompt OH and HO_2 formed in the absence of CH_3OH and were found to be ~2-3% at 100 Torr in N_2 across the entire temperature range. R6 occurred on a much shorter timescale and was decoupled from the HO_2 + $CH_3C(O)O_2$ reaction; thus, determination of α_{6b} and α_{6c} was not affected by HO_2 + $CH_3C(O)O_2$ chemistry. Detailed results on R6 will be reported in a separate publication[31].

We varied the ratio of the initial concentrations of HO_2 and $CH_3C(O)O_2$ ($[HO_2]_0/[CH_3C(O)O_2]_0$) over a wide range, as well as the total initial radical concentration, $[Cl]_0$, to minimize systematic errors introduced by unknown or poorly characterized secondary reactions. A summary of all experimental conditions is given in Tables 4.8-4.15 in the Supporting Information.

$[Cl]_0$ was determined from the NIR measurement of HO_2 formed via R3 and R4 in the absence of CH_3CHO. With the addition of CH_3CHO, $[HO_2]_0$ and $[CH_3C(O)O_2]_0$ were determined from the fraction of Cl atoms reacting with the corresponding radical precursors; i.e.,

$$[HO_2]_0 = \frac{k_3[CH_3OH]}{k_3[CH_3OH] + k_5[CH_3CHO]}[Cl]_0 \tag{4.5}$$

$$[CH_3C(O)O_2]_0 = \frac{k_5[CH_3CHO]}{k_3[CH_3OH] + k_5[CH_3CHO]}[Cl]_0 \tag{4.6}$$

$[HO_2]_0/[CH_3C(O)O_2]_0$ ratios were varied by changing the precursor concentrations. The temperature dependences of k_3 and k_5 in the 230 - 294 K temperature range have been measured using this apparatus and details will be reported in a separate publication[32]. Briefly, both k_3 and k_5 were found to be temperature-independent, with values of $(5.45 \pm 0.37) \times 10^{-11}$ cm^3 molecule^{-1} s^{-1} and $(8.00 \pm 1.27) \times 10^{-11}$ cm^3 molecule^{-1} s^{-1} (2σ uncertainties), respectively, which are consistent with the values recommended by the current JPL and IUPAC databases.

The permissible concentrations of CH_3OH and CH_3CHO were limited by the formation of complexes. At lower temperatures, HO_2 forms hydrogen-bonded adducts with CH_3OH and CH_3CHO. Rapid equilibrium is established (< 50 μs) between HO_2 and the adducts, $HO_2 \cdot CH_3OH$ and $HO_2 \cdot CH_3CHO$. The $[HO_2]_0$ measured by the high-resolution NIR probe represents only the free, unbound HO_2, because the NIR probes the overtone rovibrational transition of the O−H stretch. Furthermore, the adducts enhance the rate of the HO_2 self reaction. Experiments were conducted using low $[CH_3OH]$ and $[CH_3CHO]$ to minimize these effects; however, rate enhancement and fast loss of HO_2 could not be completely avoided, especially at lower temperatures. Adduct concentrations could be as high as 25% of $[HO_2]_0$. The impact of the adducts on the kinetics were therefore investigated by varying $[CH_3OH]$ and $[CH_3CHO]$. More details on characterizing the effects of the HO_2 adducts on the overall kinetics of R1 will be described below.

The range of $[HO_2]_0/[CH_3C(O)O_2]_0$ over which data were collected was limited

by the need to minimize competing secondary chemistry. Since k_5 is larger than k_3, [CH_3OH] had to be greater than [CH_3CHO] to ensure that enough HO_2 radicals were generated such that the $CH_3C(O)O_2$ self-reaction did not dominate. However, [CH_3OH] also had to be sufficiently low to minimize the subsequent loss of HO_2 with the adducts formed with CH_3OH and CH_3CHO, which in turn limited the range of CH_3CHO that could be used. The $[Cl]_0$ was constrained as well. It was kept low to minimize secondary loss processes, but had to be high enough to obtain detectable yields of OH.

4.3.2 Analysis

Competing fast radical recycling and secondary chemistry precluded the analysis of R1 using a conventional first-order treatment. Therefore, data analysis required the use of a kinetics model to account for all major radical loss and recycling processes. In addition to accounting for the formation chemistry for $CH_3C(O)O_2$ and HO_2 radicals and their mutual reaction, the kinetics model also had to consider the secondary reactions of $CH_3C(O)O_2$ and the effect of weakly bound HO_2 complexes on the self-reaction of HO_2. The impact of these processes on the determination of the rate constants and branching ratios for R1 is discussed below. In this section we will discuss the effects of secondary chemistry and HO_2 chaperone chemistry in subsections (4.3.2.1) and (4.3.2.2). In subsection (4.3.2.3) we will describe the method for determination of the overall rate coefficient and branching ratios for R1. The error analysis approach will be described in subsection (4.3.2.4).

4.3.2.1 Secondary $CH_3C(O)O_2$ chemistry

In the laboratory, measurements of the kinetic rate constant k_1, even at short timescales, are complicated by the self reactions of $CH_3C(O)O_2$ and HO_2 that compete with R1:

$$HO_2 + HO_2 \xrightarrow{M} H_2O_2 + O_2 \qquad \text{(R7)}$$

$$CH_3C(O)O_2 + CH_3C(O)O_2 \longrightarrow 2\,CH_3C(O)O + 2\,O_2 \qquad \text{(R8)}$$

The competition of R1, R7, R8, and the subsequent reactions of $CH_3C(O)O$ produced from R1c and R8 preclude pseudo-first order kinetics experiments, consequently preventing analytical solutions to the rate equations. For example, $CH_3C(O)O$ from R1c and R8 rapidly decomposes (assumed instantaneous) to form CH_3, which

produces CH_3O_2 upon addition of O_2:

$$CH_3C(O)O \xrightarrow{M} CH_3 + CO_2 \quad \text{(R9)}$$

$$CH_3 + O_2 \xrightarrow{M} CH_3O_2 \quad \text{(R10)}$$

CH_3O_2 subsequently undergoes self reaction via R11 as well as cross-reactions with HO_2 (R12) and with $CH_3C(O)O_2$ (R13):

$$CH_3O_2 + CH_3O_2 \longrightarrow 2\,CH_3O + O_2 \quad \text{(R11a)}$$

$$\longrightarrow CH_3OH + CH_2O + O_2 \quad \text{(R11b)}$$

$$HO_2 + CH_3O_2 \longrightarrow CH_3OOH + O_2 \quad \text{(R12a)}$$

$$\longrightarrow CH_2O + H_2O + O_2 \quad \text{(R12b)}$$

$$CH_3O_2 + CH_3C(O)O_2 \longrightarrow CH_3C(O)O + CH_3O + O_2 \quad \text{(R13a)}$$

$$\longrightarrow CH_3C(O)OH + CH_2O + O_2 \quad \text{(R13b)}$$

Under conditions where O_2 is in excess, CH_3O from R13a and R11a generates secondary HO_2:

$$CH_3O + O_2 \longrightarrow HO_2 + CH_2O \quad \text{(R14)}$$

Thus, characterization of R1 relies heavily on the accuracy of the kinetics of the secondary chemistry. Some of the main challenges in the data analysis originated from systematic errors associated with R8 and R13, which have only been investigated by a small number of experimental studies [16, 33–35], none of which have accounted for the OH product channel from R1. The current recommendations from the IUPAC and JPL [26] data evaluations are based on analogous reactions due to the limited number of temperature dependence studies of R8 and R13. As part of this work, we also carried out additional experiments in the absence of CH_3OH, where no HO_2 was initially formed, in order to characterize R8 and R13. However, unique solutions for k_8, k_{13}, and α_{13a} could not be determined from these experiments due to poorly constrained fits.

Our approach to indirectly estimate k_8, k_{13}, and α_{13a} consisted of iteratively fitting

data with various $[HO_2]_0/[CH_3C(O)O_2]_0$ ratios. A diagram summarizing the fitting procedure (Figure 4.7) is provided in section 4.3.2.3. In the first iteration, only the data sets with the highest $[HO_2]_0/[CH_3C(O)O_2]_0$ ratios (~3.5 - 5) were used, constraining k_1, α_{1b}, and α_{1c}, while fixing the values of k_8, k_{13}, and α_{13a} to the recommended values from the current JPL data evaluation [26]. Next, sensitivity of the data to R8, R13a, and R13b was explored by adjusting the values of k_8, k_{13}, and α_{13a} independently by ±20%. For data sets with high $[HO_2]_0/[CH_3C(O)O_2]_0$, the fitted values of k_1, α_{1b}, and α_{1c} did not vary by more than ±20%, confirming that these data sets were not sensitive to R8 and R13. Data sets with lower $[HO_2]_0/[CH_3C(O)O_2]_0$ ratios were found to be more sensitive to these parameters; thus, k_8, k_{13}, and α_{13a} had to be adjusted until the fitted values of k_1, α_{1c}, and α_{1b} from all data sets converged.

The estimated values of k_8 and k_{13} determined in this fitting procedure are well within the error bands of the current JPL data evaluation [26] and are provided in the Supporting Information (Figure 4.14). Values of α_{13a} ranging between 1.0 to 0.9 were also found to provide the best fits to the data across all temperatures studied. k_8, k_{13}, and α_{13a} were highly correlated with other parameters; thus, the measured values are not unique solutions and should not be interpreted as direct measurements. Rather, these kinetics parameters were determined empirically; we used values that were consistent with those in the literature (within the 95% uncertainty bounds), as well as with our data under all experimental conditions. These values of k_8, k_{13}, and α_{13a} were then used to repeat the fits to all data sets, although results from the high $[HO_2]_0/[CH_3C(O)O_2]_0$ data were not significantly affected.

4.3.2.2 Impact of HO_2 + HO_2 rate enhancement by radical adducts on k_1

An additional complication is introduced at lower temperatures, where HO_2 forms a hydrogen-bonded adduct with the radical precursors [17, 18, 20, 21, 36, 37]:

$$HO_2 + X \overset{[M]}{\rightleftharpoons} HO_2 \cdot X, \tag{R15}$$

where X = CH_3OH or CH_3CHO. Adduct formation impacts the data analysis in several ways: 1) rapid loss of HO_2 via R15 influences determination of $[HO_2]_0$; 2) the apparent HO_2 self reaction rate constant is enhanced due to the additional loss of HO_2 by reaction with $HO_2 \cdot X$. In the case of CH_3CHO, ab initio calculations suggest rapid isomerization of the initially formed $HO_2 \cdot CH_3CHO$ adduct to the α-hydroxyethylperoxy radical ($CH_3CH(OH)O_2$) [38], which can also react with HO_2. As we will discuss below, details of this process are unimportant for the present work

because we define an effective rate constant that accounts for the additional HO_2 loss pathway.

First, adduct formation led to a lower observed peak concentration of HO_2. $[Cl]_0$ at each temperature was typically determined by measuring the decay of HO_2 in the absence of CH_3CHO; i.e.,

$$[Cl]_0 = [HO_2]_0 \tag{4.7}$$

The data was fit with a simple bimolecular reaction and extrapolated to t = 0 to obtain $[HO_2]_0$. For a fixed $[Cl_2]$ and excimer energy, the measured $[HO_2]_0$ for T > 250 K was equal to the $[HO_2]_0$ determined at room temperature. However, measurements at T ≤ 250 K underdetermined $[HO_2]_0$ due to the rapid loss of HO_2 via R15 (X=CH_3OH), which was not captured by the kinetics model. $[Cl]_0$ is described by Equation 4.8:

$$[Cl]_0 = [HO_2]_{eq} + [HO_2 \cdot X]_{eq} \tag{4.8}$$

where $[HO_2]_{eq}$ and $[HO_2 \cdot X]_{eq}$ are the equilibrium concentrations of HO_2 and $HO_2 \cdot X$. The NIR detection of HO_2 selectively detected the free HO_2, and not $HO_2 \cdot X$; i.e., the concentration of HO_2 extrapolated to t = 0 is $[HO_2]_{eq}$. On the other hand, the UV signal presumably includes absorbance by both HO_2 and $HO_2 \cdot X$; therefore, $[HO_2]_0$ for the UV curves was always constrained to the value determined from the room temperature HO_2 self reaction data, which was collected at the same $[Cl_2]$ and excimer energy. Fits to the NIR curves included an additional parameter, $[HO_2]_{eq}$. Although the equilibrium constants of R15 for CH_3OH[19] and CH_3CHO have been measured previously, $[HO_2]_{eq}$ was allowed to be an additional fitted parameter in these fits. $[HO_2 \cdot X]_{eq}$ agreed within experimental error to the calculated value using the measured equilibrium constants. At the highest $[CH_3OH]$ and $[CH_3CHO]$ used, the fraction of total HO_2 bound as an adduct (i.e., $([HO_2 \cdot CH_3OH] + [HO_2 \cdot CH_3CHO])/[HO_2]_0$) was ~25% at 230 K and ~2% at 294 K.

Secondly, R15 affects the kinetics because the effective rate constant of R7 is enhanced due to the subsequent reactive losses of the radical adducts.

$$HO_2 + HO_2 \cdot X \longrightarrow \text{products} \tag{R16}$$

$$HO_2 \cdot X + HO_2 \cdot X \longrightarrow \text{products} \tag{R17}$$

In the case of X=CH_3OH, the enhanced observed rate constant results from

$HO_2 \cdot CH_3OH$ acting as a chaperone to increase the rate of formation of H_2O_2 and O_2 [20, 37]. The rate enhancement becomes more significant with the larger $[HO_2 \cdot X]$ at lower temperatures [19]. Three HO_2 decay curves collected at 230 K using the same initial amount of total radicals are plotted in Figure 4.6. The concentration of the radical precursors were varied but the ratio was kept the same; i.e., all three runs had the same relative amount of initial HO_2 to $CH_3C(O)O_2$. In the absence of rate enhancement by the radical precursors, the rate of decay should be identical, as predicted by the model (dashed lines).

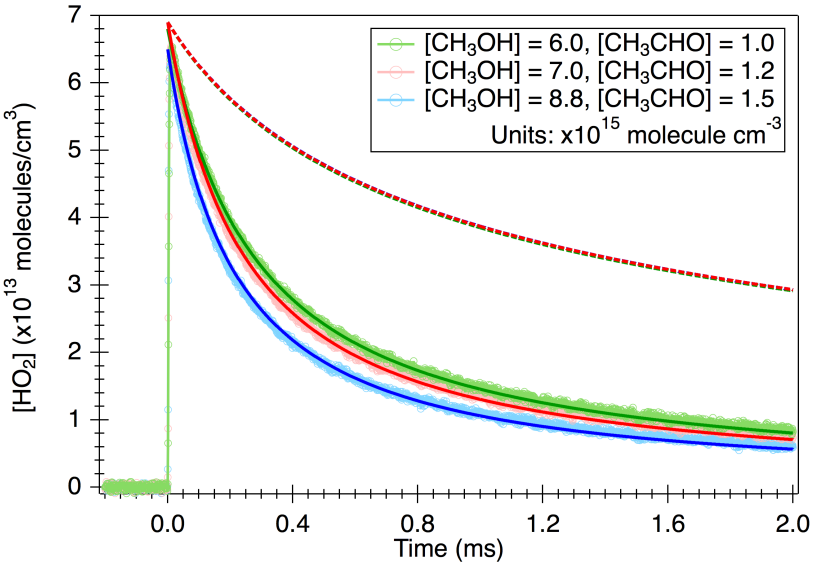

Figure 4.6: Three HO_2 (NIR) decay curves at various concentrations of CH_3OH and CH_3CHO (fixed $[CH_3OH]$:$[CH_3CHO]$=6 and $[Cl]_0 = 8.7 \times 10^{13}$ molecule cm^{-3}) at T = 230 K. Data (circle markers) shown with modeled HO_2 profiles: with (solid lines) and without (dashed lines) enhancement effects by CH_3OH and CH_3CHO.

In the absence of CH_3CHO, rate enhancement has been described by an effective rate constant, $k''_{7,M}$, with a linear dependence on $[CH_3OH]$, such that the observed second-order rate constant of the HO_2 self reaction (R7) is expressed as:

$$k_{7,\mathrm{obs,M}} = k_7 + k''_{7,M}[CH_3OH], \tag{4.9}$$

where k_7 is the pressure-dependent HO_2 + HO_2 rate constant in the limit of $[CH_3OH]$=0. The effective negative temperature dependence of $k_{7,\mathrm{obs,M}}$ is therefore dependent on the temperature dependence of $k''_{7,M}$, which has been measured in this lab and will be reported in a separate publication[39].

With the addition of CH_3CHO, the observed rate constant of the HO_2 self reaction was also found to have a linear dependence on $[CH_3CHO]$ and is denoted as $k_{7,\mathrm{obs,A}}$.

Experiments were conducted using varying [CH_3CHO] for fixed [CH_3OH] and the results demonstrated that $k_{7,\mathrm{obs,A}}$ obeyed the expression,

$$k_{7,\mathrm{obs,A}} = k_7 + k''_{7,M}[CH_3OH] + k''_{7,A}[CH_3CHO] \tag{4.10}$$

$k_{7,\mathrm{obs,A}}$ extrapolated to [CH_3CHO] = 0 was found to be in excellent agreement with $k_{7,\mathrm{obs,M}}$ calculated from Equation 4.9. Including a rate enhancement effect by both CH_3OH and CH_3CHO significantly improves the agreement between the data and the model (solid lines in Figure 4.6). More details on the determination of $k''_{7,A}$ will also be reported in a separate publication[39].

4.3.2.3 Determination of k_1, α_{1a}, α_{1b}, and α_{1c}

Values of k_1, α_{1a}, α_{1b}, and α_{1c} were determined iteratively along with the kinetics parameters of the major secondary reactions as described above. The fitted values of the rate constants and branching ratios were self-consistent across all experimental conditions. The approach for obtaining the best-fit values of k_1, α_{1a}, α_{1b}, and α_{1c} is described below and shown diagrammatically in Figure 4.7.

The NIR and MIR curves were simultaneously fitted from ~20 μs to ~1 ms after the photolysis pulse (Figure 4.8(a)) to obtain k_1 and α_{1c}. The data were observed to be insensitive to α_{1b}, which was held fixed to the current literature value. We did not use the UV data, since the UV data in the first ~150 μs after photolysis was lost due to PMT saturation from the scattered excimer pulse. This part of the analysis allowed us to probe the rapid kinetic decay of OH. Due to low OH yields, the MIR signals were small and close to the baseline. However, the baseline of the MIR signal fluctuated, which was caused by electrical noise and imperfect laser beam alignment. Limiting the fitting time range to ~1 ms avoided systematic errors. Fitting only the IR signals had the additional advantage that the NIR and MIR signals provided selective, unambiguous detection of HO_2 and OH radicals, respectively, and were not limited by uncertainties in the absorption cross-sections of various species that spectrally overlapped.

The longer timescale chemistry was captured in the second part of the data analysis. The NIR signal and the two UV absorbance signals (225 nm and 250 nm) were simultaneously fitted from 200 μs to 3.5 - 6 ms after the photolysis pulse (Figure 4.8(b)). At longer kinetics times, absorbance by O_3 dominated the UV signal at λ = 250 nm, enabling the determination of α_{1b}. Both k_1 and α_{1b} were floated, and α_{1c} was fixed to the values determined from the short timescale fits. Since the

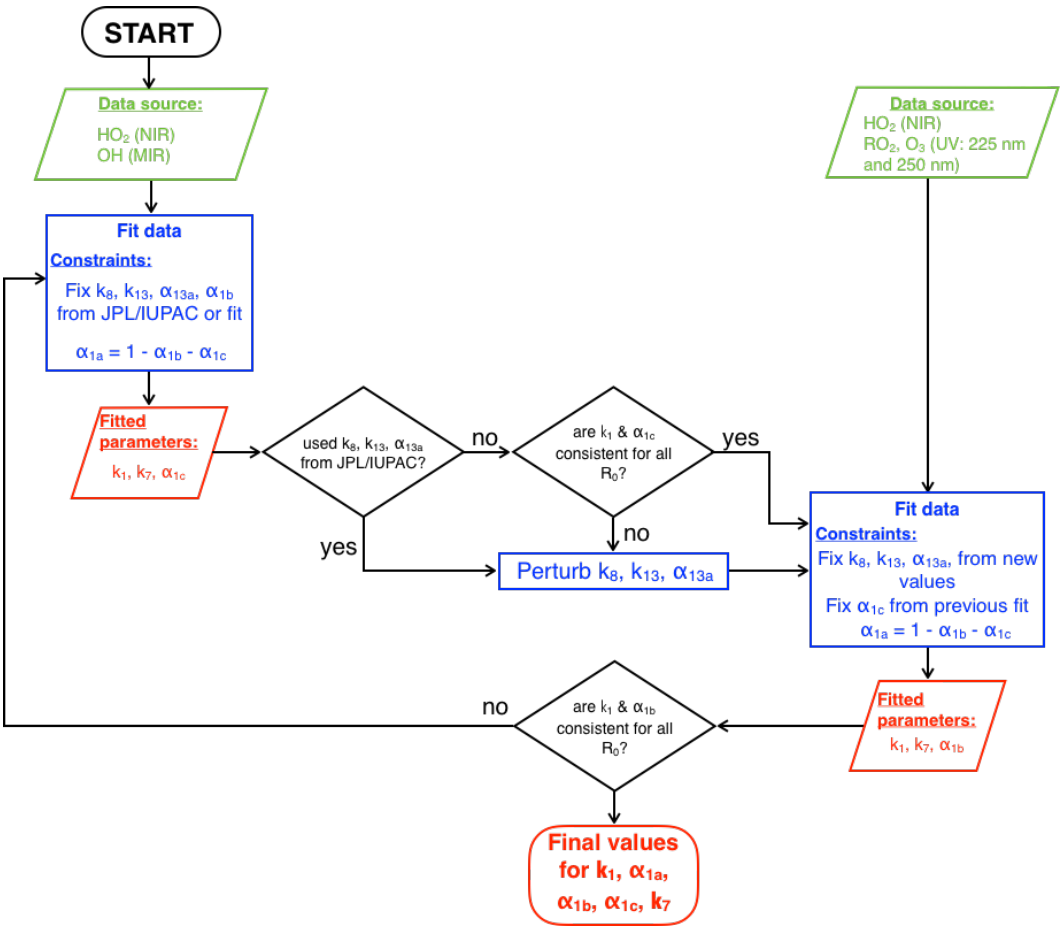

Figure 4.7: Summary of fitting procedure for determination of k_1, k_7, α_{1a}, α_{1b}, and α_{1c}. $R_0 = [HO_2]_0/[CH_3C(O)O_2]_0$. Fits are done with rate parameters k_8, k_{13}, and α_{13a} for the secondary reactions either fixed to the JPL or IUPAC recommended values or to values determined empirically.

same NIR data was used in both parts of the analysis procedure, agreement between the fitted values of k_1 determined from the short and the long timescale fits served to verify that the two analysis methods were self-consistent. We typically varied the four kinetics parameters while fixing all other rate parameters and applying the constraint given by Equation 4.2. The χ-squared distribution for each data curve was weighted by the standard errors of regression, which were determined from the root-mean-square of the noise of each curve.

Table 4.3 lists the weighted averages of k_1, α_{1a}, α_{1b}, and α_{1c} measured from data collected over a wide range of experimental conditions. The values were weighted by uncertainties determined from rigorous error analysis, which will be described in the Error Analysis section.

Figure 4.9 shows that k_1 has a negative temperature dependence, which is consis-

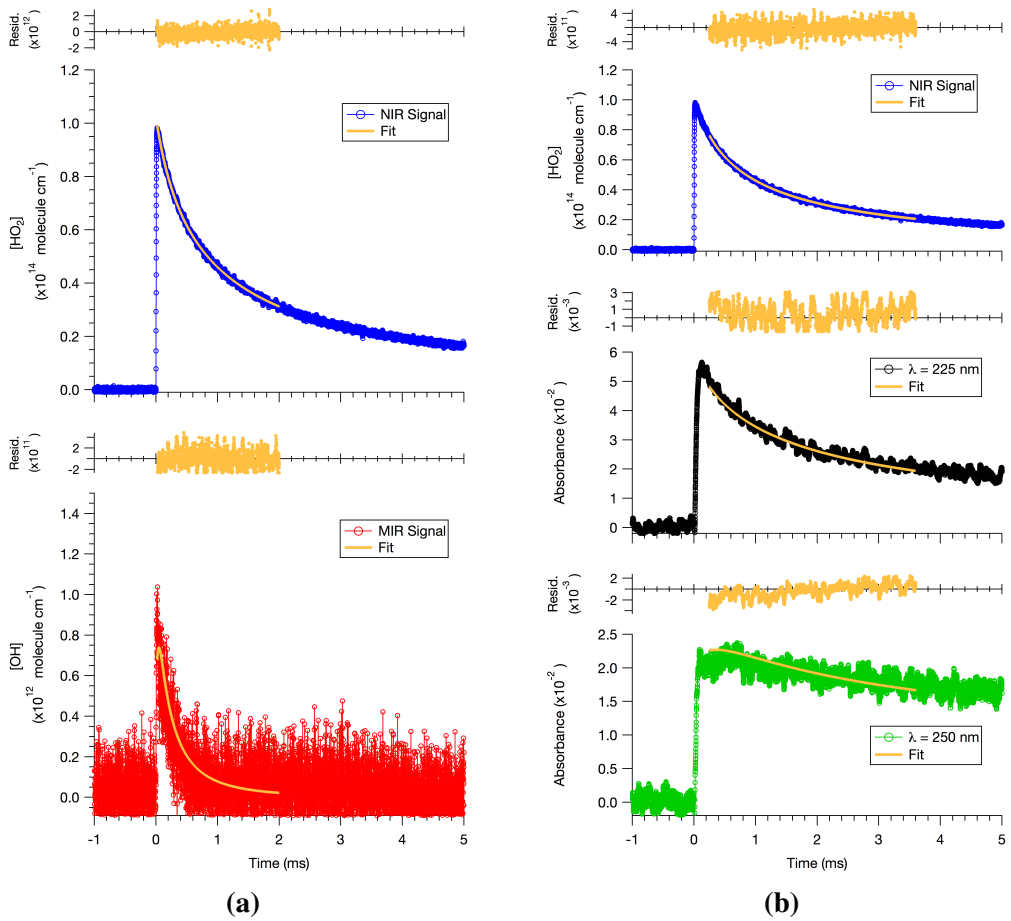

Figure 4.8: Fits (orange) to NIR (blue), MIR (red), and UV (black and green) data from the HO_2 + $CH_3C(O)O_2$ reaction, collected at T = 260 K and P = 100 Torr: (a) NIR HO_2 and MIR OH signals fitted from 0.02 to 1 ms and (b) NIR HO_2 and UV signals (black: λ = 225 nm and green: λ = 250 nm) fitted from 0.2 - 3.6 ms. Residuals to fits are shown above each curve. Precursor and radical concentrations: $[Cl_2] = 3.8 \times 10^{15}$ molecule cm^{-3}; $[CH_3OH] = 5.0 \times 10^{15}$ molecule cm^{-3}; $[CH_3CHO] = 1.0 \times 10^{15}$ molecule cm^{-3}; $[Cl]_0 = 1.2 \times 10^{14}$ molecule cm^{-3}.

tent with previous measurements [16–18]. The larger errors at lower temperatures are attributed to larger uncertainties in the kinetics parameters of secondary reactions. The temperature dependences of α_{1a}, α_{1b}, and α_{1c} are plotted in Figure 4.13. α_{1a} is relatively temperature-independent over this temperature range, while α_{1b} and α_{1c} are anti-correlated.

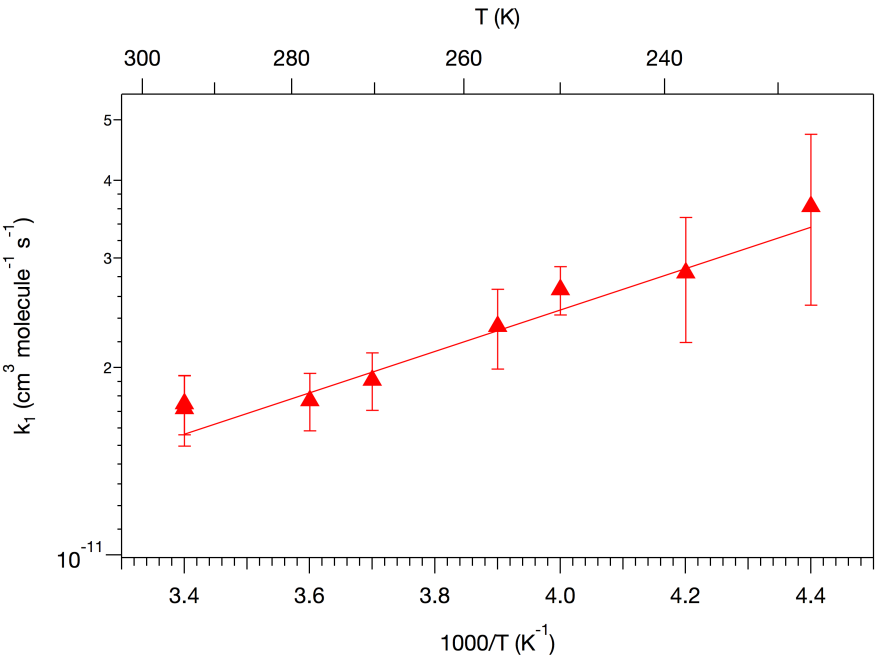

Figure 4.9: Arrhenius plot of the overall rate constant, k_1.

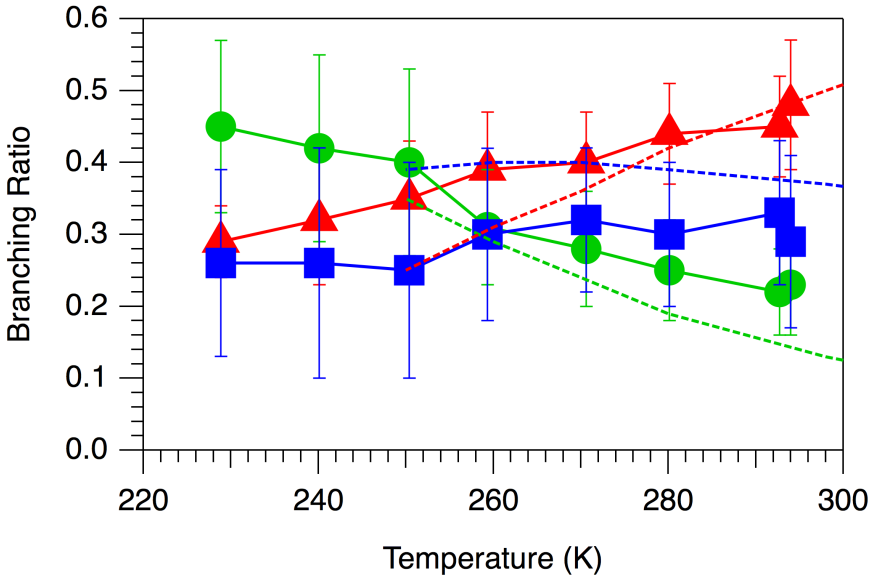

Figure 4.10: Measured temperature dependence of α_{1a} (blue squares), α_{1b} (green circles), and α_{1c} (red triangles). IUPAC recommendations over their applicable temperature ranges are shown in the dashed lines.

Table 4.3: Summary of experimental conditions and results. All experiments were conducted at a total pressure of 100 Torr in N_2 buffer gas.

T (K)	$[CH_3OH]$ ($\times 10^{15}$ cm^{-3})	$[CH_3CHO]$ ($\times 10^{15}$ cm^{-3})	$[Cl]_0$ ($\times 10^{13}$ cm^{-3})	$[HO_2]_0/[CH_3C(O)O_2]_0$	k_1 ($\times 10^{-11}$ cm^3 s^{-1})	α_{1a}	α_{1b}	α_{1c}
294.0	2.0 - 6.0	1.0	5.9 - 9.3	1.3 - 4.0	1.72 ± 0.22	0.29 ± 0.12	0.23 ± 0.07	0.48 ± 0.09
292.7	5.0 - 8.8	1.0 - 2.3	8.3	2.1 - 4.8	1.75 ± 0.19	0.33 ± 0.10	0.22 ± 0.06	0.45 ± 0.07
280.1	4.0 - 8.8	1.0 - 2.2	13	2.7 - 4.7	1.77 ± 0.19	0.30 ± 0.10	0.25 ± 0.07	0.44 ± 0.07
270.6	4.0 - 8.8	1.0 - 2.2	13	2.7 - 4.8	1.91 ± 0.20	0.32 ± 0.10	0.28 ± 0.08	0.40 ± 0.07
259.3	3.0 - 8.8	1.0 - 2.9	11 - 13	2.0 - 4.8	2.33 ± 0.34	0.30 ± 0.12	0.31 ± 0.08	0.39 ± 0.08
250.4	3.0 - 8.8	1.0 - 2.3	6.8 - 8.3	2.0 - 4.7	2.67 ± 0.24	0.25 ± 0.15	0.40 ± 0.13	0.35 ± 0.08
240.1	3.0 - 8.8	1.0 - 2.2	5.7 - 9.1	2.1 - 4.8	2.84 ± 0.65	0.26 ± 0.16	0.42 ± 0.13	0.32 ± 0.09
228.9	3.0 - 8.8	1.0 - 2.3	5.6 - 8.7	2.1 - 4.7	3.63 ± 1.11	0.26 ± 0.13	0.45 ± 0.12	0.29 ± 0.05

Table 4.4: Full list of reactions and rate constants used in the kinetics model.

	Reaction			Rate constant (cm^3 $molecule^{-1}$ s^{-1})	Ref
Methanol					
(R3)	$Cl + CH_3OH$	$\longrightarrow$	$CH_2OH + HCl$	5.5×10^{-11}	[26], this lab
(R18a)	$OH + CH_3OH$	$\longrightarrow$	$CH_2OH + H_2O$	$0.85 \times 2.90 \times 10^{-12}\exp(345/T)$	[26]
(R18b)		$\longrightarrow$	$CH_3O + H_2O$	$0.15 \times 2.90 \times 10^{-12}\exp(345/T)$	[26]
(R4)	$CH_2OH + O_2$	$\longrightarrow$	$HO_2 + CH_2O$	9.1×10^{-11}	[26]
Acetaldehyde					
(R5)	$Cl + CH_3CHO$	$\longrightarrow$	$CH_3CO + HCl$	8.0×10^{-11}	[40], this lab
(R19a)	$OH + CH_3CHO$	$\longrightarrow$	$CH_3CO + H_2O$	$0.95 \times 4.63 \times 10^{-12}\exp(350/T)$	[26]
(R19b)		$\longrightarrow$	$CH_2CHO + H_2O$	$0.05 \times 4.63 \times 10^{-12}\exp(350/T)$	[26]
(R6a)	$CH_3C(O) + O_2$	$\longrightarrow$	$CH_3C(O)O_2$	$(1 - \alpha_{6b} - \alpha_{6c}) \times 5.1 \times 10^{-12}$	overall rate constant: [40],
(R6b)		$\longrightarrow$	OH + products	$\alpha_{6b} \times 5.1 \times 10^{-12}$	branching ratios
(R6c)		$\longrightarrow$	HO_2 + products	$\alpha_{6c} \times 5.1 \times 10^{-12}$	from this lab
HO_x reactions					
(R7)	$HO_2 + HO_2$	$\xrightarrow{M}$	$H_2O_2 + O_2$	k_7	varied, see text
(R20)	$OH + HO_2$	$\longrightarrow$	$H_2O + O_2$	$4.8 \times 10^{-11}\exp(250/T)$	[26]
(R21a)	$OH + OH$	$\longrightarrow$	$H_2O + O$	1.8×10^{-12}	[26]
(R21b)	$OH + OH$	$\xrightarrow{M}$	H_2O_2	$k_0 = 6.9 \times 10^{-31}(300/T)^{-1.0}$	[26]
				$k_\infty = 2.6 \times 10^{-11}$	[26]
(R22)	$OH + H_2O_2$	$\longrightarrow$	$H_2O + HO_2$	1.8×10^{-12}	[26]
(R23)	$OH + CH_2O$	$\longrightarrow$	$H_2O + HCO$	$5.5 \times 10^{-12}\exp(125/T)$	[26]
(R24)	$HCO + O_2$	$\longrightarrow$	$HO_2 + CO$	5.2×10^{-12}	[26]
(R25)	$O + OH$	$\longrightarrow$	$O_2 + H$	$1.8 \times 10^{-11}\exp(180/T)$	[26]
(R26)	$O + HO_2$	$\longrightarrow$	$O_2 + OH$	$3.0 \times 10^{-11}\exp(200/T)$	[26]

	Reaction			Rate constant (cm^3 $molecule^{-1}$ s^{-1})	Ref
(R27)	$H + O_2$	$\xrightarrow{M}$	HO_2	$k_0 = 4.4 \times 10^{-32}(300/T)^{-1.3}$ $k_\infty = 7.5 \times 10^{-11}(300/T)^{0.2}$	
(R28)	$OH + O_3$	$\longrightarrow$	$HO_2 + O_2$	$1.7 \times 10^{-12}\exp(-940/T)$	[26]
(R29)	$HO_2 + O_3$	$\longrightarrow$	$OH + 2\,O_2$	$1.0 \times 10^{-14}\exp(-490/T)$	[26]
RO_2 reactions					
(R1a)	$HO_2 + CH_3C(O)O_2$	$\longrightarrow$	$CH_3C(O)OOH + O_2$	$(1 - \alpha_{1b} - \alpha_{1b}) \times k_1$	varied, this work
(R1b)		$\longrightarrow$	$CH_3C(O)OH + O_3$	$\alpha_{1b} \times k_1$	varied, this work
(R1c)		$\longrightarrow$	$OH + CH_3C(O)O + O_2$	$\alpha_{1c} \times k_1$	varied, this work
(R12a)	$HO_2 + CH_3O_2$	$\longrightarrow$	$CH_3OOH + O_2$	$\{1 - 1/[1 + 498\exp(-1160/T)]\} \times 3.8 \times 10^{-13}\exp(780/T)$	[26]
(R12b)		$\longrightarrow$	$CH_2O + H_2O + O_2$	$\{1/[1 + 498\exp(-1160/T)]\} \times 3.8 \times 10^{-13}\exp(780/T)$	
(R8)	$2\,CH_3C(O)O_2$	$\longrightarrow$	$2\,CH_3C(O)O + O_2$	k_8	varied, see text
(R13a)	$CH_3O_2 + CH_3C(O)O_2$	$\longrightarrow$	$CH_3C(O)O + CH_3O + O_2$	$\alpha_{13a} \times k_{13}$	varied, see text
(R13b)		$\longrightarrow$	$CH_3C(O)OH + CH_2O + O_2$	$(1\text{-}\alpha_{13a}) \times k_{13}$	varied, see text
(R11a)	$CH_3O_2 + CH_3O_2$	$\longrightarrow$	$2\,CH_3O + O_2$	$\{1 - 1/[1 + 26.2\exp(-1130/T)]\} \times 9.5 \times 10^{-14}\exp(390/T)$	[26]
(R11b)		$\longrightarrow$	$CH_3OH + CH_2O + O_2$	$\{1/[1 + 26.2\exp(-1130/T)]\} \times 9.5 \times 10^{-14}\exp(390/T)$	
(R14)	$CH_3O + O_2$	$\longrightarrow$	$CH_2O + HO_2$	$3.9 \times 10^{-14}\exp(-900/T)$	[26]
(R9)	$CH_3C(O)O$	$\longrightarrow$	$CH_3 + CO_2$	Assumed instantaneous	[26]
(R10)	$CH_3 + O_2$	$\xrightarrow{M}$	CH_3O_2	$k_0 = 4.0 \times 10^{-31}(300/T)^{-3.6}$ $k_\infty = 1.2 \times 10^{-12}(300/T)^{1.1}$	[26]

4.3.2.4 Error Analysis

The fitted values of k_1, α_{1a}, α_{1b}, and α_{1c} from all data sets were self-consistent and the random errors were small, with standard errors less than 2%. However, these errors are not representative of the overall error, as they do not include systematic errors in the kinetics model that was used in the data analysis. For example, uncertainties in the rate constants and product yields of R8 and R13, as well as uncertainties in the UV absorption cross-sections, UV path length, calibration factors, and initial radical concentrations all contribute to systematic error. To assess the impact of these errors, Monte Carlo simulations were performed, repeating the fitting procedure 2000 times for each data set. For each simulation, the values of selected input parameters were randomly generated, assuming that the each value had a Gaussian distribution with a given mean value and standard deviation. Values of α_{1b} and α_{1c} were also restricted to lie between 0 and 1. Table 4.2 and Table 4.5 list the input parameters and the range of values over which they were allowed to vary.

Table 4.5: Parameters varied in Monte Carlo simulations. All uncertainties are 1σ.

Parameter	standard dev.	Ref.
$[Cl]_0$ (molecule cm^{-3})	$0.1*[Cl]_0$	[a]
UV pathlength (cm)	10	[41]
V_{M,HO_2} (molecule cm^{-3} mV^{-1})	$0.1*V_{M,HO_2}$	[a]
$V_{M,OH}$ (molecule cm^{-3} mV^{-1})	$0.15*V_{M,OH}$	[a]
k_8 (cm^3 $molecule^{-1}$ s^{-1})	$(1.5\exp(\lvert 150 * \left(\frac{1.0}{T} - \frac{1.0}{298}\right)\rvert) - 1) * k_8$	[26]
k_{13} (cm^3 $molecule^{-1}$ s^{-1})	$(1.5\exp(\lvert 250 * \left(\frac{1.0}{T} - \frac{1.0}{298}\right)\rvert) - 1) * k_{13}$	[26]
α_{13a}	0.1	
UV absorption cross-sections	see Table 4.2	

[a] Uncertainties from Monte Carlo fits

Results from the Monte Carlo simulations were used to generate histograms of k_1, α_{1b}, and α_{1c}. The frequency distributions of the fitted values of k_1, α_{1b}, and α_{1c} for example data sets from T = 294 K and T = 230 K are shown in Figure 4.11(a) and Figure 4.11(b), respectively. Histograms generated from each experimental run were each fit with a Gaussian function, and the overall 1σ uncertainties for these parameters were taken from the single standard deviations of the Gaussian distributions. The uncertainties determined from the Monte Carlo simulations varied in magnitude depending on the experimental conditions. For example, experiments conducted under low $[HO_2]_0/[CH_3C(O)O_2]_0$ conditions were more affected by errors in k_8, k_{13}, and α_{13a} compared to high $[HO_2]_0/[CH_3C(O)O_2]_0$ experiments due to the

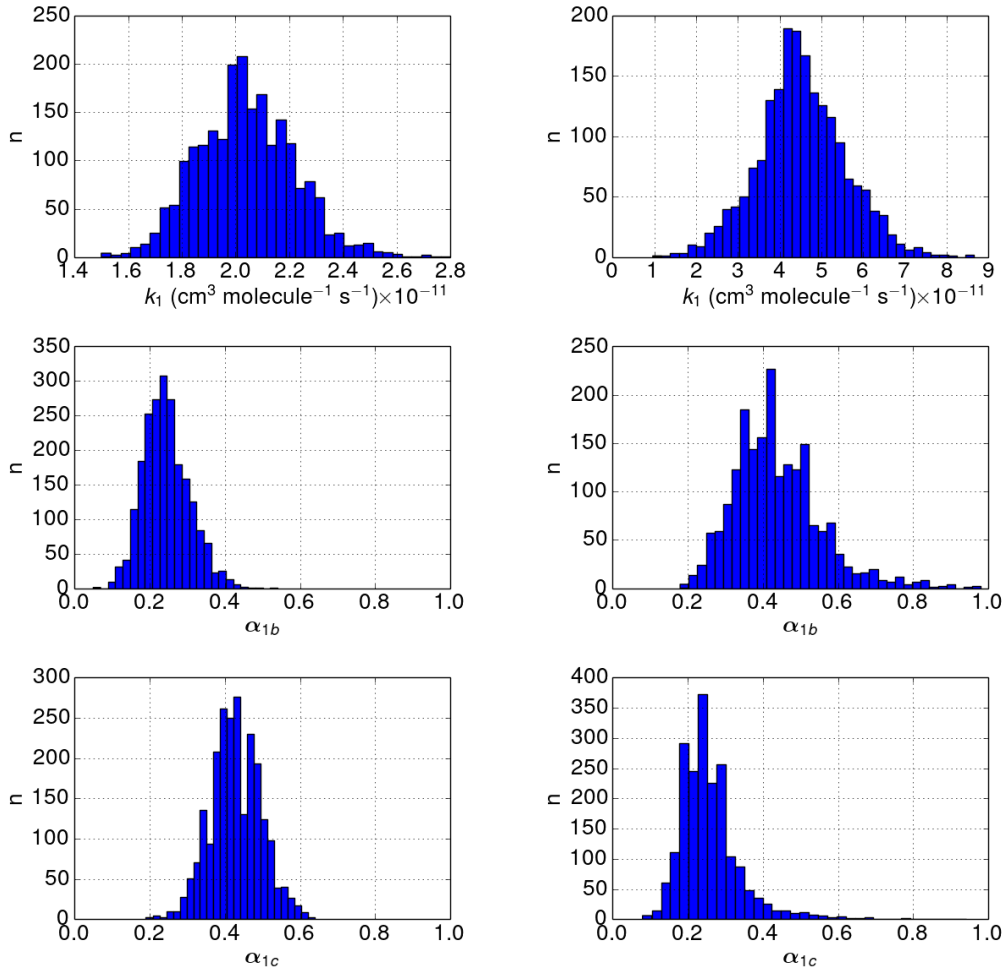

Figure 4.11: Histograms of k_1, α_{1b}, and α_{1c} of data collected at (a) T = 294 K and (b) T = 230 K. Total number of simulations = 2000; P = 100 Torr; concentrations: $[Cl]_0 = 8.8\times10^{13}$ molecule cm^{-3}; $[CH_3OH] = 5.0\times10^{15}$ molecule cm^{-3}; $[CH_3CHO] = 1.0\times10^{15}$ molecule cm^{-3}.

higher prevalence of the secondary reactions of $CH_3C(O)O_2$. The final values and uncertainties of k_1, α_{1b}, and α_{1c} at each temperature were determined by taking the weighted average of results obtained from these Monte Carlo simulations.

4.4 Discussion

4.4.1 Overall rate constant of the HO_2 + $CH_3C(O)O_2$ reaction

The value of k_1 measured at room temperature appear to be in good agreement with a majority of the previous values (Table 4.6). Our values appear to skew towards the lower range of the recent measurements by Groß et al. [14] and Winiberg et al.

[15], but are still within experimental error. Our results are also significantly lower than the values reported by Crawford et al. [17]. The higher rate constants reported by Crawford et al. [17] may be due to the high initial radical and precursor concentrations that were used. Under their experimental conditions, significant concentrations of adducts are expected, even at room temperature. Although additional HO_2 loss by reaction with CH_3CHO was taken into account, rate enhancement by CH_3OH was not, which would overestimate the HO_2 + $CH_3C(O)O_2$ rate constant.

Table 4.6: Comparison of previous and current results at room temperature.

Ref.	T (K)	k_1 [a]	α_{1a}	α_{1b}	α_{1c}
[8]	298		0.75 ± 0.03	0.25 ± 0.03	[b]
[16]	298	1.3 ± 0.3	0.67 ± 0.07	0.33 ± 0.07	[b]
[9]	298		0.73	0.27	[b]
[17]	295	4.4 ± 1.6	0.88 ± 0.04	0.12 ± 0.04	[b]
[18]	298	1.51 ± 0.07	0.80 ± 0.02	0.20 ± 0.02	[b]
[7]	298		0.40 ± 0.16	0.20 ± 0.08	0.40 ± 0.16
[11]	298	1.50 ± 0.08	0.80 ± 0.01	0.20 ± 0.01	< 0.1
[12]	296		0.38 ± 0.13	0.12 ± 0.04	0.43 ± 0.10
[13]	298	1.4 ± 0.5			0.5 ± 0.2
[14]	298	2.1 ± 0.4	0.23 ± 0.12	0.16 ± 0.08	0.61 ± 0.09
[15]	293	2.4 ± 0.4	0.37 ± 0.10	0.12 ± 0.04	0.51 ± 0.12
[1]	298	2.2	0.37 ± 0.10	0.13 ± 0.10	0.50 ± 0.10
[26, 27]	298	1.40	0.80	0.20	[b]
This work	294	1.72 ± 0.22	0.29 ± 0.12	0.23 ± 0.07	0.48 ± 0.09

[a] Units: $\times 10^{-11}$ cm^3 molecule^{-1} s^{-1}

[b] Assumed α_{1c}=0

Figure 4.12 compares the temperature dependence of k_1 with previous results. The observed temperature dependence agrees with the IUPAC values within 1σ but the overall rate constant appears to be in better agreement with the JPL values due to a difference of almost a factor of 8 between the two recommended A-factors (Table 4.7). The agreement in the observed overall rate constant with the JPL values is rather fortuitous since the recommended values were based on the Tomas et al. [18] and Moortgat et al. [16] studies, which did not include radical recycling by the OH channel. Therefore, the previously reported rate constants were likely underestimated, which is consistent with what is observed in this work if we extrapolated to higher temperatures. At lower temperatures, the recommended values appear to be slightly larger than the values determined in this work, which may be due to insufficiently accounting for rate enhancement effects as mentioned before.

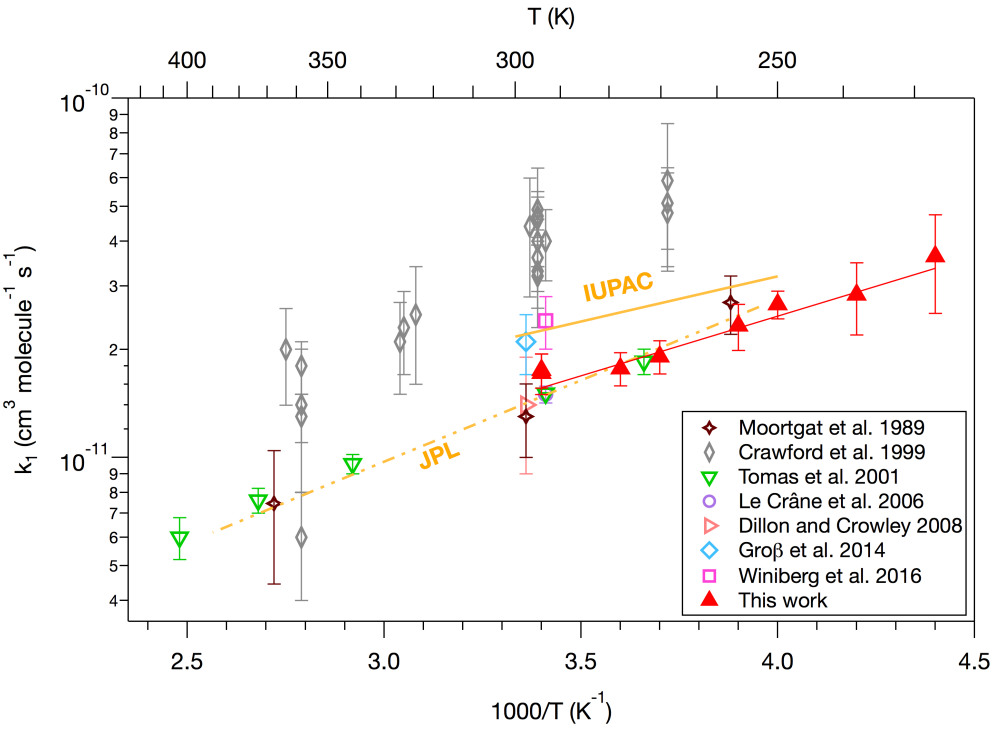

Figure 4.12: Temperature dependence of overall rate constant, k_1, determined in this work (red triangles) compared to previous works and to JPL (dash-dotted line) and IUPAC (solid line) recommendations.

Table 4.7: Comparison of previous temperature dependence studies and current results.

Ref.	T (K)	A-factor[a]	E/R (K)	α_{1a}	α_{1b}	α_{1c}
Moortgat et al. [16]	253 - 368	0.43	-1040 ± 100	0.67 ± 0.07	0.33 ± 0.07	[b]
Horie and Moortgat [9]	263 - 333			$\alpha_{1a}/\alpha_{1b} = 330\exp[(-1430 \pm 480/T)]$		[b]
Crawford et al. [17]	269 - 363	0.39	-1350 ± 250	0.88 ± 0.02	0.12 ± 0.04	[b]
Tomas et al. [18]	273 - 403	0.64	-925 ± 120	0.80 ± 0.02	0.20 ± 0.02	[b]
IUPAC [1]	250 - 230	3.14	-580 ± 400	$\alpha_{1a}/\alpha_{1b} = 340\exp[(-1430 \pm 500/T)]$		
				$\alpha_{1c}/\alpha_{1b} = 2.34 \times 10^4\exp[(-2600 \pm 3000/T)]$		
JPL 15-10 [26], Tyndall et al. [27]	253 - 403	0.43	-1040	0.80	0.20	[b]
This work	230 - 294	$1.38^{+1.17}_{-0.63}$	-730 ± 170	See Table 4.3 and Figure 4.10		

[a] Units: $\times 10^{-12}$ cm^3 molecule^{-1} s^{-1}

[b] Assumed α_{1c}=0

Figure 4.13 compares our room temperature values of the branching ratios of R1 to previous results that did not exclude OH recycling. All three product channels are consistent with previous measurements within 1σ. Our values for α_{1c} are also in good agreement with the more recent studies that used direct OH detection [13–15]. Slightly lower OH yields were reported by chamber studies [7, 12]. Chamber-type studies require complex kinetics models to determine rate constants and branching ratios from end-product analysis of stable products. Because they are more sensitive to wall-loss and secondary reactions that occur on longer timescales, systematic errors in the chemical model may explain the observed discrepancies with studies employing direct OH detection.

What we contribute to the efforts made to characterize the product distribution of this reaction is the temperature dependence. The trends that were observed (Figure 4.10) are consistent with the theoretical prediction by Hasson et al. [10], who postulated that while the peracetic acid channel proceeds via hydrogen transfer, the OH and O_3 channels are inter-linked by a common hydrotetroxide intermediate. The peracetic acid channel is relatively temperature independent over this temperature range, consistent with the IUPAC recommendation and Hasson et al. [10]'s theoretical values. The overall trend of the OH and O_3 branching ratios also appears to agree with IUPAC and with theory. It can be speculated that at higher temperatures, entropy favors the OH channel over the ozone channel, which has a tighter transition state. The observed OH yield has a weaker temperature dependence compared to the IUPAC recommendations, leading to a larger OH yield at lower temperatures than was previously predicted.

4.5 Conclusions

The present work reports the first temperature dependence investigation of the OH product channel of the $HO_2 + CH_3C(O)O_2$ reaction using techniques that enabled direct detection of HO_2 and OH radicals combined with UV absorption measurements in real time. Also of importance is the extension to lower temperatures of the range of temperatures over which the overall rate constant has been previously measured, which has more relevance for atmospheric chemistry.

Analysis of data required using a complex kinetics model to disentangle the kinetics of secondary chemistry, particularly R8 and R13. Estimated values of k_8, k_{13}, and α_{13a} were found to be within the uncertainty bounds of the recommended values from the current JPL data evaluation [26]; nonetheless, further re-investigation of the kinetics and product yields of these reactions is clearly needed.

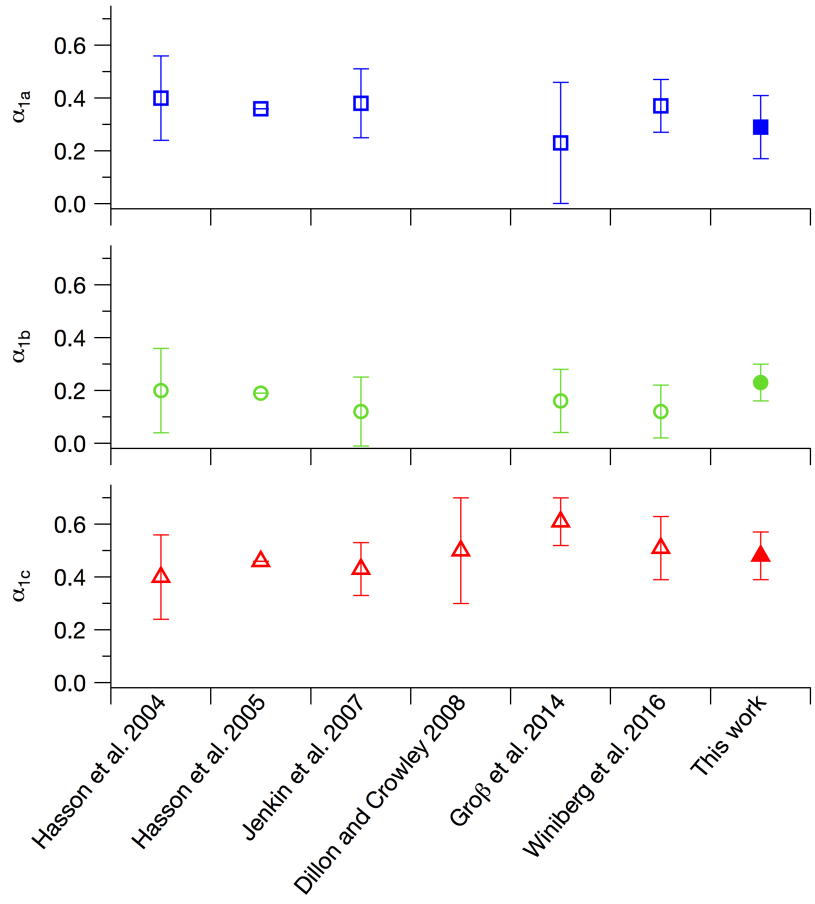

Figure 4.13: Comparison of room temperature values of α_{1a} (blue squares), α_{1b} (green circles), and α_{1c} (red triangles) measured in this work (2σ uncertainties) to previously reported values in the literature. Results from studies that assumed no OH recycling have been excluded.

This work has shown that that significant rate enhancement of the HO_2 self reaction was observed, which should be taken into account for accurate characterization of the HO_2 + $CH_3C(O)O_2$ reaction. Perhaps fortuitously, the rate constant of the title reaction appears to agree better with the JPL recommendation. Finally, our results suggest that especially at lower temperatures, higher OH regeneration may need to be included in atmospheric models.

Acknowledgments

This research was carried out by the Jet Propulsion Laboratory, California Institute of Technology, under contract with the National Aeronautics and Space Administration (NASA). The authors thank the Microdevices Lab (MDL) at the Jet Propulsion Laboratory (JPL), and in particular Mathieu Fradet and Siamak Forouhar, who were responsible for the fabrication of our mid-IR OH detection laser. Finally, A.O.H. thanks the National Science Foundation (NSF), the NASA Earth and Space Science Fellowship (NESSF), and NASA's Upper Atmospheric Research Program (UARP) and Tropospheric Chemistry Program for financial support.

4.6 Supplementary Information

4.6.1 Summary of experimental conditions at each temperature

Table 4.8: Detailed summary of experimental conditions at T = 294.0 K and P = 100 Torr in N_2 buffer gas.

$[O_2]^a$	$[Cl_2]^b$	$[CH_3OH]^b$	$[CH_3CHO]^b$	$[Cl]_0{}^c$	$[CH_3OH]/[CH_3CHO]$	$[HO_2]_0/[CH_3C(O)O_2]_0$
1.59	2.29	1.99	1.04	5.94	1.92	1.32
	3.06	2.00	1.03	7.51	1.93	1.33
		3.00	1.04		2.89	1.99
		4.00	1.04		3.87	2.66
		5.03	1.04		4.85	3.34
		6.00	1.03		5.80	3.99

[a]Units: 10^{18} molecule cm^{-3}
[b]Units: 10^{15} molecule cm^{-3}
[c]Units: 10^{13} molecule cm^{-3}

Table 4.9: Detailed summary of experimental conditions at T = 292.7 K and P = 100 Torr in N_2 buffer gas.

$[O_2]^a$	$[Cl_2]^b$	$[CH_3OH]^b$	$[CH_3CHO]^b$	$[Cl]_0{}^c$	$[CH_3OH]/[CH_3CHO]$	$[HO_2]_0/[CH_3C(O)O_2]_0$
1.60	2.30	4.97	1.01	8.70	4.94	3.40
		5.94	1.00		5.92	4.07
		6.97	1.00		6.95	4.78
		7.03	1.41		5.00	3.44
		6.97	1.76		3.96	2.72
		7.00	1.16		6.01	4.13
		6.98	2.29		3.04	2.09
		8.82	1.76		5.02	3.45
		8.80	2.18		4.03	2.77
		8.76	1.47		5.97	4.10

[a]Units: 10^{18} molecule cm^{-3}
[b]Units: 10^{15} molecule cm^{-3}
[c]Units: 10^{13} molecule cm^{-3}

Table 4.10: Detailed summary of experimental conditions at T = 280.1 K and P = 100 Torr in N_2 buffer gas.

$[O_2]^a$	$[Cl_2]^b$	$[CH_3OH]^b$	$[CH_3CHO]^b$	$[Cl]_0{}^c$	$[CH_3OH]/[CH_3CHO]$	$[HO_2]_0/[CH_3C(O)O_2]_0$
1.67	3.81	4.01	1.03	12.9	3.88	2.67
		4.96	1.03		4.82	3.32
		5.99	1.04		5.78	3.97
		7.05	1.04		6.80	4.68
		7.03	1.16		6.04	4.15
		7.05	1.40		5.03	3.45
		7.04	1.76		4.00	2.75
		8.80	1.47		6.00	4.12
		8.78	1.76		4.98	3.42
		8.76	2.16		4.06	2.79

[a]Units: 10^{18} molecule cm^{-3}
[b]Units: 10^{15} molecule cm^{-3}
[c]Units: 10^{13} molecule cm^{-3}

Table 4.11: Detailed summary of experimental conditions at T = 270.6 K and P = 100 Torr in N_2 buffer gas.

$[O_2]^a$	$[Cl_2]^b$	$[CH_3OH]^b$	$[CH_3CHO]^b$	$[Cl]_0{}^c$	$[CH_3OH]/[CH_3CHO]$	$[HO_2]_0/[CH_3C(O)O_2]_0$
1.72	3.81	3.96	1.00	13.3	3.96	2.72
		4.97	1.00		4.97	3.42
		6.04	1.00		6.04	4.16
		7.03	1.01		7.00	4.81
		7.04	1.16		6.07	4.17
		7.04	1.41		5.00	3.44
		7.03	1.75		4.01	2.76
		8.81	1.46		6.05	4.16
		8.79	1.75		5.02	3.45
		8.75	2.15		4.06	2.79

[a]Units: 10^{18} molecule cm^{-3}
[b]Units: 10^{15} molecule cm^{-3}
[c]Units: 10^{13} molecule cm^{-3}

Table 4.12: Detailed summary of experimental conditions at T = 259.3 K and P = 100 Torr in N_2 buffer gas.

$[O_2]^a$	$[Cl_2]^b$	$[CH_3OH]^b$	$[CH_3CHO]^b$	$[Cl]_0{}^c$	$[CH_3OH]/[CH_3CHO]$	$[HO_2]_0/[CH_3C(O)O_2]_0$
1.80	3.81	2.97	1.01	12.8	2.95	2.03
		4.03	1.01		4.00	2.75
		5.03	1.00		5.03	3.46
		5.98	1.01		5.94	4.08
		7.00	1.00		7.00	4.79
		7.05	1.17		6.03	4.14
		6.99	1.41		4.96	3.41
		6.99	1.76		3.98	2.73
		7.01	2.41		2.91	2.00
		8.79	1.46		6.03	4.14
		8.77	1.76		4.99	3.43
		8.80	2.18		4.04	2.78
		8.79	2.91		3.02	2.08
	3.03	8.79	1.46	10.5	6.03	4.15

[a]Units: 10^{18} molecule cm^{-3}
[b]Units: 10^{15} molecule cm^{-3}
[c]Units: 10^{13} molecule cm^{-3}

Table 4.13: Detailed summary of experimental conditions at T = 250.4 K and P = 100 Torr in N_2 buffer gas.

$[O_2]^a$	$[Cl_2]^b$	$[CH_3OH]^b$	$[CH_3CHO]^b$	$[Cl]_0{}^c$	$[CH_3OH]/[CH_3CHO]$	$[HO_2]_0/[CH_3C(O)O_2]_0$
1.86	3.05	3.00	1.03	6.84	2.91	2.00
		4.08	1.03		3.96	2.72
		5.05	1.03		4.89	3.36
		6.07	1.03		5.89	4.05
	3.81	3.00	1.03	8.32	2.91	2.00
		4.08	1.03		3.96	2.72
		5.05	1.03		4.89	3.36
		6.07	1.03		5.89	4.05
		7.09	1.03		6.87	4.73
		7.10	1.17		6.06	4.16
		7.10	1.40		5.06	3.48
		7.10	1.75		4.05	2.78
		7.10	2.32		3.05	2.10
		8.76	1.47		5.96	4.10
		8.74	1.75		4.99	3.43
		8.75	2.17		4.03	2.77

[a]Units: 10^{18} molecule cm^{-3}
[b]Units: 10^{15} molecule cm^{-3}
[c]Units: 10^{13} molecule cm^{-3}

Table 4.14: Detailed summary of experimental conditions at T = 240.1 K and P = 100 Torr in N_2 buffer gas.

$[O_2]^a$	$[Cl_2]^b$	$[CH_3OH]^b$	$[CH_3CHO]^b$	$[Cl]_0{}^c$	$[CH_3OH]/[CH_3CHO]$	$[HO_2]_0/[CH_3C(O)O_2]_0$
1.94	2.30	8.78	1.46	5.68	6.02	4.14
	3.04	8.78	1.46	7.31	6.02	4.14
	3.81	3.05	1.01	9.06	3.02	2.08
		3.95	1.01		3.93	2.70
		5.01	1.01		4.98	3.43
		5.24	1.75		2.99	2.06
		6.00	1.00		6.00	4.13
		7.00	1.00		6.97	4.79
		6.99	1.17		5.96	4.10
		6.94	1.41		4.93	3.39
		6.99	1.75		3.99	2.75
		8.77	1.46		6.02	4.14
		8.74	1.74		5.04	3.46
		8.68	2.15		4.04	2.77

[a]Units: 10^{18} molecule cm^{-3}
[b]Units: 10^{15} molecule cm^{-3}
[c]Units: 10^{13} molecule cm^{-3}

Table 4.15: Detailed summary of experimental conditions at T = 228.9 K and P = 100 Torr in N_2 buffer gas.

$[O_2]^a$	$[Cl_2]^b$	$[CH_3OH]^b$	$[CH_3CHO]^b$	$[Cl]_0{}^c$	$[CH_3OH]/[CH_3CHO]$	$[HO_2]_0/[CH_3C(O)O_2]_0$
2.04	2.36	8.76	1.44	5.57	6.07	4.17
	3.02	8.80	1.45	6.99	6.07	4.17
	3.80	3.04	1.02	8.72	3.00	2.06
		4.0 4	1.0 2		3.96	2.73
		5.06	1.02		4.96	3.41
		6.02	1.0 2		5.90	4.06
		7.01	1.02		6.87	4.72
		7.0 1	1.16		6.04	4.15
		7.0 2	1.41		4.98	3.42
		7.02	1.76		3.98	2.74
		7.02	2.32		3.03	2.08
		8.77	1.45		6.03	4.15
		8.82	1.76		5.01	3.44
		8.83	2.18		4.05	2.79

[a]Units: 10^{18} molecule cm^{-3}
[b]Units: 10^{15} molecule cm^{-3}
[c]Units: 10^{13} molecule cm^{-3}

4.7 Empirical values of k_8 and k_{13} determined at each temperature

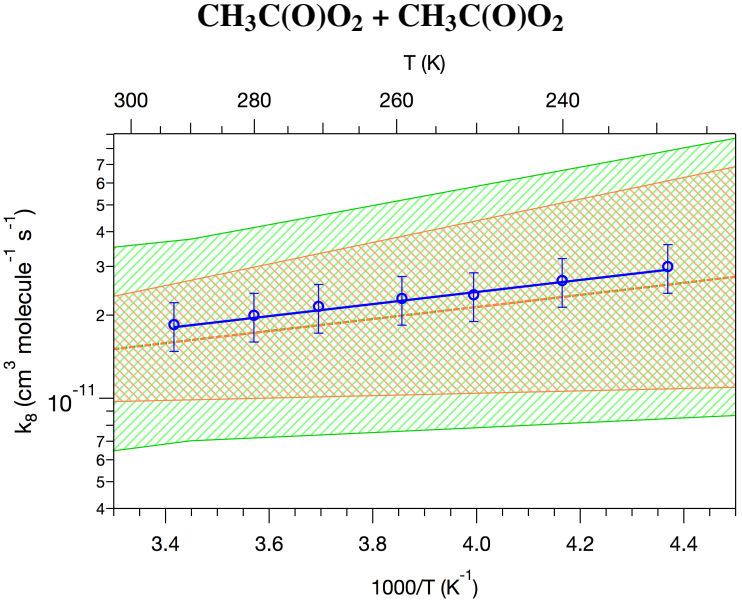

(a)

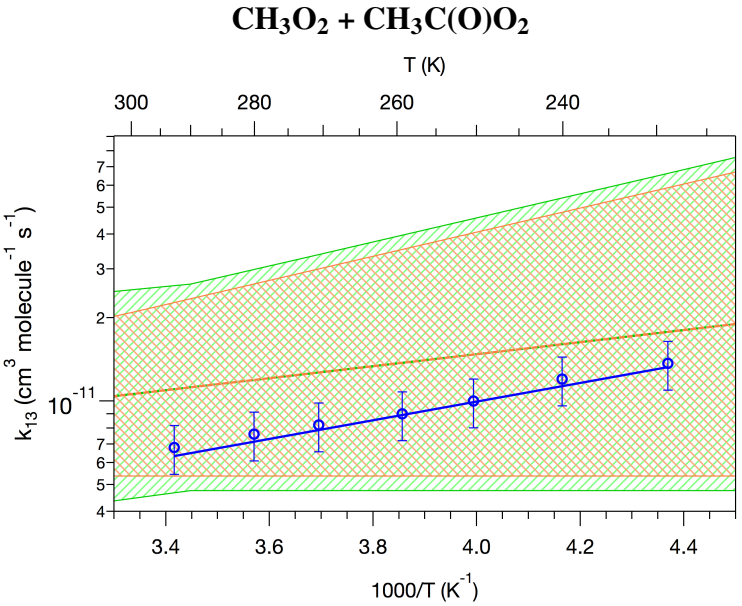

(b)

Figure 4.14: Arrhenius plots for the rate constants of the (a) $CH_3C(O)O_2$ self reaction (R8) and the (b) $CH_3O_2 + CH_3C(O)O_2$ reaction (R13). Estimated values of k_8 and k_{13} determined in this work (blue circles) are plotted with 20% uncertainty. Recommended values from the JPL and IUPAC data evaluations are also shown with 95% uncertainty bounds (green and orange shaded areas, respectively) [1, 26].

4.7.1 Fitted values of k_1 at each temperature

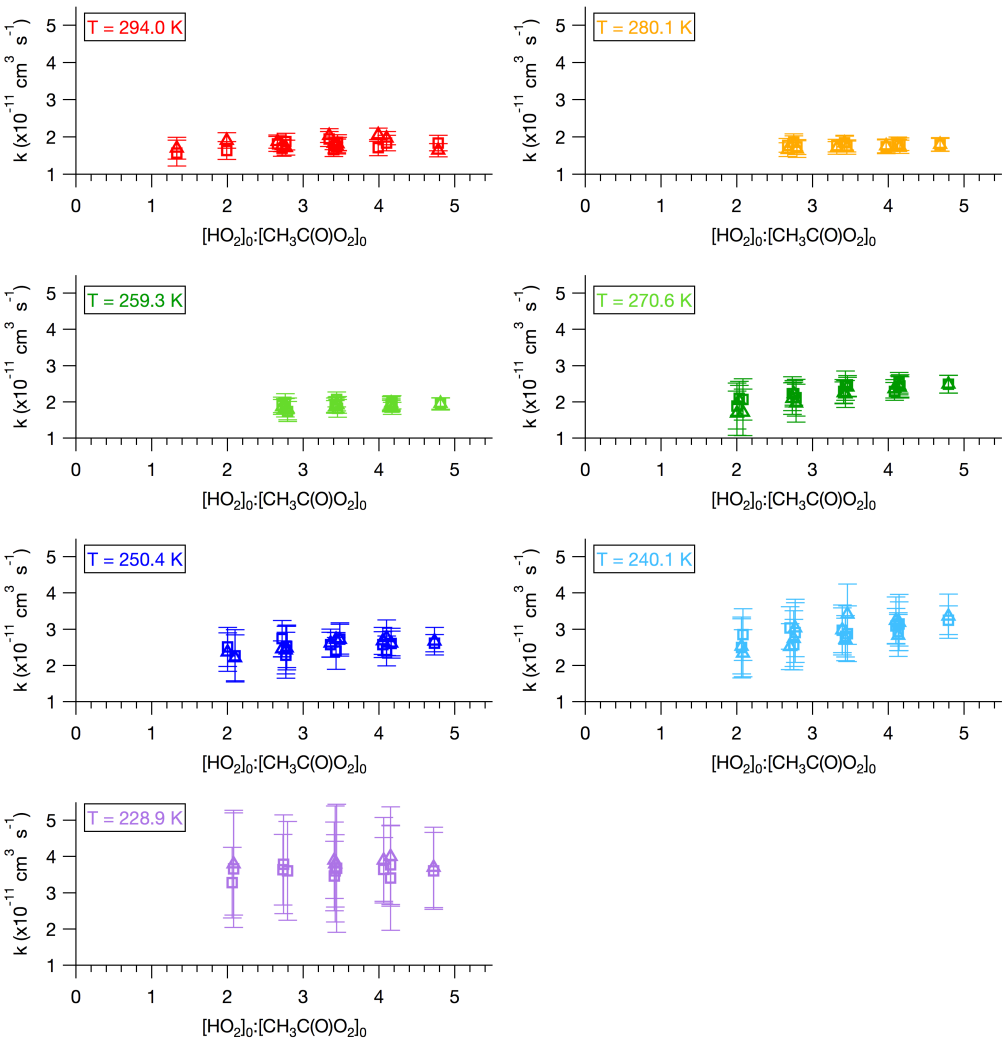

Figure 4.15: Fitted values of k_1 plotted as a function of $[HO_2]_0/[CH_3C(O)O_2]_0$, shown for all temperatures d. Values determined from the NIR and MIR fits (squares) agree with those determined from the NIR and UV fits (triangles).

4.7.2 FACSIMILE code for simultaneous fitting of HO_2 + $CH_3C(O)O_2$ data

```
* ********************************************************************** *;
* MULTI-FIT FOR HO2 + acetylO2 CHEMISTRY                                 *;
* Simultaneous IR & UV fit                                               *;
* IR: Run HO2_RUN_NUM ;                                                  *;
* UV WL_A : Run UV_RUN_NUM_A, UV WL_B : Run UV_RUN_NUM_B ;               *;
* Source chemistry Cl2-MeOH-CH3CHO-O2                                    *;
* Bath gas N2                                                            *;
* FACSIMILE variable name: max 10 characters                             *;
* ********************************************************************** *;
* Author: Aileen Oyama Hui                                               *;
* Jet Propulsion Laboratory, Pasadena, 91008                             *;
* Date Modified: 01/10/2018                                              *;
* ********************************************************************** *;
*                                                                        *;
* Attach Files for Output                                                *;
*                                                                        *;
EXECUTE ;
* Open input file: 11-bkgd-subtracted data ;
OPEN 11 "IU_run_num_in.prn" ;
* Open output files: 10-fit, 9-resids, 3-params ;
OPEN 10 "_run_num_IU2AH_p.out" ;
OPEN 9 "_run_num_IU2AH_r.out" ;
OPEN 3 "_run_num_IU2AH.prm" ;
**;
* ********************************************************************** *;
* ***** DEFINITIONS                                                      *;
* ********************************************************************** *;
*                                                                        *;
* Define chemical species                                                *;
*                                                                        *;
VARIABLE Cl2_A O2_A CH3OH_A CH3CHO_A ;
VARIABLE Cl_A CH2OH_A ac_A HCl_A H2O_A CH2O_A CH2CHO_A ;
VARIABLE HO2_A acO2_A OH_A CH3O_A ;
VARIABLE H2O2_A O_A HCO_A CO_A H_A HMPOOH_A HOCHO_A HOCH2O_A ;
VARIABLE CH3_A CO2_A acOOOH_A acOH_A O3_A ClO_A HOCl_A CH2O2_A ;
VARIABLE CH3O2_A CH3O_A CH3OOH_A HMP_A HOCO_A CMPLX_A ;
*                                                                        *;
VARIABLE Cl2_B O2_B CH3OH_B CH3CHO_B ;
VARIABLE Cl_B CH2OH_B ac_B HCl_B H2O_B CH2O_B CH2CHO_B ;
VARIABLE HO2_B acO2_B OH_B CH3O_B ;
VARIABLE H2O2_B O_B HCO_B CO_B H_B HMPOOH_B HOCHO_B HOCH2O_B ;
VARIABLE CH3_B CO2_B acOOOH_B acOH_B O3_B ClO_B HOCl_B CH2O2_B ;
VARIABLE CH3O2_B CH3O_B CH3OOH_B HMP_B HOCO_B CMPLX_B ;
*                                                                        *;
VARIABLE Cl2_C O2_C CH3OH_C CH3CHO_C ;
VARIABLE Cl_C CH2OH_C ac_C HCl_C H2O_C CH2O_C CH2CHO_C ;
VARIABLE HO2_C acO2_C OH_C CH3O_C ;
VARIABLE H2O2_C O_C HCO_C CO_C H_C HMPOOH_C HOCHO_C HOCH2O_C ;
VARIABLE CH3_C CO2_C acOOOH_C acOH_C O3_C ClO_C HOCl_C CH2O2_C ;
VARIABLE CH3O2_C CH3O_C CH3OOH_C HMP_C HOCO_C CMPLX_C ;
*                                                                        *;
```

```
* ********************************************************************** *;
*                                                                        *;
* Define parameters used in calculation                                  *;
* ---------------------------------------------------------------------- *;
* Initial reagent concentrations and experimental conditions             *;
* ---------------------------------------------------------------------- *;
PARAMETER T P M L 147 ;
PARAMETER IR_HO2_C VM_HO2 VM_HO2_INPUTVAL ;

PARAMETER UV_A UHO2_A UH2O2_A UacO2_A Uac_A UCH3O2_A ;
PARAMETER UacOH_A UCH2O_A UO3_A UCMPLX_A;

PARAMETER UV_B UHO2_B UH2O2_B UacO2_B Uac_B UCH3O2_B ;
PARAMETER UacOH_B UCH2O_B UO3_B UCMPLX_B ;

PARAMETER ClI ClI_INPUTVAL HO2I_C ClI_INPUTVAL HO2I_A HO2I_B ;
*                                                                        *;
* ---------------------------------------------------------------------- *;
* Rate Coefficients & Absorption Cross-sections                          *;
* ---------------------------------------------------------------------- *;
*                                                                        *;
PARAMETER CSHO2_A HO2_UV_XS_A CSH2O2_A H2O2_UV_XS_A CSacO2_A acO2_UV_XS_A ;
PARAMETER CSac_A ac_UV_XS_A CSCH3O2_A CH3O2_UV_XS_A CSacOH_A acOH_UV_XS_A ;
PARAMETER CSCH2O_A CH2O_UV_XS_A CSO3_A O3_UV_XS_A ;

PARAMETER CSHO2_B HO2_UV_XS_B CSH2O2_B H2O2_UV_XS_B CSacO2_B acO2_UV_XS_B ;
PARAMETER CSac_B ac_UV_XS_B CSCH3O2_B CH3O2_UV_XS_B CSacOH_B acOH_UV_XS_B ;
PARAMETER CSCH2O_B CH2O_UV_XS_B CSO3_B O3_UV_XS_B ;
*                                                                        *;
*HO2 + HO2 rate constant ;
PARAMETER K1 K1_INPUTVAL K1_UV K1_INPUTVAL K1_A K1_B K1_C Kc 2.1E-11 ;
PARAMETER Kcc 7.1E-11 ;
PARAMETER KmF KmR KM KM_INPUTVAL ;
*                                                                        *;
* HO2 + acetylO2 Params ;
PARAMETER K2 3.6E-11 K2_UV 3.6E-11 BR2C 0.31 BR2A 0.23 BR2B 0.46 ;
PARAMETER K2_A K2_B K2_C ;
*                                                                        *;
* acetylO2 self Params ;
PARAMETER K3 1.85E-11 ;
*PARAMETER K3 K3_INPUTVAL ;
*                                                                        *;
* CH3O2 + acetylO2 1Params ;
PARAMETER K4 0.68E-11 BR4A 0.97 ;
*PARAMETER K4 K4_INPUTVAL K4A K4_INPUTVAL K4B 1E-12 BR4A 0.9 ;
*                                                                        *;
* Cl + CH3O2/CH3O Params ;
PARAMETER K33 K30 1.6E-10 BR30A 0.5 ;
PARAMETER K31 1.6E-10 BR31A 0.95 ;
*                                                                        *;
* Acetyl + O2 Params ;
PARAMETER K6L K6H K6T K6B ;
```

```
PARAMETER LH6 X6 FC6 N6 K6 5.1E-12 BR6 BR6_INPUTVAL BR6H BR6H_INPUTVAL ;
PARAMETER c ;
*                                                                       *;
* MethylO2 Params ;
PARAMETER BR16A BR16B BR20 ;
PARAMETER K11 K11L K11H LH11 X11;
*                                                                       *;
* H + O2 Params ;
PARAMETER K7L K7H LH7 X7 K7 ;
*                                                                       *;
* OH + CO ;
PARAMETER K17B K17TL K17TH LH17T X17T K17T ;
*                                                                       *;
* OH + OH ;
PARAMETER K19L K19H LH19 X19 K19 ;
*                                                                       *;
* KD is the diffusion rate coefficient of HO2 at 298 K ;
PARAMETER KD 22.2 ;
PARAMETER MH2O2 MacO2 Mac MCH3O2 MacOH MCH2O MO3 ;
*                                                                       *;
* ********************************************************************* *;
* ***** INITIALIZATION                                                 *;
* ********************************************************************* *;
*                                                                       *;
INTEGER #COUNT ;
COMPILE INITIAL ;
*                                                                       *;
* Temperature (K) ;
T = T_INPUTVAL ;
* Pressure (Torr) ;
P = P_INPUTVAL ;
*                                                                       *;
M = P*3.53D16*(273.15/T) ;
*                                                                       *;
*sqrt of HO2:X mass ratio ;
MH2O2 = (33.006/34.014)@(1/2) ;
MacO2 = (33.006/75.043)@(1/2) ;
Mac = (33.006/43.045)@(1/2) ;
MCH3O2 = (33.006/47.033)@(1/2) ;
MacOH = (33.006/60.052)@(1/2) ;
MCH2O = (33.006/30.026)@(1/2) ;
MO3 = (33.006/47.997)@(1/2) ;
*                                                                       *;
* Concentrations (molecules/cm3) ;
O2_A = O2_INPUTVAL_A ;
CH3OH_A = CH3OH_INPUTVAL_A ;
CH3CHO_A = CH3CHO_INPUTVAL_A ;
Cl2_A = Cl2_INPUTVAL_A ;
*Cl_A = ClI ;
HO2I_A = ClI*5.5E-11*CH3OH_A/(5.5E-11*CH3OH_A + 8E-11*CH3CHO_A) ;
*HO2_A = HO2I_A/(KM*CH3OH_A+1) ;
*CMPLX_A = HO2I_A*KM*CH3OH_A/(KM*CH3OH_A+1) ;
```

```
HO2_A = HO2I_A ;
acO2_A = ClI*8E-11*CH3CHO_A/(5.5E-11*CH3OH_A + 8E-11*CH3CHO_A);
OH_A = BR6*ClI*8E-11*CH3CHO_A/(5.5E-11*CH3OH_A + 8E-11*CH3CHO_A);
K1_A = K1_UV ;
K2_A = K2_UV ;

O2_B = O2_INPUTVAL_B ;
CH3OH_B = CH3OH_INPUTVAL_B ;
CH3CHO_B = CH3CHO_INPUTVAL_B ;
Cl2_B = Cl2_INPUTVAL_B;
*Cl_B = ClI ;
HO2I_B = ClI*5.5E-11*CH3OH_B/(5.5E-11*CH3OH_B + 8E-11*CH3CHO_B) ;
*HO2_B = HO2I_B/(KM*CH3OH_B+1) ;
*CMPLX_B = HO2I_B*KM*CH3OH_B/(KM*CH3OH_B+1) ;
HO2_B = HO2I_B ;
acO2_B = ClI*8E-11*CH3CHO_B/(5.5E-11*CH3OH_B + 8E-11*CH3CHO_B);
OH_B = BR6*ClI*8E-11*CH3CHO_B/(5.5E-11*CH3OH_B + 8E-11*CH3CHO_B);
K1_B = K1_UV ;
K2_B = K2_UV ;

O2_C = O2_INPUTVAL_C ;
CH3OH_C = CH3OH_INPUTVAL_C ;
CH3CHO_C = CH3CHO_INPUTVAL_C ;
Cl2_C = Cl2_INPUTVAL_C;
*Cl_C = ClI ;
HO2I_C = ClI*5.5E-11*CH3OH_C/(5.5E-11*CH3OH_C + 8E-11*CH3CHO_C) ;
*HO2_C = HO2I_C/(KM*CH3OH_C+1) ;
*CMPLX_C = HO2I_C*KM*CH3OH_C/(KM*CH3OH_C+1) ;
HO2_C = HO2I_C ;
acO2_C = ClI*8E-11*CH3CHO_C/(5.5E-11*CH3OH_C + 8E-11*CH3CHO_C);
OH_C = BR6*ClI*8E-11*CH3CHO_C/(5.5E-11*CH3OH_C + 8E-11*CH3CHO_C);
K1_C = K1 ;
K2_C = K2 ;

*                                                                    *;
*HO2 = HO2I ;
*                                                                    *;
**;
*                                                                    *;
* ****************************************************************** *;
* ***** END OF BLOCK - COMPILE INITIAL                              *;
* ****************************************************************** *;
*                                                                    *;
* ****************************************************************** *;
* ***** CALCULATION OF RATE COEFFICIENTS                            *;
* ****************************************************************** *;
*                                                                    *;
COMPILE RATES;
*                                                                    *;
* HO2 + HO2 ;
*K1 = 3.0E-13*EXP(460/T) + 2.1E-33*M*EXP(920/T) ;
KmF = 2.8E-15*EXP(1800/T) ;
```

```
KmR = KmF/KM ;
*                                                                    *;
* Acetyl + O2 Rate constants (Papadimitriou 2015);
*K6L = (7.39E-30)*(T/300)@(-2.2) ;
*K6H = (4.88E-12)*(T/300)@(-0.85) ;
*LH6 = K6L*M/K6H ;
*X6 = 1/(1+(LOG10(LH6))**2) ;
*K6T = (K6L*M/(1+LH6))*0.8@X6 ;
*K6B = (6.4E-14)*EXP(820/T)*(1 - K6T/K6H) ;
*                                                                    *;
* Acetyl + O2 Rate constants (Carr 2011);
K6L = (3.64E-30)*(T/300)@(-1.89) ;
K6H = (6.11E-12)*(T/300)@(-0.01) ;
LH6 = K6L*M/K6H ;
FC6 = EXP(-T/4600) ;
N6 = 2.23-1.27*FC6 ;
X6 = 1/(1+((1/N6)*LOG10(LH6))**2) ;
K6T = (K6L*M/(1+LH6))*FC6@X6 ;
K6B = (1.44E-12)*(T/300)@(-1.58)*(1 - K6T/K6H) ;
*                                                                    *;
* Acetyl + O2 Branching Ratio (Gross 2014);
*BR6 = 1/(9.3E-18*c*M+1) ;
*                                                                    *;
*H + O2 ;
K7L = (4.4E-32)*(T/300)@(-1.3) ;
K7H = (7.5E-11)*(T/300)@(0.2) ;
LH7 = K7L*M/K7H ;
X7 = 1/(1+(LOG10(LH7))**2) ;
K7 = (K7L*M/(1+LH7))*0.6@X7 ;
*                                                                    *;
*CH3 + O2 (termolec only-bimolec. not important, JPL15-10);
K11L = (4.0E-31)*(T/300)@(-3.6) ;
K11H = (1.2E-12)*(T/300)@(1.1) ;
LH11 = K11L*M/K11H ;
X11 = 1/(1+(LOG10(LH11))**2) ;
K11 = (K11L*M/(1+LH11))*0.6@X11 ;
*                                                                    *;
* MethylO2 Self-Rxn (JPL & IUPAC) ;
BR16B = 1/(1+26.2*EXP(-1130/T)) ;
BR16A = 1 - BR16B ;
BR20 = 1/(1+498*EXP(-1160/T)) ;
*                                                                    *;
* OH + CO ;
K17TL = 5.9E-33*(T/300)@(-1) ;
K17TH = 1.1E-12*(T/300)@(1.3) ;
LH17T = K17TL*M/K17TH ;
X17T = 1/(1+(LOG10(LH17T))**2) ;
K17T = (K17TL*M/(1+LH17T))*0.6@X17T ;
*                                                                    *;
* OH + OH ;
K19L = (6.9E-31)*(T/300)@(-1) ;
K19H = 2.6E-11 ;
```

```
LH19 = K19L*M/K19H ;
X19 = 1/(1+(LOG10(LH19))**2) ;
K19 = (K19L*M/(1+LH19))*0.6@X19 ;
*                                                                    *;
* CH3O + CH3CHO ;
K33 = 5.7E-13*EXP(-625.45/T) ;
*                                                                    *;
** ;
*                                                                    *;
* ****************************************************************** *;
* ***** END OF BLOCK - COMPILE RATES                                 *;
* ****************************************************************** *;
*                                                                    *;
*                                                                    *;
* ****************************************************************** *;
* ***** QUANTITIES NEEDED DURING SIMULATION                          *;
* ****************************************************************** *;
*                                                                    *;
COMPILE GENERAL;
*                                                                    *;
* ------------------------------------------------------------------ *;
* Calibrate IR Signal and Calculate UV Absorbance                    *;
* ------------------------------------------------------------------ *;
*                                                                    *;
* IR_HO2 is HO2 concentration over voltage multiplier;
IR_HO2_C = HO2_C/VM_HO2 ;

* A(UV) = (sum (concentration*CS))*length of Herriott cell;
UHO2_A = CSHO2_A*HO2_A*L ;
UCMPLX_A = CSHO2_A*CMPLX_A*L ;
UH2O2_A = CSH2O2_A*H2O2_A*L ;
UacO2_A = CSacO2_A*acO2_A*L ;
Uac_A = CSac_A*ac_A*L ;
UCH3O2_A = CSCH3O2_A*CH3O2_A*L ;
UacOH_A = CSacOH_A*acOH_A*L ;
UCH2O_A = CSCH2O_A*CH2O_A*L ;
UO3_A = CSO3_A*O3_A*L ;

UV_A = (UHO2_A + UH2O2_A + UacO2_A + Uac_A + UCH3O2_A + UacOH_A
 + UCH2O_A + UO3_A + UCMPLX_A);

UHO2_B = CSHO2_B*HO2_B*L ;
UCMPLX_B = CSHO2_B*CMPLX_B*L ;
UacO2_B = CSacO2_B*acO2_B*L ;
Uac_B = CSac_B*ac_B*L ;
UCH3O2_B = CSCH3O2_B*CH3O2_B*L ;
UacOH_B = CSacOH_B*acOH_B*L ;
UCH2O_B = CSCH2O_B*CH2O_B*L ;
UO3_B = CSO3_B*O3_B*L ;

UV_B = (UHO2_B + UH2O2_B + UacO2_B + Uac_B + UCH3O2_B + UacOH_B
 + UCH2O_B + UO3_B + UCMPLX_B);
```

```
*                                                                     *;
* ------------------------------------------------------------------- *;
* Update Rate Coefficients                                            *;
* ------------------------------------------------------------------- *;
*                                                                     *;
BR2A = 1 - BR2C -BR2B ;
CALL RATES ;
** ;
*                                                                     *;
* ******************************************************************* *;
* ***** END OF BLOCK - COMPILE GENERAL                                *;
* ******************************************************************* *;
*
* ******************************************************************* *;
* ***** CHEMICAL MECHANISM                                            *;
* ******************************************************************* *;
*                                                                     *;
COMPILE EQUATIONS ;
*                                                                     *;
* ------------------------------------------------------------------- *;
* ------------------------------------------------------------------- *;
*                         IR SOURCE C (HO2 LASER)                     *;
* ------------------------------------------------------------------- *;
* ------------------------------------------------------------------- *;
*                                                                     *;
* ------------------------------------------------------------------- *;
* SOURCE CHEMISTRY                                                    *;
* ------------------------------------------------------------------- *;
*                                                                     *;
* Methanol ;
* ------------------------------------------------------------------- *;
% 5.5D-11                  : Cl_C + CH3OH_C = CH2OH_C + HCl_C ;
% 9.1D-12                  : CH2OH_C + O2_C = HO2_C + CH2O_C ;
% 0.85*2.9E-12*EXP(-345/T) : OH_C + CH3OH_C = CH2OH_C + H2O_C ;
% 0.15*2.9E-12*EXP(-345/T) : OH_C + CH3OH_C = CH3O_C + H2O_C ;
*                                                                     *;
* Acetaldehyde ;
* ------------------------------------------------------------------- *;
% 8.0E-11                  : Cl_C + CH3CHO_C = ac_C + HCl_C ;
% 0.95*4.63E-12*EXP(350/T) : OH_C + CH3CHO_C = ac_C + H2O_C ;
% 0.05*4.63E-12*EXP(350/T) : OH_C + CH3CHO_C = CH2CHO_C + H2O_C ;
*                                                                     *;
*% K6T                     : ac_C + O2_C = acO2_C ;
*% K6B                     : ac_C + O2_C = OH_C ;
% (1-BR6-BR6H)*K6          : ac_C + O2_C = acO2_C ;
% BR6*K6                   : ac_C + O2_C = OH_C ;
% BR6H*K6                  : ac_C + O2_C = HO2_C ;
*                                                                     *;
* ------------------------------------------------------------------- *;
* acO2 RXNS                                                           *;
* ------------------------------------------------------------------- *;
```

```
*                                                                              *;
* HO2 + acO2 = OH + acO + O2 ;
* Assumed Instantaneous: acO = CH3 + CO2 ;
* ---------------------------------------------------------------------- *;
% BR2A*K2_C      : HO2_C + acO2_C = OH_C + CH3_C + CO2_C + O2_C ;
% BR2A*K2_C      : HO2_C + acO2_C = acOOH_C + O2_C ;
% BR2B*K2_C      : HO2_C + acO2_C = acOH_C + O3_C;
*                                                                              *;
* CH3O2 + acO2 = acO + CH3O + O2 ;
* Assumed Instantaneous: acO = CH3 + CO2 ;
* ---------------------------------------------------------------------- *;
*                                                                              *;
% K4*BR4A      : acO2_C + CH3O2_C = CH3_C + CO2_C + CH3O_C + O2_C ;
% K4*(1-BR4A)  : acO2_C + CH3O2_C = acOH_C + CH2O_C + O2_C ;
*                                                                              *;
* acO2 + acO2 = acO + acO + O2 ;
* Assumed Instantaneous: acO = CH3 + CO2 ;
* ---------------------------------------------------------------------- *;
*                                                                              *;
% K3 : acO2_C + acO2_C = CH3_C + CH3_C + CO2_C + CO2_C + O2_C ;
*                                                                              *;
* ---------------------------------------------------------------------- *;
* CH3O2 RXNS                                                                   *;
* ---------------------------------------------------------------------- *;
*                                                                              *;
% K11                          : CH3_C + O2_C = CH3O2_C ;
% BR16A*9.5E-14*EXP(390/T)     : CH3O2_C + CH3O2_C = CH3O_C
+ CH3O_C + O2_C ;
% BR16B*9.5E-14*EXP(390/T)     : CH3O2_C + CH3O2_C = CH3OH_C
+ CH2O_C + O2_C ;
% 3.9E-14*EXP(-900/T)          : CH3O_C + O2_C = CH2O_C + HO2_C ;
% K33              : CH3O_C + CH3CHO_C = CH3OH_C + ac_C ;
*                                                                              *;
% (1-BR20)*3.8E-13*EXP(780/T) : HO2_C + CH3O2_C = CH3OOH_C + O2_C ;
% BR20*3.8E-13*EXP(780/T)     : HO2_C + CH3O2_C = CH2O_C
+ H2O_C + O2_C ;
*                                                                              *;
* ---------------------------------------------------------------------- *;
* HOx FORMATION, INTERCONVERSION AND REMOVAL                                   *;
* ---------------------------------------------------------------------- *;
*                                                                              *;
% K1_C                     : HO2_C + HO2_C = H2O2_C + O2_C;
*% Kc                      : HO2_C + CMPLX_C = ;
*% Kcc                     : CMPLX_C + CMPLX_C = ;
*% KmF % KmR               : HO2_C + CH3OH_C = CMPLX_C ;
% 4.8E-11*EXP(250/T)       : OH_C + HO2_C = H2O_C + O2_C ;
% 1.8E-12                  : OH_C + OH_C = H2O_C + O_C ;
% K19                      : OH_C + OH_C = H2O2_C ;
% 1.8E-12                  : OH_C + H2O2_C = H2O_C + HO2_C ;
% 5.5E-12*EXP(125/T)       : OH_C + CH2O_C = H2O_C + HCO_C ;
% 5.2E-12                  : HCO_C + O2_C = HO2_C + CO_C ;
% 1.8E-11*EXP(180/T)       : O_C + OH_C = O2_C + H_C ;
```

```
% 3.0E-11*EXP(200/T)       : O_C + HO2_C = O2_C + OH_C ;
% K7                       : H_C + O2_C = HO2_C ;
% 6.7E-15*EXP(600/T)       : HO2_C + CH2O_C = HMP_C ;
% 2.4E12*EXP(-7000/T)      : HMP_C = CH2O_C + HO2_C ;
% 0.5*5.6E-15*EXP(2300/T)  : HO2_C + HMP_C = HMPOOH_C + O2_C ;
% 0.3*5.6E-15*EXP(2300/T)  : HO2_C + HMP_C = HOCHO_C + H2O_C + O2_C ;
% 0.2*5.6E-15*EXP(2300/T)  : HO2_C + HMP_C = OH_C + HOCH2O_C + O2_C ;
% K17T                     : OH_C + CO_C = HOCO_C ;
% K17B                     : OH_C + CO_C = H_C + CO2_C ;
% 2E-12                    : HOCO_C + O2_C = HO2_C + CO2_C ;
% BR31A*K31                : OH_C + CH3O2_C = CH3O_C + HO2_C ;
% (1-BR31A)*K31            : OH_C + CH3O2_C = CH2O2_C + H2O_C ;
*% K31                     : OH_C + acO2_C = CH3_C + HO2_C + CO2_C;
% 1.7E-12*EXP(-940/T)      : OH_C + O3_C = HO2_C + O2_C ;
% 1.0E-14*EXP(-490/T)      : HO2_C + O3_C = OH_C + O2_C + O2_C ;
*                                                                    *;
* ------------------------------------------------------------------ *;
* ClOx FORMATION, INTERCONVERSION AND REMOVAL                        *;
* ------------------------------------------------------------------ *;
*                                                                    *;
% BR30A*K30                : Cl_C + CH3O2_C = CH3O_C + ClO_C ;
% (1-BR30A)*K30            : Cl_C + CH3O2_C = CH2O2_C + HCl_C ;
% 8.1E-11*EXP(-30/T)       : Cl_C + CH2O_C = HCl_C + HCO_C ;
% 7.4E-12*EXP(270/T)       : OH_C + ClO_C = Cl_C + HO2_C ;
% 6.0E-13*EXP(230/T)       : OH_C + ClO_C = HCl_C + O2_C ;
% 2.6E-12*EXP(-1100/T)     : OH_C + Cl2_C = HOCl_C + Cl_C ;
% 3.0E-12*EXP(-500/T)      : OH_C + HOCl_C = H2O_C + ClO_C ;
% 2.6E-12*EXP(290/T)       : HO2_C + ClO_C = HOCl_C + O2_C ;

*                                                                    *;
* ------------------------------------------------------------------ *;
* DIFFUSION                                                          *;
* ------------------------------------------------------------------ *;
*                                                                    *;
*% KD*(T/298)@(3/2)        : HO2_C = ;
*% KD*MH2O2*(T/298)@(3/2)  : H2O2_C = ;
*% KD*MacO2*(T/298)@(3/2)  : acO2_C = ;
*% KD*Mac*(T/298)@(3/2)    : ac_C = ;
*% KD*MCH3O2*(T/298)@(3/2) : CH3O2_C = ;
*% KD*MacOH*(T/298)@(3/2)  : acOH_C = ;
*% KD*MCH2O*(T/298)@(3/2)  : CH2O_C = ;
*% KD*MO3*(T/298)@(3/2)    : O3_C = ;
*                                                                    *;
* ------------------------------------------------------------------ *;
* ------------------------------------------------------------------ *;
*                              UV SOURCE A                           *;
* ------------------------------------------------------------------ *;
* ------------------------------------------------------------------ *;
*                                                                    *;
* ------------------------------------------------------------------ *;
* SOURCE CHEMISTRY                                                   *;
* ------------------------------------------------------------------ *;
```

```
*                                                                              *;
* Methanol ;
* ---------------------------------------------------------------------- *;
% 5.5D-11                  : Cl_A + CH3OH_A = CH2OH_A + HCl_A ;
% 9.1D-12                  : CH2OH_A + O2_A = HO2_A + CH2O_A ;
% 0.85*2.9E-12*EXP(-345/T) : OH_A + CH3OH_A = CH2OH_A + H2O_A ;
% 0.15*2.9E-12*EXP(-345/T) : OH_A + CH3OH_A = CH3O_A + H2O_A ;
*                                                                              *;
* Acetaldehyde ;
* ---------------------------------------------------------------------- *;
% 8.0E-11                  : Cl_A + CH3CHO_A = ac_A + HCl_A ;
% 0.95*4.63E-12*EXP(350/T) : OH_A + CH3CHO_A = ac_A + H2O_A ;
% 0.05*4.63E-12*EXP(350/T) : OH_A + CH3CHO_A = CH2CHO_A + H2O_A ;
*                                                                              *;
*% K6T                     : ac_A + O2_A = acO2_A ;
*% K6B                     : ac_A + O2_A = OH_A ;
% (1-BR6-BR6H)*K6          : ac_A + O2_A = acO2_A ;
% BR6*K6                   : ac_A + O2_A = OH_A ;
% BR6H*K6                  : ac_A + O2_A = HO2_A ;
*                                                                              *;
* ---------------------------------------------------------------------- *;
* acO2 RXNS                                                                    *;
* ---------------------------------------------------------------------- *;
*                                                                              *;
* HO2 + acO2 = OH + acO + O2 ;
* Assumed Instantaneous: acO = CH3 + CO2 ;
* ---------------------------------------------------------------------- *;
% BR2A*K2_A      : HO2_A + acO2_A = OH_A + CH3_A + CO2_A + O2_A ;
% BR2A*K2_A      : HO2_A + acO2_A = acOOOH_A + O2_A ;
% BR2B*K2_A      : HO2_A + acO2_A = acOH_A + O3_A;
*                                                                              *;
* CH3O2 + acO2 = acO + CH3O + O2 ;
* Assumed Instantaneous: acO = CH3 + CO2 ;
* ---------------------------------------------------------------------- *;
*                                                                              *;
% K4*BR4A      : acO2_A + CH3O2_A = CH3_A + CO2_A + CH3O_A + O2_A ;
% K4*(1-BR4A)  : acO2_A + CH3O2_A = acOH_A + CH2O_A + O2_A ;
*                                                                              *;
* acO2 + acO2 = acO + acO + O2 ;
* Assumed Instantaneous: acO = CH3 + CO2 ;
* ---------------------------------------------------------------------- *;
*                                                                              *;
% K3 : acO2_A + acO2_A = CH3_A + CH3_A + CO2_A + CO2_A + O2_A ;
*                                                                              *;
* ---------------------------------------------------------------------- *;
* CH3O2 RXNS                                                                   *;
* ---------------------------------------------------------------------- *;
*                                                                              *;
% K11                        : CH3_A + O2_A = CH3O2_A ;
% BR16A*9.5E-14*EXP(390/T)    : CH3O2_A + CH3O2_A = CH3O_A
+ CH3O_A + O2_A ;
% BR16B*9.5E-14*EXP(390/T)    : CH3O2_A + CH3O2_A = CH3OH_A
```

```
+ CH2O_A + O2_A ;
% 3.9E-14*EXP(-900/T)         : CH3O_A + O2_A = CH2O_A + HO2_A ;
% K33             : CH3O_A + CH3CHO_A = CH3OH_A + ac_A ;
*                                                                    *;
% (1-BR20)*3.8E-13*EXP(780/T) : HO2_A + CH3O2_A = CH3OOH_A + O2_A ;
% BR20*3.8E-13*EXP(780/T)     : HO2_A + CH3O2_A = CH2O_A
+ H2O_A + O2_A ;
*                                                                    *;
* ------------------------------------------------------------------ *;
* HOx FORMATION, INTERCONVERSION AND REMOVAL                         *;
* ------------------------------------------------------------------ *;
*                                                                    *;
% K1_A                     : HO2_A + HO2_A = H2O2_A + O2_A;
% Kc                       : HO2_A + CMPLX_A = ;
% Kcc                      : CMPLX_A + CMPLX_A = ;
*% KmF % KmR                : HO2_A + CH3OH_A = CMPLX_A ;
% 4.8E-11*EXP(250/T)       : OH_A + HO2_A = H2O_A + O2_A ;
% 1.8E-12                  : OH_A + OH_A = H2O_A + O_A ;
% K19                      : OH_A + OH_A = H2O2_A ;
% 1.8E-12                  : OH_A + H2O2_A = H2O_A + HO2_A ;
% 5.5E-12*EXP(125/T)       : OH_A + CH2O_A = H2O_A + HCO_A ;
% 5.2E-12                  : HCO_A + O2_A = HO2_A + CO_A ;
% 1.8E-11*EXP(180/T)       : O_A + OH_A = O2_A + H_A ;
% 3.0E-11*EXP(200/T)       : O_A + HO2_A = O2_A + OH_A ;
% K7                       : H_A + O2_A = HO2_A ;
% 6.7E-15*EXP(600/T)       : HO2_A + CH2O_A = HMP_A ;
% 2.4E12*EXP(-7000/T)      : HMP_A = CH2O_A + HO2_A ;
% 0.5*5.6E-15*EXP(2300/T)  : HO2_A + HMP_A = HMPOOH_A + O2_A ;
% 0.3*5.6E-15*EXP(2300/T)  : HO2_A + HMP_A = HOCHO_A + H2O_A + O2_A ;
% 0.2*5.6E-15*EXP(2300/T)  : HO2_A + HMP_A = OH_A + HOCH2O_A + O2_A ;
% K17T                     : OH_A + CO_A = HOCO_A ;
% K17B                     : OH_A + CO_A = H_A + CO2_A ;
% 2E-12                    : HOCO_A + O2_A = HO2_A + CO2_A ;
% BR31A*K31                : OH_A + CH3O2_A = CH3O_A + HO2_A ;
% (1-BR31A)*K31            : OH_A + CH3O2_A = CH2O2_A + H2O_A ;
*% K31                      : OH_A + acO2_A = CH3_A + HO2_A + CO2_A;
% 1.7E-12*EXP(-940/T)      : OH_A + O3_A = HO2_A + O2_A ;
% 1.0E-14*EXP(-490/T)      : HO2_A + O3_A = OH_A + O2_A + O2_A ;
*                                                                    *;
* ------------------------------------------------------------------ *;
* ClOx FORMATION, INTERCONVERSION AND REMOVAL                        *;
* ------------------------------------------------------------------ *;
*                                                                    *;
% BR30A*K30                : Cl_A + CH3O2_A = CH3O_A + ClO_A ;
% (1-BR30A)*K30            : Cl_A + CH3O2_A = CH2O2_A + HCl_A ;
% 8.1E-11*EXP(-30/T)       : Cl_A + CH2O_A = HCl_A + HCO_A ;
% 7.4E-12*EXP(270/T)       : OH_A + ClO_A = Cl_A + HO2_A ;
% 6.0E-13*EXP(230/T)       : OH_A + ClO_A = HCl_A + O2_A ;
% 2.6E-12*EXP(-1100/T)     : OH_A + Cl2_A = HOCl_A + Cl_A ;
% 3.0E-12*EXP(-500/T)      : OH_A + HOCl_A = H2O_A + ClO_A ;
% 2.6E-12*EXP(290/T)       : HO2_A + ClO_A = HOCl_A + O2_A ;
*                                                                    *;
```

```
* ------------------------------------------------------------------ *;
* DIFFUSION                                                          *;
* ------------------------------------------------------------------ *;
*                                                                    *;
% KD*(T/298)@(3/2)        : HO2_A = ;
% KD*MH2O2*(T/298)@(3/2)  : H2O2_A = ;
% KD*MacO2*(T/298)@(3/2)  : acO2_A = ;
% KD*Mac*(T/298)@(3/2)    : ac_A = ;
% KD*MCH3O2*(T/298)@(3/2) : CH3O2_A = ;
% KD*MacOH*(T/298)@(3/2)  : acOH_A = ;
% KD*MCH2O*(T/298)@(3/2)  : CH2O_A = ;
% KD*MO3*(T/298)@(3/2)    : O3_A = ;
*                                                                    *;
* ------------------------------------------------------------------ *;
* ------------------------------------------------------------------ *;
*                             UV SOURCE B                            *;
* ------------------------------------------------------------------ *;
* ------------------------------------------------------------------ *;
*                                                                    *;
* ------------------------------------------------------------------ *;
* SOURCE CHEMISTRY                                                   *;
* ------------------------------------------------------------------ *;
*                                                                    *;
* Methanol ;
* ------------------------------------------------------------------ *;
% 5.5D-11                  : Cl_B + CH3OH_B = CH2OH_B + HCl_B ;
% 9.1D-12                  : CH2OH_B + O2_B = HO2_B + CH2O_B ;
% 0.85*2.9E-12*EXP(-345/T) : OH_B + CH3OH_B = CH2OH_B + H2O_B ;
% 0.15*2.9E-12*EXP(-345/T) : OH_B + CH3OH_B = CH3O_B + H2O_B ;
*                                                                    *;
* Acetaldehyde ;
* ------------------------------------------------------------------ *;
% 8.0E-11                  : Cl_B + CH3CHO_B = ac_B + HCl_B ;
% 0.95*4.63E-12*EXP(350/T) : OH_B + CH3CHO_B = ac_B + H2O_B ;
% 0.05*4.63E-12*EXP(350/T) : OH_B + CH3CHO_B = CH2CHO_B + H2O_B ;
*                                                                    *;
*% K6T                     : ac_B + O2_B = acO2_B ;
*% K6B                     : ac_B + O2_B = OH_B ;
% (1-BR6-BR6H)*K6          : ac_B + O2_B = acO2_B ;
% BR6*K6                   : ac_B + O2_B = OH_B ;
% BR6H*K6                  : ac_B + O2_B = HO2_B ;
*                                                                    *;
* ------------------------------------------------------------------ *;
* acO2 RXNS                                                          *;
* ------------------------------------------------------------------ *;
*                                                                    *;
* HO2 + acO2 = OH + acO + O2 ;
* Assumed Instantaneous: acO = CH3 + CO2 ;
* ------------------------------------------------------------------ *;
% BR2A*K2_B      : HO2_B + acO2_B = OH_B + CH3_B + CO2_B + O2_B ;
% BR2A*K2_B      : HO2_B + acO2_B = acOOOH_B + O2_B ;
% BR2B*K2_B      : HO2_B + acO2_B = acOH_B + O3_B;
```

```
*                                                                              *;
* CH3O2 + acO2 = acO + CH3O + O2 ;
* Assumed Instantaneous: acO = CH3 + CO2 ;
* ---------------------------------------------------------------------- *;
*                                                                              *;
% K4*BR4A      : acO2_B + CH3O2_B = CH3_B + CO2_B + CH3O_B + O2_B ;
% K4*(1-BR4A)  : acO2_B + CH3O2_B = acOH_B + CH2O_B + O2_B ;
*                                                                              *;
* acO2 + acO2 = acO + acO + O2 ;
* Assumed Instantaneous: acO = CH3 + CO2 ;
* ---------------------------------------------------------------------- *;
*                                                                              *;
% K3 : acO2_B + acO2_B = CH3_B + CH3_B + CO2_B + CO2_B + O2_B ;
*                                                                              *;
* ---------------------------------------------------------------------- *;
* CH3O2 RXNS                                                             *;
* ---------------------------------------------------------------------- *;
*                                                                              *;
% K11                          : CH3_B + O2_B = CH3O2_B ;
% BR16A*9.5E-14*EXP(390/T)     : CH3O2_B + CH3O2_B = CH3O_B
+ CH3O_B + O2_B ;
% BR16B*9.5E-14*EXP(390/T)     : CH3O2_B + CH3O2_B = CH3OH_B
+ CH2O_B + O2_B ;
% 3.9E-14*EXP(-900/T)          : CH3O_B + O2_B = CH2O_B + HO2_B ;
% K33              : CH3O_B + CH3CHO_B = CH3OH_B + ac_B ;
*                                                                              *;
% (1-BR20)*3.8E-13*EXP(780/T) : HO2_B + CH3O2_B = CH3OOH_B + O2_B ;
% BR20*3.8E-13*EXP(780/T)     : HO2_B + CH3O2_B = CH2O_B
+ H2O_B + O2_B ;
*                                                                              *;
* ---------------------------------------------------------------------- *;
* HOx FORMATION, INTERCONVERSION AND REMOVAL                             *;
* ---------------------------------------------------------------------- *;
*                                                                              *;
% K1_B                      : HO2_B + HO2_B = H2O2_B + O2_B;
% Kc                        : HO2_B + CMPLX_B = ;
% Kcc                       : CMPLX_B + CMPLX_B = ;
*% KmF % KmR                 : HO2_B + CH3OH_B = CMPLX_B ;
% 4.8E-11*EXP(250/T)        : OH_B + HO2_B = H2O_B + O2_B ;
% 1.8E-12                   : OH_B + OH_B = H2O_B + O_B ;
% K19                       : OH_B + OH_B = H2O2_B ;
% 1.8E-12                   : OH_B + H2O2_B = H2O_B + HO2_B ;
% 5.5E-12*EXP(125/T)        : OH_B + CH2O_B = H2O_B + HCO_B ;
% 5.2E-12                   : HCO_B + O2_B = HO2_B + CO_B ;
% 1.8E-11*EXP(180/T)        : O_B + OH_B = O2_B + H_B ;
% 3.0E-11*EXP(200/T)        : O_B + HO2_B = O2_B + OH_B ;
% K7                        : H_B + O2_B = HO2_B ;
% 6.7E-15*EXP(600/T)        : HO2_B + CH2O_B = HMP_B ;
% 2.4E12*EXP(-7000/T)       : HMP_B = CH2O_B + HO2_B ;
% 0.5*5.6E-15*EXP(2300/T)   : HO2_B + HMP_B = HMPOOH_B + O2_B ;
% 0.3*5.6E-15*EXP(2300/T)   : HO2_B + HMP_B = HOCHO_B + H2O_B + O2_B ;
% 0.2*5.6E-15*EXP(2300/T)   : HO2_B + HMP_B = OH_B + HOCH2O_B + O2_B ;
```

```
% K17T                    : OH_B + CO_B = HOCO_B ;
% K17B                    : OH_B + CO_B = H_B + CO2_B ;
% 2E-12                   : HOCO_B + O2_B = HO2_B + CO2_B ;
% BR31A*K31               : OH_B + CH3O2_B = CH3O_B + HO2_B ;
% (1-BR31A)*K31           : OH_B + CH3O2_B = CH2O2_B + H2O_B ;
*% K31                     : OH_B + acO2_B = CH3_B + HO2_B + CO2_B;
% 1.7E-12*EXP(-940/T)     : OH_B + O3_B = HO2_B + O2_B ;
% 1.0E-14*EXP(-490/T)     : HO2_B + O3_B = OH_B + O2_B + O2_B ;
*                                                                    *;
* ------------------------------------------------------------------ *;
* ClOx FORMATION, INTERCONVERSION AND REMOVAL                        *;
* ------------------------------------------------------------------ *;
*                                                                    *;
% BR30A*K30               : Cl_B + CH3O2_B = CH3O_B + ClO_B ;
% (1-BR30A)*K30           : Cl_B + CH3O2_B = CH2O2_B + HCl_B ;
% 8.1E-11*EXP(-30/T)      : Cl_B + CH2O_B = HCl_B + HCO_B ;
% 7.4E-12*EXP(270/T)      : OH_B + ClO_B = Cl_B + HO2_B ;
% 6.0E-13*EXP(230/T)      : OH_B + ClO_B = HCl_B + O2_B ;
% 2.6E-12*EXP(-1100/T)    : OH_B + Cl2_B = HOCl_B + Cl_B ;
% 3.0E-12*EXP(-500/T)     : OH_B + HOCl_B = H2O_B + ClO_B ;
% 2.6E-12*EXP(290/T)      : HO2_B + ClO_B = HOCl_B + O2_B ;
*                                                                    *;
* ------------------------------------------------------------------ *;
* DIFFUSION                                                          *;
* ------------------------------------------------------------------ *;
*                                                                    *;
% KD*(T/298)@(3/2)        : HO2_B = ;
% KD*MH2O2*(T/298)@(3/2)  : H2O2_B = ;
% KD*MacO2*(T/298)@(3/2)  : acO2_B = ;
% KD*Mac*(T/298)@(3/2)    : ac_B = ;
% KD*MCH3O2*(T/298)@(3/2) : CH3O2_B = ;
% KD*MacOH*(T/298)@(3/2)  : acOH_B = ;
% KD*MCH2O*(T/298)@(3/2)  : CH2O_B = ;
% KD*MO3*(T/298)@(3/2)    : O3_B = ;
*                                                                    *;
**;
*                                                                    *;
* ****************************************************************** *;
* ***** END OF BLOCK - COMPILE EQUATIONS                             *;
* ****************************************************************** *;
*                                                                    *;
* ****************************************************************** *;
* ***** PRINT STREAMS                                               *;
* ****************************************************************** *;
*                                                                    *;
SETPSTREAM 1 10 ;
TIME IR_HO2_C UV_A OH_C UV_B ;
**;
* Setup Residuals Output ;
SETPSTREAM 2 9 ;
**;
```

```
* Setup Fitted Params Output ;
SETPSTREAM 8 3 ;
K3 ;
**;

DATA ;
TIME IR_HO2_C UV_A UV_B ;
RANGE  1000 0.1 0.1;
STANDERROR 2 1.1E-3 1.1E-3;
INPUT 11 ;
SETVARY K2 BR2B K1_UV ClI K2_UV K1;

BEGIN ;
COMPILE INSTANT ;
PSTREAM 8 ;
#COUNT=0 ;
**;
*                                                                          *;
COMPILE PRINT ;
* Output routine called during the final phase ;
#COUNT=#COUNT+1 ;
DO 10 FOR #2=#COUNT-1 ;
WRITE 1=10, ((E14,6))TIME, IR_HO2_C, UV_A, OH_C, UV_B ;
LABEL 10 ;
**;
*                                                                          *;
SETNOFIT ;
WHENEVER TIME = TOBS % CALL PRINT ;
*WHENEVER TIME = 0 + .0000002*50000 % CALL PRINT ;
**;
*                                                                          *;
* ************************************************************************ *;
* ***** START SIMULATION                                                  *;
* ************************************************************************ *;
*                                                                          *;
BEGIN ;
*                                                                          *;
* ************************************************************************ *;
* ***** EXIT                                                              *;
* ************************************************************************ *;
*                                                                          *;
STOP ;
*;
```

References

[1] Atkinson, R.; Baulch, D. L.; Cox, R. A.; Hampson, R. F.; Kerr, J. A.; Troe, J. Evaluated Kinetic and Photochemical Data for Atmospheric Chemistry: Supplement IV. IUPAC Subcommittee on Gas Kinetic Data Evaluation for Atmospheric Chemistry. *Journal of Physical and Chemical Reference Data* **1992**, *21*, 1125–1568.

[2] Tan, D.; Faloona, I.; Simpas, J. B.; Brune, W.; Shepson, P. B.; Couch, T. L.; Sumner, A. L.; Carroll, M. A.; Thornberry, T.; Apel, E.; Riemer, D.; Stockwell, W. HO x Budgets in a Deciduous Forest: Results from the PROPHET Summer 1998 Campaign. *Journal of Geophysical Research: Atmospheres* **2001**, *106*, 24407–24427.

[3] Hofzumahaus, A. et al. Amplified Trace Gas Removal in the Troposphere. *Science* **2009**, *324*, 1702–1704.

[4] Lu, K. D. et al. Observation and Modelling of OH and HO_2 Concentrations in the Pearl River Delta 2006: A Missing OH Source in a VOC Rich Atmosphere. *Atmospheric Chemistry and Physics* **2012**, *12*, 1541–1569.

[5] Lou, S. et al. Atmospheric OH Reactivities in the Pearl River Delta – China in Summer 2006: Measurement and Model Results. *Atmos. Chem. Phys.* **2010**, *10*, 11243–11260.

[6] Whalley, L. K.; Edwards, P. M.; Furneaux, K. L.; Goddard, A.; Ingham, T.; Evans, M. J.; Stone, D.; Hopkins, J. R.; Jones, C. E.; Karunaharan, A.; Lee, J. D.; Lewis, A. C.; Monks, P. S.; Moller, S. J.; Heard, D. E. Quantifying the Magnitude of a Missing Hydroxyl Radical Source in a Tropical Rainforest. *Atmospheric Chemistry and Physics* **2011**, *11*, 7223–7233.

[7] Hasson, A. S.; Tyndall, G. S.; Orlando, J. J. A Product Yield Study of the Reaction of HO2 Radicals with Ethyl Peroxy (C2H5O2), Acetyl Peroxy (CH3C(O)O2), and Acetonyl Peroxy (CH3C(O)CH2O2) Radicals. *The Journal of Physical Chemistry A* **2004**, *108*, 5979–5989.

[8] Niki, H.; Maker, P. D.; Savage, C. M.; Breitenbach, L. P. FTIR Study of the Kinetics and Mechanism for Chlorine-Atom-Initiated Reactions of Acetaldehyde. *The Journal of Physical Chemistry* **1985**, *89*, 588–591.

[9] Horie, O.; Moortgat, G. K. Reactions of CH3C(O)O2 Radicals with CH3O2 and HO2 between 263 and 333 K. A Product Study. *Journal of the Chemical Society, Faraday Transactions* **1992**, *88*, 3305–3312.

[10] Hasson, A. S.; Kuwata, K. T.; Arroyo, M. C.; Petersen, E. B. Theoretical Studies of the Reaction of Hydroperoxy Radicals (HO2) with Ethyl Peroxy (CH3CH2O2), Acetyl Peroxy (CH3C(O)O2), and Acetonyl Peroxy (CH3C(O)CH2O2) Radicals. *Journal of Photochemistry and Photobiology A: Chemistry* **2005**, *176*, 218–230.

[11] Le Crâne, J.-P.; Rayez, M.-T.; Rayez, J.-C.; Villenave, E. A Reinvestigation of the Kinetics and the Mechanism of the CH3C(O)O2 + HO2 Reaction Using Both Experimental and Theoretical Approaches. *Physical Chemistry Chemical Physics* **2006**, *8*, 2163–2171.

[12] Jenkin, M. E.; Hurley, M. D.; Wallington, T. J. Investigation of the Radical Product Channel of the CH3C(O)O2 + HO2 Reaction in the Gas Phase. *Physical Chemistry Chemical Physics* **2007**, *9*, 3149–3162.

[13] Dillon, T. J.; Crowley, J. N. Direct Detection of OH Formation in the Reactions of HO2 with CH3C(O)O2 and Other Substituted Peroxy Radicals. *Atmospheric Chemistry and Physics* **2008**, *8*, 4877–4889.

[14] Groß, C. B. M.; Dillon, T. J.; Schuster, G.; Lelieveld, J.; Crowley, J. N. Direct Kinetic Study of OH and O3 Formation in the Reaction of CH3C(O)O2 with HO2. *The Journal of Physical Chemistry A* **2014**, *118*, 974–985.

[15] Winiberg, F. A. F.; Dillon, T. J.; Orr, S. C.; Groß, C. B. M.; Bejan, I.; Brumby, C. A.; Evans, M. J.; Smith, S. C.; Heard, D. E.; Seakins, P. W. Direct Measurements of OH and Other Product Yields from the HO2 + CH3C(O)O2 Reaction. *Atmos. Chem. Phys.* **2016**, *16*, 4023–4042.

[16] Moortgat, G.; Veyret, B.; Lesclaux, R. Absorption Spectrum and Kinetics of Reactions of the Acetylperoxy Radical. **1989**, *93*, 2362–2368.

[17] Crawford, M. A.; Wallington, T. J.; Szente, J. J.; Maricq, M. M.; Francisco, J. S. Kinetics and Mechanism of the Acetylperoxy + HO2 Reaction. *The Journal of Physical Chemistry A* **1999**, *103*, 365–378.

[18] Tomas, A.; Villenave, E.; Lesclaux, R. Reactions of the HO2 Radical with CH3CHO and CH3C(O)O2 in the Gas Phase. *The Journal of Physical Chemistry A* **2001**, *105*, 3505–3514.

[19] Christensen, L. E.; Okumura, M.; Hansen, J. C.; Sander, S. P.; Francisco, J. S. Experimental and Ab Initio Study of the HO2CH3OH Complex: Thermodynamics and Kinetics of Formation. *J. Phys. Chem. A* **2006**, *110*, 6948–6959.

[20] Andersson, B. Y.; Cox, R. A.; Jenkin, M. E. The Effect of Methanol on the Self Reaction of HO2 Radicals. *International Journal of Chemical Kinetics* **1988**, *20*, 283–295.

[21] Bloss, W. J.; Rowley, D. M.; Cox, R. A.; Jones, R. L. Rate Coefficient for the BrO + HO2 Reaction at 298 K. *Physical Chemistry Chemical Physics* **2002**, *4*, 3639–3647.

[22] Christensen, L. E.; Okumura, M.; Sander, S. P.; Friedl, R. R.; Miller, C. E.; Sloan, J. J. Measurements of the Rate Constant of HO2 + NO2 + N2 $\rightarrow$ HO2NO2 + N2 Using Near-Infrared Wavelength-Modulation Spectroscopy and UV-Visible Absorption Spectroscopy. *The Journal of Physical Chemistry A* **2004**, *108*, 80–91.

[23] Noell, A. C.; Alconcel, L. S.; Robichaud, D. J.; Okumura, M.; Sander, S. P. Near-Infrared Kinetic Spectroscopy of the HO2 and C2H5O2 Self-Reactions and Cross Reactions. *The Journal of Physical Chemistry A* **2010**, *114*, 6983–6995.

[24] Grieman, F. J.; Noell, A. C.; Davis-Van Atta, C.; Okumura, M.; Sander, S. P. Determination of Equilibrium Constants for the Reaction Between Acetone and HO2 Using Infrared Kinetic Spectroscopy. *The Journal of Physical Chemistry A* **2011**, *115*, 10527–10538.

[25] Keller-Rudek, H.; Moortgat, G. K.; Sander, R.; Sörensen, R. The MPI-Mainz UV/VIS Spectral Atlas of Gaseous Molecules of Atmospheric Interest. *Earth System Science Data* **2013**, *5*, 365–373.

[26] Sander, S. P.; Abbat, J.; Barker, J.R.; Burkholder, J.B.; Huie, R.E.; Kolb, C.E.; Kurylo, M.J.; Wilmouth, D.M.; Orkin, V.L.; Wine, P.H. *Chemical Kinetics and Photochemical Data for Use in Atmospheric Studies, Evaluation No. 18*; Jet Propulsion Laboratory, Pasadena: JPL Publication 15-10, 2015.

[27] Tyndall, G. S.; Cox, R. A.; Granier, C.; Lesclaux, R.; Moortgat, G. K.; Pilling, M. J.; Ravishankara, A. R.; Wallington, T. J. Atmospheric Chemistry of Small Organic Peroxy Radicals. *Journal of Geophysical Research: Atmospheres* **2001**, *106*, 12157–12182.

[28] Fradet, M.; Hosoda, T.; Frez, C.; Shterengas, L.; Sander, S.; Forouhar, S.; Belenky, G. In *Novel In-Plane Semiconductor Lasers XV*, Novel In-Plane Semiconductor Lasers XV, International Society for Optics and Photonics: 2016; Vol. 9767, 97670U.

[29] *FACSIMILE* version 4.1.41 [computer software]; Faringdon, Oxon, UK, 2003.

[30] HITRAN on the Web. `http://hitran.org/`.

[31] Hui, A. O.; Okumura, M.; Sander, S. P. Temperature and Pressure Dependence Studies of the OH and HO2 Yields from the CH3C(O) + O2 Reaction., Manuscript in preparation, Manuscript in preparation, 2018.

[32] Hui, A. O.; Okumura, M.; Sander, S. P. Temperature Dependence of the Reaction of Chlorine Atoms with CH3OH and CH3CHO., Manuscript submitted for publication, Manuscript submitted for publication, 2018.

[33] Roehl, C. M.; Bauer, D.; Moortgat, G. K. Absorption Spectrum and Kinetics of the Acetylperoxy Radical. *The Journal of Physical Chemistry* **1996**, *100*, 4038–4047.

[34] Maricq, M. M.; Szente, J. J. The CH3C(O)O2 Radical. Its UV Spectrum, Self-Reaction Kinetics, and Reaction with CH3O2. *The Journal of Physical Chemistry* **1996**, *100*, 4507–4513.

[35] Villenave, E.; Lesclaux, R. Kinetics of the Cross Reactions of CH3O2 and C2H5O2 Radicals with Selected Peroxy Radicals.

[36] Clegg, S. M.; Abbatt, J. P. D. Oxidation of SO2 by H2O2 on Ice Surfaces at 228 K: A Sink for SO2 in Ice Clouds. *Atmos. Chem. Phys.* **2001**, *1*, 73–78.

[37] Christensen, L. E.; Okumura, M.; Sander, S. P.; Salawitch, R. J.; Toon, G. C.; Sen, B.; Blavier, J.-F.; Jucks, K. W. Kinetics of HO2 + HO2 $\rightarrow$ H2O2 + O2: Implications for Stratospheric H2O2. *Geophysical Research Letters* **2002**, *29*, 13–1.

[38] Da Silva, G.; Bozzelli, J. W. Role of the -Hydroxyethylperoxy Radical in the Reactions of Acetaldehyde and Vinyl Alcohol with HO2. *Chemical Physics Letters* **2009**, *483*, 25–29.

[39] Hui, A. O.; Okumura, M.; Sander, S. P. Rate Enhancement of the \ce{HO2} Self Reaction by Hydrogen-Bonded Adducts of \ce{HO2} with \ce{CH3OH} and with \ce{CH3CHO}., Manuscript in preparation, Manuscript in preparation, 2018.

[40] Atkinson, R.; Baulch, D. L.; Cox, R. A.; Crowley, J. N.; Hampson, R. F.; Hynes, R. G.; Jenkin, M. E.; Rossi, M. J.; Troe, J.; IUPAC Subcommittee Evaluated Kinetic and Photochemical Data for Atmospheric Chemistry: Volume II – Gas Phase Reactions of Organic Species. *Atmos. Chem. Phys.* **2006**, *6*, 3625–4055.

[41] Noell, A. C. Laboratory Studies of the Self and Cross Reactions of Atmospheric Peroxy Radicals., Ph.D. Pasadena, CA: California Institute of Technology, 2009.

Chapter 5

TEMPERATURE AND PRESSURE DEPENDENCE STUDIES OF THE OH AND HO_2 YIELDS FROM THE $CH_3C(O) + O_2$ REACTION

Abstract

The pressure dependence of the yields of OH and HO_2 from the $CH_3C(O) + O_2$ reaction (R1) have been measured at room temperature over the range P = 51.1 - 230 Torr using N_2 as the bath gas. The temperature dependence has also been investigated at 100 Torr in N_2 over the range T = 228.8 - 295.2 K. OH and HO_2 radicals were directly monitored in real time using 2f heterodyne IR wavelength modulation spectroscopy (WMS). The yield of OH (α_{1a}) was found to have a weak, positive temperature dependence consistent with results from previous temperature dependence studies; however, the measured values of α_{1a} were a factor of 4 - 10 times smaller than those in the literature. This work also reports the first measurements of the HO_2 yield (α_{1b}). α_{1b} was found to be temperature-independent, suggesting that hot chemistry may be responsible for the observed HO_2 signals. R1 appeared to be near the high-pressure limit over the range P = 51.1 - 230 Torr, with only a small change in the yields. The OH and HO_2 yields at 51.1 Torr were $\alpha_{1a} = 0.049 \pm 0.009$ and $\alpha_{1b} = 0.014 \pm 0.002$, respectively. At 230 Torr, the yields were $\alpha_{1a} = 0.010 \pm 0.004$ and $\alpha_{1b} = 0.0083 \pm 0.002$.

5.1 Introduction

The acetyl radical (CH_3CO) is an important intermediate in the atmospheric photo-oxidation of carbonyl compounds such as acetone ($CH_3C(O)CH_3$) and acetaldehyde (CH_3CHO). In the atmosphere, $CH_3C(O)$ predominantly reacts with O_2 via a chemically activated reaction mechanism forming the activated acetylperoxy radical ($CH_3C(O)O_2^*$), as shown in Scheme 5.1. Once formed, $CH_3C(O)O_2^*$ can decompose back to the reactants or proceed to products either through a termolecular (i.e., pressure-dependent) pathway, forming the collisionally stabilized $CH_3C(O)O_2$ radical, or through one of two possible pressure-independent decomposition pathways forming either the hydroxy (OH) or the hydroperoxy (HO_2) radical.

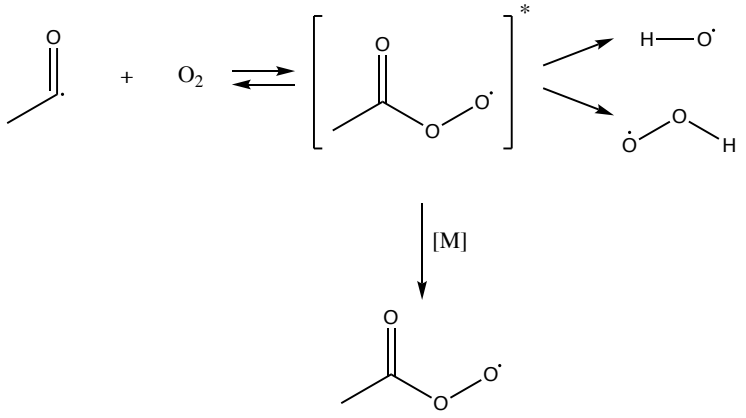

Scheme 5.1

Simplifying Scheme 5.1, the reaction of CH_3CO with O_2 can be written as

$$CH_3C(O) + O_2 \longrightarrow OH + \text{product} \quad \text{(R1a)}$$

$$\longrightarrow HO_2 + \text{product} \quad \text{(R1b)}$$

$$CH_3C(O) + O_2 + M \longrightarrow CH_3C(O)O_2 + M, \quad \text{(R1c)}$$

where the phenomenological rate constants of all three product channels exhibit bimolecular and termolecular behavior that depend on both temperature and pressure. The overall rate constant for R1, k_1, can then be expressed as the sum of three pressure-dependent, second-order rate constants (Equation 5.1).

$$k_1 = k_{1a} + k_{1b} + k_{1c} \quad (5.1)$$

The fraction of R1 that forms OH (α_{1a}) and HO_2 (α_{1b}) is defined by Equation 5.2 and Equation 5.3, respectively:

$$\alpha_{1a} = \frac{k_{1a}}{k_1} \quad (5.2)$$

$$\alpha_{1b} = \frac{k_{1b}}{k_1} \quad (5.3)$$

Numerous studies have investigated the kinetics of R1 [1–8], and the phenomenologicical rate constants were derived from the observation of the loss of the reactant (CH_3CO) and/or formation of the products (OH, HO_2, and $CH_3C(O)O_2$). There are still large disagreements between the reported pressure dependence of the OH product channel. There has been one experimental evidence of R1b based on the observation of ketene (CH_2CO) [9], the predicted co-product of HO_2 [6]; however, there are currently no studies in the literature that have directly detected HO_2 from

R1.

This work directly detected OH and HO_2 in real time using Infrared Kinetics and Spectroscopy (IRKS). IRKS employs MIR and NIR wavelength modulation spectroscopy (WMS), a high-resolution heterodyne detection technique, to selectively detect OH and HO_2 radicals, respectively. Radicals were generated by pulsed laser photolysis and time-resolved measurements of OH and HO_2 were recorded. The OH and HO_2 yields (α_{1a} and α_{1b}, respectively) were determined using pseudo-first order kinetics. In this study, we measured α_{1a} and α_{1b} over the temperature range T = 228.2 - 295.2 K at 100 Torr in N_2. The pressure dependences of α_{1a} and α_{1b} were also investigated for pressures in the range P = 49.8 - 230 Torr (N_2 buffer gas) at room temperature (T = 295.2 K).

The last section of this chapter also describes the work carried out to determine the rate constant of the $CH_3C(O)O_2$ self reaction (R2), k_2.

$$CH_3C(O)O_2 + CH_3C(O)O_2 \longrightarrow 2\,CH_3C(O)O + 2\,O_2 \qquad \text{(R2)}$$

Since IRKS enables simultaneous detection in the IR and UV, all three optical probes (NIR, MIR, and UV) were used to constrain the kinetics parameters. In addition to the NIR and MIR time profiles, we obtained time-resolved measurements in the UV at two wavelengths λ = 225 nm and λ = 250 nm to detect $CH_3C(O)O_2$. However, spectral interference by other peroxy radicals and complex secondary chemistry precluded the determination of unique solutions to k_2. Thus, the data presented here serve as preliminary work for future studies to fully characterize R2.

5.2 Experimental Methods

Experiments were carried out using the Infrared Kinetics Spectroscopy (IRKS) apparatus, which is described in detail in Chapter 2. Pulsed laser photolysis was used to generate CH_3CO radicals in a jacketed, Pyrex flow cell containing gas mixtures of $Cl_2/CH_3CHO/O_2/N_2$. For the temperature dependence studies, liquid nitrogen-cooled methanol was circulated through the jacket of the Pyrex flow cell to control the temperature. OH and HO_2 radicals were monitored temporally using 2f-heterodyne MIR and NIR WMS, respectively. The 2f signals were converted to absolute concentrations by calibrating against the UV absorption cross-section of HO_2 at λ = 225 nm ($\sigma_{HO_2} = 2.88 \times 10^{-18}$ cm^2 molecule^{-1}). The MIR and NIR signals were calibrated daily at the beginning of each experiment. Details on the calibration are provided in Chapter 2. For the pressure dependence studies, calibration was also performed at every pressure. More details on the pressure

dependence of the calibrations are provided later.

5.2.1 Radical generation

351 nm light from a XeF excimer laser (Compex 301) operating in the constant energy mode was directed coaxially through the flow cell to initiate the chemistry by photolyzing Cl_2 molecules to form Cl atoms. CH_3CO was generated with nearly unity yield from the reaction of CH_3CHO with Cl atoms:

$$Cl_2 + h\nu \longrightarrow 2\,Cl \tag{R3}$$

$$Cl + CH_3CHO \longrightarrow CH_3CO + HCl \tag{R4}$$

Reagent gases were pre-mixed and pre-cooled in a Pyrex manifold prior to entering the cell. Room temperature N_2 purge gas flowed from the aluminum chambers on either ends of the cell towards the gas pump-out ports to confine the main gas flow to the temperature controlled region. The purge flow also served to protect the Herriott mirrors that formed the multi-pass optical cavity for the IR probes. The gas flows were regulated by mass flow controllers (MKS Instruments). For a given pressure, the total flow rate was adjusted to maintain a 10 s residence time inside the flow cell; e.g., for a total pressure of 100 ± 2 Torr, the total flow rate was approximately 2000 cm^3 (STP) min^{-1}. A photolysis repetition rate of 0.2 Hz was used, resulting in two photolysis events occurring per residence time. It was verified that decreasing the photolysis rate to 0.1 Hz made no difference in the kinetics traces.

CH_3CHO was introduced into the cell by flowing N_2 through a glass bubbler containing the liquid compound, held at T = 0 °C inside temperature-controlled baths. The pressures in the main reaction cell and the bubbler were measured by absolute capacitance pressure gauges (MKS Baratron) and the concentration of CH_3CHO vapor was determined manometrically. All experiments were conducted in excess amounts of O_2 and CH_3CHO relative to the initial radical concentrations, such that all the Cl atoms generated from photolysis were assumed to form CH_3CO via R4. Typical concentrations of the reagents were: $[CH_3CHO] = (0.86 - 4.5) \times 10^{15}$ molecule cm^{-3}, $[O_2] = (0.74 - 2.5) \times 10^{18}$ molecule cm^{-3}, and $[Cl_2] = (2.4 - 3.8) \times 10^{15}$ molecule cm^{-3}. The total radical concentration, $[Cl]_0$, was in the range $(5.3 - 18) \times 10^{13}$ molecule cm^{-3} (determined from the HO_2 self reaction, as described in Section 5.2.3.1).

5.2.2 UV probe

Broadband UV light was provided by a laser-driven light source (Energetiq EQ-99XFC). The collimated UV beam was coaligned with and counter-propagated the excimer beam, making a single pass through the cell. A monochromator (Acton Research Corporation Spectra Pro-300i) placed in front of a photomultiplier tube (PMT) was used for wavelength-specific detection of the transmitted UV light. Baffles were placed on both ends of the flow cell to ensure that only light that sampled the photolysis volume entered the monochromator.

As mentioned previously, the NIR and MIR signals were calibrated against the UV absorption cross-section of HO_2. For the determination of α_{1a} and α_{1b}, the UV probe was only used for the determination of $[Cl]_0$ and for the calibration of the NIR signal, which in turn was used to calibrate the MIR signal. The last section of this chapter describes the preliminary work on the $CH_3C(O)O_2$ self reaction, where the time-resolved UV absorbance was used in the data analysis.

5.2.3 NIR and MIR probes

Two continuous-wave (CW) distributed feedback (DFB) lasers operating in the NIR (3 mW) and MIR (6 mW) were used for selective detection of HO_2 and OH radicals, respectively. The NIR laser probed the first overtone of the OH stretch of HO_2 ($2\nu_1$: 6638.2 cm^{-1}) and MIR laser monitored OH radicals by probing the fundamental vibrational transition ($\nu_1, P(3.5)f$: 3407.6 cm^{-1}). Back-to-back experiments were carried out, using flip mirrors to switch between the two IR probes. Much care was taken to ensure that the experimental conditions were identical between the data collected with the two lasers. Both the NIR and MIR beams were focused, collimated, and spatially filtered prior to entering the cell. Protected gold Herriott mirrors placed on either ends of the cell folded the optical paths of the IR beams, enabling 30 passes inside the cell to amplify the path length to approximately 2700 cm. InGaAs (New Focus 1811) and InSb (Infrared Associates IS-0.25) photodiode detectors were used to detect the transmitted NIR and MIR light, respectively.

Both IR lasers were wavelength modulated at 6.8 MHz by using an external function generator to modulate the injection current. 2f-heterodyne detection was implemented by demodulating the detected signal at twice the modulation frequency (13.6 MHz). The demodulated signal was amplified by a factor of 200 and low-pass filtered at 1 MHz. The noise-equivalent concentrations for the HO_2 and OH lasers normalized to one excimer shot was 2.9×10^9 molecule/$cm^3 \cdot Hz^{-1/2}$ and 5.0×10^8

molecule/cm^3·Hz$^{-1/2}$, respectively. For a typical experimental run, the HO_2 and OH signals were collected at sampling rate of 2.5 MHz and averaged for 50 and 75 excimer laser shots, respectively.

Since WMS only measures the relative changes in concentration, both the NIR and MIR lasers required daily calibration to obtain absolute concentrations from the 2f signals. The calibration runs were also used to determine the total radical concentrations, $[Cl]_0$. More details on the calibration methods are provided in Chapter 2. The HO_2 and OH lines probed by the NIR and MIR lasers, respectively, are also pressure-broadened. Thus, for the pressure dependence experiments, both lasers were also calibrated at every pressure.

5.2.3.1 Pressure dependence of NIR calibration

The NIR laser was calibrated against UV absorption at λ = 225 nm by measuring the NIR and UV decay signals simultaneously when HO_2 was the only peroxy radical present; i.e., $[CH_3CHO] = 0$. HO_2 radicals were generated by replacing CH_3CHO with CH_3OH in the reagent gas mixture. CH_3OH vapor was introduced into the cell in the same method as for CH_3CHO; i.e., dry N_2 gas was bubbled though the liquid compound that was held at a constant temperature ($T_{bubbler}$ = 0 °C). All of the calibration runs were performed at room temperature, where the HO_2 kinetics are described by diffusion (unimolecular diffusion rate constant: $k_D \sim 22.2$ s^{-1}) and by known reactions with no rate enhancement by CH_3OH (Chapter 3).

In the absence of CH_3CHO, all of the Cl atoms generated from photolysis are converted to HO_2 via the R5 and R6:

$$Cl + CH_3OH \longrightarrow CH_2OH + HCl \quad \text{(R5)}$$

$$CH_2OH + O_2 \longrightarrow HO_2 + CH_2O \quad \text{(R6)}$$

Despite a different geometric overlap due to the off-axis orientation of the Herriott mirrors, the IR and UV probe beams should capture the same physical processes at relatively short timescales (< 20 ms); i.e., before diffusion becomes a significant loss process.

The 2f signal of the NIR laser was converted to absolute HO_2 concentrations by simultaneously fitting both the IR and UV traces with a bimolecular decay using a non-linear least-squares algorithm (Levenberg-Marquardt) provided by the kinetics modeling program, FACSIMILE [10]. The fits were performed to optimize the calibration factor, V_{M,HO_2}, and $[Cl]_0$. V_{M,HO_2} relates the NIR signal in mV, S_{NIR}, to

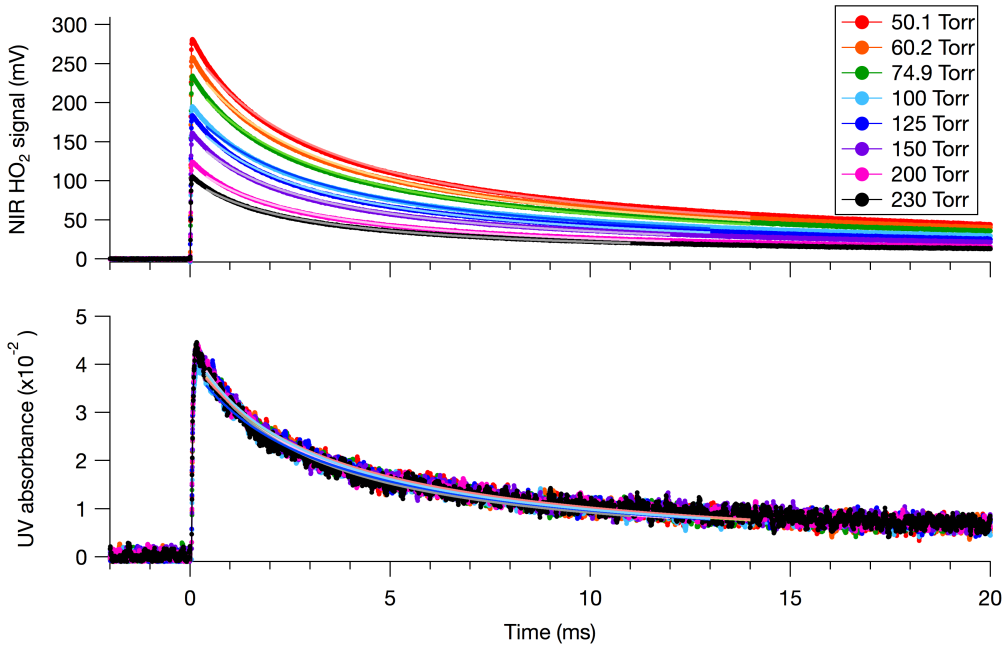

(a) Time profiles obtained in the NIR HO_2 (top) and in the UV at λ = 225 nm (bottom) from the HO_2 self reaction at various pressures. The lighter colored lines are the fits to the data. Concentrations: $[Cl_2] = 4.5 \times 10^{15}$ molecule cm^{-3}; $[HO_2]_0 = 7.9 \times 10^{13}$ molecule cm^{-3}; $[CH_3OH] = 4.0 \times 10^{15}$ molecule cm^{-3}.

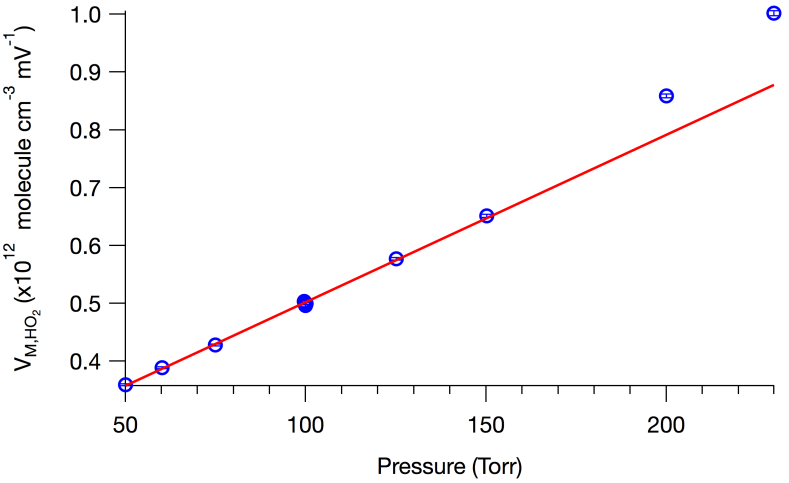

(b) Fitted values of V_{M,HO_2} versus pressure. Note that the linear fit is only shown to demonstrate the deviation from linearity at higher pressure and was not used to calculate V_{MHO_2} at each pressure.

Figure 5.1: Calibration of the NIR laser with $HO_2 + HO_2$: (a) time-dependent NIR and UV (λ = 225 nm) signals at various pressures and (b) fitted values of V_{M,HO_2} plotted as a function of pressure.

the HO_2 concentration, $[HO_2]$:

$$[HO_2] = V_{M,HO_2} \times S_{NIR} \tag{5.4}$$

Figure 5.1(a) shows the NIR signals from the HO_2 self-reaction that were collected at various pressures using the same $[Cl]_0$. Increasing the pressure led to a decrease in the NIR signal due to pressure broadening of the HO_2 lines. The corresponding UV signals (λ = 225 nm), on the other hand, were identical across all pressures; thus, larger values of V_{M,HO_2} were obtained at higher pressures. Calibration at each pressure was necessary because V_{M,HO_2} was not perfectly linear with pressure. Figure 5.1(b) demonstrates that V_{M,HO_2} exhibits a relatively linear dependence on the total pressure for pressures up to P ~150 Torr, above which V_{M,HO_2} begins to deviate from linearity. Thus, the directly measured values of V_{M,HO_2} at each pressure were ultimately used in the data analysis.

5.2.3.2 Pressure dependence of MIR calibration

The MIR laser was calibrated by titrating HO_2 with NO and measuring the kinetics traces of HO_2 and OH from the reaction of HO_2 + NO, which generates OH with unity yield (R7) [11].

$$HO_2 + NO \longrightarrow OH + NO_2 \qquad \text{(R7)}$$

The MIR calibration runs were performed immediately after the NIR calibration runs. Back-to-back experiments were carried out using the NIR and MIR lasers to obtain the HO_2 and OH kinetics traces, respectively, from R7 at each pressure. Excess amounts of NO and CH_3OH were used, such that the primary loss processes of OH were reaction with NO and CH_3OH. Typical concentrations of NO and CH_3OH were [NO] $\sim 1 \times 10^{15}$ molecule cm^{-3} and [CH_3OH] $\sim 5 \times 10^{15}$ molecule cm^{-3}.

Since the rate constant of the HO_2 + NO reaction is known (k_7(298 K) = 8.0×10^{-12} cm^3 molecule^{-1} s^{-1} [11]) and the major loss processes of OH are well-characterized, the absolute OH concentration could be determined from the formation and subsequent decay of the OH signal provided that the initial radical concentrations are known. $[Cl]_0$ was assumed to be the same as the HO_2 calibration runs since the same Cl_2 concentrations and excimer power were used. Loss of OH by reaction with NO and with CH_3OH was rapid (OH lifetime ~700 μs); thus, in order to accurately capture the OH formation kinetics, only the two lowest initial radical concentrations ($[Cl]_0 \sim (5-7) \times 10^{13}$ molecule cm^{-3}) were used.

Figure 5.2(a) shows that for a fixed $[Cl]_0$, the MIR OH signals from the reaction of HO_2 + NO decrease with increasing pressures, as was seen for the NIR HO_2 signals from the HO_2 self reaction. The 2f signal of the MIR laser was calibrated by

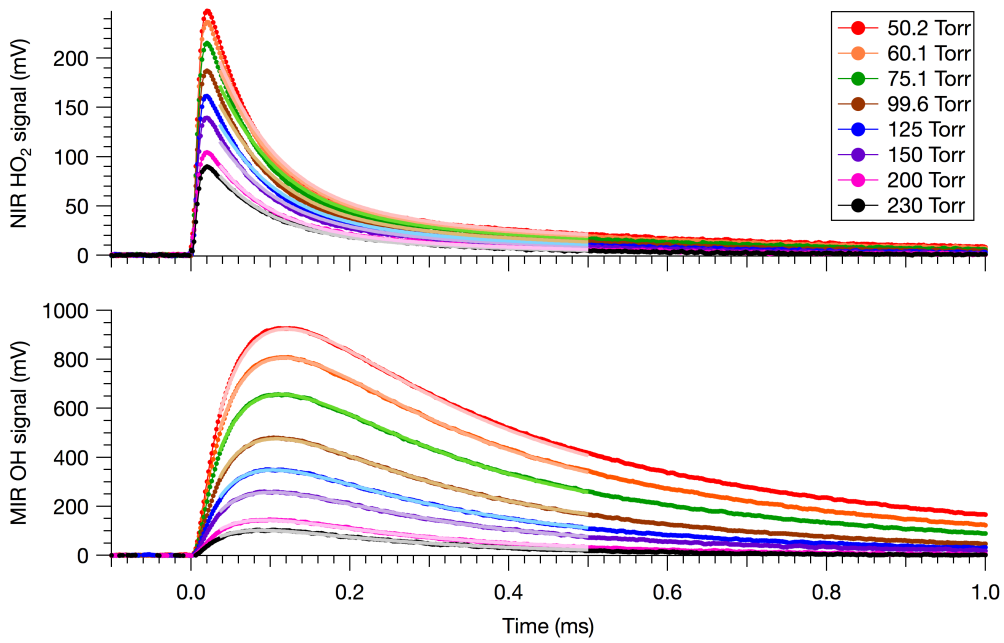

(a) Time profiles of the MIR OH (top) and NIR HO_2 (bottom) signals obtained from the HO_2 + NO reaction at various pressures. Lighter colored lines are the fits to the data. Concentrations: $[Cl_2] = 4.5 \times 10^{15}$ molecule cm^{-3}; $[HO_2]_0 = 7.9 \times 10^{13}$ molecule cm^{-3}; $[CH_3OH] = 4.0 \times 10^{15}$ molecule cm^{-3}; $[NO] = 1.2 \times 10^{15}$ molecule cm^{-3}.

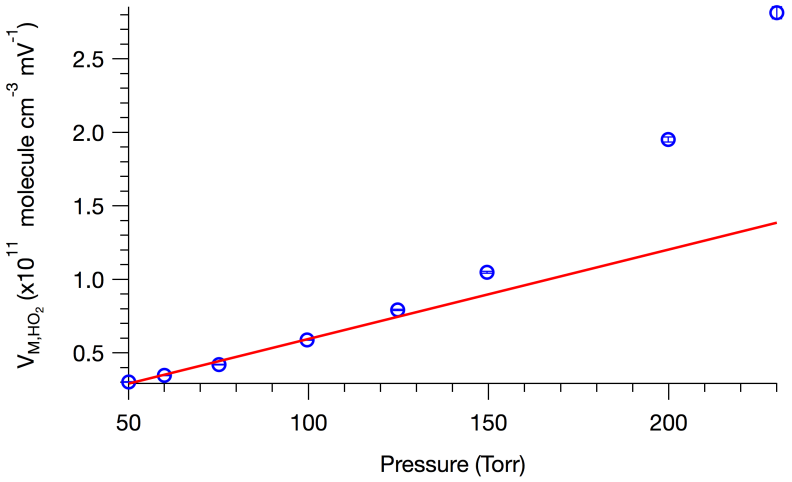

(b) Fitted values of $V_{M,OH}$ versus pressure. Note that the linear fit is only shown to demonstrate the deviation from linearity at higher pressure and was not used to calculate V_{MOH} at each pressure.

Figure 5.2: Calibration of the MIR laser with HO_2 + NO: (a) time-dependent MIR and NIR signals at various pressures and (b) fitted values of $V_{M,OH}$ plotted as a function of pressure.

simultaneously fitting the HO_2 and OH kinetics traces with a kinetics model using FACSIMILE. The calibration factor, $V_{M,OH}$, converts the MIR signal in mV, S_{MIR},

to absolute OH concentrations, [OH]:

$$[OH] = V_{M,OH} \times S_{MIR} \tag{5.5}$$

In the fits, $V_{M,OH}$ was optimized and $[Cl]_0$ was fixed to the fitted value determined from the NIR HO_2 self reaction calibration runs. The fitted values of $V_{M,OH}$ appear to be linear in pressure for pressures up to P ~125 Torr, above which $V_{M,OH}$ starts to deviate from linearity (Figure 5.2(b)). Therefore, as for the case with V_{M,HO_2}, the directly measured values of $V_{M,OH}$ at each pressure were used in the data analysis.

5.3 Results

OH and HO_2 formed via R1a and R1b, respectively, were monitored as a function of time at each temperature for a variety of initial radical and CH_3CHO concentrations. In some cases, the O_2 concentration was also varied. All experiments were performed using excess amounts of O_2 and CH_3CHO relative to $[Cl]_0$, such that the pseudo-first order approximation could be applied for R1 and R4. Furthermore, $[O_2] \gg [CH_3CHO]$, such that the rate-limiting step for OH and HO_2 formation was R4. For typical concentrations of $[CH_3CHO] = 1 \times 10^{15}$ molecule cm^{-3} and $[O_2] = 2 \times 10^{18}$ molecule cm^{-3}, the pseudo-first order rates at room temperature were:

$$k_1^{'} = k_1[O_2] \qquad \sim 5 \times 10^6 \text{ s}^{-1} \tag{5.6}$$

$$k_4^{'} = k_4[CH_3CHO] \qquad \sim 2 \times 10^4 \text{ s}^{-1} \tag{5.7}$$

where k_1 and k_4 are the rate constants of R1 and R4, respectively, with values of $k_1(298\text{ K}) = 5.1 \times 10^{-12}$ cm^3 molecule^{-1} s^{-1} [7] and $k_4(298\text{ K}) = 8.0 \times 10^{-11}$ cm^3 molecule^{-1} s^{-1} (Chapter 6, [12]).

Since $k_1^{'} \gg k_4^{'}$, the rate-limiting step for OH and HO_2 formation is R4; thus, OH and HO_2 growths are pseudo-first order in $[CH_3CHO]$. OH is subsequently lost via reaction with CH_3CHO (R8), which recycles CH_3CO with a yield of $\alpha_{8a} = 0.95$ (R8a).

$$OH + CH_3CHO \longrightarrow CH_3CO + H_2O \tag{R8a}$$

$$\longrightarrow CH_2CHO + H_2O \tag{R8b}$$

The integrated rate law for OH was approximated by Equation 5.8:

$$[OH] = \frac{\alpha_{1a}[Cl]_0 k_4^{'}}{k_{8,\text{eff}}^{'} - k_4^{'}} \left(e^{-k_4^{'}t} - e^{-k_{8,\text{eff}}^{'}t} \right), \tag{5.8}$$

where $[Cl]_0$ is the initial radical concentration, $k'_{8,\text{eff}} = (1 - \alpha_{1a}\alpha_{8a})k'_8$, and α_{1a} is the fraction of R1 proceeding via R1a.

On the other hand, subsequent loss of HO_2 as well as radical recycling via R8 were negligible for $t < 50$ μs. This was corroborated by a plateau in the HO_2 time profile following prompt HO_2 formation. Secondary formation of HO_2 from the self-reaction of $CH_3C(O)O_2$ was also observed for $t > 50$ μs, but was de-coupled from the fast HO_2 formation via R1b. Thus, integrated rate law for HO_2 was approximated as:

$$[HO_2] = \alpha_{1b}[Cl]_0(1 - e^{-k'_4 t}), \tag{5.9}$$

where α_{1b} is the fraction of R1 proceeding via R1b.

Modified forms of Equation 5.8 and Equation 5.9 were used to fit the data to account for inherent time delay, t_0, introduced by the detection electronics:

$$[OH] = A_{0,\text{MIR}} \frac{k'_4}{k'_{8,\text{eff}} - k'_4} \left(e^{-k'_4(t-t_0)} - e^{k'_{8,\text{eff}}(t-t_0)} \right) \tag{5.10}$$

$$[HO_2] = A_{0,\text{NIR}}(1 - e^{-k'_4(t-t_0)}) \tag{5.11}$$

where $A_{0,\text{MIR}} = \alpha_{1a}[Cl]_0$ and $A_{0,\text{NIR}} = \alpha_{1b}[Cl]_0$. The MIR and NIR signals were fit to Equation 5.10 and Equation 5.11, respectively, using the Levenberg-Marquardt algorithm built in to the Igor Pro data analysis software [13]. The data were typically fit over ~16 - 90 μs after the photolysis pulse. The constrained parameters are summarized in Table 5.1.

Table 5.1: Summary of parameters constrained in the fits to the MIR and NIR data.

Data	Varied parameters
MIR	$A_{0,\text{MIR}}$, k'_4, $k'_{8,\text{eff}}$, t_0
NIR	$A_{0,\text{NIR}}$, k'_4, t_0

In all the fits, k'_4 and k'_8 were constrained to an interval covering ±10% of the previously measured values. α_{1a} and α_{1b} were calculated from the fitted values of $A_{0,\text{MIR}}$ and $A_{0,\text{NIR}}$, respectively. Values of $[Cl]_0$ were determined from the NIR calibration runs that were performed using the same $[Cl_2]$ and excimer pulse energy. t_0 was typically < 1 μs for the NIR signals and < 400 ns for the MIR signals.

5.3.1 Pressure dependence

Experiments for studying the pressure dependence of the OH yield from R1a were conducted at room temperature (T = 295.2 K) using N_2 as the bath gas. The OH time traces obtained at varying pressures are shown with the corresponding fits in Figure 5.3. Table 5.2 summarizes the fitted values of the yields. As expected, the data shows that the OH yield decreases with increasing pressures.

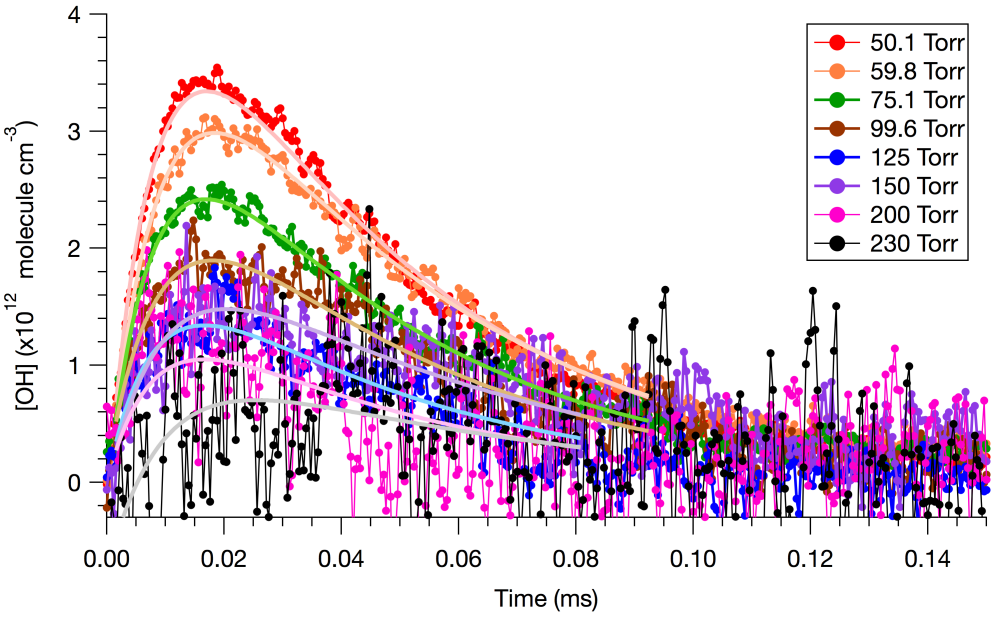

Figure 5.3: OH time traces obtained at various pressures. The fits to the data are also shown (solid lines, color-coded accordingly). T = 295.2 K; bath gas = N_2; concentrations: $[Cl_2] = 3.0 \times 10^{15}$ molecule cm^{-3}; $[Cl]_0 = 1.0 \times 10^{14}$ molecule cm^{-3}; $[CH_3CHO] = 1.4 \times 10^{15}$ molecule cm^{-3}; $[O_2] = 1.2 \times 10^{15}$ molecule cm^{-3}.

Table 5.2: Experimental conditions for the determination of α_{1a} and α_{1b} at various pressures. Data were collected at T = 295.2 K in N_2; concentrations: $[Cl_2] = 3.0 \times 10^{15}$ molecule cm^{-3}; $[Cl]_0 = 1.0 \times 10^{14}$ molecule cm^{-3}; $[CH_3CHO] = 1.4 \times 10^{15}$ molecule cm^{-3}; $[O_2] = 1.2 \times 10^{18}$ molecule cm^{-3}. Uncertainties are 1σ.

P (Torr)	α_{1a}	α_{1b}
50.1	0.049 ± 0.009	0.014 ± 0.002
59.8	0.044 ± 0.008	0.013 ± 0.002
75.1	0.035 ± 0.006	0.013 ± 0.002
99.6	0.029 ± 0.005	0.0094 ± 0.002
125	0.020 ± 0.004	0.0068 ± 0.002
150	0.021 ± 0.004	0.0078 ± 0.002
200	0.015 ± 0.004	0.0066 ± 0.002
230	0.010 ± 0.004	0.0083 ± 0.002

The measured OH yields are plotted as a function of the total gas density, [M], and are compared to literature values in Figure 5.4. As shown, the measured OH yields measured in this work are in excellent agreement with the results of Groß et al. [7], particularly at higher pressures. It should be noted, however, that our data at higher pressures have larger uncertainties due to lower signal-to-noise (SNR) resulting from pressure broadening of the probed OH line.

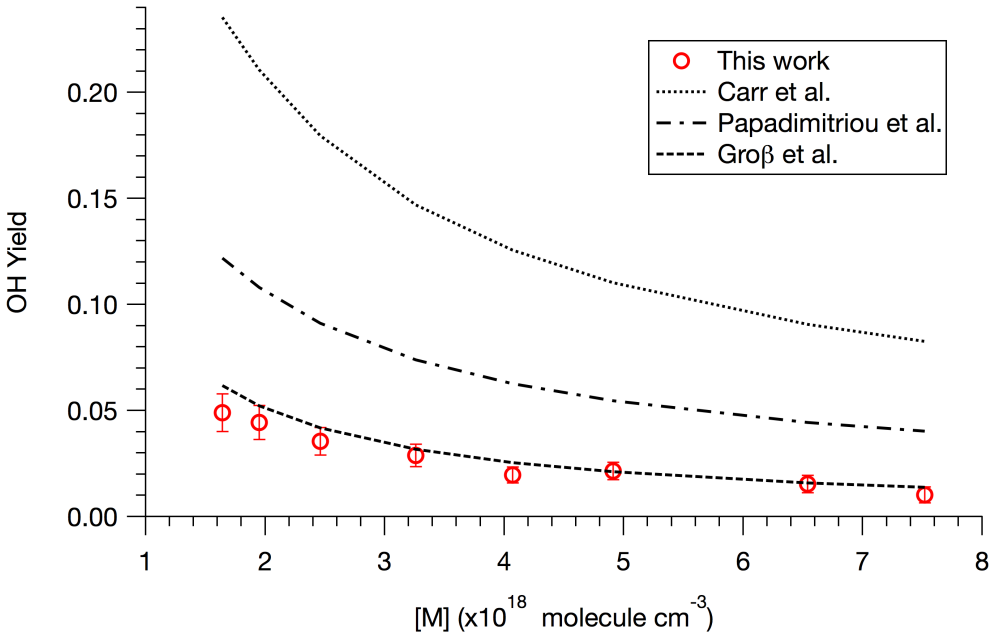

Figure 5.4: Comparison of the pressure-dependent OH yields in N_2 measured in this work (red circles, 1σ uncertainties) with the calculated values from literature data: Carr et al. [6] (dotted line); Papadimitriou et al. [8] (dashed-dotted line); and Groß et al. [7] (dashed line).

On the other hand, the HO_2 time traces did not appear to exhibit any pressure dependence. Figure 5.5 shows the data obtained at the lowest and highest pressures. As shown, the HO_2 traces obtained at 49.8 Torr and 230 Torr appear to be identical, including the prompt HO_2 signal at $t < 20$ μs (inset). Figure 5.6 shows the plot of the measured HO_2 yields as a function of [M], and demonstrates that α_{1b} is pressure-independent. The average HO_2 yield across all pressures was $\alpha_{1b} = 0.010 \pm 0.002$.

As mentioned previously, there have been no prior experimental studies that have investigated HO_2 as a product of R1. However, previous theoretical calculations [6] have postulated that the co-product of HO_2 is ketene (CH_2CO), which was detected by Dr. Leah Dodson using photoionization-mass spectroscopy (PI-MS), as reported in her thesis [9]. A direct comparison between her results and those from the

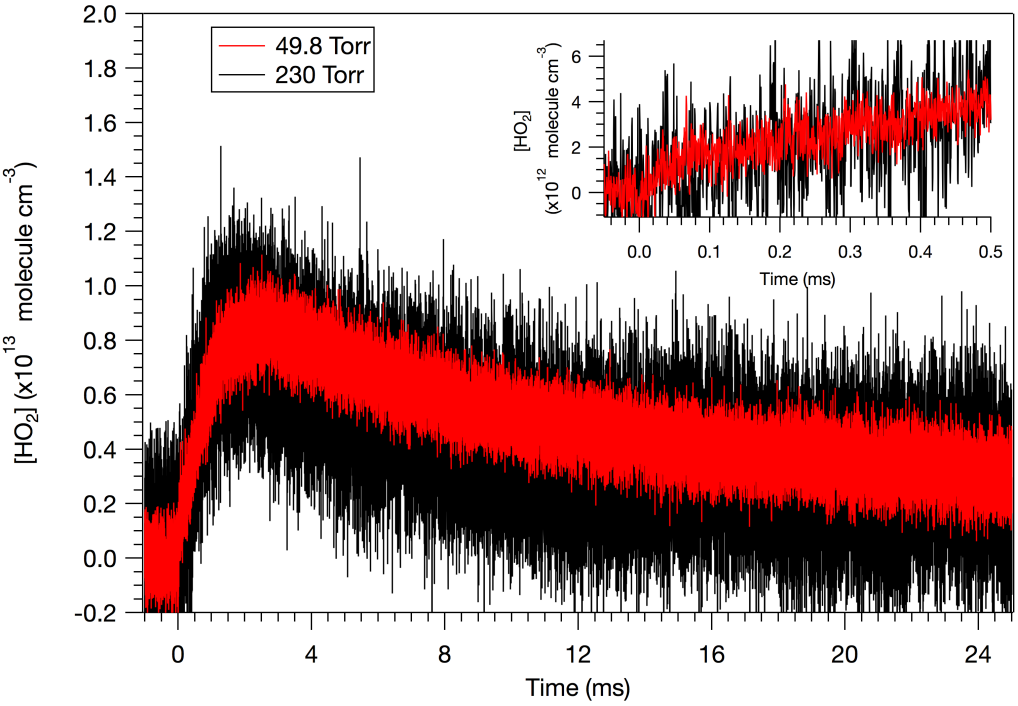

Figure 5.5: HO_2 time traces obtained at P = 49.8 Torr (red) and P = 230 Torr (black). The data obtained at other pressures have been excluded for clarity. The inset shows a zoomed-in view of the data, emphasizing that the prompt HO_2 signal also appears to be pressure-independent. T = 295.2 K; bath gas = N_2; concentrations: $[Cl_2] = 3.0 \times 10^{15}$ molecule cm^{-3}; $[Cl]_0 = 1.0 \times 10^{14}$ molecule cm^{-3}; $[CH_3CHO] = 1.4 \times 10^{15}$ molecule cm^{-3}; $[O_2] = 1.2 \times 10^{18}$ molecule cm^{-3}.

present work cannot be made since the PI-MS experiments were conducted at much lower pressures (8 Torr) using He (a less efficient quencher than N_2) as a bath gas. Furthermore, even though $k_{1b} = 2.5 \times 10^{14}$ cm^3 molecule^{-1} s^{-1} was reported, α_{1b} could not be inferred since neither k_1 nor k_{1a} were presented. However, a rough estimation of α_{1b} from that work will be provided here. Assuming a 1% depletion of the radical precursor, Cl_2, the total initial radical concentration was $\sim 8 \times 10^{12}$ molecule cm^{-3}. From the reported concentration of CH_2CO ($[CH_2CO] \sim 10^{11}$ molecule cm^{-3}), the estimated product yield is $\alpha_{1b} \sim 0.01$. At the lowest pressure studied in this present work (50 Torr in N_2), a comparable value of $\alpha_{1b} = 0.014 \pm 0.001$ was measured, which was unexpected due to the higher quenching efficiency of N_2 and total pressure. This assessment suggests that the observed prompt HO_2 signal is likely due to hot chemistry involving excited CH_3CO, since R4 is exothermic (ΔH = -13.15 kcal/mol [14]). Although some pressure dependence would be expected (i.e., less prompt HO_2 signal at higher pressures), the internal energy acquired from the excimer pulse may out-compete collisional quenching for pressure to have a significant effect. Future

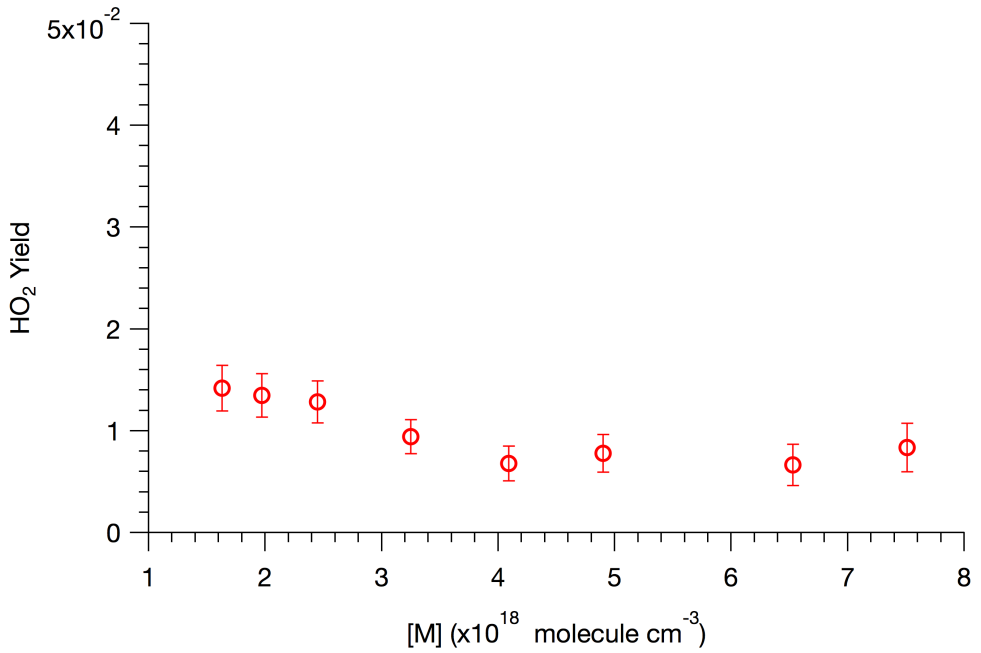

Figure 5.6: Plot of measured HO_2 yields as a function of total gas density. T = 295.2 K; bath gas = N_2; concentrations: $[Cl_2] = 3.0 \times 10^{15}$ molecule cm^{-3}; $[Cl]_0 = 1.0 \times 10^{14}$ molecule cm^{-3}; $[CH_3CHO] = 1.4 \times 10^{15}$ molecule cm^{-3}; $[O_2] = 1.2 \times 10^{15}$ molecule cm^{-3}.

experimental studies of this reaction using various excimer pulse energies while maintaining the same initial radical concentration (by varying $[Cl_2]$) would provide useful information for explaining the observed data. Experiments carried out using SF_6 as the bath gas could also be carried out to further investigate the apparent hot chemistry. SF_6 is a highly efficient collisional quencher; thus, by measuring the HO_2 signal using varying SF_6 concentrations could reveal the effects of collisional quenching on the HO_2 yield.

5.3.2 Temperature dependence at 100 Torr

The temperature dependences of α_{1a} and α_{1b} were also investigated over the temperature range T = 228.8 K - 295.2 K. Experiments were conducted at a total pressure of 100 Torr, using N_2 as the bath gas. At each temperature, data were collected using at least three different values of $[Cl]_0$. In some cases, data were also collected using varying concentrations of CH_3CHO.

Figure 5.7 shows some example data collected at T = 280.1 K using varying $[CH_3CHO]$ with fixed $[Cl]_0$ (Figure 5.7(a)) and varying $[Cl]_0$ with fixed $[CH_3CHO]$ (Figure 5.7(b)). The OH traces shown in the bottom plot of Figure 5.7(a) show that the formation and decay rates of OH both appear to increase with increasing $[CH_3CHO]$,

as expected. The formation and subsequent decay of OH are described by R4 and R8, respectively, and are both approximately pseudo-first order in $[CH_3CHO]$ since $[CH_3CHO] \gg [Cl]_0$. The OH traces shown in the bottom plot of Figure 5.7(b) also appear as expected: the formation rates for all three traces appear to be identical (since $[CH_3CHO]$ was fixed), while the peak OH signals decrease with decreasing $[Cl]_0$. Trends in the corresponding HO_2 traces shown in the upper panels of Figure 5.7(a) and Figure 5.7(b) are not as obvious; nonetheless, all the data were fit to derive the yields, as described previously.

Table 5.3 summarizes the experimental conditions over which α_{1a} and α_{1b} were measured at each temperature. For a given temperature, the listed values of α_{1a} and α_{1b} are the weighted averages of values obtained under all concentration conditions. The uncertainties are the weighted standard deviation calculated from the uncertainties in each fit.

Table 5.3: Experimental conditions for determination of α_{1a} and α_{1b}. Uncertainties are 1σ.

T (K)	$[O_2]^a$	$[Cl_2]^b$	$[CH_3CHO]^b$	$[Cl]_0{}^c$	α_{1a}	α_{1b}
295.2	1.2	3.0	1.4	10	0.029 ± 0.005	0.010 ± 0.002
294.9	1.6 - 2.5	3.0 - 6.0	0.86 - 4.1	10 - 18	0.020 ± 0.002	0.012 ± 0.002
294.0	1.6	2.3 - 3.8	1.0	5.9 - 9.3	0.032 ± 0.007	0.015 ± 0.003
292.8	1.6	2.3 - 3.8	1.5	8.7 - 14	0.019 ± 0.005	0.014 ± 0.002
280.1	1.7	2.3 - 3.8	1.0 - 4.0	8.0 - 13	0.024 ± 0.005	0.012 ± 0.002
270.6	1.7	2.3 - 3.8	1.0 - 4.0	8.4 - 13	0.020 ± 0.004	
259.3	1.8	2.3 - 3.8	1.0 - 4.5	8.1 - 13	0.017 ± 0.004	0.016 ± 0.003
250.4	1.9	2.3 - 3.8	1.0 - 3.3	5.3 - 8.3	0.017 ± 0.004	0.017 ± 0.003
240.1	1.9	2.3 - 3.8	1.0	5.7 - 9.0	0.013 ± 0.003	0.012 ± 0.002
228.8	2.0	2.4 - 3.8	1.0 - 3.8	5.6 - 8.7	0.011 ± 0.003	0.010 ± 0.002

[a] Units: 10^{18} molecule cm^{-3}
[b] Units: 10^{15} molecule cm^{-3}
[c] Units: 10^{13} molecule cm^{-3}

Figure 5.8 shows that while α_{1a} appears to have a weak positive dependence on temperature, no obvious temperature dependence is observed for α_{1b}. The lack of temperature dependence of α_{1b} further supports that the hypothesis that the observed prompt HO_2 signals are attributed to hot chemistry involving excited CH_3CO. The internal energy gained by CH_3CHO from the excimer pulse would overpower the energy gained purely from thermal atomic motion, resulting in temperature-independent behavior.

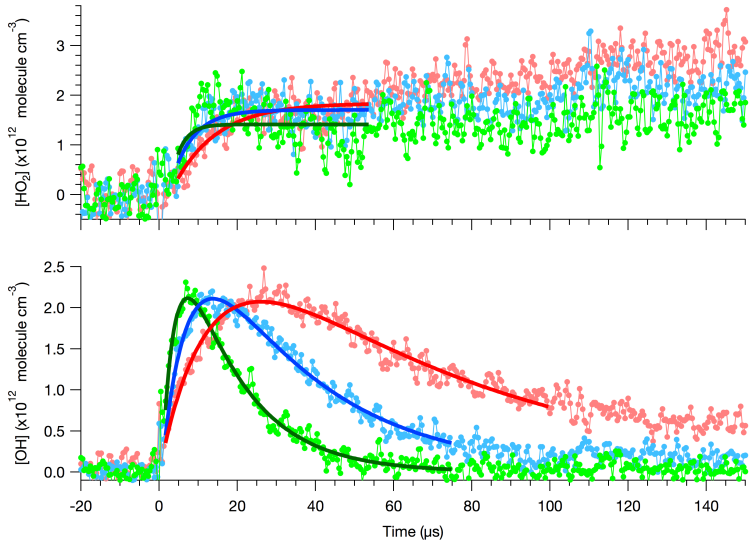

(a) [CH_3CHO] (units: $\times 10^{15}$ molecule cm^{-3}) = 1.0 (red), 2.0 (blue), and 4.0 (green).

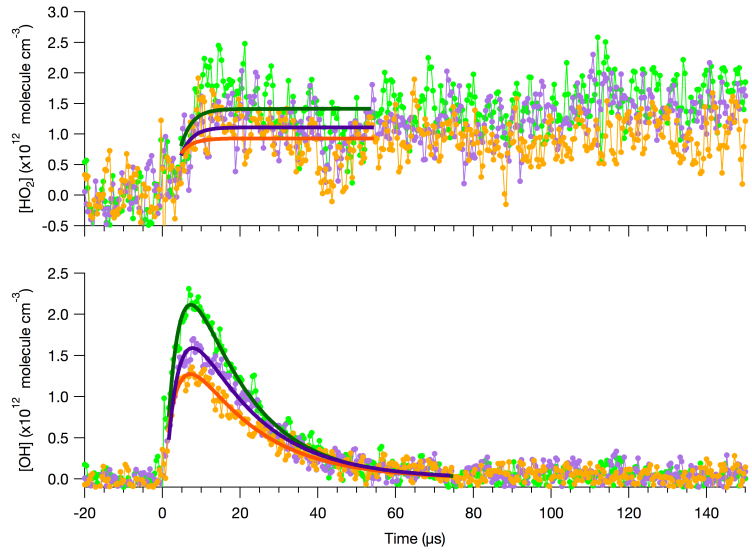

(b) $[Cl]_0$ (units: $\times 10^{14}$ molecule cm^{-3}) = 0.80 (black), 1.0 (purple), and 1.3 (green).

Figure 5.7: HO_2 and OH time traces obtained at T = 280.1 K and P = 100 Torr for (a) varying [CH_3CHO] with fixed $[Cl]_0 = 1.3 \times 10^{14}$ molecule cm^{-3} and for (b) varying $[Cl]_0$ with fixed [CH_3CHO] = 4.0×10^{15} molecule cm^{-3}. The fits to the data are also shown (solid lines).

5.3.3 MIR baseline

The OH signals were challenged by issues with the baselines of the time profiles, as demonstrated in Figure 5.9. The shift in the baseline after photolysis did not depend on the flow or concentrations of the precursor or radical concentrations. As

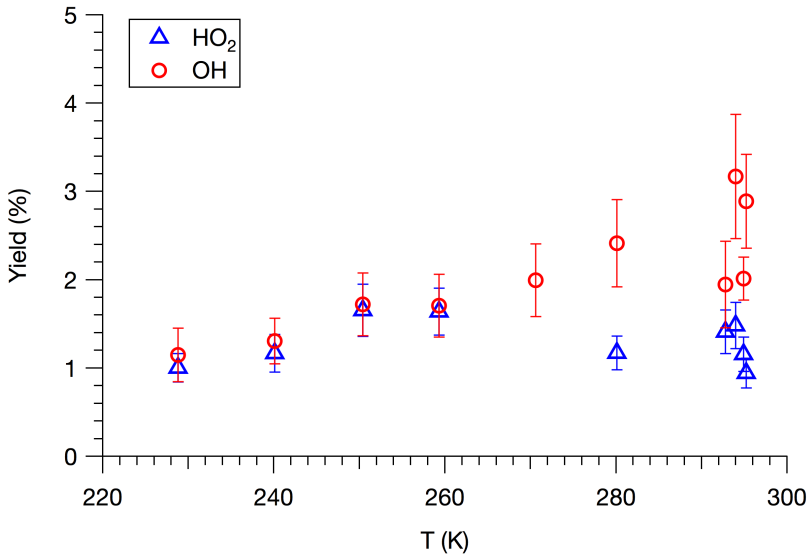

Figure 5.8: Temperature dependence of OH (red circles) and HO_2 (blue triangles) yields from the reaction of $CH_3C(O) + O_2$.

described in Chapter 2, the behavior of the baseline was highly dependent on the quality of the laser beam as well as the beam alignment. Although various measures (e.g. optimizing the MIR beam profile and alignment) were taken to minimize this effect, baseline shifts in the MIR signals could not completely be removed.

The baseline especially impacted low signal levels that lied closed to the baseline. The shift in the baseline varied from run to run, at times shifting as much as ~30% of the peak OH signal. Visually, the post-photolysis baseline appears to be true baseline as shown in the OH time profiles in Figure 5.9. By approximately 5 ms after photolysis, the OH time profiles essentially decayed to the baseline, indicating complete consumption of OH radicals. Furthermore, the fitted values of α_{1a} across all experimental runs were self-consistent if the post-photolysis baseline was used.

5.3.4 $CH_3C(O)O_2$ self reaction

This section of this chapter evaluates the data that have been presented in the previous sections in the context of the $CH_3C(O)O_2$ self reaction (R2), specifically to investigate the secondary sources of HO_2. The corresponding time-resolved UV absorbance signals are also provided, although comprehensive quantitative analysis was not possible because the data was not sensitive to specific kinetics parameters. Qualitative trends observed in the NIR and MIR data under various controlled experimental conditions are also given.

As mentioned previously, isolation of R2 was not possible due to competing

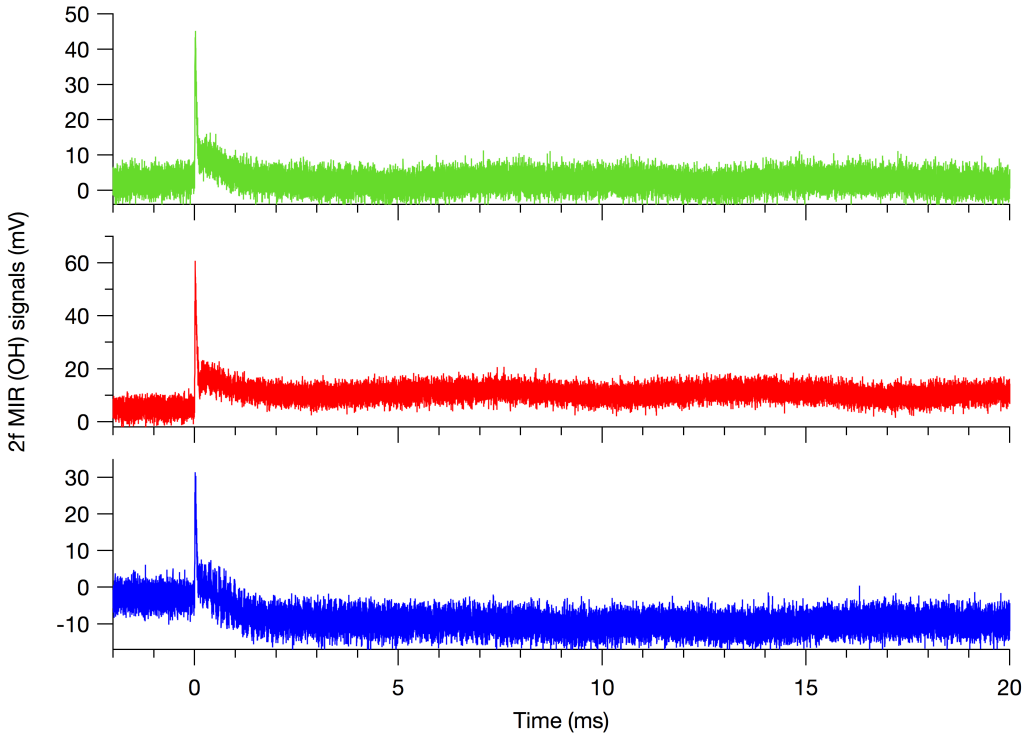

Figure 5.9: Time-resolved, raw 2f MIR OH signals from the $CH_3C(O) + O_2$ reaction demonstrating the shift in the baseline after photolysis. The shift in the baseline was not dependent on any of the reagent precursor gas or radical concentrations. The top panel shows an example of a good OH time profile (green), with no shift in the baseline after photolysis. The bottom two panels show OH traces with an increase (red) and decrease (blue) in the baseline signal.

secondary chemistry. The secondary reactions are responsible for producing HO_2. $CH_3C(O)O$ generated from R2 rapidly decomposes to form CO_2 and CH_3 R9. The subsequent reaction of CH_3 with O_2 (R10).

$$CH_3C(O)O \xrightarrow{M} CH_3 + CO_2 \qquad \text{(R9)}$$

$$CH_3 + O_2 \xrightarrow{M} CH_3O_2 \qquad \text{(R10)}$$

CH_3O_2 undergoes reactive loss by reaction with $CH_3C(O)O_2$ (R12) and by self reaction R11.

$$CH_3O_2 + CH_3O_2 \longrightarrow 2\,CH_3O + O_2 \qquad \text{(R11a)}$$

$$\longrightarrow CH_3OH + CH_2O + O_2 \qquad \text{(R11b)}$$

$$CH_3O_2 + CH_3C(O)O_2 \longrightarrow CH_3C(O)O + CH_3O + O_2 \quad \text{(R12a)}$$
$$\longrightarrow CH_3C(O)OH + CH_2O + O_2 \quad \text{(R12b)}$$

The radical propagating channels, R11a and R12b, generates CH_3O, which reacts with O_2 to produce HO_2 (R13).

$$CH_3O + O_2 \longrightarrow HO_2 + CH_2O \quad \text{(R13)}$$

Determination of k_2 was complicated by R12, which includes two product channels. The product yields of R12a (α_{12a}) and R12b (α_{12b}) are defined by

$$\alpha_{12a} = \frac{k_{12a}}{k_{12}} \quad (5.12)$$

$$\alpha_{12b} = \frac{k_{12b}}{k_{12}} \quad (5.13)$$

where

$$k_{12} = k_{12a} + k_{12b} \quad (5.14)$$

and k_{12a} and k_{12b} are the respective rate constants. Previous studies on R12 are scarce [15–18] and are all based on time-resolved UV absorption measurements. Since spectral isolation of $CH_3C(O)O_2$ is not possible due to the overlapping absorbance spectra of CH_3O_2 and other product species, kinetics analysis involved complex kinetics modeling, which can introduce systematic errors.

In addition to time-resolved UV absorbance spectroscopy, this work provided selective detection of HO_2, which could be used to determine the yield of CH_3O from R12a. The yield of CH_3O produced from R11a is well-characterized and can be taken into account in the kinetics model [11]. The NIR HO_2 and UV (λ = 225 nm and λ = 250 nm) time profiles were fitted simultaneously using a kinetics model (provided in Chapter 4) with FACSIMILE. The range of data that was fit was adjusted to minimize the error in the fits. Typically, the data were typically fit from ~300 μs to 4 - 7 ms. Due to the large uncertainties in the OH signals beyond the first 100 μs, the MIR OH data were excluded from the fits. The UV data in the first ~150 μs after photolysis was lost due to PMT saturation from the scattered excimer pulse. On this timescale, the initial MIR OH signals had decayed close to the baseline, which was difficult to define, as described previously. Furthermore, we observed an

unknown secondary source of OH that could not be reproduced by the model, as will be discussed later.

Figure 5.10 the shows the NIR and UV data obtained at T = 294.4 K. The higher peak UV signals at λ = 225 nm compared to λ = 250 nm were attributed to the slightly higher absorption cross-section of $CH_3C(O)O_2$ ($\sigma_{\lambda=225\text{ nm}} = 3.66 \times 10^{-18}$ cm^2 molecule^{-1}, and $\sigma_{\lambda=250\text{ nm}} = 3.22 \times 10^{-18}$ cm^2 molecule^{-1} [11]). The black traces are the fits and residuals to the data. The varied parameters in the fits were k_2, k_{12}, and α_{12a}. α_{12b} was constrained by $\alpha_{12b} = 1 - \alpha_{12a}$.

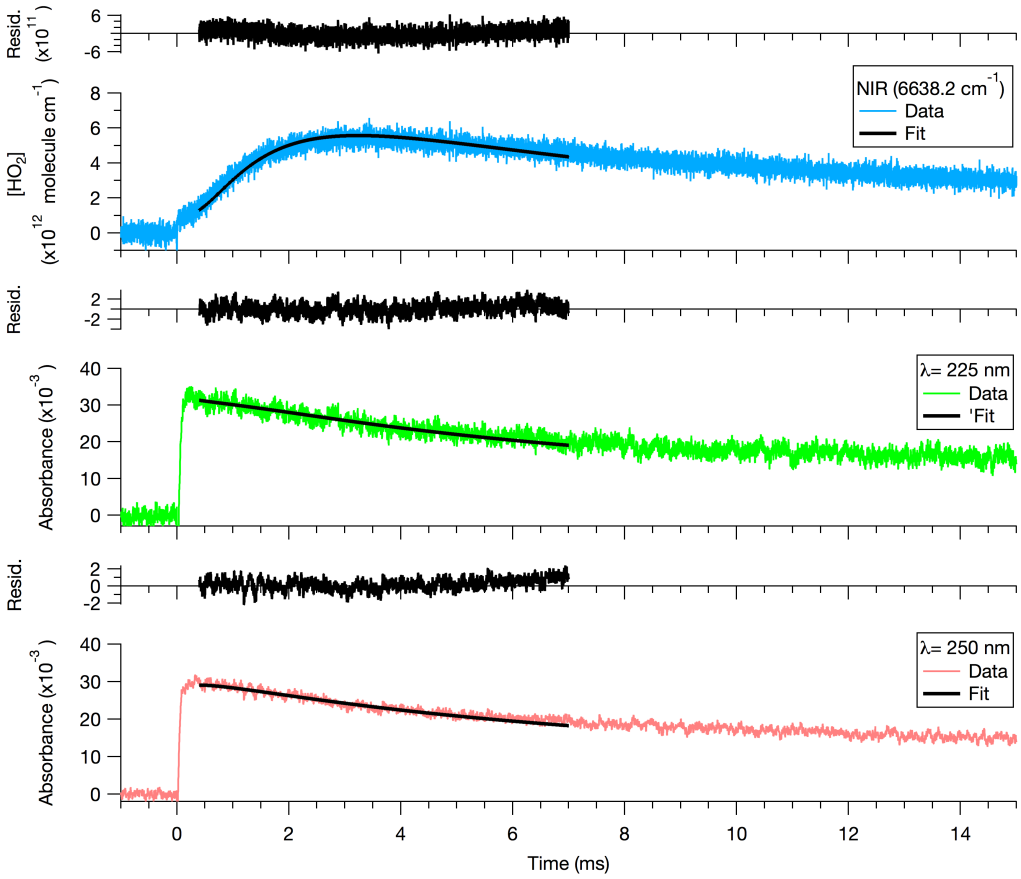

Figure 5.10: Time-resolved NIR HO_2 signals (light blue) and UV absorbance signals at λ = 225 nm (light green) and λ = 250 nm (pink) from the $CH_3C(O)O_2$ self reaction obtained using $[Cl]_0 = 5.9 \times 10^{13}$ molecule cm^{-3} at T = 294.4 K, P = 100 Torr. The fits to the data are shown in black and the residuals are shown above each curve.

Table 5.4 compares the fitted values for all three parameters using two different sets of initial guesses for each parameter: one that used the JPL recommended values and one that used values determined using an alternative method for estimating k_2, α_{12a}, and k_{12} from the work in Chapter 4, which will be discussed later. Values

of k_2 and k_{12} were observed to be self-consistent; however, α_{12a} was both poorly constrained by the model and appeared to depend on $[Cl]_0$, which was not a varied parameter.

Table 5.4: Comparison of fitted values of k_2, k_{12}, and α_{12a} using two sets of initial guesses for each parameter.

$[Cl]_0$[a]	$[CH_3CHO]$[b]	k_2[c]		k_{12}[c]		α_{12a}	
		d	*e*	*d*	*e*	*d*	*e*
5.9	1.0	23.0	18.7	6.45	6.70	0.93	1.0
7.5	1.0	24.3	18.9	6.81	6.46	1.0	1.0
8.7	1.5	17.0	16.5	7.59	7.35	0.75	0.74
9.3	1.0	22.9	19.8	6.70	6.54	0.97	0.99
11.2	1.5	20.6	20.2	7.18	6.81	0.68	0.68
13.8	1.5	28.6	23.9	7.66	7.14	0.57	0.56

[a]Units: $\times 10^{13}$ molecule cm^{-3}

[b]Units: $\times 10^{15}$ molecule cm^{-3}

[c]Units: 10^{-12} cm^3 molecule^{-1} s^{-1}

[d]Initial guesses: $k_2 = 1.6 \times 10^{-11}$ molecule cm^{-3} s^{-1}, $k_2 = 1.1 \times 10^{-11}$ cm^3 molecule^{-1} s^{-1}, $\alpha_{12a} = 0.9$

[e]Initial guesses: $k_2 = 1.8 \times 10^{-11}$ molecule cm^{-3} s^{-1}, $k_2 = 0.67 \times 10^{-11}$ cm^3 molecule^{-1} s^{-1}, $\alpha_{12a} = 0.95$

Although optimization reached conversion, unique solutions for k_2, α_{12a}, and k_{12} could not be obtained under all conditions at all temperatures due to the high covariance between these parameters. For example, k_2 and k_{12} were strongly correlated to each other, with correlation coefficients, $c_{k_2,k_{12}}$, that were as high as 0.9 for the highest $[Cl]_0$ data at room temperature. At lower temperatures, c_{k_3,k_4} was close to unity, even for the lowest $[Cl]_0$ data. α_{12a} did not appear to be strongly correlated to either of the rate constants at room temperature, with correlation coefficients of less than 0.1. At lower temperatures, the correlation coefficients between α_{12a} and k_2 (c_{α_{12a},k_2}) or between α_{12a} and k_{12} (c_{α_{12a},k_2}) were both typically ~0.6.

Figure 5.11 shows the data and fits from experiments carried out at T = 228.9 K. Lower quality fits to the UV data were obtained, which could not be improved by adjusting the weight of the χ-squared distribution for the UV curves relative to the NIR HO_2 curve. Visually, the observed UV decay rates appear faster than the model can explain, suggesting that there are unknown radical sinks that need to be investigated. The fitted values of k_2 were on the order of 10^{-10} cm^3 molecule^{-1} s^{-1}, which is unrealistically high for RO_2 reactions. Values of k_{12} were not self-consistent, while those of α_{12a} were generally close to 1.0.

Chapter 4 describes an alternative approach that was used to estimate the temperature dependence of k_2, k_{12}, and α_{12a} from the $HO_2 + CH_3C(O)O_2$ experiments.

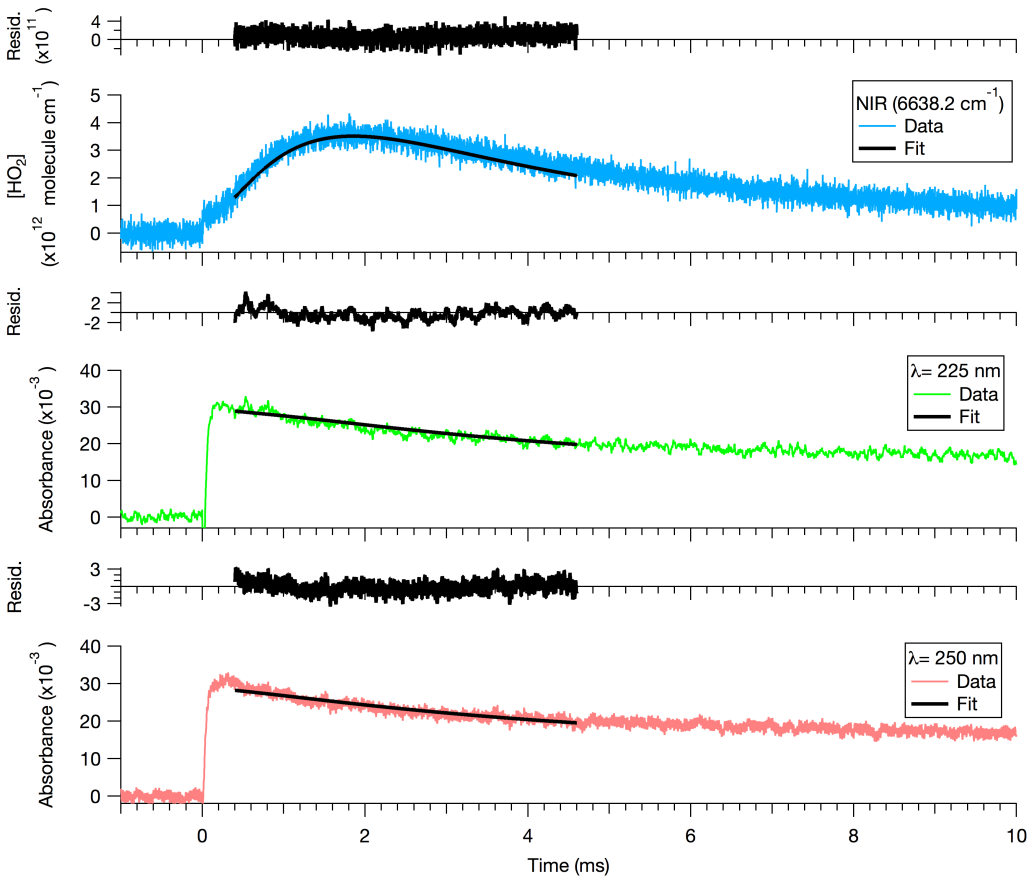

Figure 5.11: Time-resolved NIR HO_2 signals (light blue) and UV absorbance signals at λ = 225 nm (light green) and λ = 250 nm (pink) from the $CH_3C(O)O_2$ self reaction obtained using $[Cl]_0 = 5.6 \times 10^{13}$ molecule cm^{-3} at T = 228.9 K, P = 100 Torr. The fits to the data are shown in black and the residuals are shown above each curve.

Figure 5.12 shows the NIR and UV traces obtained using the lowest (Figure 5.12(a)) and highest initial radical concentrations (Figure 5.12(b)) at room temperature. To demonstrate the effect of temperature on the kinetics, the one data set collected at T = 228.9 K is provided in Figure 5.13. Each figure also compares the modeled time profiles using the values of k_2, k_{12}, and α_{12a} from the JPL data evaluation [11] to those using values determined in this work (Chapter 4). Table 5.5 summarizes the values of these kinetics parameters calculated at the lowest and highest temperature.

The lower value of k_{12} measured in this work is reflected as a lower yield in HO_2 and decreased decay rate of $CH_3C(O)O_2$. Using our values of k_2 and k_{12} resulted in improved agreement between the model and the data for both the low and high $[Cl]_0$ data. However, at higher $[Cl]_0$ and at lower temperatures, the model overestimated the HO_2 yield. Furthermore, at longer kinetics times (> 5 ms), the model also

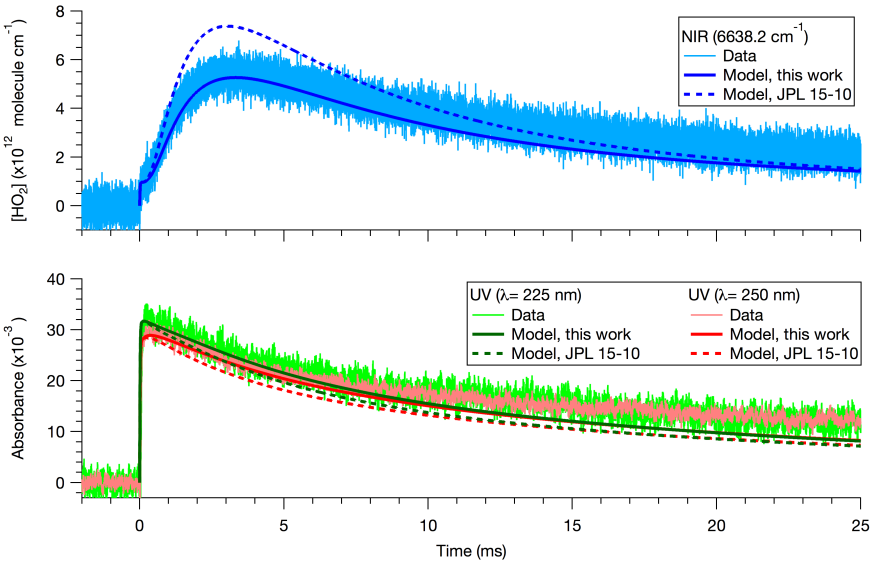

(a)

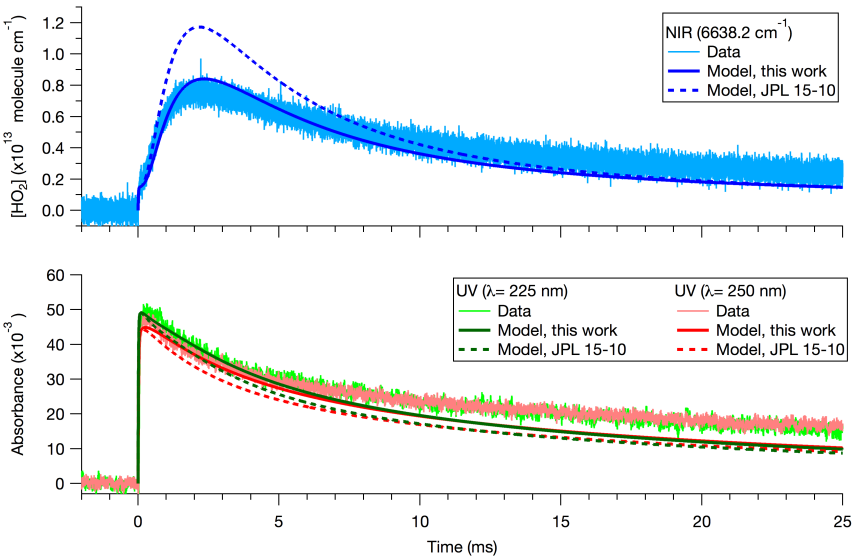

(b)

Figure 5.12: Time-resolved NIR HO_2 signals (light blue) and UV absorbance signals at λ = 225 nm (light green) and λ = 250 nm (pink) from the $CH_3C(O)O_2$ self reaction obtained using (a) $[Cl]_0 = 5.9 \times 10^{13}$ molecule cm^{-3} and (b) $[Cl]_0 = 9.3 \times 10^{13}$ molecule cm^{-3}. The corresponding modeled time profiles for each trace are shown in darker colors. The solid lines were modeled using values of k_2, k_{12}, and α_{12a} determined in this work. The dashed lines were modeled using the values from the JPL data evaluation [11]. See Table 5.5 for the values. [CH_3CHO] = 1.0×10^{15}; T = 294.4 K, P = 100 Torr.

predicted faster decay rates for the NIR and UV time profiles.

It should be noted that additional loss of HO_2 can occur by reaction with

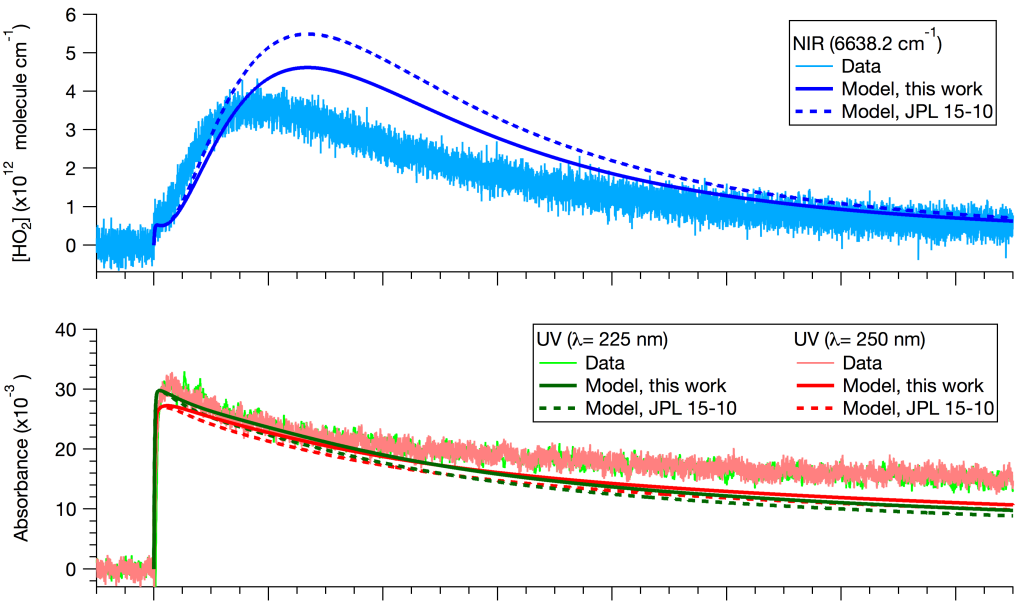

Figure 5.13: Time-resolved NIR HO_2 signals (light blue) and UV absorbance signals at λ = 225 nm (light green) and λ = 250 nm (pink) from the $CH_3C(O)O_2$ self reaction obtained using $[Cl]_0 = 5.6 \times 10^{13}$ molecule cm^{-3}. The corresponding modeled time profiles for each trace are shown in darker colors. The solid lines were modeled using values of k_2, k_{12}, and α_{12a} determined in this work. The dashed lines were modeled using the values from the JPL data evaluation [11]. See Table 5.5 for the values. $[CH_3CHO] = 1.0 \times 10^{15}$; T = 228.9 K, P = 100 Torr.

Table 5.5: Values of k_2, k_{12}, and α_{12a} (calculated at T = 294.4 K and T = 228.9 K) used for the kinetics model shown in Figure 5.12 and Figure 5.13. α_{12a} was found to be temperature-independent.

Ref.	k_2[a]		k_{12}[a]		α_{12a}
	T = 294.4 K	T = 228.9 K	T = 294.4 K	T = 228.9 K	
JPL data evaluation [11]	16	25.8	11	17.8	0.90
This work (Chapter 4)	18	29.7	6.7	13.7	0.95

[a]Units: 10^{-12} cm^3 molecule^{-1} s^{-1}

CH_3CHO, which has been suggested previously to undergo isomerization to produce the α-hydroxyethylperoxy ($CH_3CH(OH)O_2$) radical (R14) [19–22]

$$HO_2 + CH_3CHO \underset{}{\overset{M}{\rightleftharpoons}} CH_3CH(OH)O_2 \qquad \text{(R14)}$$

Tomas et al. [19] measured the equilibrium constant and the forward rate constant of R14 ($K_{eq,14}$ and k_{14}, respectively) using flash photolysis and UV absorption spectroscopy. Using the reported value of $K_{eq,14} = 3.1 \times 10^{-17}$ cm^3 molecule^{-1} and

$k_{14} = 4.4 \times 10^{-14}$ cm^3 molecule^{-1} s^{-1} at room temperature, the rate constant for the reverse reaction, k_{-14}, was calculated to be $k_{-14} = k_{14}/K_{eq,14} = 1.4 \times 10^3$ s^{-1}. Inclusion of R14 and absorbance by $CH_3CH(OH)O_2$ ($\sigma_{\lambda=225\text{ nm}} = 2.4 \times 10^{-18}$ cm^2 molecule^{-1}, and $\sigma_{\lambda=250\text{ nm}} = 1.9 \times 10^{-18}$ cm^2 molecule^{-1} [19]) did not significantly impact the modeled kinetics profiles or the fits across all temperatures. However, as it will be shown in the next section, the HO_2 profiles were demonstrated to depend on $[CH_3CHO]$. One implication from these observations is that the reported value of k_{14} may be under-predicted.

These results suggest that additional secondary chemistry needs to be considered to improve the kinetics model. Although the values of k_2, k_{12} determined in this work demonstrated better agreement between the model and the data, a more thorough re-investigation of R2 and R12 is still warranted to validate these new values and to characterize unresolved secondary chemistry.

5.3.4.1 Secondary OH formation

Following the rapid OH formation (< 20 μs) via R1 and subsequent decay via R8, a small rise in the OH signal was observed between 0.2 - 1 ms after photolysis. Figure 5.14 shows that the second maxima in the OH time profiles appear to be decoupled from the rapid OH chemistry of R1 and R8. The peak OH signals from both the rapid and slower kinetics also scaled with $[Cl]_0$. The secondary OH formation has also evidently been observed by other groups studying this reaction using a different experimental technique [23], providing confidence that the detected signal was not an instrumental artifact specific to the IRKS apparatus.

The OH signal on this timescale could not be reproduced by the kinetics model, suggesting that there is a secondary source of OH that has not previously been taken into account. Identification of the secondary OH formation was beyond the scope of this work; thus, the observed trends presented here are qualitative and serve as preliminary work to instigate future investigation of the chemistry. Figure 5.15 compares the OH time profiles previously shown in Figure 5.14 to the corresponding HO_2 time profiles obtained in the NIR. The prompt and secondary HO_2 signals were also found to scale with $[Cl]_0$; however, the yield of OH from the $HO_2 + CH_3C(O)O_2$ reaction (Chapter 7) was insufficient to explain the observed OH signals for $t > 100$ μs.

Additional experiments were carried out to investigate the source of the secondary OH formation. The OH and HO_2 time profiles obtained using varying $[O_2]$ are shown in Figure 5.16. No significant dependence of the prompt OH and HO_2 signals

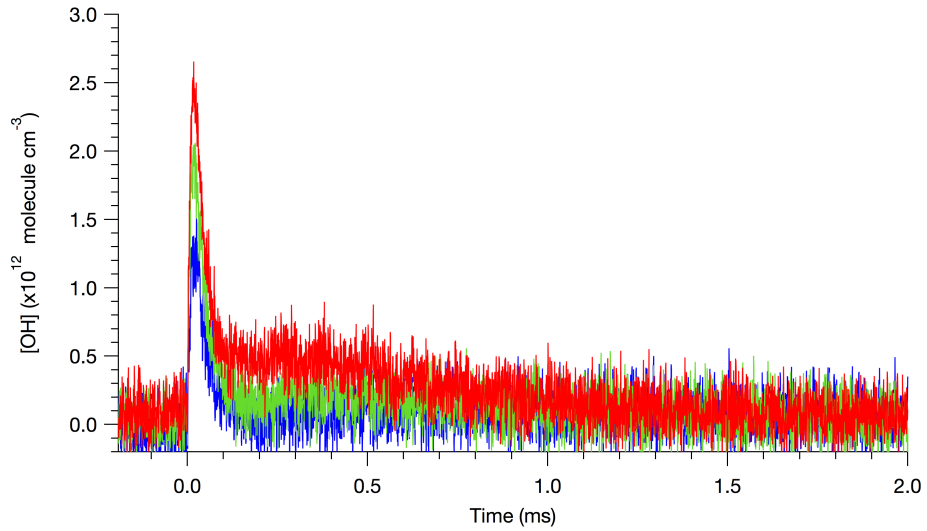

Figure 5.14: OH time profiles from the $CH_3C(O) + O_2$ reaction obtained using three different initial radical concentrations, demonstrating observation of secondary OH formation between 0.2 - 1 ms after photolysis. $[Cl]_0 = 1.8 \times 10^{14}$ molecule cm^{-3} (red), $[Cl]_0 = 1.4 \times 10^{14}$ molecule cm^{-3} (green), and $[Cl]_0 = 1.0 \times 10^{14}$ molecule cm^{-3} (blue) T = 295.2 K, P = 100 Torr.

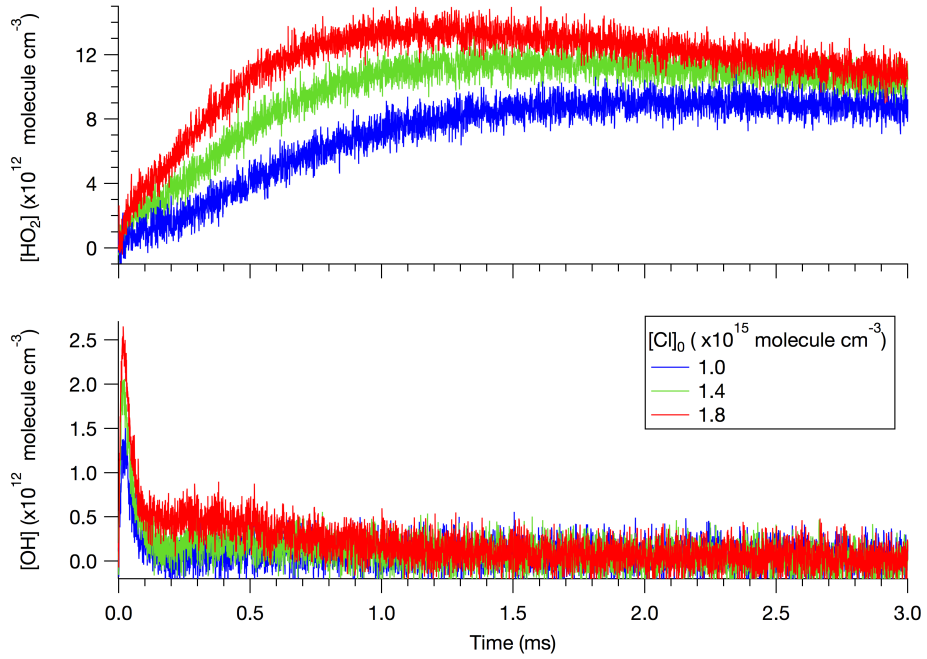

Figure 5.15: NIR HO_2 (upper panel) and MIR OH (lower panel) time profiles from the $CH_3C(O) + O_2$ reaction obtained using three different initial radical concentrations. T = 294.9 K, P = 100 Torr.

on $[O_2]$ was observed, validating the assumption that the rate-limiting step for the prompt OH and HO_2 formation is R4. Visually, the secondary OH signal appears to

grow faster with decreasing [O_2], although definitive conclusions cannot be made due the noise in the data. The HO_2 signals on the ms timescale were observed to

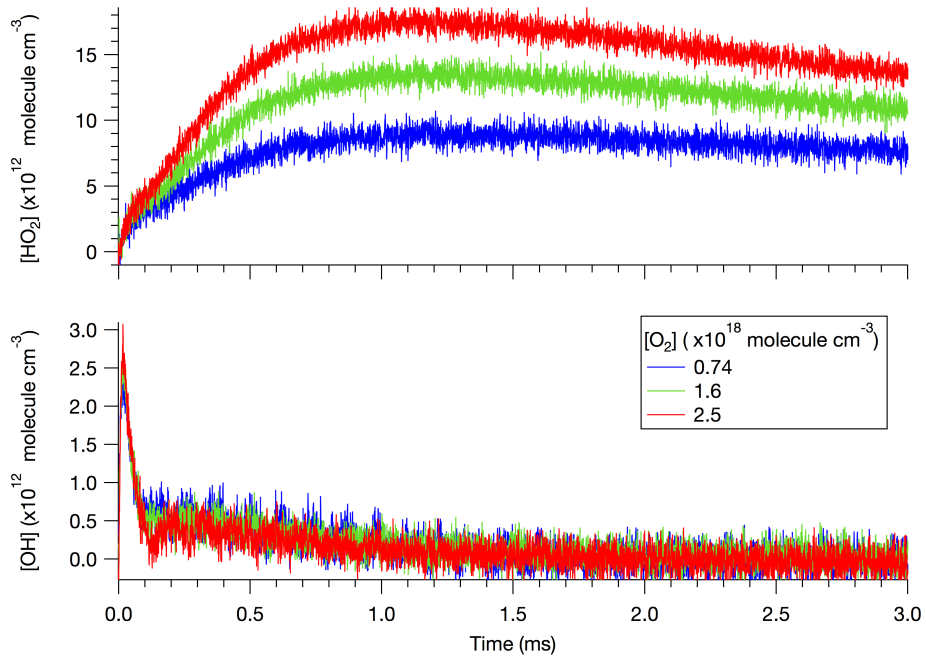

Figure 5.16: NIR HO_2 (upper panel) and MIR OH (lower panel) time profiles from the $CH_3C(O) + O_2$ reaction obtained using three different [O_2]. T = 294.9 K, P = 100 Torr.

increase with increasing [O_2, which can be explained by secondary chemistry; i.e., R13.

Figure 5.17 shows the time-resolved HO_2 and OH signals obtained using varying [CH_3CHO]. The OH signals show faster decay rates with increasing [CH_3CHO], which are explained by the faster loss of OH via R8. The prompt and secondary HO_2 yield appeared to decrease with increasing [CH_3CHO]. One explanation for this observation is the loss of HO_2 by reaction with CH_3CHO to form the hydrogen-bonded complex, $HO_2 \cdot CH_3CHO$. Chapter 3 and Chapter 4 demonstrated that the observed decay rate of HO_2 from the reaction of HO_2 with $CH_3C(O)O_2$ could only be explained by rate enhancement of the HO_2 self reaction by CH_3CHO, which was found to be significant, even at room temperature. As described in Chapter 7, a similar trend was observed from the $CH_3C(O)CH_2O_2$ self reaction, where the HO_2 signal decreased with increasing [$CH_3C(O)CH_3$], which was also found to have a strong rate enhancement effect on the HO_2 self reaction.

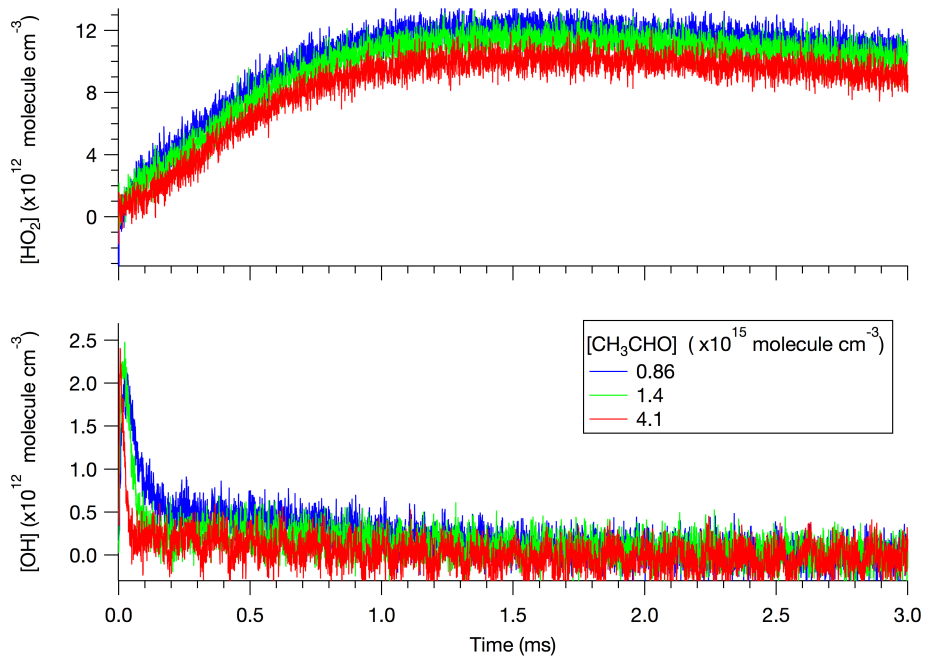

Figure 5.17: NIR HO_2 (upper panel) and MIR OH (lower panel) time profiles from the $CH_3C(O) + O_2$ reaction obtained using three different $[CH_3CHO]$. T = 294.9 K, P = 100 Torr.

5.4 Conclusion

The yields of OH and HO_2 from the $CH_3C(O) + O_2$ reaction were measured over a wide range of pressures and temperatures using MIR and NIR WMS for direct detection of OH and HO_2 radicals. The time-resolved OH and HO_2 signals were analyzed using pseudo-first order kinetics. The pressure dependences of α_{1a} and α_{1b} were determined over the range P = 50 - 230 Torr using N_2 as the bath gas. The temperature dependences were also investigated over the range T = 228.2 - 295.3 K at 100 Torr.

α_{1a} was observed to be negatively correlated with pressure and positively correlated with temperature, as expected. The measured values of α_{1a} were in relatively good agreement with the results reported by Groß et al. [7], and were lower than those reported by Papadimitriou et al. [8] and by Carr et al. [6] by as much as factor of ~2.5 and ~4, respectively, at lower pressures. Prompt HO_2 signals were used to determine α_{1b}, which was found to be independent of both pressure and temperature. These observations suggest that hot chemistry from excited CH_3CO may be the best explanation for the prompt HO_2 formation; however, further experimental studies are needed to confirm this hypothesis.

The time-resolved NIR HO_2 and UV absorbance signals were also examined

to investigate the self-reaction of $CH_3C(O)O_2$. Accurate determination of k_2 was impeded by secondary reactions that themselves are not well-characterized. This had a stronger impact at lower temperatures and higher radical concentrations. Furthermore, the MIR OH time profiles also exhibited unexplained secondary formation of OH, which appeared to be decoupled from the rapid $CH_3C(O) + O_2$ chemistry. Further experiments are needed to characterize R2 as well the main competing secondary reaction, $CH_3O_2 + CH_3C(O)O_2$ (R5.14).

References

[1] Tyndall, G. S.; Orlando, J. J.; Wallington, T. J.; Hurley, M. D. Pressure Dependence of the Rate Coefficients and Product Yields for the Reaction of CH3CO Radicals with O2. *International Journal of Chemical Kinetics* **1997**, *29*, 655–663.

[2] Sehested, J.; Christensen, L. K.; Nielsen, O. J.; Bilde, M.; Wallington, T. J.; Schneider, W. F.; Orlando, J. J.; Tyndall, G. S. Atmospheric Chemistry of Acetone: Kinetic Study of the CH3C(O)CH2O2+NO/NO2 Reactions and Decomposition of CH3C(O)CH2O2NO2. *International Journal of Chemical Kinetics* **1998**, *30*, 475–489.

[3] Blitz, M. A.; Heard, D. E.; Pilling, M. J. OH Formation from CH3CO+O2: A Convenient Experimental Marker for the Acetyl Radical. *Chemical Physics Letters* **2002**, *365*, 374–379.

[4] Kovács, G.; Zádor, J.; Farkas, E.; Nádasdi, R.; Szilágyi, I.; Dóbé, S.; Bérces, T.; Márta, F.; Lendvay, G. Kinetics and Mechanism of the Reactions of CH3CO and CH3C(O)CH2 Radicals with O2. Low-Pressure Discharge Flow Experiments and Quantum Chemical Computations. *Physical Chemistry Chemical Physics* **2007**, *9*, 4142–4154.

[5] Carr, S. A.; Baeza-Romero, M. T.; Blitz, M. A.; Pilling, M. J.; Heard, D. E.; Seakins, P. W. OH Yields from the CH3CO+O2 Reaction Using an Internal Standard. *Chemical Physics Letters* **2007**, *445*, 108–112.

[6] Carr, S. A.; Glowacki, D. R.; Liang, C.-H.; Baeza-Romero, M. T.; Blitz, M. A.; Pilling, M. J.; Seakins, P. W. Experimental and Modeling Studies of the Pressure and Temperature Dependences of the Kinetics and the OH Yields in the Acetyl + O2 Reaction. *The Journal of Physical Chemistry A* **2011**, *115*, 1069–1085.

[7] Groß, C. B. M.; Dillon, T. J.; Crowley, J. N. Pressure Dependent OH Yields in the Reactions of CH3CO and HOCH2CO with O2. *Physical Chemistry Chemical Physics* **2014**, *16*, 10990–10998.

[8] Papadimitriou, V. C.; Karafas, E. S.; Gierczak, T.; Burkholder, J. B. CH3CO + O2 + M (M = He, N2) Reaction Rate Coefficient Measurements and Implications for the OH Radical Product Yield. *The Journal of Physical Chemistry A* **2015**, *119*, 7481–7497.

[9] Dodson, L. G. Gas Phase Spectroscopy and Kinetics of Atmospheric Radicals., Ph.D. Pasadena, CA: California Institute of Technology, 2016.

[10] *FACSIMILE* version 4.1.41 [computer software]; Faringdon, Oxon, UK, 2003.

[11] Sander, S. P.; Abbat, J.; Barker, J.R.; Burkholder, J.B.; Huie, R.E.; Kolb, C.E.; Kurylo, M.J.; Wilmouth, D.M.; Orkin, V.L.; Wine, P.H. *Chemical Kinetics and Photochemical Data for Use in Atmospheric Studies, Evaluation No. 18*; Jet Propulsion Laboratory, Pasadena: JPL Publication 15-10, 2015.

[12] Atkinson, R.; Baulch, D. L.; Cox, R. A.; Hampson, R. F.; Kerr, J. A.; Troe, J. Evaluated Kinetic and Photochemical Data for Atmospheric Chemistry: Supplement IV. IUPAC Subcommittee on Gas Kinetic Data Evaluation for

Atmospheric Chemistry. *Journal of Physical and Chemical Reference Data* **1992**, *21*, 1125–1568.

[13] *IGOR Pro* version 6.37; Lake Oswego, Oregon, 2015.

[14] Linstrom, P.; Mallard, W. *NIST Chemistry WebBook, NIST Standard Reference Database Number 69*; Gaithersburg MD, 20899: National Institute of Standards and Technology.

[15] Moortgat, G.; Veyret, B.; Lesclaux, R. Absorption Spectrum and Kinetics of Reactions of the Acetylperoxy Radical. **1989**, *93*, 2362–2368.

[16] Roehl, C. M.; Bauer, D.; Moortgat, G. K. Absorption Spectrum and Kinetics of the Acetylperoxy Radical. *The Journal of Physical Chemistry* **1996**, *100*, 4038–4047.

[17] Maricq, M. M.; Szente, J. J. The CH3C(O)O2 Radical. Its UV Spectrum, Self-Reaction Kinetics, and Reaction with CH3O2. *The Journal of Physical Chemistry* **1996**, *100*, 4507–4513.

[18] Villenave, E.; Lesclaux, R. Kinetics of the Cross Reactions of CH3O2 and C2H5O2 Radicals with Selected Peroxy Radicals.

[19] Tomas, A.; Villenave, E.; Lesclaux, R. Reactions of the HO2 Radical with CH3CHO and CH3C(O)O2 in the Gas Phase. *The Journal of Physical Chemistry A* **2001**, *105*, 3505–3514.

[20] Crawford, M. A.; Wallington, T. J.; Szente, J. J.; Maricq, M. M.; Francisco, J. S. Kinetics and Mechanism of the Acetylperoxy + HO2 Reaction. *The Journal of Physical Chemistry A* **1999**, *103*, 365–378.

[21] Da Silva, G.; Bozzelli, J. W. Role of the -Hydroxyethylperoxy Radical in the Reactions of Acetaldehyde and Vinyl Alcohol with HO2. *Chemical Physics Letters* **2009**, *483*, 25–29.

[22] Da Silva, G.; Bozzelli, J. W.; Liang, L.; Farrell, J. T. Ethanol Oxidation: Kinetics of the -Hydroxyethyl Radical + O2 Reaction. *The Journal of Physical Chemistry A* **2009**, *113*, 8923–8933.

[23] Personal Communication., in collab. with Whiting, F., 2018.

Chapter 6

TEMPERATURE DEPENDENCE OF THE REACTION OF CHLORINE ATOMS WITH CH_3OH AND CH_3CHO

Abstract

Rate constants of the reactions Cl + $CH_3OH \longrightarrow CH_2OH$ + HCl (k_1) and Cl + $CH_3CHO \longrightarrow CH_3C(O)$ + HCl (k_3) were measured at 100 Torr over the temperature range 230.3 - 297.1 K. Radical chemistry was initiated by pulsed laser photolysis of Cl_2 in mixtures of CH_3OH and CH_3CHO in a flow reactor. Heterodyne near-IR (NIR) wavelength modulation spectroscopy was used to directly detect HO_2 produced from the subsequent reaction of CH_2OH with O_2 in real-time to determine the rate of reaction of Cl with CH_3OH. The rate of Cl + CH_3CHO was measured relative to that of the Cl + CH_3OH reaction. Secondary chemistry, including that of the adducts $HO_2 \cdot CH_3OH$ and $HO_2 \cdot CH_3CHO$, were taken into account. The Arrhenius expressions were found to be $k_1(T) = 5.02^{+1.8}_{-1.5} \times 10^{-11} \exp[(20 \pm 88)/T]$ cm^3 molecule^{-1} s^{-1} and $k_3(T) = 6.38^{+2.4}_{-2.0} \times 10^{-11} \exp[(56 \pm 90)/T]$ cm^3 molecule^{-1} s^{-1} (2σ uncertainties). The average values of the rate constants over this temperature range were $k_1 = (5.45 \pm 0.37) \times 10^{-11}$ cm^3 molecule^{-1} s^{-1} and $k_3 = (8.00 \pm 1.27) \times 10^{-11}$ cm^3 molecule^{-1} s^{-1} (2σ uncertainties), consistent with current literature values.

6.1 Introduction

Cl atoms are commonly used to generate free radicals in laboratory studies of gas phase reactions. For example, the reactions of Cl atoms with CH_3OH (R1) and CH_3CHO (R3) have been widely used to source hydroperoxy (HO_2) and acetylperoxy ($CH_3C(O)O_2$) radicals, respectively, for studying the kinetics and product yields of their cross-reaction [1–9].

$$Cl + CH_3OH \longrightarrow CH_2OH + HCl \quad \text{(R1)}$$

$$CH_2OH + O_2 \longrightarrow HO_2 + CH_2O \quad \text{(R2)}$$

$$Cl + CH_3CHO \longrightarrow CH_3C(O) + HCl \quad \text{(R3)}$$

$$CH_3C(O) + O_2 \xrightarrow{M} CH_3C(O)O_2 \quad \text{(R4)}$$

Numerous room temperature studies have investigated the rate constants of R1 [10–17] and R3 [11, 14–16, 18–21] (k_1 and k_3, respectively) using relative and absolute rate methods, with consistent results in the reported values. Although the temperature dependence of k_1 has been extensively studied [22–25], only one study has investigated the temperature dependence of k_3 [26]. The current IUPAC data evaluation recommends k_3 to be temperature-independent based on the single study.

This work measured the temperature dependence of $k1$ and $k3$ over the temperature range 230.3 - 297.1 K using pulsed laser photolysis coupled to IR $2f$ wavelength modulation spectroscopy (WMS). This technique was used to monitor the formation of HO_2 in the near-IR (NIR) following the photolysis of gas mixtures containing Cl_2 /O_2 /N_2 /CH_3OH or Cl_2 /O_2 /N_2 / CH_3OH /CH_3CHO to determine k_1 and k_3, respectively, using pseudo-first order kinetics. All experiments were carried out at 100 Torr under conditions where the O_2, CH_3OH, and CH_3CHO concentrations were all in excess relative to Cl atoms by at least a factor of 10.

6.2 Experimental Methods

The Infrared Kinetics Spectroscopy (IRKS) apparatus consisted of a temperature-controlled pulsed laser photolysis flow cell coupled to simultaneous IR and UV absorption spectroscopy and has been described in detail previously [27–29]. Only the details pertinent to the present work will be provided, including modifications that were made since the last publication.

The flow cell was a jacketed Pyrex cell of length 175 cm and diameter 5 cm and was temperature-controlled by flowing liquid nitrogen-cooled methanol circulating through the jacket of the cell. The temperature was measured with a calibrated type T thermocouple (Omega). Reagent gases were pre-mixed and pre-cooled in a Pyrex manifold prior to entering the cell. Room temperature N_2 purge gas flowed from the aluminum chambers on either end of the cell towards the gas pump-out ports to confine the main gas flow to the temperature controlled region and to protect the Herriott mirrors that formed the multi-pass optical cavity for the IR probes. The gas flows were regulated by mass flow controllers (MKS Instruments) and the total flow rate was kept at approximately 2000 cm^3 (STP) min^{-1}, maintaining a 10 s residence time inside the flow cell at a total pressure of 100 ± 2 Torr. CH_3OH and CH_3CHO were introduced into the cell by flowing N_2 through glass bubblers containing the liquid compounds, held inside temperature-controlled baths. The pressures in the reaction cell and bubblers were measured by absolute capacitance pressure gauges (MKS Baratron), and the concentrations of CH_3OH and CH_3CHO

vapors were determined from their flow rates using the known vapor pressures of the pure compounds and assuming complete saturation in the bubblers.

351 nm light from a XeF excimer laser (Compex 301) operating in the constant energy mode was directed coaxially through the flow cell to initiate the chemistry by photolyzing Cl_2 molecules in gas mixtures of $Cl_2/N_2/O_2/CH_3OH/CH_3CHO$. A photolysis repetition rate of 0.2 Hz was used, resulting in two photolysis events occurring per residence time. Decreasing the repetition rate to 0.1 Hz made no difference in the kinetics traces. All experiments were conducted in excess amounts of O_2, CH_3OH, and CH_3CHO relative to the initial radical concentrations, such that all Cl atoms generated from photolysis were assumed to form either HO_2 or $CH_3C(O)O_2$ via R1 and R3, respectively. Typical concentrations of the reagents were: $[CH_3OH] = (2.4-10.7)\times10^{15}$ molecule cm^{-3}, $[CH_3CHO] = (0.9-8.4)\times10^{15}$ molecule cm^{-3}, $[O_2] = (1.6-2.0)\times10^{18}$ molecule cm^{-3}; $[Cl_2] = (0.8-5.3)\times10^{15}$ molecule cm^{-3}, with total radical concentrations of $[Cl]_0 = (1.8-19)\times10^{13}$ molecule cm^{-3}.

A 3 mW continuous-wave (CW) distributed feedback (DFB) laser operating in the NIR was used for sensitive detection of HO_2 radicals. The diode laser was tuned to the rovibrational transitions of the first overtone of the OH stretch of HO_2 ($2\nu_1$: 6638.2 cm^{-1}), and the laser output was wavelength modulated at 6.8 MHz by sinusoidally modulating the injection current with an external function generator. 2f-heterodyne detection was implemented by demodulating the detected signal at 13.6 MHz. The demodulated signal was collected at a sampling rate of 2.5 MHz, amplified by a factor of 200, and low-pass filtered at 1 MHz using a low-noise preamplifier (SRS SR560). The noise-equivalent concentration of HO_2 normalized to one excimer shot was 3.7×10^9 molecule $cm^{-3}Hz^{-1/2}$. For a typical experimental run, the HO_2 signal was averaged for 65 - 75 excimer laser shots.

Since WMS only measures the relative changes in concentration, the HO_2 laser was calibrated daily to obtain absolute concentrations. The HO_2 laser was calibrated against UV absorption at λ= 225 nm ($\sigma_{HO_2} = 2.88\times10^{-18}$ cm^2 $molecule^{-1}$) by measuring the NIR and UV decay signals simultaneously when HO_2 was the only peroxy radical present; i.e., $[CH_3CHO] = 0$. Broadband UV light was provided by a laser-driven light source (Energetiq EQ-99XFC). The collimated UV beam was coaligned with and counter-propagated the excimer beam, making a single pass through the cell. A monochromator (Acton Research Corporation Spectra Pro-300i) placed in front of a photomultiplier tube (PMT) was used for wavelength-specific detection of the transmitted UV light. Baffles were placed on both ends of the

flow cell to ensure that only light that sampled the photolysis volume entered the monochromator. Despite a different geometric overlap due to the off-axis orientation of the Herriott mirrors, the IR and UV probe beams should capture the same physical processes at relatively short timescales (< 20 ms); i.e., before diffusion becomes a significant loss process. At the beginning of every experiment, the kinetics traces from the HO_2 self-reaction were collected at three different initial radical concentrations at room temperature, and the IR and UV traces were simultaneously fit to a bimolecular decay with the kinetics modeling program, FACSIMILE [30], to obtain the calibration factor, which relates the IR signal in mV (S_{HO_2}) to the absolute HO_2 concentration.

6.3 Results and Discussion

All experiments were conducted using excess amounts of O_2, CH_3OH, and CH_3CHO relative to the total initial radical concentration, $[Cl]_0$. The O_2 concentration was also in excess of both CH_3OH and CH_3CHO, such that the first order loss rates of R4 and R2 were at least 10 times greater than both R1 and R3. For example, at the lowest O_2 concentration ($[O_2]$=1.6×10^{18} molecule cm^{-3}) and highest CH_3OH and CH_3CHO concentrations ($\sim1\times10^{16}$ molecule cm^{-3}), the first order loss rates were

$$k_2[O_2] \sim 8\times10^6\ \text{s}^{-1} \qquad \approx 15k_1[CH_3OH] \approx 14k_3[CH_3CHO] \tag{6.1}$$

$$k_4[O_2] \sim 1\times10^8\ \text{s}^{-1} \qquad \approx 160k_1[CH_3OH] \approx 150k_3[CH_3CHO] \tag{6.2}$$

where

$$k_2 \sim 9.1\times10^{-11}\ \text{cm}^3\ \text{molecule}^{-1}\ \text{s}^{-1} \qquad \text{(ref: JPL 15-10 [31])} \tag{6.3}$$

$$k_4 \sim 5.1\times10^{-12}\ \text{cm}^3\ \text{molecule}^{-1}\ \text{s}^{-1} \qquad \text{(ref: Atkinson et al. [32])} \tag{6.4}$$

$$k_1 \sim 5.5\times10^{-11}\ \text{cm}^3\ \text{molecule}^{-1}\ \text{s}^{-1} \qquad \text{(ref: JPL 15-10 [31])} \tag{6.5}$$

$$k_3 \sim 8.0\times10^{-11}\ \text{cm}^3\ \text{molecule}^{-1}\ \text{s}^{-1} \qquad \text{(ref: IUPAC [33])} \tag{6.6}$$

Thus, the rate-limiting steps for the formation of HO_2 and $CH_3C(O)O_2$ can be approximated to be R1 and R3, respectively; i.e.,

$$Cl + CH_3OH \longrightarrow HO_2 \tag{R5}$$

$$Cl + CH_3CHO \longrightarrow CH_3C(O)O_2 \tag{R6}$$

The formation of HO_2 and $CH_3C(O)O_2$ were pseudo-first order since both CH_3OH and CH_3CHO were in excess relative to $[Cl]_0$; therefore, the rate law for HO_2 can be written as

$$\frac{d[HO_2]}{dt} = k_1[CH_3OH][Cl]_0 \exp[-(k_1[CH_3OH] + k_3[CH_3CHO])t] \quad (6.7)$$

$$= k_1^{'}[Cl]_0 \exp[-(k_1^{'} + k_3^{'})t], \quad (6.8)$$

where $[Cl]_0$ is the initial radical concentration and $k_1^{'}$ and $k_3^{'}$ are the pseudo-first order rate constants for R1 and R1, respectively; i.e.,

$$k_1^{'} = k_1[CH_3OH] \quad (6.9)$$

and

$$k_3^{'} = k_3[CH_3CHO] \quad (6.10)$$

Experimental conditions were chosen to minimize subsequent losses of HO_2 via the self reaction (R7) and reaction with $CH_3C(O)O_2$ (R8).

$$HO_2 + HO_2 \xrightarrow{M} H_2O_2 + O_2 \quad (R7)$$

$$HO_2 + CH_3C(O)O_2 \longrightarrow \text{products} \quad (R8)$$

This was achieved by using sufficiently low initial radical concentrations such that the decrease in the HO_2 signal from ~20-30 μs (i.e., after conversion of Cl to HO_2 and $CH_3C(O)O_2$ was completed) to ~50 μs was less than 5%.

At low temperatures, the range of experimental conditions that could be explored were additionally limited by the need to minimize the rapid loss of HO_2 by reaction with CH_3OH and/or with CH_3CHO via R9 and R10, respectively, such that Equation 6.8 was still valid.

$$HO_2 + CH_3OH \underset{M}{\overset{M}{\rightleftharpoons}} HO_2 \cdot CH_3OH \quad (R9)$$

$$HO_2 + CH_3CHO \underset{M}{\overset{M}{\rightleftharpoons}} HO_2 \cdot CH_3CHO \quad (R10)$$

The formation of the hydrogen-bonded adducts via R9 and R10 becomes more favored at lower temperatures. Previous studies have also shown that these adducts introduce additional loss processes for HO_2 via R11 and R12, resulting in an enhanced observed HO_2 decay rate that becomes more significant at lower temperatures, even

at relatively low CH_3OH and CH_3CHO concentrations [34] (Chapter 3).

$$HO_2 + HO_2 \cdot CH_3OH \longrightarrow \text{products} \quad \text{(R11)}$$

$$HO_2 + HO_2 \cdot CH_3CHO \longrightarrow \text{products} \quad \text{(R12)}$$

Therefore, $[CH_3OH]$ and $[CH_3CHO]$ were typically limited to less than $\sim 1 \times 10^{16}$ molecule cm^{-3} and $\sim 5 \times 10^{15}$ molecule cm^{-3}, respectively, for temperatures below T = 250 K in order to minimize the adduct formation and rapid loss of HO_2. Using the previously determined equilibrium constants for R9 and R10 (to be reported in a separate publication), the upper limit of the uncertainty in the HO_2 yield, calculated from the highest $[CH_3OH]$ and $[CH_3CHO]$ used, was ~2% at T = 297.1 K and ~20% at T = 230.3 K.

6.3.1 Rate constant of Cl + CH_3OH (k_1)

R1 was investigated by measuring the formation signal of HO_2 in the absence of CH_3CHO at various concentrations of CH_3OH. In the absence of CH_3CHO, the integrated rate law for HO_2 is given by Equation 6.11:

$$[HO_2] = [Cl]_0 - [Cl]_0 e^{-k_1' t} \quad (6.11)$$

The data were fit with a single exponential function with an effective rate constant, k_1', as given by Equation 6.9. The HO_2 formation curves measured at T = 297.1 K and at T = 230.3 K using varying $[CH_3OH]$ are shown in Figure 6.1(a) and Figure 6.1(b), respectively. Both figures demonstrate that the HO_2 formation rate increases with increasing $[CH_3OH]$, as expected. Figure 6.1(a) shows that at room temperature, the HO_2 signals level off to a common value by ~50 μs, indicating complete conversion of Cl to HO_2 without significant subsequent loss of HO_2 via reaction with $[CH_3OH]$ (R9).

On the other hand, the HO_2 signals in Figure 6.1(b) do not level off to the same value; rather, the yields of HO_2 appear to decrease with increasing $[CH_3OH]$. The negative dependence of the HO_2 yield on $[CH_3OH]$ is attributed to the rapid loss of HO_2 from the formation of the hydrogen-bonded adduct with CH_3OH (R9). This effect was evident at temperatures below 250 K for $[CH_3OH] > 1 \times 10^{16}$ molecule cm^{-3}, which was used as the upper limit of the range of $[CH_3OH]$ that was used so that Equation 6.11 was still valid. $[Cl]_0$ was also kept below 1×10^{14} molecule cm^{-3} for T < 250 K to decrease the HO_2 loss rate; at T = 230.3 K, however, rapid loss of HO_2 could not completely be avoided even at the lowest $[Cl]_0$ and $[CH_3OH]$

conditions, and the reported k_1 at this temperature is likely overestimated. Based on the equilibrium constant of R9 determined in a separate study, approximately 15% of HO_2 is the predicted to be complexed at the highest $[CH_3OH] = 8.5 \times 10^{15}$ molecule cm^{-3}, which would translate to an uncertainty of 30% the fitted value of k_1'.

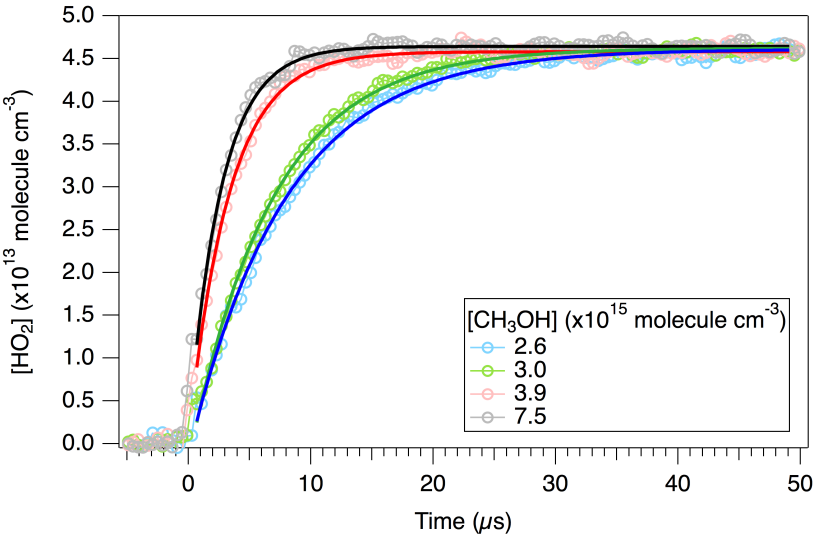

(a)

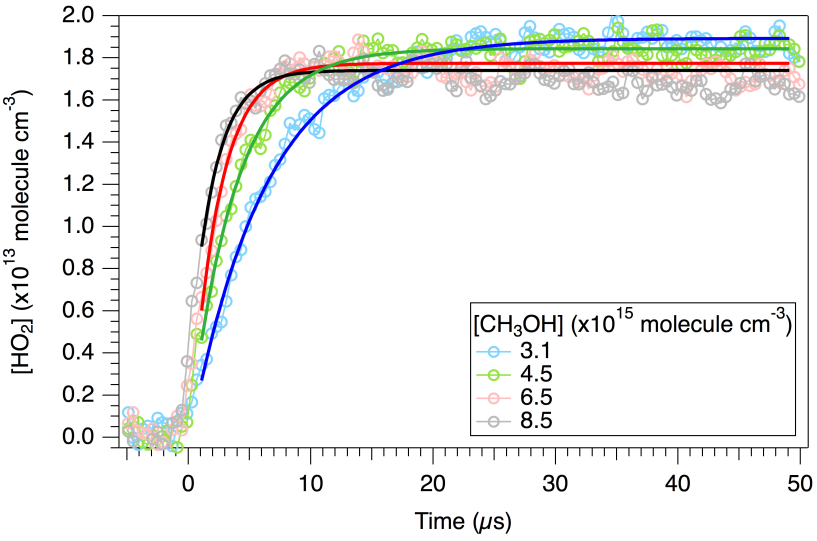

(b)

Figure 6.1: Example data demonstrating pseudo-first order growths of HO_2 using varying $[CH_3OH]$ with $[CH_3CHO] = 0$ at (a) T = 297.1 K, $[Cl]_0 = 4.6 \times 10^{13}$ molecule cm^{-3}, and (b) T = 230.3 K, $[Cl]_0 = 1.8 \times 10^{13}$ molecule cm^{-3}.

The measured values of k_1' at each temperature were plotted against $[CH_3OH]$ and total linear least-squares regressions to the data were used to determine k_1. The pseudo-first order plots of R1 at three temperatures are shown in Figure 6.2. The fitted values of k_1 are tabulated in 6.1 along with the range of experimental conditions

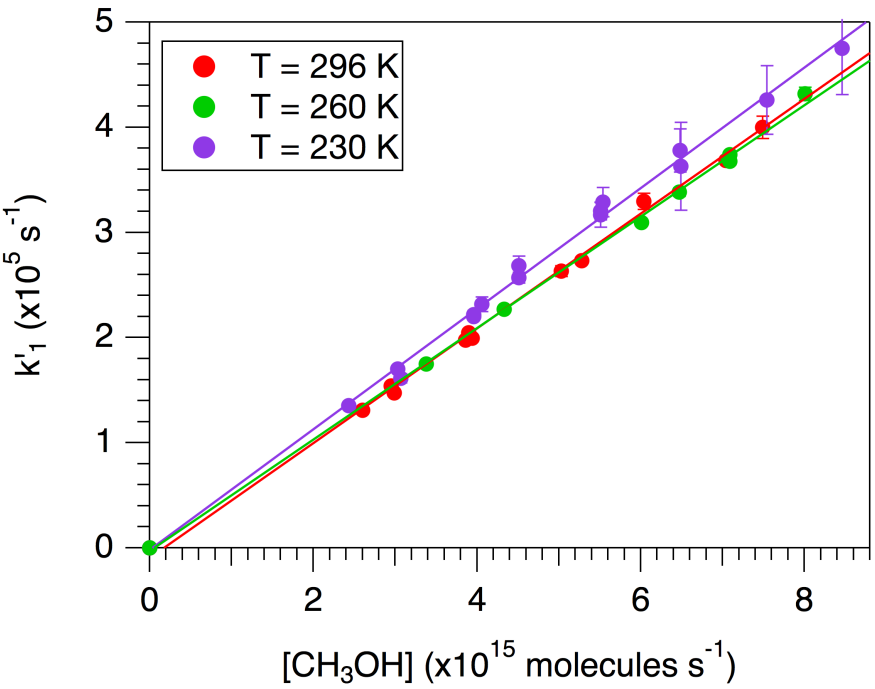

Figure 6.2: Plot of k_1 as a function of CH_3OH at T = 230.3 K, 260.1 K, and 297.1 K.

that were used to measure $k_1^{'}$. The uncertainties in k_1 (1σ) include the random errors in $k_1^{'}$ (typical: ~1 - 2%, maximum: ~10%) as well as systematic errors in the pressures, flows, and temperatures (total uncertainty in $[CH_3OH]$: ~2.5%).

Table 6.1: Experimental conditions for determination of k_1. Uncertainties in k_1 are 1σ.

T (K)	$[O_2]^a$	$[Cl_2]^b$	$[CH_3OH]^b$	$[Cl]_0{}^c$	$k_1{}^d$
297.1	1.58	1.49	2.60 - 7.49	4.5	5.58 ± 0.18
294.8	1.58	5.30	2.99 - 8.84	19	5.53 ± 0.21
280.2	1.66	1.56 - 3.8	2.98 - 8.01	5.1 - 13	5.21 ± 0.16
269.8	1.72	1.20 - 2.44	2.45 - 9.13	5.2 - 9.1	5.44 ± 0.14
260.1	1.79	1.68 - 3.8	3.38 - 8.01	6.0 - 12	5.33 ± 0.17
250.4	1.86	1.93 - 5.29	5.21 - 12.1	7.0 - 18	5.42 ± 0.15
240.3	1.93	1.82 - 3.8	2.95 - 6.47	5.0 - 9.0	5.39 ± 0.23
230.3	2.02	0.75 - 1.90	2.43 - 8.46	1.8 - 5.2	5.99 ± 0.21

[a]Units: 10^{18} molecule cm^{-3}
[b]Units: 10^{15} molecule cm^{-3}
[c]Units: 10^{13} molecule cm^{-3}
[d]Units: 10^{-11} cm^3 $molecule^{-1}$ s^{-1}

The Arrhenius expression was found to be $k_1(T) = 5.02^{+1.8}_{-1.5} \times 10^{-11} \exp[(20 \pm 88)/T]$ cm^3 $molecule^{-1}$ s^{-1}. Within experimental uncertainty, the rate constant

was temperature-independent over the temperature range 230.3 - 297.1 K. An average value of $k_1 = (5.45 \pm 0.37) \times 10^{-11}$ cm^3 molecule^{-1} s^{-1} (2σ uncertainty) was determined from the values measured at each temperature weighted by the corresponding uncertainties. The results are in excellent agreement with previous measurements and with the recommended values from the JPL and IUPAC data evaluations. Table 6.2 compares the results from this work with those of previous works in the literature.

Table 6.2: Comparison of measured k_1 with literature values

Ref	T (K)	P (Torr)	k_1 [a]	Method [b]
Michael et al. [22]	200 - 500	760	6.33 ± 1.40	FP/RF
Payne et al. [10]	298	1	5.1 ± 1.0	DF/MS
Wallington et al. [11]	295	760	4.57 ± 0.40	RR/UVP/GC[c]
Lightfoot et al. [23]	248 - 573	210 - 760	5.3 ± 2.4	RR/FP/UVA[d]
Nelson et al. [12]	298	730 - 750	4.79 ± 0.36	RR/UVP/GC[e]
Dóbé et al. [13]	298	1.35	6.14 ± 1.33	DF/EPR
Tyndall et al. [14]	295	700	5.1 ± 0.4	PLP/RF
			5.6 ± 0.6	RR/PLP/RF[c,f]
Smith et al. [15]	295	10	5.6 ± 0.2	PLP/IR
Seakins et al. [16]	298	25	5.83 ± 0.77	PLP/IR
			5.38 ± 0.25	PLP/CL
Taketani et al. [17]	295	3	5.35 ± 0.24	PLP/LIF
Garzón et al. [24]	264 - 382	20 - 200	$(35.5 \pm 2.2)\exp[-(559 \pm 40)/T]$	PLP/RF
Kaiser and Wallington [25]	291 - 475	500 - 950	$8.6 \pm 1.3\exp[-(167 \pm 60)/T]$	RR/UVP/GC[c]
This work	230.3 - 297.1	100	5.45 ± 0.37	PLP/IR
JPL [31]	200 - 253		5.5	
IUPAC [33]	200 - 400		$7.1\exp(-75/T)$	

[a] Units: 10^{-11} cm^3 molecule^{-1} s^{-1}; errors are 2σ

[b] FP = flash photolysis; DF = discharge flow; PLP = pulsed laser photolysis; UVP = UV photolysis; MS = mass spectrometry; GC = gas chromatography; UVA = UV absorption; EPR = electron paramagnetic resonance; RF = resonance fluorescence; IR = IR absorption; CL = chemical luminescence; LIF = laser-induced fluorescence; FTIR = Fourier transform IR spectroscopy; RR= relative rate.

[c] Reference reaction: $Cl + C_2H_6$; $k_{ref} = 5.7 \times 10^{-11}$ cm^3 molecule^{-1} s^{-1}

[d] $Cl + CH_4$; $k_{ref} = 1.0 \times 10^{-13}$ cm^3 molecule^{-1} s^{-1}

[e] $Cl + c\text{-}C_6H_{12}$; $k_{ref} = 3.11 \times 10^{-10}$ cm^3 molecule^{-1} s^{-1}

[f] Reference reaction: $Cl + C_2H_4$; $k_{ref} = 9.3 \times 10^{-11}$ cm^3 molecule^{-1} s^{-1}

The uncertainty in the average value of k_1 is the weighted standard deviation and includes both random errors in the fits and systematic errors in the measured concentrations of [CH_3OH]; systematic errors from secondary chemistry are not included. Under the conditions of these experiments, loss of HO_2 from R7 is estimated to be less than 5% across all temperatures, contributing to less than 10% error in the fitted values of k_1'. For temperatures below 250 K, the loss of HO_2 via R11 becomes more significant; at T = 230.3 K, this is estimated to introduce between 1% to 30% error to k_1' at the lowest and largest [CH_3OH].

6.3.2 Rate constant of Cl + CH_3CHO (k_3)

In the presence of CH_3CHO, a fraction of the Cl radicals is lost via R3, and the integrated rate law for HO_2 is given by Equation 6.12:

$$[HO_2] = \left(\frac{k_1^{'}}{k_{\text{eff}}}\right)[Cl]_0(1 - e^{-k_{\text{eff}}t}) \tag{6.12}$$

where

$$k_{\text{eff}} = k_1^{'} + k_3^{'} \tag{6.13}$$

$k_3^{'}$ was measured at each temperature for varying concentrations of CH_3OH and CH_3CHO. For data sets where the CH_3CHO was varied for a fixed amount of CH_3OH, it was confirmed that the intercept of the linear fit to k_{eff} vs CH_3CHO yielded $k_1[CH_3OH]$, where k_1 was consistent within experimental uncertainty with the measured value of 5.45×10^{-11} cm^3 molecule^{-1} s^{-1} (Table 6.6). From Equation 6.13, $k_3^{'}$ was calculated using the value of k_1 determined in this work. Figure 6.3 shows a plot of $k_3^{'}$ versus $[CH_3CHO]$ for three different temperatures. Data from all other temperatures were revealed to have similar linear dependences and have been excluded in the figure for clarity. Values of k_3 at each temperature were determined from the slopes of the linear fits to the data.

The average value of k_3 determined at each temperature and the range of precursor and initial radical concentrations that were used are summarized in Table 6.3. The uncertainties in k_3 (1σ) include the random errors in $k_3^{'}$ (typical: ~2 - 3%, maximum: ~10%) as well as systematic errors in k_{eff} and in the pressures, flows, and temperatures (total uncertainty in $[CH_3CHO]$: ~5%).

The Arrhenius expression was found to be $k_3(T) = 6.38^{+2.4}_{-2.0} \times 10^{-11} \exp[(56 \pm 90)/T]$ cm^3 molecule^{-1} s^{-1}. Similarly to R1, R3 was revealed to have no discernible temperature dependence in the temperature range T = 230.3 - 297.1 K, with an average value of $k_3 = (8.00 \pm 1.27) \times 10^{-11}$ cm^3 molecule^{-1} s^{-1} (2σ uncertainty). The uncertainty is the weighted standard deviation and includes both systematic and random errors. This is in excellent agreement with previous measurements and with the IUPAC recommendation (Table 6.4).

6.4 Conclusion

The absolute rate constants of the reactions of Cl atoms with CH_3OH and CH_3CHO have been determined at 100 Torr over the temperature range 230.3 K -

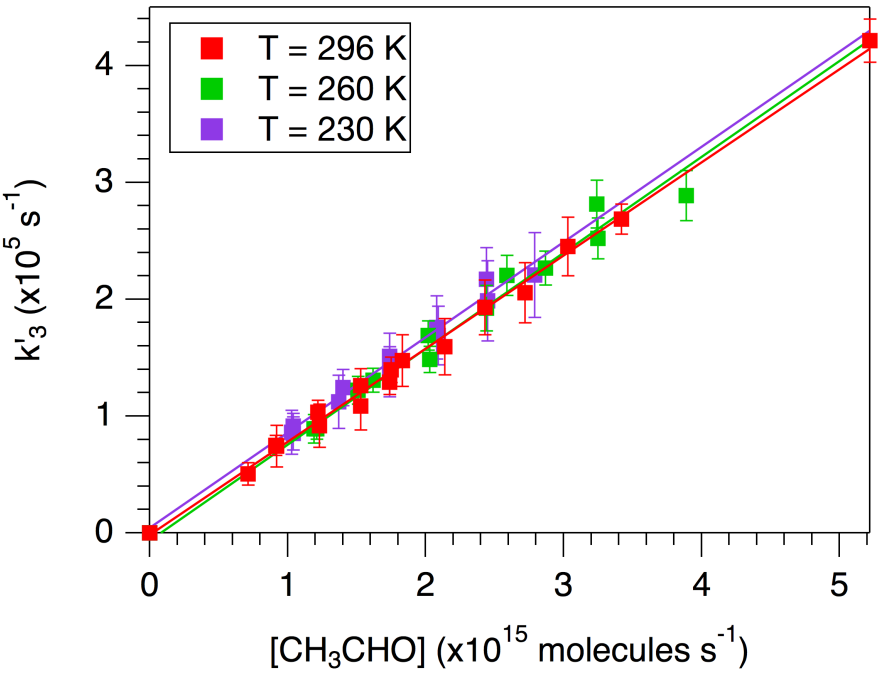

Figure 6.3: Plot of k_3 as a function of CH_3CHO at T = 230 K, 260 K, and 297 K shown with linear fits. All other temperatures have been excluded for clarity. Total linear regression

Table 6.3: Experimental conditions for determination of k_3. Uncertainties in k_3 are 1σ.

T (K)	$[O_2]^a$	$[Cl_2]^b$	$[CH_3OH]^b$	$[CH_3CHO]^b$	$[CH_3OH]/[CH_3CHO]$	$[Cl]_0{}^c$	$k_3{}^d$
297.1	1.58	3.02 - 5.29	3.90	0.71 - 5.22	2.25 - 6.60	4.5	8.16 ± 0.54
294.8	1.58	1.49	3.00 - 6.08	0.92 - 3.03	0.75 - 5.46	19	7.61 ± 0.89
280.2	1.66	1.56	2.97 - 4.99	0.95 - 1.93	1.87 - 6.80	5.1 - 13	7.24 ± 1.17
269.8	1.72	1.61 - 2.12	4.01 - 6.06	0.97 - 5.11	0.97 - 5.14	5.3 - 7.5	7.78 ± 0.50
260.1	1.79	1.68	3.44 - 4.40	1.19 - 3.89	1.12 - 3.73	6.0	8.21 ± 0.63
250.4	1.86	1.93 - 3.53	5.23 - 6.35	1.26 - 8.43	0.62 - 4.14	7.1 - 1.2	8.11 ± 0.37
240.3	1.93	1.82	2.96 - 5.98	0.98 - 4.56	1.31 - 6.10	5.0	7.95 ± 0.61
230.3	2.02	0.75	3.08 - 5.10	1.03 - 2.80	1.45 - 4.93	1.8	8.16 ± 1.18

[a]Units: 10^{18} molecule cm^{-3}
[b]Units: 10^{15} molecule cm^{-3}
[c]Units: 10^{13} molecule cm^{-3}
[d]Units: 10^{-11} cm^3 $molecule^{-1}$ s^{-1}

297.1 K by measuring the formation rate of HO_2 in various relative concentrations of CH_3OH and CH_3CHO. Both reactions were found to be temperature independent over this temperature range, and the values of the rate constants are in excellent agreement with previous measurements and support the current recommendations by the NASA/JPL and IUPAC Panels.

Table 6.4: Comparison of measured k_3 with literature values

Ref	T (K)	P (Torr)	k_3[a]	Method [b]
Niki et al. [18]	298	700	7.6 ± 0.4	RR/UVP/FTIR[c]
Wallington et al. [11]	295	760	8.45 ± 0.79	RR/UVP/GC[c]
Bartels et al. [19]	298	0.75	6.0 ± 0.9	RR/DF/MS[c]
Payne et al. [26]	210 - 343	25 - 200	6.6 ± 1.4	FP/RF
Scollard et al. [20]	298	730 - 750	7.9 ± 0.6	RR/UVP/GC[d]
Tyndall et al. [14]	295	700	7.3 ± 0.7	PLP/RF
			8.4 ± 1.0	RR/PLP/RF[c,e]
Kegley-Owen et al. [21]	298	10 - 50	7.5 ± 0.8	PLP/IR
Smith et al. [15]	295	10	8.3 ± 0.1	PLP/IR
Seakins et al. [16]	298	25	7.7 ± 1.1	PLP/IR
	298		8.8 ± 1.5	PLP/CL
This work	230.3 - 297.1	100	8.00 ± 1.27	PLP/IR
IUPAC Panel [33]	210 - 340		8.0	

[a]Units: 10^{-11} cm^3 molecule^{-1} s^{-1}; errors are 2σ

[b]FP = flash photolysis; PLP = pulsed laser photolysis; UV = UV photolysis; RF = resonance fluorescence; IR = IR absorption; CL = CL chemical luminescence; FTIR = Fourier transform IR spectroscopy; GC = gas chromatography; MS = mass spectrometry; RR= relative rate.

[c]Reference reaction: Cl + C_2H_6; $k_{ref} = 5.7 \times 10^{-11}$ cm^3 molecule^{-1} s^{-1}

[d]Reference reaction: Cl + $(CH_3)_2O$; $k_{ref} = 1.76 \times 10^{-10}$ cm^3 molecule^{-1} s^{-1}

[e]Reference reaction: Cl + C_2H_4; $k_{ref} = 9.3 \times 10^{-11}$ cm^3 molecule^{-1} s^{-1}

6.5 Acknowledgements

This research was carried out by the Jet Propulsion Laboratory, California Institute of Technology, under contract with the National Aeronautics and Space Administration (NASA). The authors thank the National Science Foundation (NSF), the NASA Earth and Space Science Fellowship (NESSF), and NASA's Upper Atmospheric Research Program (UARP) and Tropospheric Chemistry Program for financial support.

6.6 Supplementary material

6.6.1 Rate constant of Cl + CH_3OH (k_1)

A complete list of experimental conditions used for the determination of k_1 is provided in Table 6.5. The values of k_1 (1σ uncertainties) were determined from the total linear least-squares fits to the pseudo-first order plots, as described in the main text.

Table 6.5: Full list of experimental conditions for determination of k_1 from data collected with $[CH_3CHO] = 0$. Values of k_1 determined from pseudo-first order analysis are also provided with 1σ uncertainties.

T (K)	$[O_2]$ ($\times 10^{18}$ cm^{-3})	$[Cl_2]$ ($\times 10^{15}$ cm^{-3})	$[CH_3OH]$ ($\times 10^{15}$ cm^{-3})	$[Cl]_0$ ($\times 10^{13}$ cm^{-3})	k_1 ($\times 10^{-11}$ cm^3 s^{-1})
297.1 ± 0.2	1.58	5.30	2.99	19	5.58 ± 0.18
			3.90		
			3.94		
			5.28		
			7.04		
			8.84		
294.8 ± 0.2	1.58	1.49	2.60	4.5	5.53 ± 0.21
			2.95		
			3.86		
			5.03		
			6.04		
			7.49		
280.2 ± 0.1	1.66	1.56	2.98	5.1	5.21 ± 0.16
			4.01		
			5.04		
			5.97		
			7.00		
			8.01		
		2.30	6.96	8.0	
		3.03	6.97	10.	
		3.81	7.01	13	
269.8 ± 0.6	1.72	1.20	2.45	5.3	5.44 ± 0.14
			4.08		
			5.54		
			6.09		
		1.62	2.99	5.3	
		1.61	5.01	6.0	
			6.03		
		2.12	9.13	7.5	
		2.44	4.32	9.0	
			5.02		
260.1 ± 0.1	1.79	1.68	3.38	6.0	5.33 ± 0.17

T (K)	$[O_2]$ ($\times 10^{18}$ cm^{-3})	$[Cl_2]$ ($\times 10^{15}$ cm^{-3})	$[CH_3OH]$ ($\times 10^{15}$ cm^{-3})	$[Cl]_0$ ($\times 10^{13}$ cm^{-3})	k_1 ($\times 10^{-11}$ cm^3 s^{-1})
			4.33		
			6.47		
			8.01		
		3.02	7.07	10.	
		2.32	7.09	7.9	
		3.81	7.09	12	
		3.81	6.01	12	
250.4 ± 0.1	1.86	1.93	5.21	7.1	5.42 ± 0.15
			6.27		
			7.83		
			10.1		
			12.1		
		3.54	6.38	12	
			9.61		
			10.7		
		5.29	4.58	18	
			5.71		
			7.39		
			8.61		
			9.65		
			10.7		
240.3 ± 0.1	1.93	1.82	2.95	5.0	5.34 ± 0.23
			4.01		
			4.97		
			6.00		
			6.47		
		2.30	4.80	5.7	
		3.04	4.80	7.3	
		3.81	4.80	9.0	
230.3 ± 0.1	2.02	1.90	2.43	5.2	5.99 ± 0.21
			3.03		
			3.96		
		1.13	3.96	3.1	
			4.51		
			5.51		
		0.85	5.51	1.9	
			6.49		
		0.75	3.07	1.8	
			4.06		
			4.51		
			5.54		
			6.48		
			7.54		
			8.46		

6.6.2 Rate constant of Cl + CH_3CHO (k_3)

Table 6.6 shows a complete, detailed list of the experimental conditions that were used for the determination of k_3. Values of k_3 and k_1 (1σ uncertainties) listed in this table were determined from the slopes and intercepts, respectively, of the total linear least-square fits to the plots of k_{eff} versus [CH_3CHO] for data sets with a fixed [CH_3OH] (data sets with less than four different values of [CH_3CHO] for a given value of [CH_3OH] were omitted for this analysis). This is only to demonstrate that k_1 derived from the intercepts was consistent with the value determined in the experiments carried out in the absence of CH_3CHO. The final values of k_1 at each temperature were derived from the analysis method described in the main text and are listed in Table 6.3.

Table 6.6: Full list of experimental conditions and for the determination of k_3. Values of k_3 and k_1 (1σ uncertainties) listed here are the slopes and intercepts, respectively, of the total linear least-square fits to the plots of k_{eff} versus [CH_3CHO].

T (K)	[O_2] ($\times 10^{18}$ cm^{-3})	[Cl_2] ($\times 10^{15}$ cm^{-3})	[CH_3OH] ($\times 10^{15}$ cm^{-3})	[CH_3CHO] ($\times 10^{15}$ cm^{-3})	[Cl]$_0$ ($\times 10^{13}$ cm^{-3})	k_1 ($\times 10^{-11}$ cm^3 s^{-1})	k_3 ($\times 10^{-11}$ cm^3 s^{-1})
297.1 ± 0.2	1.58	3.02	3.90	1.74	4.5	5.24 ± 0.10	8.16 ± 0.25
		5.29	3.90	0.71			
				1.75			
				3.42			
				5.22			
294.8 ± 0.2	1.58	1.49	3.00	0.92	4.5		
				1.22			
				1.53			
			6.08	0.92		5.41 ± 0.24	7.89 ± 0.82
				1.23			
				1.53			
				1.83			
				2.14			
				2.43			
				2.72			
				3.03			
280.2 ± 0.1	1.66	1.56	2.97	0.95	5.1		
				1.26			
				1.58			
			4.00	0.95			
				1.27			
				1.59			
			4.50	0.96			

T (K)	$[O_2]$ ($\times 10^{18}$ cm^{-3})	$[Cl_2]$ ($\times 10^{15}$ cm^{-3})	$[CH_3OH]$ ($\times 10^{15}$ cm^{-3})	$[CH_3CHO]$ ($\times 10^{15}$ cm^{-3})	$[Cl]_0$ ($\times 10^{13}$ cm^{-3})	k_1 ($\times 10^{-11}$ cm^3 s^{-1})	k_3 ($\times 10^{-11}$ cm^3 s^{-1})
				1.27			
			4.99	1.93			
269.8 ± 0.6	1.72	1.61	6.06	1.18	6.0		
				1.55			
				1.96			
		2.12	4.92	1.19	7.5	5.14 ± 0.68	8.05 ± 1.65
				1.95			
				2.34			
				3.15			
				3.96			
				5.11			
		1.62	2.45	0.97	5.3		
				1.32			
			2.99	1.33			
				1.67			
			4.01	1.01			
				1.66			
				2.00			
260.1 ± 0.1	1.79	1.68	3.44	1.21	6.0	5.26 ± 1.11	8.06 ± 2.17
				1.62			
				2.03			
				2.44			
				2.87			
				3.25			
			4.40	1.19		5.31 ± 0.98	8.36 ± 2.24
				1.51			
				2.02			
				2.59			

T (K)	$[O_2]$ ($\times 10^{18}$ cm^{-3})	$[Cl_2]$ ($\times 10^{15}$ cm^{-3})	$[CH_3OH]$ ($\times 10^{15}$ cm^{-3})	$[CH_3CHO]$ ($\times 10^{15}$ cm^{-3})	$[Cl]_0$ ($\times 10^{13}$ cm^{-3})	k_1 ($\times 10^{-11}$ cm^3 s^{-1})	k_3 ($\times 10^{-11}$ cm^3 s^{-1})
				3.24			
				3.89			
250.4 ± 0.1	1.86	1.93	5.23	1.26	7.1	5.46 ± 0.73	8.54 ± 1.44
				2.52			
				3.80			
				5.06			
				6.34			
				7.55			
				8.43			
		3.54	6.35	2.06	12	5.70 ± 0.94	7.95 ± 1.61
				3.29			
				4.18			
				5.41			
				6.80			
				8.43			
240.3 ± 0.1	1.93	1.82	2.96	0.98	5.0		
				1.30			
				1.62			
				1.95			
			3.47	1.11			
				1.50			
				1.95			
				2.28			
			5.98	0.98		5.50 ± 0.40	7.92 ± 1.23
				1.31			
				1.64			
				1.95			
				2.28			

T (K)	$[O_2]$ ($\times 10^{18}$ cm^{-3})	$[Cl_2]$ ($\times 10^{15}$ cm^{-3})	$[CH_3OH]$ ($\times 10^{15}$ cm^{-3})	$[CH_3CHO]$ ($\times 10^{15}$ cm^{-3})	$[Cl]_0$ ($\times 10^{13}$ cm^{-3})	k_1 ($\times 10^{-11}$ cm^3 s^{-1})	k_3 ($\times 10^{-11}$ cm^3 s^{-1})
				2.61			
				2.94			
				3.25			
				3.88			
				4.56			
230.3 ± 0.1	2.02	0.75	3.08	1.04	1.8	5.49 ± 1.38	8.71 ± 3.03
				1.40			
				1.74			
				2.80			
				2.44			
			4.05	1.04		5.56 ± 1.15	7.84 ± 2.91
				1.74			
				2.09			
				2.45			
				2.79			
			5.10	1.03			
				1.37			

References

[1] Moortgat, G.; Veyret, B.; Lesclaux, R. Absorption Spectrum and Kinetics of Reactions of the Acetylperoxy Radical. **1989**, *93*, 2362–2368.

[2] Crawford, M. A.; Wallington, T. J.; Szente, J. J.; Maricq, M. M.; Francisco, J. S. Kinetics and Mechanism of the Acetylperoxy + HO2 Reaction. *The Journal of Physical Chemistry A* **1999**, *103*, 365–378.

[3] Tomas, A.; Villenave, E.; Lesclaux, R. Reactions of the HO2 Radical with CH3CHO and CH3C(O)O2 in the Gas Phase. *The Journal of Physical Chemistry A* **2001**, *105*, 3505–3514.

[4] Hasson, A. S.; Tyndall, G. S.; Orlando, J. J. A Product Yield Study of the Reaction of HO2 Radicals with Ethyl Peroxy (C2H5O2), Acetyl Peroxy (CH3C(O)O2), and Acetonyl Peroxy (CH3C(O)CH2O2) Radicals. *The Journal of Physical Chemistry A* **2004**, *108*, 5979–5989.

[5] Le Crâne, J.-P.; Rayez, M.-T.; Rayez, J.-C.; Villenave, E. A Reinvestigation of the Kinetics and the Mechanism of the CH3C(O)O2 + HO2 Reaction Using Both Experimental and Theoretical Approaches. *Physical Chemistry Chemical Physics* **2006**, *8*, 2163–2171.

[6] Jenkin, M. E.; Hurley, M. D.; Wallington, T. J. Investigation of the Radical Product Channel of the CH3C(O)O2 + HO2 Reaction in the Gas Phase. *Physical Chemistry Chemical Physics* **2007**, *9*, 3149–3162.

[7] Dillon, T. J.; Crowley, J. N. Direct Detection of OH Formation in the Reactions of HO2 with CH3C(O)O2 and Other Substituted Peroxy Radicals. *Atmospheric Chemistry and Physics* **2008**, *8*, 4877–4889.

[8] Groß, C. B. M.; Dillon, T. J.; Schuster, G.; Lelieveld, J.; Crowley, J. N. Direct Kinetic Study of OH and O3 Formation in the Reaction of CH3C(O)O2 with HO2. *The Journal of Physical Chemistry A* **2014**, *118*, 974–985.

[9] Winiberg, F. A. F.; Dillon, T. J.; Orr, S. C.; Groß, C. B. M.; Bejan, I.; Brumby, C. A.; Evans, M. J.; Smith, S. C.; Heard, D. E.; Seakins, P. W. Direct Measurements of OH and Other Product Yields from the HO2 + CH3C(O)O2 Reaction. *Atmos. Chem. Phys.* **2016**, *16*, 4023–4042.

[10] Payne, W. A.; Brunning, J.; Mitchell, M. B.; Stief, L. J. Kinetics of the Reactions of Atomic Chlorine with Methanol and the Hydroxymethyl Radical with Molecular Oxygen at 298 K. *International Journal of Chemical Kinetics* **1988**, *20*, 63–74.

[11] Wallington, T. J.; Skewes, L. M.; Siegl, W. O.; Wu, C.-H.; Japar, S. M. Gas Phase Reaction of Cl Atoms with a Series of Oxygenated Organic Species at 295 K. *International Journal of Chemical Kinetics* **1988**, *20*, 867–875.

[12] Nelson, L.; Rattigan, O.; Neavyn, R.; Sidebottom, H.; Treacy, J.; Nielsen, O. J. Absolute and Relative Rate Constants for the Reactions of Hydroxyl Radicals and Chlorine Atoms with a Series of Aliphatic Alcohols and Ethers at 298 K. *International Journal of Chemical Kinetics* **1990**, *22*, 1111–1126.

[13] Dóbé, S.; Otting, M.; Temps, F.; Wagner, H. G.; Ziemer, H. Fast Flow Kinetic Studies of the Reaction CH2OH + HCl CH3OH + Cl. The Heat of Formation

of Hydroxymethyl. *Berichte der Bunsengesellschaft für physikalische Chemie* **1993**, *97*, 877–883.

[14] Tyndall, G. S.; Orlando, J. J.; Kegley-Owen, C. S.; Wallington, T. J.; Hurley, M. D. Rate Coefficients for the Reactions of Chlorine Atoms with Methanol and Acetaldehyde. *International Journal of Chemical Kinetics* **1999**, *31*, 776–784.

[15] Smith, J. D.; DeSain, J. D.; Taatjes, C. A. Infrared Laser Absorption Measurements of HCl(V=1) Production in Reactions of Cl Atoms with Isobutane, Methanol, Acetaldehyde, and Toluene at 295 K. *Chemical Physics Letters* **2002**, *366*, 417–425.

[16] Seakins, P. W.; Orlando, J. J.; Tyndall, G. S. Rate Coefficients and Production of Vibrationally Excited HCl from the Reactions of Chlorine Atoms with Methanol, Ethanol, Acetaldehyde and Formaldehyde. *Physical Chemistry Chemical Physics* **2004**, *6*, 2224–2229.

[17] Taketani, F.; Takahashi, K.; Matsumi, Y.; Wallington, T. J. Kinetics of the Reactions of Cl*(2P1/2) and Cl(2P3/2) Atoms with CH3OH, C2H5OH, n-C3H7OH, and i-C3H7OH at 295 K. *The Journal of Physical Chemistry A* **2005**, *109*, 3935–3940.

[18] Niki, H.; Maker, P. D.; Savage, C. M.; Breitenbach, L. P. FTIR Study of the Kinetics and Mechanism for Chlorine-Atom-Initiated Reactions of Acetaldehyde. *The Journal of Physical Chemistry* **1985**, *89*, 588–591.

[19] Bartels, M.; Hoyermann, K.; Lange, U. An Experimental Study of the Reactions CH3CHO + Cl, C2H4O + Cl, and C2H4O + F in the Gas-Phase. *Berichte der Bunsengesellschaft für physikalische Chemie* **1989**, *93*, 423–427.

[20] Scollard, D. J.; Treacy, J. J.; Sidebottom, H. W.; Balestra-Garcia, C.; Laverdet, G.; LeBras, G.; MacLeod, H.; Teton, S. Rate Constants for the Reactions of Hydroxyl Radicals and Chlorine Atoms with Halogenated Aldehydes. *The Journal of Physical Chemistry* **1993**, *97*, 4683–4688.

[21] Kegley-Owen, C. S.; Tyndall, G. S.; Orlando, J. J.; Fried, A. Tunable Diode Laser Studies of the Reaction of Cl Atoms with CH3CHO. *International Journal of Chemical Kinetics* **1999**, *31*, 766–775.

[22] Michael, J. V.; Nava, D. F.; Payne, W. A.; Stiefb), L. J. Rate Constants for the Reaction of Atomic Chlorine with Methanol and Dimethyl Ether from 200 to 500 K. *The Journal of Chemical Physics* **1979**, *70*, 3652–3656.

[23] Lightfoot, P. D.; Veyret, B.; Lesclaux, R. Flash Photolysis Study of the Methylperoxy + Hydroperoxy Reaction between 248 and 573 K. *The Journal of Physical Chemistry* **1990**, *94*, 708–714.

[24] Garzón, A.; Cuevas, C. A.; Ceacero, A. A.; Notario, A.; Albaladejo, J.; Fernández-Gómez, M. Atmospheric Reactions Cl+CH3–(CH2)n–OH (N=0–4): A Kinetic and Theoretical Study. *The Journal of Chemical Physics* **2006**, *125*, 104305.

[25] Kaiser, E. W.; Wallington, T. J. Rate Constant of the Reaction of Chlorine Atoms with Methanol over the Temperature Range 291–475 K. *International Journal of Chemical Kinetics* **2010**, *42*, 113–116.

[26] Payne, W. A.; Nava, D. F.; Nesbitt, F. L.; Stief, L. J. Rate Constant for the Reaction of Atomic Chlorine with Acetaldehyde from 210 to 343 K. *The Journal of Physical Chemistry* **1990**, *94*, 7190–7193.

[27] Christensen, L. E.; Okumura, M.; Sander, S. P.; Friedl, R. R.; Miller, C. E.; Sloan, J. J. Measurements of the Rate Constant of HO2 + NO2 + N2 → HO2NO2 + N2 Using Near-Infrared Wavelength-Modulation Spectroscopy and UV-Visible Absorption Spectroscopy. *The Journal of Physical Chemistry A* **2004**, *108*, 80–91.

[28] Noell, A. C.; Alconcel, L. S.; Robichaud, D. J.; Okumura, M.; Sander, S. P. Near-Infrared Kinetic Spectroscopy of the HO2 and C2H5O2 Self-Reactions and Cross Reactions. *The Journal of Physical Chemistry A* **2010**, *114*, 6983–6995.

[29] Grieman, F. J.; Noell, A. C.; Davis-Van Atta, C.; Okumura, M.; Sander, S. P. Determination of Equilibrium Constants for the Reaction Between Acetone and HO2 Using Infrared Kinetic Spectroscopy. *The Journal of Physical Chemistry A* **2011**, *115*, 10527–10538.

[30] *FACSIMILE* version 4.1.41 [computer software]; Faringdon, Oxon, UK, 2003.

[31] Sander, S. P.; Abbat, J.; Barker, J.R.; Burkholder, J.B.; Huie, R.E.; Kolb, C.E.; Kurylo, M.J.; Wilmouth, D.M.; Orkin, V.L.; Wine, P.H. *Chemical Kinetics and Photochemical Data for Use in Atmospheric Studies, Evaluation No. 18*; Jet Propulsion Laboratory, Pasadena: JPL Publication 15-10, 2015.

[32] Atkinson, R.; Baulch, D. L.; Cox, R. A.; Crowley, J. N.; Hampson, R. F.; Hynes, R. G.; Jenkin, M. E.; Rossi, M. J.; Troe, J.; IUPAC Subcommittee Evaluated Kinetic and Photochemical Data for Atmospheric Chemistry: Volume II – Gas Phase Reactions of Organic Species. *Atmos. Chem. Phys.* **2006**, *6*, 3625–4055.

[33] Atkinson, R.; Baulch, D. L.; Cox, R. A.; Hampson, R. F.; Kerr, J. A.; Troe, J. Evaluated Kinetic and Photochemical Data for Atmospheric Chemistry: Supplement IV. IUPAC Subcommittee on Gas Kinetic Data Evaluation for Atmospheric Chemistry. *Journal of Physical and Chemical Reference Data* **1992**, *21*, 1125–1568.

[34] Christensen, L. E.; Okumura, M.; Hansen, J. C.; Sander, S. P.; Francisco, J. S. Experimental and Ab Initio Study of the HO2CH3OH Complex: Thermodynamics and Kinetics of Formation. *J. Phys. Chem. A* **2006**, *110*, 6948–6959.

Chapter 7

MEASUREMENTS OF THE UV ABSORPTION CROSS-SECTION AND REACTION RATE CONSTANTS OF $CH_3C(O)CH_2O_2$ AND THE INVESTIGATION OF THE HO_2 SELF REACTION RATE ENHANCEMENT BY $CH_3C(O)CH_3$

Abstract

Acetonylperoxy radicals ($CH_3C(O)CH_2O_2$) in the atmosphere are produced from the OH oxidation of acetone ($CH_3C(O)CH_3$). In remote regions of the world where NO_x concentrations are low, the primary loss of $CH_3C(O)CH_2O_2$ is reaction with HO_2 and other peroxy radicals. Previous studies on the kinetics of $CH_3C(O)CH_2O_2$ are scarce and are poorly constrained. In this work, the rate constants of the HO_2 + $CH_3C(O)CH_2O_2$ and $CH_3C(O)CH_2O_2$ self reaction were measured at room temperature and P = 100 Torr (in N_2) using the Infrared Kinetic Spectroscopy (IRKS) apparatus, which employed pulsed laser photolysis coupled with simultaneous IR and UV absorption spectroscopy. IRKS enabled time-resolved detection of HO_2 in the near-IR and $CH_3C(O)CH_2O_2$ in the UV at a wavelength that was isolated from absorption by other peroxy radicals. The UV absorption cross-sections of $CH_3C(O)CH_2O_2$, $\sigma(\lambda)$, were also measured over a narrow spectral region (λ = 300 - 315 nm) and compared to previous results.

We also investigated the impact on the kinetics by the adducts of HO_2 formed from the reaction of HO_2 with the radical precursors, CH_3OH and $CH_3C(O)CH_3$. At room temperature, CH_3OH had no effect on the observed HO_2 decay rate, as expected. Meanwhile, hydrogen-bonded adducts of HO_2 with $CH_3C(O)CH_3$ were found to significantly enhance the HO_2 self reaction rate.

7.1 Introduction

Acetone ($CH_3C(O)CH_3$) is among the most abundant oxygenated organic compounds in unpolluted regions of the atmosphere (low NO_x), with surface mixing ratios ranging from 500 to 2000 pptv[1]. $CH_3C(O)CH_3$ oxidation occurs either through photolysis (R1) or by reaction with OH radicals (R2).

$$CH_3C(O)CH_3 + h\nu \longrightarrow CH_3C(O) + CH_3 \quad \text{(R1)}$$

$$OH + CH_3C(O)CH_3 \longrightarrow CH_3C(O)CH_2 + H_2O \quad \text{(R2)}$$

Under tropospheric conditions, R2 occurs twice as fast as R1 and produces the acetonylperoxy radical ($CH_3C(O)CH_2O_2$) by reaction of $CH_3C(O)CH_2$ with O_2 (R3).

$$CH_3C(O)CH_2 + O_2 \xrightarrow{M} CH_3C(O)CH_2O_2 \quad \text{(R3)}$$

In the remote atmosphere, the primary loss processes of $CH_3C(O)CH_2O_2$ are the self reaction (R4) and reactions with other peroxy radicals, such as HO_2 (R5).

$$2\,CH_3C(O)CH_2O_2 \longrightarrow CH_3C(O)CH_2OH + CH_3C(O)CHO + O_2 \quad \text{(R4a)}$$
$$\longrightarrow 2\,CH_3C(O)CH_2O + O_2 \quad \text{(R4b)}$$

$$HO_2 + CH_3C(O)CH_2O_2 \longrightarrow CH_3C(O)CH_2OOH + O_2 \quad \text{(R5a)}$$
$$\longrightarrow CH_3C(O)CH_2O + OH + O_2 \quad \text{(R5b)}$$

Table 7.1 and Table 7.2 summarize all the previous studies of the R5 and R4, respectively. While product yields of R5 [2–5] and R4 have been reported previously in the literature, kinetics studies are sparse and have only been conducted at room temperature. For example, the rate constant of R4 (k_4) has only been measured by two studies [6, 7], one of which only provided an upper limit of the rate constant [7]. Both kinetics studies used UV absorption techniques to determine k_5 and k_4; however, there is disagreement in the reported values of the $CH_3C(O)CH_2O_2$ UV absorption cross-sections, which propagates into uncertainties in the measured rate constants. The rate constant of R5 (k_5) is also not well constrained as it has only been investigated by Bridier et al. [6]. Furthermore, no experimental temperature-dependence studies have yet been conducted for either of these reactions; thus, the current JPL and IUPAC recommendations for k_4 and k_5 are either only provided at room temperature [8] or the temperature dependences are estimated based on analogous reactions [9]. Additional experimental investigations of both of these reactions are clearly needed to reduce the uncertainties in the current recommended values.

The goal of this work was to resolve some of these issues by measuring k_5 and k_4 using simultaneous detection of HO_2 in the near-infrared (NIR) and the disappearance of $CH_3C(O)CH_2O_2$ in the UV. The UV absorption cross-sections of $CH_3C(O)CH_2O_2$, $\sigma(\lambda)$, were also measured over a narrow spectral region (λ = 300

Table 7.1: Summary of previous HO_2 + $CH_3C(O)CH_2O_2$ studies. FP = flash photolysis; PLP = pulsed laser photolysis; UVAS = UV absorption spectroscopy; HPLC = high performance liquid chromatography; FTIR = Fourier Transform infrared spectroscopy; LIF = laser induced fluorescence.

Ref.	T (K)	P (Torr)	Method	k_5 (cm^3 $molecule^{-1}$ s^{-1})	α_{5a} [a]	α_{5b} [b]
[6][c]	298	760	FP/UVAS	$(9.0 \pm 1.0) \times 10^{-12}$	assumed 1	assumed 0
[2]	298	800	UVP/FTIR/HPLC		0.33 ± 0.10	0.67 ± 0.20
[3]	296	700	UVP/FTIR			0.15 ± 0.08
[4]	298	~170	PLP/LIF			0.15 ± 0.10
[5]	295	800	UVP/FTIR/HPLC		0.75 ± 0.13	0.25 ± 0.13
IUPAC [8]	298			9.0×10^{-12}	0.85 ± 0.1	0.15 ± 0.1
JPL [9], [10]	298			$8.6 \times 10^{-13} \exp(700/T)$		
This work[d]	296	100	PLP/IR/UVAS			

Table 7.2: Summary of previous $CH_3C(O)CH_2O_2$ self reaction studies. PR = pulsed radiolysis; FP = flash photolysis; PLP = pulsed laser photolysis; UVAS = UV absorption spectroscopy; FTIR = Fourier Transform infrared spectroscopy; GC = gas chromatography.

Ref.	T (K)	P (Torr)	Method	k_4	α_{4a} [a]	α_{4b} [b]
[7][c]	298	760	PR/UVAS	$(8.3 \pm 1.6) \times 10^{-12}$		
[6][d]	298	760	FP/UVAS	$(9.0 \pm 1.0) \times 10^{-12}$		0.75 ± 0.1[e]
[11][f]		765	UVP/GC			0.50 ± 0.05
IUPAC [8]	298			8.0×10^{-12}	0.37	0.63 ± 0.2
This work[d]	296	100	PLP/IR/UVAS			

[a] $\alpha_{4a} = k_{4a}/k_4 = 1 - \alpha_{4b}$
[b] $\alpha_{4b} = k_{4b}/k_4 = 1 - \alpha_{4a}$
[c] SF_6 /$CH_3C(O)CH_3$ /O_2
[d] Cl_2/$CH_3C(O)CH_3$/O_2/N_2
[e] Derived by kinetic analysis of UV absorption time profiles obtained at several wavelengths
[f] Cl_2 /$CH_3C(O)CH_3$ /O_2 /NO_2 /N_2

- 315 nm) that is isolated from absorption by other peroxy radicals. Experiments were conducted to investigate the temperature dependence of k_5 and k_4 at 100 Torr in N_2 for the temperature range 230 - 340 K. This chapter presents a complete analysis of the kinetics at room temperature; for all other temperatures, general trends and qualitative assessments will be provided. Comprehensive analysis of the temperature dependence will be reported in a future publication. We also present kinetics measurements of the adducts of HO_2 formed from the reaction of HO_2 with the radical precursors, CH_3OH and $CH_3C(O)CH_3$. At room temperature, hydrogen-bonded adducts of HO_2 with $CH_3C(O)CH_3$ were found to significantly enhance the HO_2 self reaction rate, while those of CH_3OH had no effect on the observed HO_2 decay rate.

7.2 Experimental Methods

The experiments were carried out using the Infrared Kinetic Spectroscopy (IRKS) apparatus, which is described in detail in Chapter 2; thus, only a brief summary of the instrument and the details relevant to this work will be given. The experimental technique used pulsed laser photolysis (PLP) for radical generation, and simultaneous NIR wavelength modulation spectroscopy (WMS) and UV absorption spectroscopy for the real-time detection of HO_2 and $CH_3C(O)CH_2O_2$ radicals, respectively. Experiments were conducted in a jacketed, Pyrex flow cell measuring 175 cm in length and 2 inches in diameter. The temperature in the cell was controlled by flowing either heated H_2O or liquid nitrogen-cooled CH_3OH through the jacket. The cell temperature was measured by a calibrated, type-T thermocouple inserted into the jacket of the cell and in contact with the temperature-controlling fluid.

Reagent gas mixtures containing $Cl_2/CH_3OH/CH_3C(O)CH_3/O_2/N_2$ or $Cl_2/CH_3C(O)CH_3/O_2/N_2$ were pre-cooled and pre-mixed in a meter-long jacketed Pyrex manifold before entering the main flow cell. The flows of the precursor gases were regulated using mass flow controllers (MKS Instruments). The total flow rate was kept at ~2000 cm^3 (STP) min^{-1}, maintaining a total pressure of 100 ± 2 Torr with a residence time of 10 s. Pulsed, 351 nm light from a XeF excimer laser (301 Compex) operating in the constant energy mode (~120 - 150 mJ $pulse^{-1}$) was directed along the length of the cell to initiate the radical chemistry by photolyzing Cl_2 molecules. A photolysis repetition rate of 0.2 Hz was used, allowing for two photolysis events to occur per residence time.

$$Cl_2 + h\nu\,(351\,nm) \longrightarrow 2\,Cl \qquad \text{(R6)}$$

Subsequent reaction of Cl atoms with CH_3OH and $CH_3C(O)CH_3$ in the presence of O_2 produced HO_2 via R7 and R8, and $CH_3C(O)CH_2O_2$ via R9 and R3.

$$Cl + CH_3OH \longrightarrow CH_2OH + HCl \qquad \text{(R7)}$$

$$CH_2OH + O_2 \longrightarrow HO_2 + CH_2O \qquad \text{(R8)}$$

$$Cl + CH_3C(O)CH_3 \longrightarrow CH_3C(O)CH_2 + HCl \qquad \text{(R9)}$$

$$CH_3C(O)CH_2 + O_2 \xrightarrow{M} CH_3C(O)CH_2O_2 \qquad \text{(R3)}$$

Experiments on the $CH_3C(O)CH_2O_2$ UV absorption cross-section and self reaction kinetics were carried out in the absence of CH_3OH.

The total pressure inside the cell was monitored using an absolute capacitance

manometer (MKS Baratron). CH_3OH and $CH_3C(O)CH_3$ vapors were introduced into the cell by flowing N_2 through glass bubblers containing the liquid compounds, both held at 0 °C in temperature-controlled baths. The bubbler temperatures and pressures were measured using type-T thermocouples (Omega) and absolute capacitance manometers (MKS Baratron), respectively, and the vapor concentrations were calculated manometrically. Typical concentrations of the reagent gases were (molecule cm^{-3}): $[Cl_2] = (4.5 - 7.6) \times 10^{15}$, $[CH_3OH] = (3.9 - 8.6) \times 10^{15}$, $[CH_3C(O)CH_3] = (2.2 - 11) \times 10^{16}$, and $[O_2] = (0.74 - 2.2) \times 10^{18}$.

Collimated broadband UV light from a 150 W deuterium D_2 lamp (Hamamatsu L1314) made a single pass through the length of the cell, counter-propagating and aligned with the photolysis beam. The transmitted light was passed through a monochromator (Acton Research Corporation Spectra Pro-300i) and the wavelength-selected light was detected with a photomultiplier tube (PMT). The monochromator was calibrated against atomic emission lines from Hg, Cd, and Zn penray lamps. Since many of the products from R4 also absorb in the UV (Figure 7.1), the cross-section of $CH_3C(O)CH_2O_2$ was only measured at wavelengths where spectral interferences by other species were minimized; i.e. $\lambda = 300 - 315$ nm (5 nm increments). For the kinetics experiments, UV data were collected at 300 nm (indicated by the dashed red line in the inset).

NIR light from a 3 mW distributed feedback laser (DFB) was coupled to a pair of gold-coated Herriott optics for sensitive and selective detection of HO_2. The laser was tuned to the group of blended ro-vibrational overtone transitions of the O–H stretch near 6638.2 cm^{-1}. The NIR light made 30 passes inside the cell before being detected by an InGaAs detector (New Focus 1811). The laser frequency was modulated at 6.8 MHz and heterodyne detection was employed by detecting the 2-f signal at 13.6 MHz. Data were collected using a sampling rate of 1 MHz at a bandwidth of 100 kHz. For a typical experimental run, the NIR and UV signals were averaged for 200 excimer laser shots.

The relative change in the 2-f NIR signal was calibrated to absolute HO_2 concentrations by simultaneously measuring the HO_2 signal in the NIR and in the UV at 225 nm when HO_2 was the only radical present (i.e., $[CH_3C(O)CH_3] = 0$). The calibration experiments were performed daily at room temperature, where the HO_2 kinetics were described by known reactions; i.e., by the HO_2 self reaction (with no rate enhancement by CH_3OH) and by diffusion (unimolecular diffusion rate constant: $k_D \sim 22.2$ s^{-1}). The FACSIMILE kinetics modeling software was used to simultaneously fit the time-resolved NIR and UV signals with a kinetics model

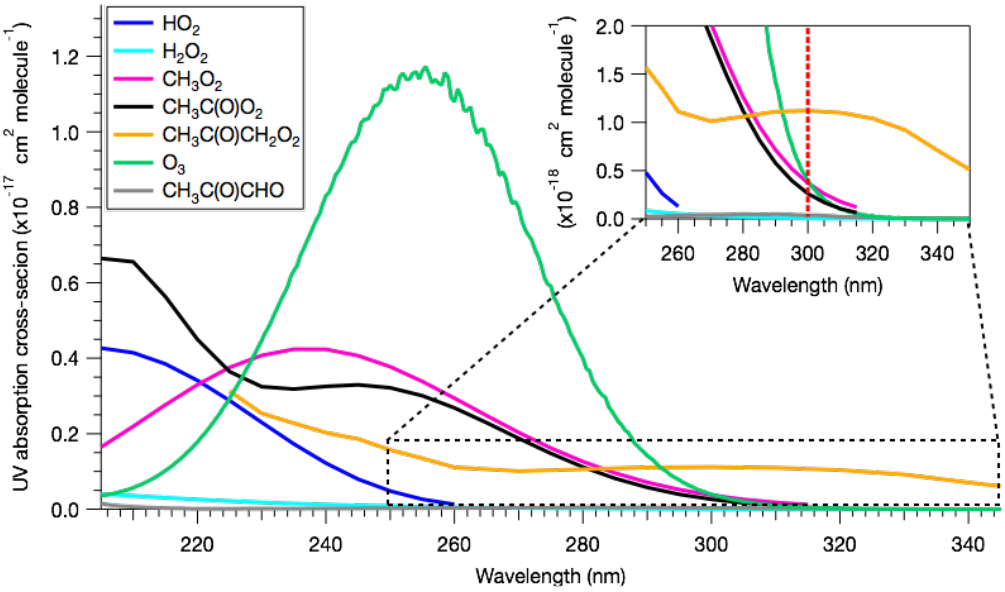

Figure 7.1: UV absorption cross-sections of various reactant and product pieces generated from the $HO_2 + CH_3C(O)CH_2O_2$ and/or $CH_3C(O)CH_2O_2 + CH_3C(O)CH_2O_2$ reactions [9]. A zoomed perspective around 300 nm is shown in the inset, where the dashed red line indicates the wavelength at which the UV data were collected.

to determine the calibration factor as well as the total radical concentration, $[Cl]_0$. Subsequent experiments carried out in the presence of $CH_3C(O)CH_3$ were conducted using the same Cl_2 and excimer pulse energy. The total initial radical concentrations ranged from $[Cl]_0 = (0.7 - 2.2) \times 10^{14}$.

7.3 Results

7.3.1 Overview

Using simultaneous NIR WMS and UV absorption spectroscopy, we measured $\sigma(\lambda)$ for λ = 300 - 315 nm, k_4, and k_5 at room temperature and at 100 Torr. R4 and R5 could not be perfectly isolated due to competitive loss of radicals and/or radical recycling by secondary chemistry. The initial amount of HO_2 relative to $CH_3C(O)CH_3$ dictated the sensitivity of the data to k_4 and k_5. Thus, experiments were carried out using various reagent gas concentrations that maximized sensitivity to these parameters, while minimizing the influence of secondary chemistry.

R4 and R5 were independently investigated by conducting experiments without and with initial generation of HO_2, respectively. k_4 and $\sigma_{CH_3C(O)CH_2O_2}$ were determined from experiments performed in the absence of CH_3OH, where no HO_2 were generated via R7. In the absence of CH_3OH, all of the Cl atoms generated from photolysis were converted to $CH_3C(O)CH_2O_2$ via R3 and R9. Since excess amounts of O_2

were used, the reaction of $CH_3C(O)CH_2$ with Cl_2 was assumed to be negligible. k_5 was determined under conditions where CH_3OH and $CH_3C(O)CH_3$ were both present, using concentrations such that the initial radical ratios, $[HO_2]_0/[CH_3C(O)CH_2O]_0$, were greater than 1. Using $[HO_2]_0/[CH_3C(O)CH_2O]_0 > 1$ enhanced the sensitivity of the data to k_5 relative to k_4 and to other secondary chemistry.

7.3.2 Secondary chemistry

The kinetics of R4 and R5 were explored by recording the time profiles of HO_2 in the NIR and of $CH_3C(O)CH_2O_2$ in the UV under various experimental conditions. Due to complex secondary chemistry, determination of the rate constants required the use of a kinetics model. A table of the full kinetics model is shown in Table 7.9. The key components of the kinetics model are described below. The data were fit to the kinetics model using a nonlinear least-squares algorithm (Levenberg-Marquardt) provided by the FACSIMILE software [12]. Both k_4 and k_5 were determined from the optimization of the fits.

$CH_3C(O)CH_2O$ formed via R4b and R5b can either decompose (R10) to form the acetyl radical ($CH_3C(O)$) or react with O_2 to form HO_2 (R11).

$$CH_3C(O)CH_2O \longrightarrow CH_3C(O) + CH_2O \quad \text{(R10)}$$

$$CH_3C(O)CH_2O + O_2 \longrightarrow CH_3C(O)CHO + HO_2 \quad \text{(R11)}$$

Under the experimental conditions of this work, the dominant fate of $CH_3C(O)CH_2O$ was assumed to be R10. This was verified in experiments carried out where the O_2 concentration was varied from ~20 to ~70 Torr, with no apparent differences in the observed UV time profiles as well the prompt NIR HO_2 signals, which will be discussed later. Previous experimental studies carried out at 1 atm also concluded that R10 was negligible [6, 13].

$CH_3C(O)$ reacts with O_2, which rapidly forms $CH_3C(O)O_2$ via R12 with nearly unity yield, with less than 3% yield of OH and HO_2 being formed via R12b and R12c, respectively (Chapter 5).

$$CH_3C(O) + O_2 \xrightarrow{M} CH_3C(O)O_2 \quad \text{(R12a)}$$

$$\longrightarrow OH + \text{products} \quad \text{(R12b)}$$

$$\longrightarrow HO_2 + \text{products} \quad \text{(R12c)}$$

$CH_3C(O)O_2$ is subsequently lost via self reaction (R13) and by reactions with HO_2 (R14) and $CH_3C(O)CH_2O_2$ (R15), all of which include radical propagating and

terminating product channels.

$$2\,CH_3C(O)O_2 \longrightarrow 2\,CH_3C(O)O + O_2 \quad \text{(R13)}$$

$$HO_2 + CH_3C(O)O_2 \longrightarrow CH_3C(O)OOH + O_2 \quad \text{(R14a)}$$
$$\longrightarrow CH_3C(O)OH + O_3 \quad \text{(R14b)}$$
$$\longrightarrow OH + CH_3C(O)O + O_2 \quad \text{(R14c)}$$

$$CH_3C(O)O_2 + CH_3C(O)CH_2O_2 \longrightarrow CH_3C(O)OH + CH_3C(O)CHO + O_2 \quad \text{(R15a)}$$
$$\longrightarrow CH_3C(O)O + CH_3C(O)CH_2O + O_2 \quad \text{(R15b)}$$

Rapid decomposition of $CH_3C(O)O$ generated from R13, R14c, and R15b produces CH_3, which in turn forms CH_3O_2 in the presence of O_2 (R16).

$$CH_3 + O_2 \xrightarrow{M} CH_3O_2 \quad \text{(R16)}$$

Subsequent self (R17) and cross reactions of CH_3O_2 with $CH_3C(O)CH_2O_2$ (R18), $CH_3C(O)O_2$ (R19), and HO_2 (R20) also contribute to the overall kinetics.

$$CH_3O_2 + CH_3O_2 \longrightarrow 2\,CH_3O + O_2 \quad \text{(R17a)}$$
$$\longrightarrow CH_3OH + CH_2O + O_2 \quad \text{(R17b)}$$

$$CH_3O_2 + CH_3C(O)CH_2O_2 \longrightarrow CH_3OH + CH_3C(O)CHO + O_2 \quad \text{(R18a)}$$
$$\longrightarrow CH_2O + CH_3C(O)CH_2OH + O_2 \quad \text{(R18b)}$$
$$\longrightarrow CH_3O + CH_3C(O)CH_2O + O_2 \quad \text{(R18c)}$$

$$CH_3O_2 + CH_3C(O)O_2 \longrightarrow CH_3C(O)O + CH_3O + O_2 \quad \text{(R19a)}$$
$$\longrightarrow CH_3C(O)OH + CH_2O + O_2 \quad \text{(R19b)}$$

$$HO_2 + CH_3O_2 \longrightarrow CH_3OOH + O_2 \quad \text{(R20a)}$$
$$\longrightarrow CH_2O + H_2O + O_2 \quad \text{(R20b)}$$

7.3.3 Determination of $\sigma_{CH_3C(O)CH_2O_2}$

$\sigma(\lambda)$ was measured over the spectral region λ = 300 - 315 nm. Gas mixtures containing $Cl_2/CH_3C(O)CH_3/O_2N_2$ were photolyzed at room temperature and P = 100 Torr. For each wavelength, the UV time profiles were averaged for 200 excimer shots and recorded with a time resolution of 1 μs. Values of $\sigma(\lambda)$ were determined by extrapolating the UV data to t = 0 s (i.e., time of photolysis), using pseudo-second order analysis. For a bimolecular reaction, a plot of the inverse absorbance, $1/A$, vs time exhibits a straight line described by the integrated rate law of a second-order reaction. For R4, the integrated raw law is expressed by Equation 7.1 and is written in terms of $1/A$ by Equation 7.2:

$$\frac{1}{[CH_3C(O)CH_2O_2]} = 2k_{4,\text{eff}}t + \frac{1}{[CH_3C(O)CH_2O_2]_0} \quad (7.1)$$

$$\frac{1}{A} = \frac{2k_{4,\text{eff}}t}{\sigma_{CH_3C(O)CH_2O_2} * l} + \frac{1}{[CH_3C(O)CH_2O_2]_0\sigma_{CH_3C(O)CH_2O_2} * l} \quad (7.2)$$

where $k_{4,\text{eff}}$ is the effective bimolecular rate constant, l is the pathlength, and $[CH_3C(O)CH_2O_2]_0$ is the initial concentration of $CH_3C(O)CH_2O_2$ at t = 0 s; i.e., immediately following photolysis of the radical precursor, Cl_2. The rate constant for R9 (k_9) is 2.1×10^{-12} cm^3 molecule^{-1} s^{-1} [9] at room temperature. For the lowest $[CH_3C(O)CH_2O_2]$ of 2.2×10^{16} molecule cm^{-3}, the pseudo-first order rate of Cl consumption was $\sim 5 \times 10^5$ s^{-1}. O_2 was also in excess of Cl and $CH_3C(O)CH_3$ and the rate of R3 was twice as fast as R9. The effective second order, pressure-dependent rate constant for R3 (k_3) at T = 298 K and P = 100 Torr is 8.9×10^{-12} cm^3 molecule^{-1} s^{-1} [9]. The pseudo-first order rate for $CH_3C(O)CH_2$ consumption was $\sim 1 \times 10^6$ s^{-1}. Thus, all of the Cl atoms were essentially converted to $CH_3C(O)CH_2O_2$ in the first ~20 μs.

In Equation 7.2, $k_{4,\text{eff}}$ represents the upper limit for k_4, accounting for loss of $CH_3C(O)CH_2O_2$ by the self reaction as well as by competing secondary reactions with other peroxy radicals and by diffusion (more discussion will be given in the next section). Spectral interference by other peroxy radicals generated from secondary

reactions was assumed to be negligible over the region λ = 300 - 315 nm due to their low absorption cross-sections and concentrations.

Figure 7.2 shows a plot of the inverse UV absorbance as a function of time. As shown in the figure, the data shows linear behavior until ~1.5 ms. Beyond this point, $1/A$ deviates from linearity as secondary reactions begin to dominate the chemistry. Linear regression of the data in the linear range was performed to determine $\sigma_{CH_3C(O)CH_2O_2}$ from the intercept, as given in Equation 7.2. The UV data in the first ~200 μs after photolysis was lost due to saturation of the PMT by the excimer pulse; therefore, the data was fit from 0.2 to ~0.8 ms. $[CH_3C(O)CH_2O_2]_0$ was determined

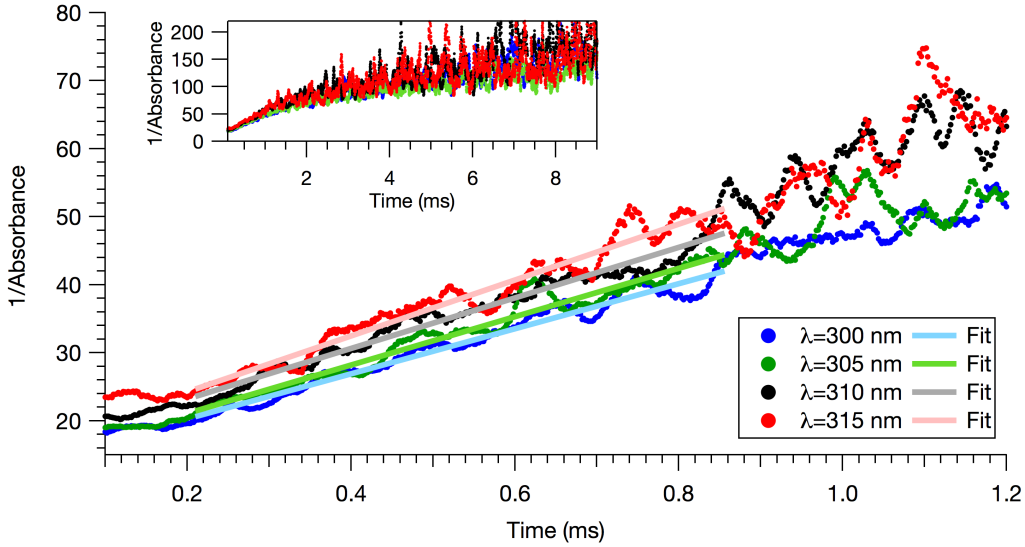

Figure 7.2: Plot of $1/A$ versus time from the $CH_3C(O)CH_2O_2$ self reaction. The zoomed out perspective of the plot shown in the inset demonstrates the deviation from linearity at t > ~ 1.5 ms.

by measuring the initial HO_2 concentration, $[HO_2]_0$ in the absence of $CH_3C(O)CH_3$. Since the same $[Cl_2]$ and excimer energy were used, $[CH_3C(O)CH_2O_2]_0$ was assumed to be the same as $[HO_2]_0$. The UV path length was taken to be 147 ± 10 cm, as determined from the temperature probe measurements described in Chapter 2.

Table 7.3 lists the values of $\sigma_{CH_3C(O)CH_2O_2}$ and $k_{4,eff}$ measured at four different wavelengths. $k_{4,eff}$ was calculated from the slope of $1/A$ versus time at each wavelength using the corresponding $\sigma_{CH_3C(O)CH_2O_2}$. The average value weighted by the uncertainties gave $k_{4,eff} = (5.2 \pm 0.52) \times 10^{-12}$ molecule cm^{-3}. The uncertainties (1σ) were calculated from the uncertainties in the path length, random errors from the linear regression (~15%), and systematic errors in $[CH_3C(O)CH_2O_2]_0$ (~10%). The latter were estimated from Monte Carlo analysis of the HO_2 self reaction runs

(used to determine $[Cl]_0$ and the NIR calibration factor), which took into account the uncertainties in the HO_2 absorption cross-section, path length, and rate constant of the HO_2 self reaction.

Table 7.3: Measured values of $\sigma_{CH_3C(O)CH_2O_2}$ and $k_{4,eff}$ (with 1σ uncertainties) at four different wavelengths at T = 298.2 K and P = 100 Torr. Concentrations: $[Cl_2] = 6.8 \times 10^{15}$ molecule cm^{-3}; $[CH_3C(O)CH_2O_2]_0 = 2.4 \times 10^{14}$ molecule cm^{-3}; $[CH_3C(O)CH_3] = 4.6 \times 10^{16}$ molecule cm^{-3}; $[O_2]_0 = 1.5 \times 10^{18}$ molecule cm^{-3}.

λ (nm)	$\sigma_{CH_3C(O)CH_2O_2}$ [a]	$k_{4,eff}$ [b]
300	2.11 ± 0.35	5.16 ± 0.46
305	2.02 ± 0.24	5.25 ± 0.33
310	1.83 ± 0.30	5.00 ± 0.45
315	1.80 ± 0.30	5.43 ± 0.49

[a] Units: 10^{-18} cm^2 molecule^{-1}
[b] Units: 10^{-12} cm^3 molecule^{-1}

Figure 7.3 and Table 7.4 compare the values of $\sigma_{CH_3C(O)CH_2O_2}$ measured in this work to those reported by previous studies. It should be noted that the agreement between the values of k_4 reported by Bridier et al. [6] and by Cox et al. [7] is fortuitous due to disagreements in the measured values of $\sigma_{CH_3C(O)CH_2O_2}$ in those studies. The value of $k_{4,eff}$ measured in this work is over a factor of 1.5 less than the values of k_4 reported by Bridier et al. [6] and by Cox et al. [7]. In the studies conducted by Cox et al. [7], k_4 was estimated assuming pseudo-second order loss as was done in this work (Equation 7.1). However, Cox et al. [7] used very high initial radical concentrations on the order of $[CH_3C(O)CH_2O_2]_0 \sim 10^{15}$ molecule cm^{-3} (i.e., as much as 10 times higher than was used in this work), making their estimate for k_4 more susceptible to systematic errors caused by rapid secondary chemistry that consume $CH_3C(O)CH_2O_2$.

On the other hand, the studies conducted by Bridier et al. [6] used initial radical concentrations of $\sim 1 \times 10^{14}$ molecule cm^{-3} or less, and $k_{4,eff} = 9.0 \times 10^{-12}$ molecule cm^{-3} was derived from UV absorption traces obtained at 330 nm (where $CH_3C(O)CH_2O_2$ is presumably the only absorbing species). In their work, $\sigma_{CH_3C(O)CH_2O_2}$ and k_4 were determined simultaneously from kinetics analysis of UV absorption time profiles obtained at several wavelengths. Systematic errors associated with the secondary chemistry in the kinetics model as well as the calibration methods used to determine $[CH_3C(O)CH_2O_2]_0$ may explain the observed discrepancy in the value of $k_{4,eff}$ reported by Bridier et al. [6] and that measured in this work.

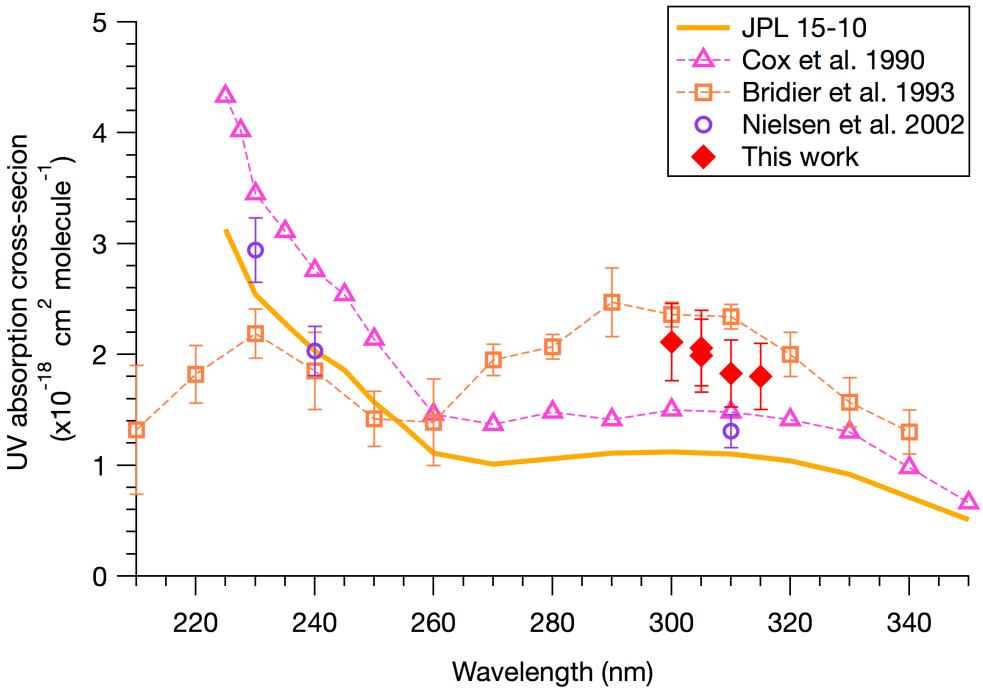

Figure 7.3: UV absorption cross-sections of $CH_3C(O)CH_2O_2$ measured in this work compared to values determined by previous studies.

Table 7.4: Comparison of $\sigma_{CH_3C(O)CH_2O_2}$ and k_4. Uncertainties, if provided, correspond to 1σ.

Ref.	$\sigma(\lambda)^a$				k_4 [b]
	300 nm	305 nm	310 nm	315 nm	
This work	2.11 ± 0.35	2.02 ± 0.24	1.83 ± 0.30	1.80 ± 0.30	5.2 ± 0.52[c]
Bridier et al. [6]	2.36 ± 0.11		2.34 ± 0.11		8.0 ± 2.0
Cox et al. [7]	1.51		1.48 ± 0.10		8.3 ± 1.6[c]
Nielsen et al. [14]			1.31 ± 0.15		
JPL [9]	1.12		1.10		

[a] Units: 10^{-18} cm^2 molecule^{-1}
[b] Units: 10^{-12} cm^3 molecule^{-1}
[c] Upper limit

7.3.4 $CH_3C(O)CH_2O_2$ self reaction kinetics

The kinetics of the $CH_3C(O)CH_2O_2$ self reaction was investigated at room temperature and P = 100 Torr. k_4 was determined from kinetic analysis of UV time profiles obtained at λ = 300 nm. Simultaneous NIR and UV time profiles were recorded from the photolysis of gas mixtures containing $Cl_2/CH_3C(O)CH_3/O_2/N_2$; however, the NIR time profile was ultimately not used for the determination of k_4 for reasons that will be described later. Experiments were carried out using varying $[CH_3C(O)CH_3]$ and $[O_2]$ to qualitatively explore the prompt and secondary

formation of HO_2 that was observed in the NIR.

7.3.4.1 Prompt and secondary HO_2

Figure 7.4 displays some example data of the simultaneous NIR and UV time traces obtained at room temperature. Figure 7.4(a) and Figure 7.4(b) show the kinetics traces obtained from varying [$CH_3C(O)CH_3$] (with [O_2] fixed) and varying [O_2] (with [$CH_3C(O)CH_3$] fixed), respectively, while keeping all other experimental conditions the same. In each case, only the highest and lowest concentrations of the varied species are shown for clarity. While no discernible differences were observed in the UV data (λ = 300 nm) in both cases, the NIR HO_2 kinetics traces clearly show dependence on both [O_2] and [$CH_3C(O)CH_3$]; i.e., the HO_2 signals are shown to be positively and negatively correlated with [O_2] and with [$CH_3C(O)CH_3$], respectively.

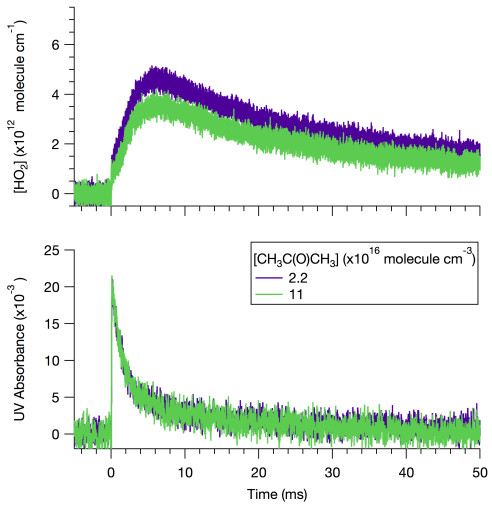

(a) Varying [$CH_3C(O)CH_3$]. Concentrations: [Cl_2] = 4.5×10^{15} molecule cm^{-3}; [$CH_3C(O)CH_2O_2$]$_0$ = 7.9×10^{13} molecule cm^{-3}; [O_2] = 1.6×10^{18} molecule cm^{-3}.

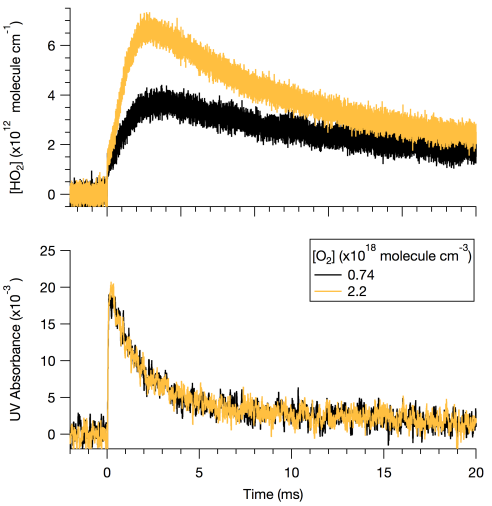

(b) Varying [O_2]. Concentrations: [Cl_2] = 5.1×10^{15} molecule cm^{-3}; [$CH_3C(O)CH_2O_2$]$_0$ = 7.2×10^{13} molecule cm^{-3}; [$CH_3C(O)CH_3$] = 2.9×10^{16} molecule cm^{-3}.

Figure 7.4: NIR HO_2 (top) and UV (λ = 300 nm) (bottom) time traces obtained with [CH_3OH] = 0 for (a) varying [$CH_3C(O)CH_3$] and (b) varying [O_2]. In each case, only the data from the lowest and highest concentrations are shown for clarity. T = 298 K and P = 100 Torr.

The dependence of HO_2 on [O_2] can be explained by the secondary formation of HO_2 from the subsequent reaction of CH_3O (formed from various secondary

reactions as described previously) with O_2 (R21):

$$CH_3O + O_2 \longrightarrow CH_2O + HO_2 \qquad \text{(R21)}$$

Increasing O_2 leads to faster formation of HO_2 via R21, which agrees with observations. On the other hand, the negative dependence of HO_2 on $[CH_3C(O)CH_3]$ is not immediately obvious. One possible explanation for the observed trend is the loss of HO_2 via reaction with $CH_3C(O)CH_3$, forming the hydrogen-bonded adduct, $HO_2 \cdot CH_3C(O)CH_3$. More details on the adduct chemistry will be discussed later. A comprehensive investigation exploring all the secondary sources of HO_2 was beyond the scope of this work; however, these qualitative assessments of the observed trends may provide direction for future studies.

The NIR signals also exhibited evidence of prompt HO_2 formation occurring in less than ~40 μs after photolysis, which was not reproduced by the kinetics model. The prompt HO_2 signal was typically < 2% of the total initial radical concentration. Figure 7.5(a) and Figure 7.5(b) show several NIR HO_2 signals obtained from varying $[CH_3C(O)CH_3]$ and $[O_2]$, respectively, on the ms and μs timescales. In contrast to the HO_2 signals on the ms time scale, the prompt HO_2 signals appeared to be independent of both $[CH_3C(O)CH_3]$ and $[O_2]$.

Although determination of the true nature of the source of prompt HO_2 was beyond the scope of this work, four possible mechanisms were explored:

1. Cl substitution of $CH_3C(O)CH_3$ (R22)

$$CH_3C(O)CH_3 + Cl \longrightarrow CH_3C(O)CH_2Cl + H \qquad \text{(R22)}$$

2. Cl addition to $CH_3C(O)CH_3$ (R23) followed by Cl substitution of acetylchloride ($CH_3C(O)Cl$) (R24)

$$CH_3C(O)CH_3 + Cl \longrightarrow CH_3C(O)Cl + CH_3 \qquad \text{(R23)}$$
$$CH_3C(O)Cl + Cl \longrightarrow ClCH_2C(O)Cl + H \qquad \text{(R24)}$$

3. $CH_3C(O)CH_3$ photolysis (R1)

4. Reaction of $CH_3C(O)CH_2$ with O_2

For both #2 and #3, CH_3O_2 formed from the reaction of CH_3 with O_2 (R16) is a source of HO_2. HO_2 is formed from the self reaction of CH_3O_2 (R17) and subsequent reaction of CH_3O with O_2 (R21).

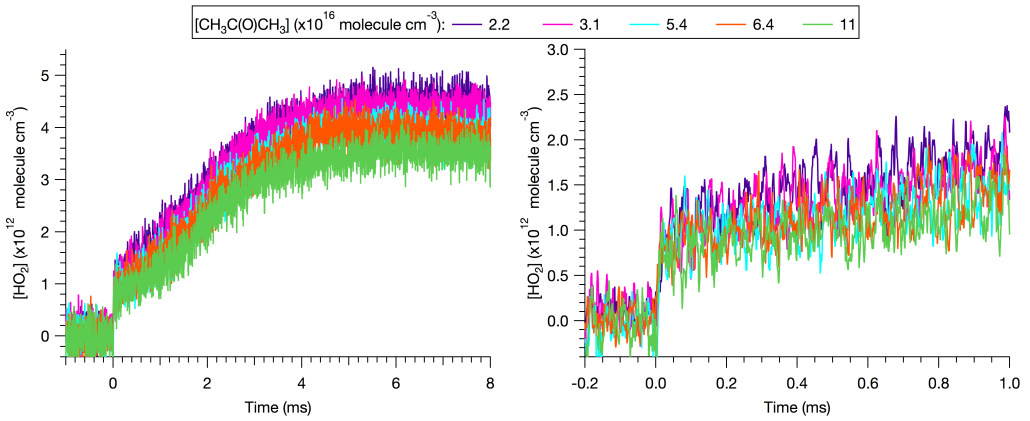

(a) Varying $[CH_3C(O)CH_3]$ under the same experimental conditions as in Figure 7.4(a), shown with additional data.

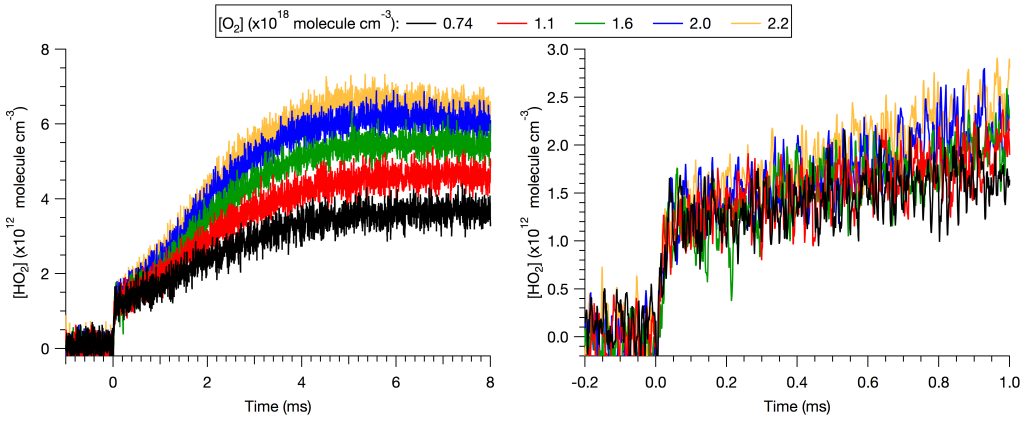

(b) Varying $[O_2]$ under the same experimental conditions as in Figure 7.4(b), shown with additional data.

Figure 7.5: NIR HO_2 time traces obtained with $[CH_3OH]$ = 0 for (a) varying $[CH_3C(O)CH_3]$ and (b) varying $[O_2]$. The plots on the right are zoomed in views of the corresponding plots on the left, emphasizing the prompt HO_2 signals. T = 298 K and P = 100 Torr.

However, the subsequent reactions of R17 and R21 both occur too slowly to explain the prompt HO_2 and only produces HO_2 on timescales > 40 μs. Thus, although R23 is exothermic, this reaction alone cannot explain the prompt HO_2 formation. $CH_3C(O)CH_3$ photolysis is also unlikely since the absorption cross-section of $CH_3C(O)CH_3$ is very small at 351 nm (literature values varies between 8×10^{-23} cm^2 and 1×10^{-21} cm^2[15]) and the quantum yield is less than 0.01 at room temperature [9]. In addition, $CH_3C(O)CH_3$ photolysis would not explain the observed $[Cl_2]$ dependence of the prompt HO_2 signal.

Alternatively, Cl substitution of $CH_3C(O)CH_3$ or $CH_3C(O)Cl$ via R22 and R24, respectively, to form H atoms could account for prompt HO_2 formation from the

reaction of H + O_2 (R25).

$$H + O_2 \longrightarrow HO_2 \quad \text{(R25)}$$

Since R22 and R23 or R24 are the rate-limiting steps for HO_2 production, prompt HO_2 formation via this mechanism would be independent of [O_2], which agrees with observations. However, both R22 and R24 are endothermic by 80.9 kJ mol^{-1} and 102.1 kJ mol^{-1}, respectively. Because of the high endothermicity, both mechanisms are unlikely to explain the observed prompt HO_2 formation.

#4 was the most plausible explanation for prompt HO_2:

$$CH_3C(O)CH_2 + O_2 \longrightarrow HO_2 + \text{products} \quad \text{(R26)}$$

Inclusion of R26 in the model showed that the prompt HO_2 formation was decoupled from the slower HO_2 formation observed between 0.4 and 5 ms; thus, R26 served as a good proxy to model the prompt HO_2. Under our experimental conditions where [O_2] and [$CH_3C(O)CH_3$] were in excess relative to $[Cl]_0$, the HO_2 yield from R26 does not depend on [O_2] or [$CH_3C(O)CH_3$], which is consistent with observations. It should also be noted that the prompt HO_2 signal could also be a result of hot chemistry, as was suggested for R12c in Chapter 5; however, further experimental studies are needed to support this hypothesis.

7.3.4.2 Determination of k_4

Figure 7.6 shows the NIR HO_2 and UV (λ = 300 nm) data obtained at T = 298.6 K, and P = 100 Torr, each compared to four modeled time profiles using the kinetics scheme in Bridier et al. [6] (solid, dashed, and dotted black lines) and the kinetics model used in this work (solid green line), which is shown in Table 7.9. The kinetics model shown in Table 7.9 includes additional secondary reactions and also has updated rate constants and branching ratios of the various reactions. Each of the modeled HO_2 profiles included a conversion of ~1.8% of the total initial radical concentration to HO_2. The raw UV time profile is the average of five runs (total of 1000 excimer laser shots), which were obtained under varying concentrations of O_2 ([O_2]=$(0.74 - 2.2) \times 10^{18}$ molecule cm^{-3}) but otherwise identical conditions and showed no discernible differences in the observed UV time profiles.

The dashed and dotted lines were obtained using values of $\sigma_{CH_3C(O)CH_2O_2}$ and k_4 from Bridier et al. [6] and from the JPL/IUPAC data evaluations [8, 9], respectively, and the solid lines were obtained using the values determined in this work, assuming

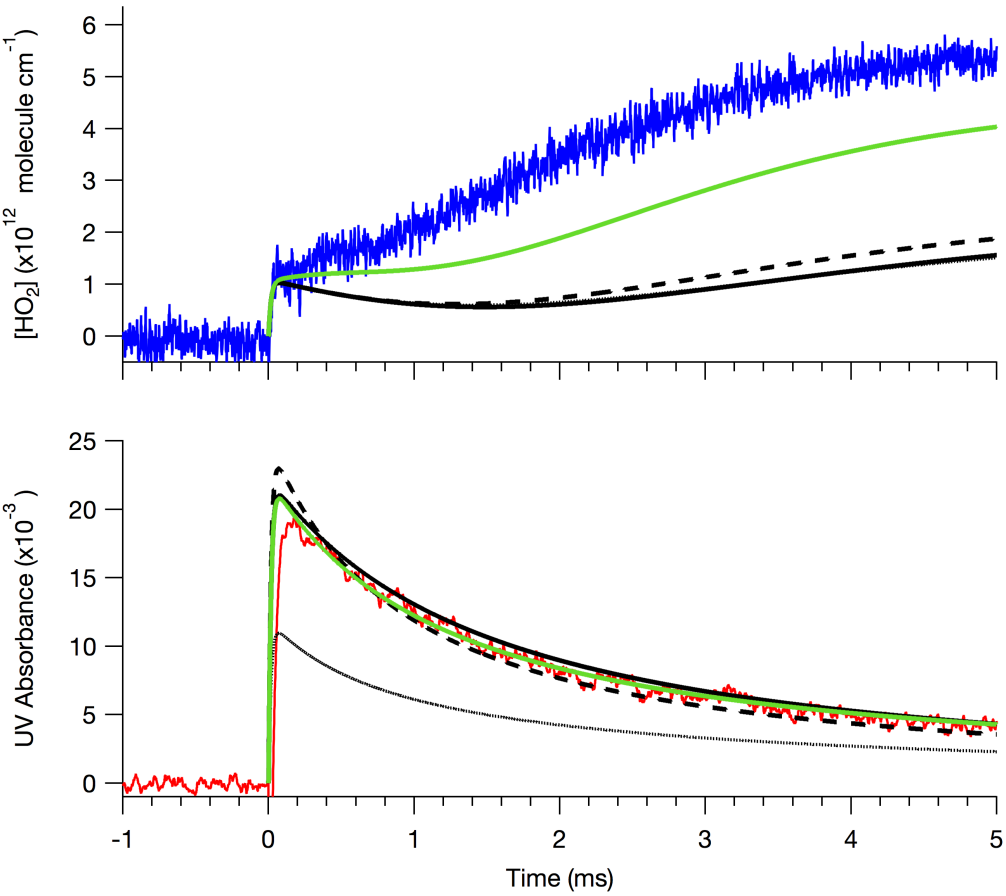

Figure 7.6: NIR HO_2 (blue) and UV (red) data obtained at λ = 300 nm, T = 298.6 K, P = 100 Torr, averaged from 5 different experimental runs (1000 total excimer laser shots) compared to simulated time profiles using the kinetics scheme in Bridier et al. [6] (black lines) and the kinetics model shown in Table 7.9 (green line), using values of $\sigma_{CH_3C(O)CH_2O_2}$ and k_4 from Bridier et al. [6] (dashed line), JPL/IUPAC ($\sigma_{CH_3C(O)CH_2O_2}$ from [9], k_4 and branching ratios from [8]) (dotted line), and this work (solid line), where the latter assumed $k_4 = k_{4,eff}$. Each of the modeled HO_2 profiles included conversion of ~1.8% of the total initial radical concentration to HO_2. Concentrations: $[Cl_2] = 5.1 \times 10^{15}$ molecule cm^{-3}; $[CH_3C(O)CH_2O_2]_0 = 7.2 \times 10^{13}$ molecule cm^{-3}; $[CH_3C(O)CH_3] = 2.9 \times 10^{16}$ molecule cm^{-3}; $[O_2] = 1.6 \times 10^{18}$ molecule cm^{-3}.

$k_4 = k_{4,eff}$. The simulated UV time profiles using the kinetics model from Bridier et al. [6] show that the values of $\sigma_{CH_3C(O)CH_2O_2}$ and k_4 from Bridier et al. [6] model the data much better than the JPL/IUPAC values; however, the model still overestimates the initial radical concentration and the observed decay rate. Better agreement between the model and the data is observed when the values determined in this work were used, and even further improvement is evident when these values were used with the updated model from Table 7.9.

On the other hand, the models were far less successful in predicting the HO_2 time profile. To further aid in searching for possible sources of HO_2, a sensitivity analysis was conducted to the model used in this work to determine the dominant reactions at specific times. Figure 7.7 is a plot of the UV data from Figure 7.6 with modeled UV absorption profiles at 300 nm of key peroxy radical species generated from R4 and subsequent reactions. As shown, contribution to the total absorbance by both $CH_3C(O)O_2$ and CH_3O_2 is small but non-negligible, for t > 0.5 ms after photolysis. Not surprisingly, the HO_2 signals on the ms time scale were sensitive to the self reactions of $CH_3C(O)O_2$ (R13) and CH_3O_2 (R17) as well as their cross-reactions with $CH_3C(O)CH_2O_2$ (R15 and R18, respectively), and with each other (R19).

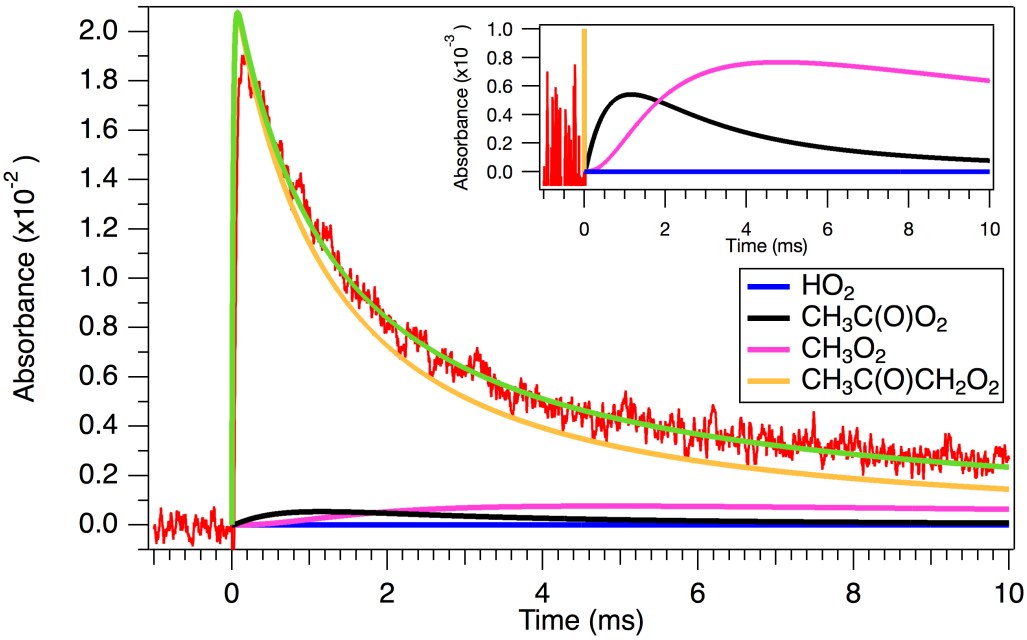

Figure 7.7: Experimental and simulated time-dependent absorption profiles of various peroxy radical species at 300 nm. The modeled total UV absorbance is also shown in green. Inset shows a zoomed in view to emphasize the rapid generation of $CH_3C(O)O_2$ and CH_3O_2. The UV data is the same as that shown in Figure 7.6, and the kinetics model from Table 7.9 was used.

Simultaneous fits of the NIR and UV data resulted in unphysical values of $\sigma_{CH_3C(O)CH_2O_2}$ and k_4, suggesting that some of the kinetic rate constants and product yields of the secondary chemistry used in the kinetics model were incorrect. Sensitivity analysis showed that fits to the data were particularly sensitive to the rate constants and product yields of R15 and R18; however, these parameters could not be derived from the data because direct measurements of CH_3O_2 and $CH_3C(O)O_2$ were not available. Since the NIR data were far more sensitive to these parameters

than the UV data and were thus more susceptible to systematic error, only the UV data were fitted with the kinetics model to determine $\sigma_{CH_3C(O)CH_2O_2}$ and k_4.

Using the average value of $k_{4,eff}$ determined above as an initial guess, the UV data were fitted with a kinetics model (Table 7.9) using the FACSIMILE software, to constrain both k_4 and $\sigma_{CH_3C(O)CH_2O_2}$. Figure 7.8 shows that the data are well-constrained by the model. The optimized values of the fitted parameters were in relatively good agreement with the initial estimates.

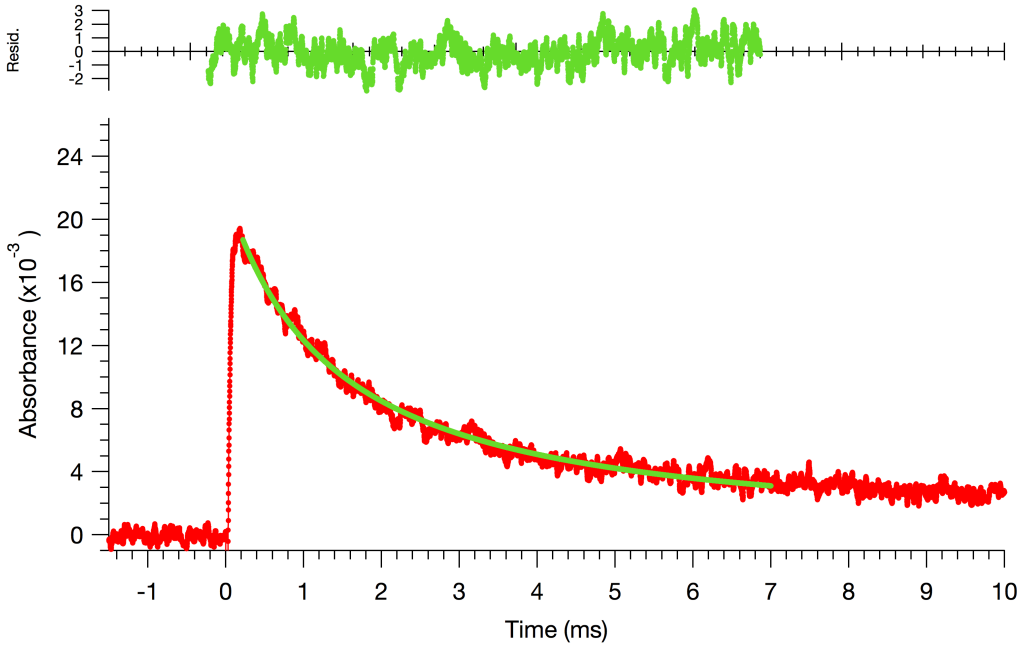

Figure 7.8: UV data from Figure 7.6 plotted with the fit constraining $\sigma_{CH_3C(O)CH_2O_2}$ and k_4. Residuals are shown above the kinetics traces.

Table 7.5: Summary of data collected for determination of $\sigma_{CH_3C(O)CH_2O_2}$ and k_4 at λ = 300 nm, T = 298.7 K, and P = 100 Torr.

$[Cl_2]^a$	$[CH_3C(O)CH_3]^a$	$[O_2]^b$	$[Cl]_0{}^c$	$\sigma_{CH_3C(O)CH_2O_2}{}^d$	$k_4{}^e$	# of runs
5.1	29	0.74 - 2.2	0.72	2.02 ± 0.012	5.44 ± 0.07	5
8.3	29	0.73 - 2.2	1.2	2.03 ± 0.015	5.43 ± 0.08	5

[a]Units: 10^{15} molecule cm^{-3}
[b]Units: 10^{18} molecule cm^{-3}
[c]Units: 10^{14} molecule cm^{-3}
[d]Units: 10^{-18} cm^2 molecule^{-1}
[e]Units: 10^{-12} cm^3 molecule^{-1}

7.3.5 HO_2 + $CH_3C(O)CH_2O_2$ kinetics

The kinetics of R5 was investigated by adding CH_3OH to the reagent gas mixture. Simultaneous NIR and UV time profiles were recorded from the photolysis of gas mixtures containing Cl_2 /CH_3OH/ $CH_3C(O)CH_3$ /O_2 /N_2. All the UV time profiles were obtained at λ = 300 nm. Data were collected using varying $[HO_2]_0/[CH_3C(O)CH_2O_2]_0$ ratios, covering the range $[HO_2]_0/[CH_3C(O)CH_2O_2]_0$ = 3.6 - 6.5. For each experimental condition, the NIR and UV time profiles were simultaneously fitted with a kinetics model using FACSIMILE to constrain k_5. Since $[HO_2]_0$ was always in excess of $[CH_3C(O)CH_2O_2]_0$, the NIR HO_2 signals were not affected by the prompt HO_2 chemistry described in the previous section where experiments were carried out in the absence of CH_3OH.

With the addition of CH_3OH, a fraction of the Cl atoms generated from photolysis is lost via R7, which generates HO_2 via R8 in the presence of O_2. The determination of k_5 was complicated by the secondary reactions described previously in addition to the self reactions of $CH_3C(O)CH_2O_2$ (R4) and HO_2 (R27) competing with R5.

$$HO_2 + HO_2 \xrightarrow{M} H_2O_2 + O_2 \qquad \text{(R27)}$$

The sensitivity of the data to these reactions depended on the relative amount of the initial HO_2 and $CH_3C(O)CH_2O_2$ radicals, which can be expressed as:

$$[HO_2]_0 = \frac{k_7[CH_3OH]}{k_7[CH_3OH] + k_9[CH_3C(O)CH_3]}[Cl]_0 \qquad (7.3)$$

$$[CH_3C(O)CH_2O_2]_0 = \frac{k_9[CH_3C(O)CH_3]}{k_7[CH_3OH] + k_9[CH_3C(O)CH_3]}[Cl]_0 \qquad (7.4)$$

From Equation 7.3 and Equation 7.4, the relative amount of $[HO_2]_0$ and $[CH_3C(O)CH_2O]_0$ is proportional to the ratio of the radical precursors (Equation 7.5):

$$\frac{[HO_2]_0}{[CH_3C(O)CH_3]_0} = \frac{k_7[CH_3OH]}{k_9[CH_3C(O)CH_3]} \qquad (7.5)$$

k_7 was previously measured (Chapter 6) to be $k_7 = (5.45 \pm 0.24) \times 10^{-11}$ cm^3 molecule^{-1} s^{-1}, in excellent agreement with the recommendations by the current JPL [9] and IUPAC [8] data evaluations. The value of k_9 is also well-characterized and was taken from the JPL data evaluation, which was based on work done by numerous relative and absolute rate studies (see references in JPL 15-10 [9]).

7.3.5.1 Rate enhancement of HO_2 + HO_2 by radical adducts

Previous studies have shown that increasing the radical precursor concentrations can introduce additional complications due to the formation of a hydrogen-bonded adduct from the reaction of HO_2 with CH_3OH (Chapter 3, [16]) and with $CH_3C(O)CH_3$ [17]. This affects the overall kinetics due to the rapid loss of HO_2 from the equilibrium reaction with CH_3OH (R28) and/or with $CH_3C(O)CH_3$ (R29).

$$HO_2 + CH_3OH \overset{M}{\rightleftharpoons} HO_2 \cdot CH_3OH \tag{R28}$$

$$HO_2 + CH_3C(O)CH_3 \overset{M}{\rightleftharpoons} HO_2 \cdot CH_3C(O)CH_3 \tag{R29}$$

As explained in Chapter 3, the NIR provided specific measurement of monomeric HO_2 and not HO_2 bound in the adducts. Thus, the peak NIR signal in the time traces represented the equilibrium concentration of HO_2, $[HO_2]_{eq}$, which is expressed as

$$[HO_2]_{eq} = [HO_2]_0 - [HO_2 \cdot CH_3OH]_{eq} - [HO_2 \cdot CH_3C(O)CH_3]_{eq} \tag{7.6}$$

In addition, subsequent loss of HO_2 via reaction with the radical adducts (R30 and R31) results in an enhanced observed rate constant for R27.

$$HO_2 + HO_2 \cdot CH_3OH \longrightarrow \text{products} \tag{R30}$$

$$HO_2 + HO_2 \cdot CH_3C(O)CH_3 \longrightarrow \text{products} \tag{R31}$$

For sufficiently low concentrations of CH_3OH and $[CH_3C(O)CH_3]$, the observed HO_2 self reaction rate constant, k_{27obs}, increases linearly in CH_3OH and $[CH_3C(O)CH_3]$ (Equation 7.7):

$$k_{27obs} = k_{27} + k''_{27,M}[CH_3OH] + k''_{27,A}[CH_3C(O)CH_3] \tag{7.7}$$

With decreasing temperatures, adduct formation becomes more favorable and rate enhancement effects become more significant, as was observed for CH_3OH (Chapter 3). To investigate possible enhancement effects by $CH_3C(O)CH_3$, data were collected under three general conditions:

1. Varying both $[CH_3OH]$ and $[CH_3C(O)CH_3]$ with a fixed $[CH_3OH]/[CH_3C(O)CH_3]$ ratio
2. Varying $[CH_3OH]$ for a fixed $[CH_3C(O)CH_3]$
3. Varying $[CH_3C(O)CH_3]$ for a fixed $[CH_3OH]$

Data was obtained using five different concentrations for each of the three sets of conditions, and each experimental run was averaged for 200 excimer laser shots. All experiments were carried at 100 Torr, using N_2 as the bath gas. The data were analyzed by simultaneously fitting the NIR and UV time traces with the kinetics model and constraining k_{27obs} in addition to k_5. $[Cl]_0$ and $[HO_2]_{eq}$ were also allowed to vary in the multi-parameter fits, where $[HO_2]_{eq}$ was constrained by the NIR signal extrapolated to t ~0 s.

Varying $[CH_3OH]$ and $[CH_3C(O)CH_3]$ with fixed $[CH_3OH]/[CH_3C(O)CH_3]$
From Equation 7.5, a fixed $[CH_3OH]/[CH_3C(O)CH_3]$ ratio results in a fixed $[HO_2]_0/[CH_3C(O)CH_3]_0$ ratio, and the observed decay rates should be identical if no adduct chemistry occurred. Figure 7.9 shows the NIR and UV data obtained from experiments conducted at three different temperatures. For each temperature, data were collected over four different experimental conditions that used the same $[Cl]_0$ (same $[Cl_2]$ and excimer pulse energy), for varying $[CH_3OH]$ and $[CH_3C(O)CH_3]$, with the ratio fixed at $[CH_3OH]/[CH_3C(O)CH_3] = 6$. At T = 339.9 K, both the NIR and UV data show no discernible differences in the peak signals, or in the decay rates between all four runs (Figure 7.9(a)). However, at T = 299.1 K and at T = 258.6 K (Figure 7.9(b) and Figure 7.9(c), respectively), the HO_2 signals exhibit faster decay rates with increasing $[CH_3OH]$ and $[CH_3C(O)CH_3]$, while the UV signals after t = 1 ms appear to be identical for all four runs. At T = 258.6 K, rapid decrease in the peak $[HO_2]$ and UV signals (< 50 μs) was also observed with increasing $[CH_3OH]$ and $[CH_3C(O)CH_3]$; however, the observed trend in the peak UV signals may not be statistically significant due to the noise on the UV signals. At lower temperatures, lower amounts of $CH_3C(O)CH_2O_2$ are generated due to the positive temperature dependence of k_9. The maximum $[Cl]_0$ that could be used were generally limited by the need to minimize secondary chemistry resulting in reduced signal-to-noise on the UV signal for a given $[Cl]_0$.

The decrease in the peak HO_2 signal observed at T = 258.6 K (and also at T = 299.1 K, albeit to a lesser extent) near t = 0 s can be explained by the fast equilibrium reaction of HO_2 with CH_3OH (R28) and/or with $CH_3C(O)CH_3$ (R29). This was corroborated by the fact that the NIR only measures monomeric HO_2. Furthermore, adduct formation is more energetically favored at lower temperatures, which agrees with observations. Investigation of R28 is discussed in detail in Chapter 3 as well as in Christensen et al. [16], and R29 has been studied previously by Grieman et al. [17].

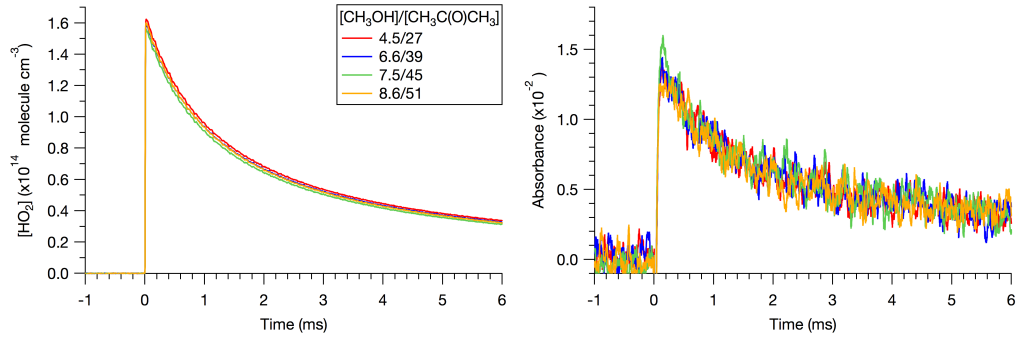

(a) T = 339.9 K: $[Cl_2] = 7.6 \times 10^{15}$ molecule cm^{-3}, $[Cl]_0 = 1.6 \times 10^{14}$ molecule cm^{-3}.

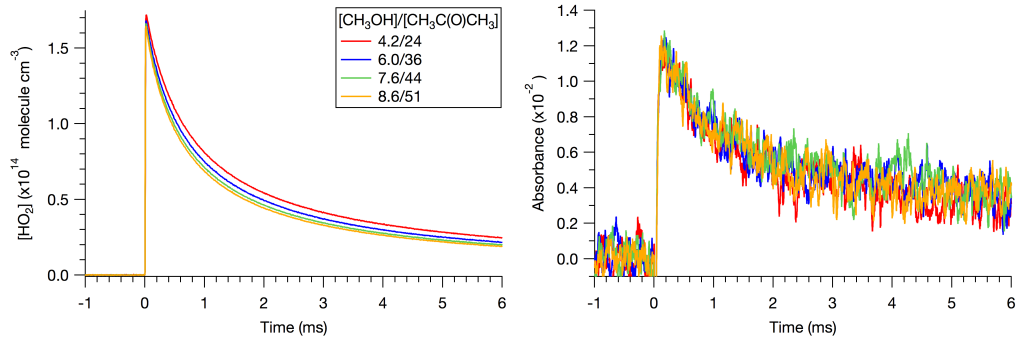

(b) T = 299.1 K: $[Cl_2] = 7.6 \times 10^{15}$ molecule cm^{-3}, $[Cl]_0 = 1.6 \times 10^{14}$ molecule cm^{-3}.

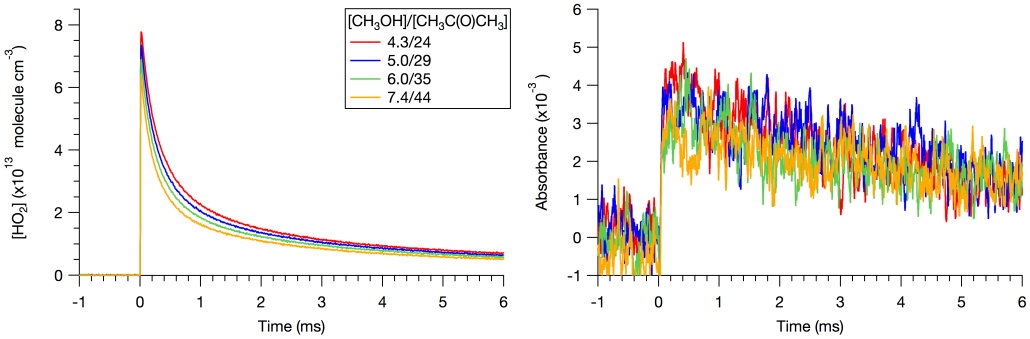

(c) T = 258.6 K: $[Cl_2] = 6.0 \times 10^{15}$ molecule cm^{-3}, $[Cl]_0 = 1.2 \times 10^{14}$ molecule cm^{-3}.

Figure 7.9: NIR signals (left) and UV absorbance at $\lambda = 300$ nm (right) from HO_2 + $CH_3C(O)CH_2O_2$ experiments conducted at P = 100 Torr in N_2 at three different temperatures. Only four runs for each temperature are shown for clarity. Both $[CH_3OH]$ and $[CH_3C(O)CH_3]$ were varied (units are in $\times 10^{15}$ molecule cm^{-3}), but the ratio was fixed at $[CH_3C(O)CH_3]/[CH_3OH] = 6$. For a given temperature, the total initial radical concentration was also kept the same.

The fraction of HO_2 bound in an adduct as $HO_2 \cdot CH_3OH$ (f_M) and as $HO_2 \cdot CH_3C(O)CH_3$ (f_A) can be calculated from their respective equilibrium con-

stants, $K_{c,M}$ and $K_{c,Ac}$:

$$f_M \equiv \frac{[HO_2 \cdot CH_3OH]_{eq}}{[HO_2]_0} = \frac{K_{c,M}[CH_3OH]}{1 + K_{c,M}[CH_3OH] + K_{c,Ac}[CH_3C(O)CH_3]} \tag{7.8}$$

$$f_A \equiv \frac{[HO_2 \cdot CH_3C(O)CH_3]_{eq}}{[HO_2]_0} = \frac{K_{c,Ac}[CH_3C(O)CH_3]}{1 + K_{c,M}[CH_3OH] + K_{c,Ac}[CH_3C(O)CH_3]} \tag{7.9}$$

where

$$K_{c,M} = \frac{[HO_2 \cdot CH_3OH]_{eq}}{[HO_2]_{eq}[CH_3OH]} \qquad K_{c,Ac} = \frac{[HO_2 \cdot CH_3C(O)CH_3]_{eq}}{[HO_2]_{eq}[CH_3C(O)CH_3]} \tag{7.10}$$

A zoomed in perspective of the NIR data from Figure 7.9(c) is shown in Figure 7.10, which also includes the data collected absence of $CH_3C(O)CH_3$ using the same $[Cl]_0$, at the same temperature. The dashed lines indicate the values of $[HO_2]_{eq}$ calculated using Equation 7.8, Equation 7.9, and Equation 7.6, and show excellent agreement with the observed peak HO_2 signals. $K_{c,M}$ and $K_{c,Ac}$ were calculated from the thermodynamic parameters of R28 and R29, respectively, which have been measured previously (Chapter 3 for $K_{c,M}$ and Grieman et al. [17] for $K_{c,Ac}$).

Using Equation 7.8 and Equation 7.9, the percentage of HO_2 complexed at the highest $[CH_3OH]$ and $[CH_3C(O)CH_3]$ were: 2%, 9%, and 35% at T = 339.9 K, 299.1 K, and 258.6 K, respectively. Table 7.6 summarizes the range of experimental conditions over which data were collected and lists the estimated percentage of HO_2 bound as $HO_2 \cdot CH_3OH$ and as $HO_2 \cdot CH_3C(O)CH_3$, calculated from the corresponding equilibrium constants.

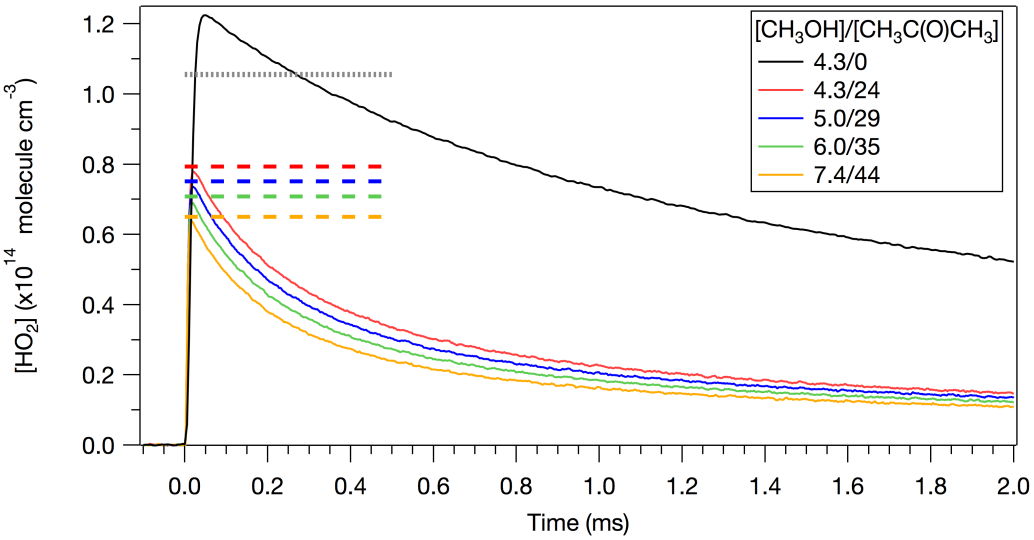

Figure 7.10: NIR HO_2 decay signals collected at T = 258.6 K using varying concentrations of $[CH_3OH]$ and $[CH_3C(O)CH_3]$, with fixed ratio $[CH_3OH]/[CH_3C(O)CH_3] = 6$. Data collected in the absence of $CH_3C(O)CH_3$ (black trace) is also shown for reference. The gray dotted line indicates the expected peak HO_2 signal calculated from Equation 7.3 for $[CH_3C(O)CH_3] \neq 0$ and $[CH_3OH]/[CH_3C(O)CH_3] = 6$. The colored dashed lines indicate the expected peak HO_2 signals for each run (color-coded appropriately) accounting for the rapid loss of HO_2 from the reactions with CH_3OH (R28) and with $CH_3C(O)CH_3$ (R29). $[Cl_2] = 6.0 \times 10^{15}$ molecule cm^{-3}, $[Cl]_0 = 1.2 \times 10^{14}$ molecule cm^{-3}.

Table 7.6: Summary of data collected with fixed $[CH_3OH]/[CH_3C(O)CH_3]$=6. $f_M = [HO_2 \cdot CH_3OH]/[HO_2]_0$, $f_A = [HO_2 \cdot CH_3C(O)CH_3]/[HO_2]_0$

T (K)	$[Cl_2]^a$	$[CH_3OH]^a$	$[CH_3C(O)CH_3]^a$	$[Cl]_0{}^b$	f_M(%)	f_A(%)	$f_M + f_A$ (%)	# of runs
339.9	7.6	3.3 - 8.6	19 - 51	1.6	0.14 - 0.36	0.61 - 1.6	0.75 - 1.9	5
319.9	7.6	3.5 - 8.6	21 - 51	1.8	0.25 - 0.61	1.3 - 3.2	1.6 - 3.8	5
310.0	7.6	3.6 - 8.5	21 - 51	1.2	0.35 - 0.80	2.0 - 4.6	2.3 - 5.4	6
299.1	7.6	4.2 - 8.8	24 - 51	2.1	0.59 - 1.2	3.7 - 7.5	4.3 - 8.7	5
280.5	6.1	3.2 - 8.5	25 - 50	1.5	1.1 - 2.0	8.3 - 15	9.4 - 17	5
269.7	6.1	3.2 - 8.7	19 - 50	1.4	1.2 - 2.7	11 - 24	12 - 27	6
258.6	6.1	3.3 - 7.4	20 - 44	1.2	1.7 - 3.2	18 - 32	20 - 35	5

[a]Units: 10^{15} molecule cm^{-3}
[b]Units: 10^{14} molecule cm^{-3}

In addition to the rapid loss of HO_2 via R29, Figure 7.9(b) and Figure 7.9(c) also show significant rate enhancement in the NIR HO_2 decay signals for T = 299.1 K and below. The observed increase in the HO_2 decay was due to the subsequent loss of HO_2 via reaction with $HO_2 \cdot CH_3OH$ (R30) and with $HO_2 \cdot CH_3C(O)CH_3$ (R31). Extensive investigation of the rate enhancement effect by CH_3OH is described in Chapter 3 as well as in Christensen et al. [16]. The results from those studies showed that rate enhancement by $HO_2 \cdot CH_3OH$ is negligible at room temperature, suggesting that $HO_2 \cdot CH_3C(O)CH_3$ was responsible for the additional loss of HO_2 observed in this work.

Varying [CH_3OH] for a fixed [$CH_3C(O)CH_3$] The effect of CH_3OH on k_{27obs} and k_5 is demonstrated in Figure 7.11(a) and Figure 7.11(b), respectively, and the values of all the fitted parameters are provided in Table 7.7. The results show that k_5 is not enhanced by CH_3OH. As expected, k_{27obs} also shows no dependence on CH_3OH, which forms little to no complex with HO_2 at room temperature; however, the values of k_{27obs} were higher than the calculated value of $k_{27} = 1.55 \times 10^{-12}$ cm^3 molecule^{-1} s^{-1} and beyond the upper 2σ uncertainty bound of 2.05×10^{-12} cm^3 molecule^{-1} s^{-1}[9]. This was attributed to rate enhancement of R27 by $CH_3C(O)CH_3$, which is demonstrated in the next section.

Table 7.7: Summary of fitted parameters from data collected with varying [CH_3OH] with fixed [$CH_3C(O)CH_3$] = 3.0×10^{16} molecule cm^{-3}. Uncertainties in the fitted parameters were <3% for $[Cl]_0$, ~0.3% for $[HO_2]_{eq}$, ~1% for k_{27obs}, and ~3-5% for k_5. T = 299.1 K; P = 100 Torr; concentrations: $[Cl_2] = 7.6 \times 10^{15}$ molecule cm^{-3}; $[O_2] = 1.56 \times 10^{18}$ molecule cm^{-3}.

[CH_3OH][a]	Fitted paramters			
	$[Cl]_0$[b]	$[HO_2]_{eq}$[b]	k_{27obs}[c]	k_5[c]
3.9	2.09	1.48	2.55	3.12
4.3	2.41	1.52	2.35	2.98
4.9	2.24	1.59	2.47	2.94
6.2	2.21	1.67	2.46	2.89
7.5	2.10	1.73	2.51	2.93

[a]Units: 10^{15} molecule cm^{-3}
[b]Units: 10^{14} molecule cm^{-3}
[c]Units: 10^{-12} cm^3 molecule^{-1} s^{-1}

Varying [$CH_3C(O)CH_3$] for a fixed [CH_3OH] Characterization of the HO_2 self reaction rate enhancement effect by $HO_2 \cdot CH_3C(O)CH_3$ was investigated by varying [$CH_3C(O)CH_3$], while keeping [CH_3OH] fixed. While Figure 7.12(b) shows that k_5

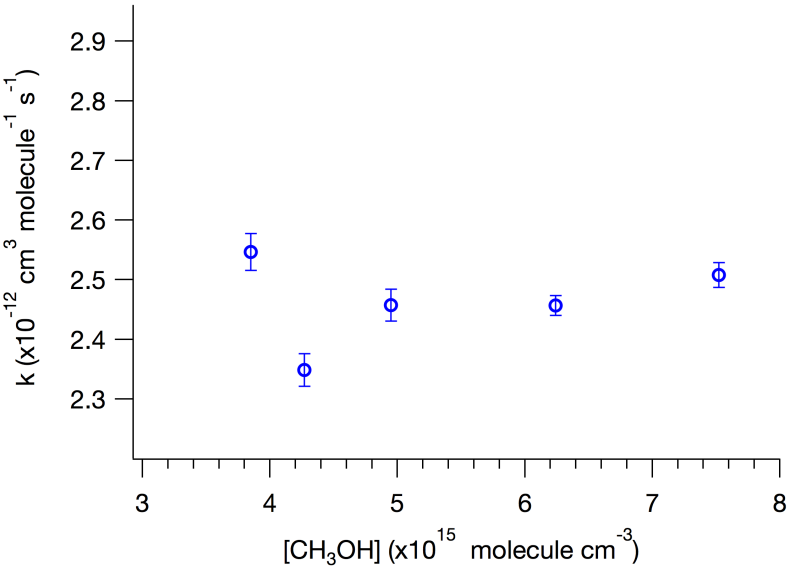

(a)

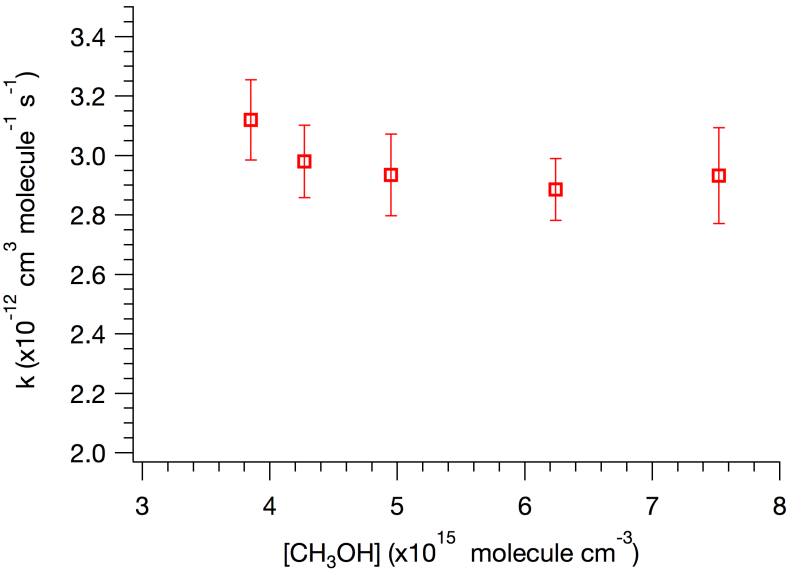

(b)

Figure 7.11: Fitted values of (a) $k_{27\text{obs}}$ and (b) k_5, from fixed $[CH_3C(O)CH_3]$ = 3.0×10^{16} molecule cm^{-3} data, plotted as a function of $[CH_3OH]$.

displays no clear dependence on $[CH_3C(O)CH_3]$, Figure 7.12(a) demonstrates that $k_{27\text{obs}}$ is linear in $[CH_3C(O)CH_3]$ and that significant rate enhancement of R27 is observed, even at room temperature. A full summary of the fitted parameters from this set of data is given in Table 7.8.

The values of $k_{27\text{obs}}$ were plotted against $[CH_3C(O)CH_3]$ and a weighted linear fit to the data gave $k_{27} + k''_{27,\text{M}}[CH_3OH] = (1.6 \pm 0.05) \times 10^{-12}$ cm^3 molecule^{-1} s^{-1}

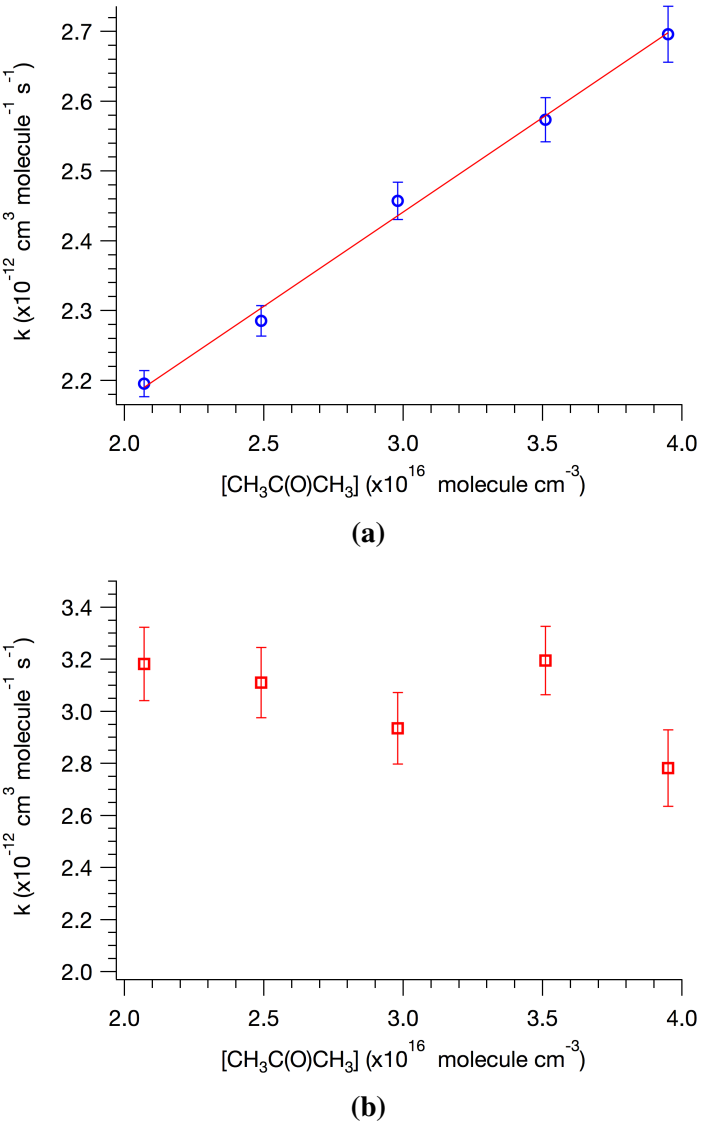

Figure 7.12: Fitted values of (a) $k_{27\text{obs}}$ and (b) k_5, from fixed $[CH_3OH] = 4.9\times10^{15}$ molecule cm^{-3} data, plotted as a function of $[CH_3C(O)CH_3]$.

from the y-intercept, and $k''_{27,A} = (2.7 \pm 0.18) \times 10^{-29}$ cm^6 molecule^{-2} s^{-1} from the slope. Subtrating k_{27} from the slope using the JPL recommended value at T = 299 K and P = 100 Torr ($k_{27} = 1.55 \times 10^{-12}$ cm^3 molecule^{-1} s^{-1}) and dividing by $[CH_3OH] = 4.9 \times 10^{15}$ molecule cm^{-3} gives $k''_{27,M} = (1.7 \pm 0.32) \times 10^{-29}$ cm^6 molecule^{-2} s^{-1} (1σ uncertainty). The calculated error include uncertainties in [M] (~10%), k_{27} (error bounds from JPL data evaluation [9]), and the random error in the linear regression. This is in excellent agreement with the calculated value of $k''_{27,M} = 1.86\times10^{-29}$ cm^6 molecule^{-2} s^{-1} using the Arrhenius parameters determined in a previous study (Chapter 3).

Table 7.8: Summary of fitted parameters from data collected with varying $[CH_3C(O)CH_3]$ with fixed $[CH_3OH] = 4.9 \times 10^{16}$ molecule cm^{-3}. Uncertainties in the fitted parameters were <3% for $[Cl]_0$, ~0.3% for $[HO_2]_{eq}$, ~1% for k_{27obs}, and ~3-5% for k_5. T = 299.1 K; P = 100 Torr; concentrations: $[Cl_2] = 7.6 \times 10^{15}$ molecule cm^{-3}; $[O_2] = 1.56 \times 10^{18}$ molecule cm^{-3}.

$[CH_3C(O)CH_3]^a$	Fitted paramters			
	$[Cl]_0{}^b$	$[HO_2]_{eq}{}^b$	$k_{27obs}{}^c$	$k_5{}^c$
2.1	2.24	1.72	2.20	3.18
2.5	2.23	1.61	2.29	3.11
3.0	2.24	1.59	2.46	2.94
3.5	2.35	1.44	2.57	3.19
4.0	2.33	1.38	2.70	2.78

[a]Units: 10^{16} molecule cm^{-3}
[b]Units: 10^{14} molecule cm^{-3}
[c]Units: 10^{-12} cm^3 molecule^{-1} s^{-1}

7.3.5.2 Determination of k_5

Figure 7.13 shows that the fitted values of k_5 from all data sets are self-consistent and invariant of $[HO_2]_0/[CH_3C(O)CH_2O_2]_0$. An average value of $k_5 = 2.98 \pm 0.14 \times 10^{-12}$ cm^3 molecule^{-1} s^{-1} (1σ uncertainty) was obtained from the weighted average of all fitted values.

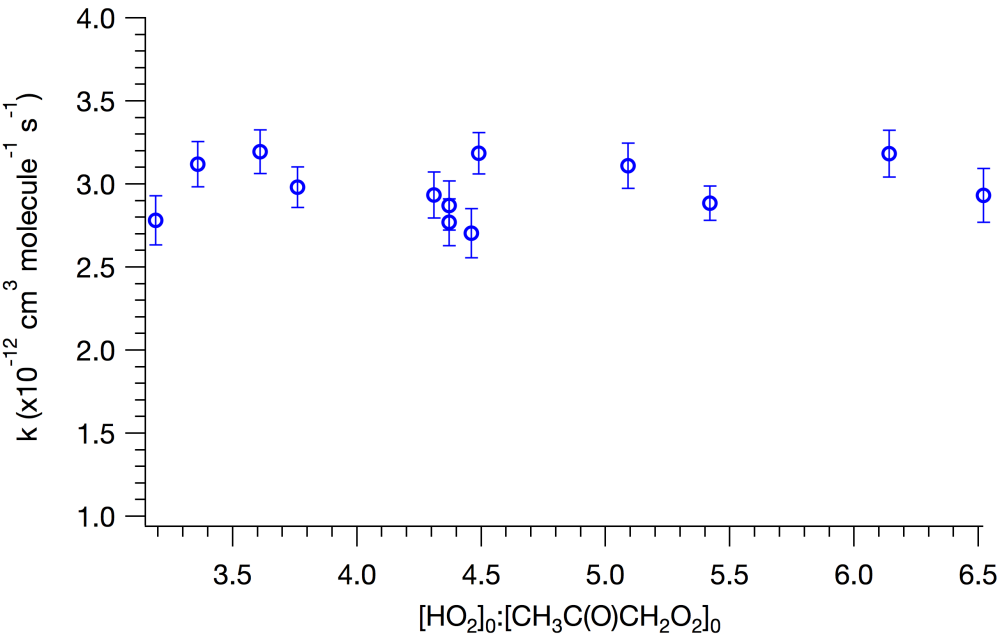

Figure 7.13: Fitted values of k_5 from all data sets, plotted as a function of $[HO_2]_0/[CH_3C(O)CH_2O_2]_0$.

Figure 7.14 shows the fits to the NIR HO_2 and UV (λ = 300 nm) signals obtained at room temperature for $[HO_2]_0/[CH_3C(O)CH_2O_2]_0$ = 6.5 (Figure 7.14(a)) and $[HO_2]_0/[CH_3C(O)CH_2O_2]_0$ = 3.4 (Figure 7.14(b)). The simulated time profiles using the values of k_5 and $\sigma_{CH_3C(O)CH_2O_2}$ from Bridier et al. [6] with and without R27 rate enhancement (dashed and dotted black lines, respectively) show that rate enhancement is an important factor in achieving acceptable agreement with the observed NIR HO_2 profile. Still, the UV time profile cannot be reproduced using the values of k_5 and $\sigma_{CH_3C(O)CH_2O_2}$ from Bridier et al. [6], suggesting that these parameters need to be revised in the current data evaluations.

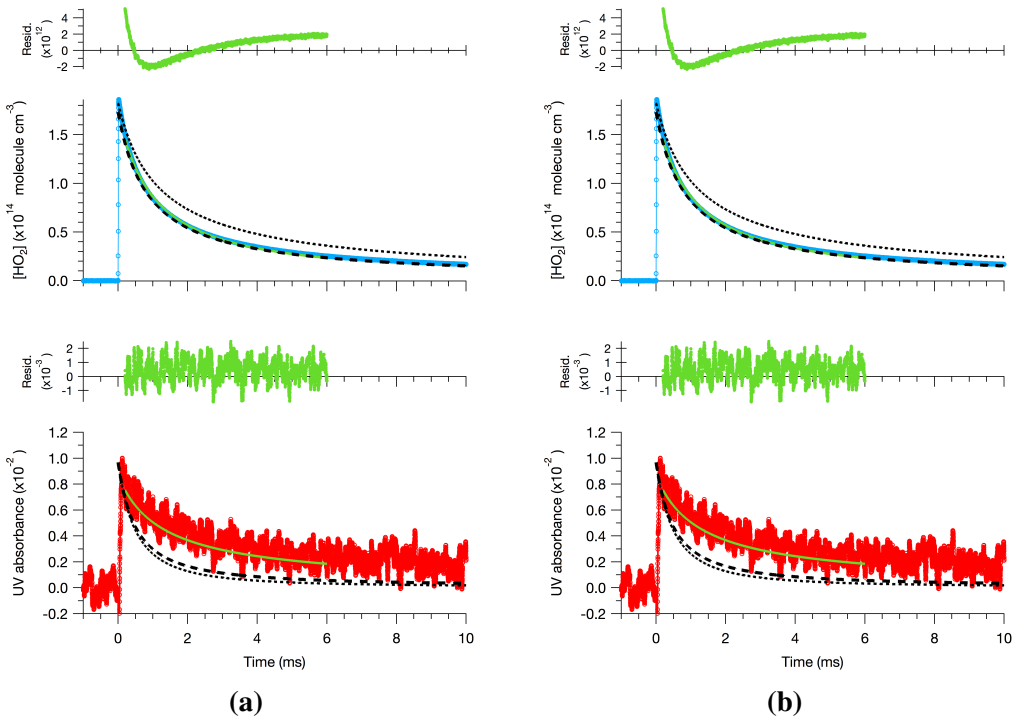

Figure 7.14: Fits (green) to the NIR HO_2 (blue) and UV (λ = 300 nm) (red) data obtained with (a) $[HO_2]_0/[CH_3C(O)CH_2O_2]_0$ = 6.5 and (b) $[HO_2]_0/[CH_3C(O)CH_2O_2]_0$ = 3.4. Residuals are shown above each curve. The black lines are the simulated time profiles using the values of k_5 and $\sigma_{CH_3C(O)CH_2O_2}$ from Bridier et al. [6]. The dashed line includes rate enhancement of R27, while the dotted line does not.

7.3.6 Mystery absorber

This section describes the work carried out to measure the product yield of methylglyoxal ($CH_3C(O)CHO$) formed from the radical terminating channel of R4

(R4a). The branching fraction of R4a, α_{4a}, is defined as:

$$\alpha_{4a} = \frac{k_{4a}}{k_4}, \tag{7.11}$$

where k_{4a} is the rate constant of R4a and k_4 is the overall rate constant of R4. The motivation behind this part of the work was to resolve the large discrepancies in the values of α_{4a} reported by previous end-product studies [11, 13]. Furthermore, $CH_3C(O)CHO$ is also a product of R11, which was assumed to be negligible under our experimental conditions; thus, having sensitivity to $CH_3C(O)CHO$ would also provide validation for this assumption. Ultimately, the data were unable to provide sensitivity to the product yields due to the presence of an unidentified absorber; observations will nonetheless be presented for reference purposes in future investigations.

Experiments were carried out as was described for the determination of k_4 and $\sigma_{CH_3C(O)CH_2O_2}$; i.e., gas mixtures of $Cl_2/CH_3C(O)CH_3/O_2/N_2$ were photolyzed at room temperature and P = 100 Torr. In order to measure absorbance by $CH_3C(O)CHO$ in addition to $CH_3C(O)CH_2O_2$, two light emitting diode (LED) sources were used instead of the D_2 lamp with nominal emission wavelengths of 310 nm (Thorlabs M310L3) and 420 nm (Thorlabs M420L3). The 310 nm LED light source was used to monitor $CH_3C(O)CH_2O_2$, and was used in place of the D_2 lamp to gain enhanced signal-to-noise of the UV signal (the 310 nm LED emits at a power of over 10 times higher than that of the D_2 lamp). The 420 nm LED was used to monitor $CH_3C(O)CHO$. $CH_3C(O)CHO$ has two broad absorption bands in the visible spectral region, with the larger peak centered around 420 nm (Figure 7.15). Back-to-back experiments were carried out, switching between the two LEDs using a flip mirror while maintaining all other experimental conditions identical.

Figure 7.16 shows the time profiles obtained in the NIR and at 310 nm and 420 nm from experiments carried out using varying $[O_2]$ in the absence of CH_3OH. Only the data obtained using the lowest and highest $[O_2]$ concentrations are shown for clarity. The signals at 310 nm and 420 nm did not appear to have any dependence on $[O_2]$, while the NIR HO_2 signal increased with increasing $[O_2]$, as was observed in the $CH_3C(O)CH_2O_2$ self reaction data shown previously.

At first glance, the lack of $[O_2]$ dependence of the 420 nm data appears to support the assumption that R11 is negligible; however, the axes on the right in Figure 7.16 shows that scaling the 310 nm and 410 nm absorbance signals by the absorption cross-sections of $CH_3C(O)CH_2O_2$ ($\sigma_{CH_3C(O)CH_2O_2}(\lambda = 310\text{ nm}) = 1.83 \times 10^{-18}$

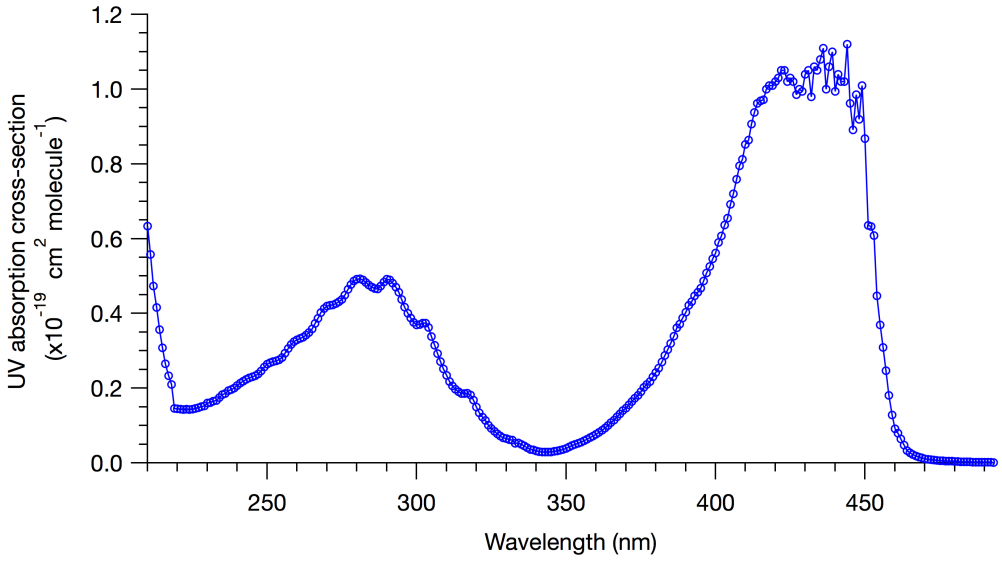

Figure 7.15: UV absorption cross-section of $CH_3C(O)CHO$ from JPL 15-10 [9].

cm^2 $molecule^{-1}$, determined in this work) and $CH_3C(O)CHO$ ($\sigma_{CH_3C(O)CHO}(\lambda$ = 420 nm) = 1.02×10^{-19} cm^2 $molecule^{-1}$ [9]) the observed peak concentration of $CH_3C(O)CHO$ is almost 6 times higher than the initial radical concentrations of $[CH_3C(O)CH_2O_2]_0 = 1.35 \times 10^{14}$ molecule $^{-3}$. Since $CH_3C(O)CHO$ is presumably only produced from R4a and R11, the apparent high levels of $CH_3C(O)CHO$ are unlikely to be explained by radical recycling; rather, the observed UV absorbance may be due to an incorrect value of $\sigma_{CH_3C(O)CHO}$, or to additional absorbance by some unknown absorber.

Values of $\sigma_{CH_3C(O)CHO}$ at λ = 420 nm have been reported by four independent studies [18–21], three of which are in good agreement [19–21]. The value reported by Plum et al. [18] was smaller by a factor of ~0.5, which would result in an even higher $[CH_3C(O)CHO]$. Although a systematic error in the three consistent values of $\sigma_{CH_3C(O)CHO}$ cannot completely be ruled out without additional verification, an error of a factor of 6 is unlikely. An alternative explanation for the observed absorbance signal at 420 nm is the presence of an unknown absorber.

Several additional experiments for the $CH_3C(O)CH_2O_2$ self reaction were carried out to identify the absorber by measuring the absorbance signal over several wavelengths in the visible up to 550 nm. The absorption band of $CH_3C(O)CHO$ centered around 420 nm has a sharp, characteristic band edge at around 450 nm (Figure 7.15). Thus, a significant drop in the absorption signal was expected for λ > 450 nm. Figure 7.17 shows the absorption time profiles for wavelengths in the range λ = 430 - 550 nm. Figure 7.17(a) shows absorbance signals for λ = 440 - 465 nm obtained under

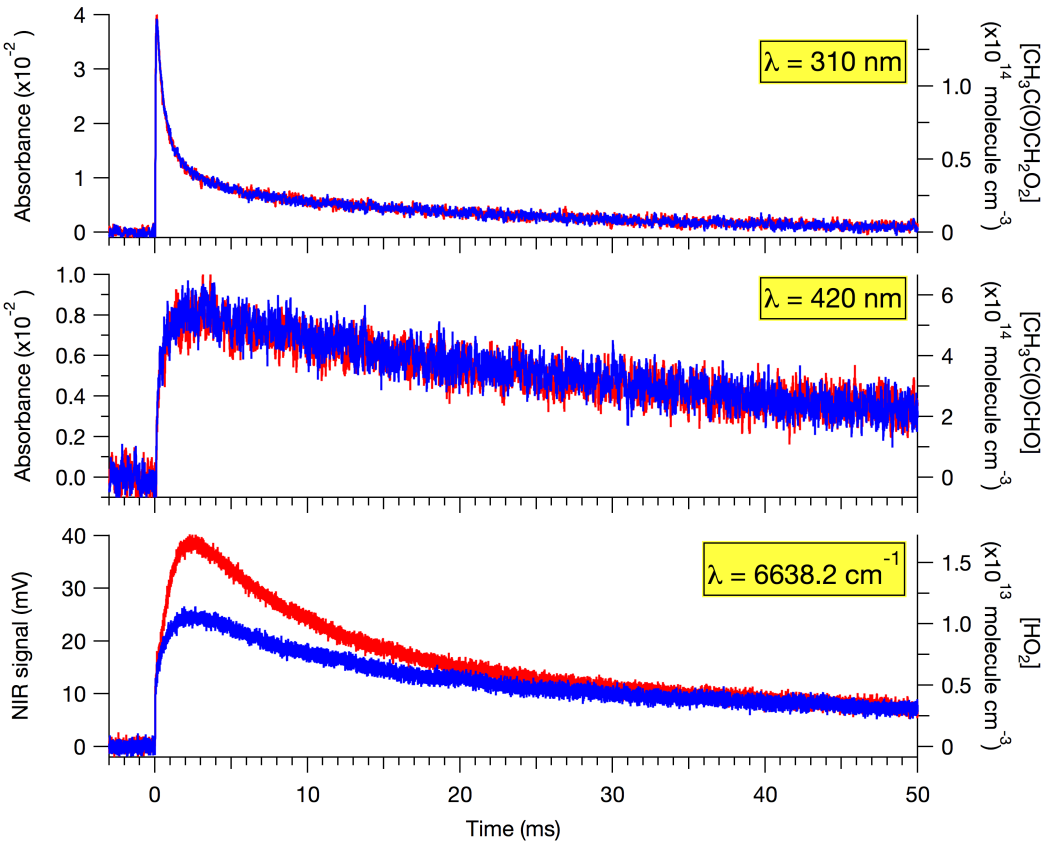

Figure 7.16: Time profiles from the $CH_3C(O)CH_2O_2$ self reaction with varying $[O_2]$ obtained using the LED light sources at λ = 310 nm (top panel) and λ = 420 nm (middle panel) and the NIR laser (bottom panel). Only the lowest and highest concentrations of $[O_2]$ are shown for clarity: $[O_2] = 7.0 \times 10^{17}$ molecule cm^{-3} (blue) and $[O_2] = 2.2 \times 10^{18}$ molecule cm^{-3} (red) Conversion to absolute concentrations (axes on the right) for the 310 nm and 420 nm data were calculated using the UV absorption cross-sections of $CH_3C(O)CH_2O_2$ and $CH_3C(O)CHO$, respectively, and the NIR signal was converted to HO_2 using the NIR calibration factor (see text). T = 298 K; P = 100 Torr; concentrations: $[Cl_2] = 7.5 \times 10^{15}$ molecule cm^{-3}; $[CH_3C(O)CH_3] = 3.0 \times 10^{16}$ molecule cm^{-3}; $[CH_3C(O)CH_2O_2]_0 = 1.35 \times 10^{14}$ molecule cm^{-3}.

otherwise identical experimental conditions using an LED source with a nominal wavelength of 455 nm (Thorlabs 455L3). The absorbance signals in Figure 7.17(b) were collected using a quartz halogen lamp with a tungsten filament, extending the wavelength range to 550 nm. Both Figure 7.17(a) and Figure 7.17(b) demonstrate that the time profiles across all wavelengths were observed to be identical, even for λ > 450 nm, where $CH_3C(O)CHO$ should not absorb. Furthermore, the initial radical concentration used in the data shown in Figure 7.17(a) was 1.5 times less than that used in the data shown in Figure 7.17(b); however, the absorbance signals do not

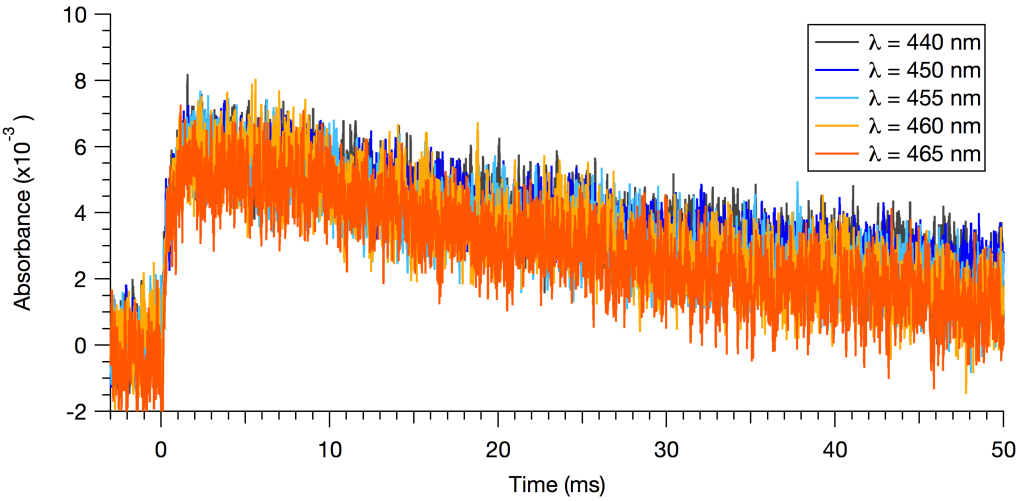

(a) $[CH_3C(O)CH_2O_2]_0 = 1.2 \times 10^{14}$ molecule cm^{-3}.

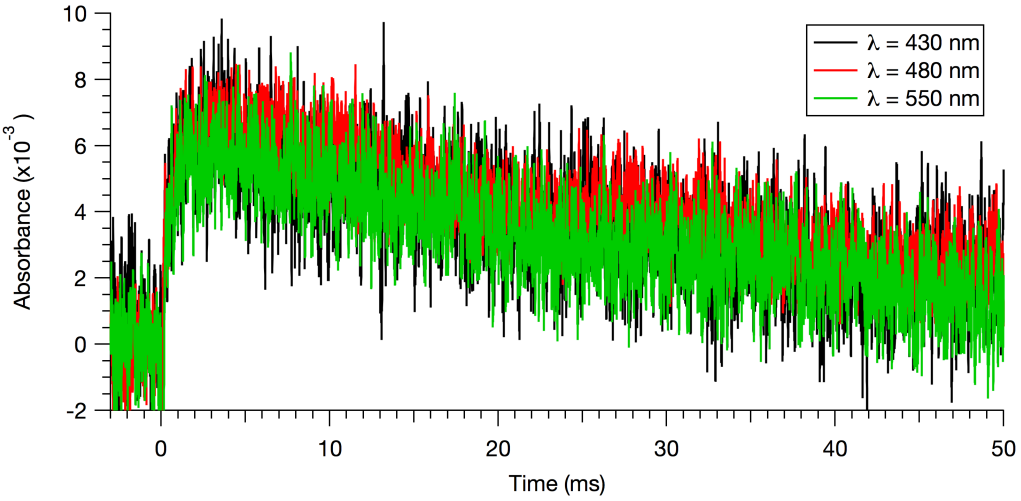

(b) $[CH_3C(O)CH_2O_2]_0 = 1.8 \times 10^{14}$ molecule cm^{-3}.

Figure 7.17: Time-resolved absorbance signals of the $CH_3C(O)CH_2O_2$ self reaction at T = 298 K and P = 100 Torr obtained at various wavelengths in the range λ = 430 - 550 nm. Identical time profiles were observed in the absorbance signals for all wavelengths. Absorbance signals were obtained using (a) an LED source (nominal wavelength λ = 455 nm and (b) a quartz halogen lamp. Each trace is an average of 200 excimer laser shots. Concentrations: $[Cl_2] = 6.6 \times 10^{15}$ molecule cm^{-3}; $[CH_3C(O)CH_3] = 2.9 \times 10^{16}$ molecule cm^{-3}; $[O_2] = 1.6 \times 10^{18}$ molecule cm^{-3}.

appear to scale with the radical concentrations. Across all wavelengths, the peak absorbance signal appeared to be constant, with ~0.6% absorbance.

On the other hand, zero absorbance was seen in control experiments carried out in the absence of Cl_2 or $CH_3C(O)CH_3$ (Figure 7.18). This demonstrates that the observed absorbance signals shown in Figure 7.17 are only present with active $CH_3C(O)CH_2O_2$ chemistry.

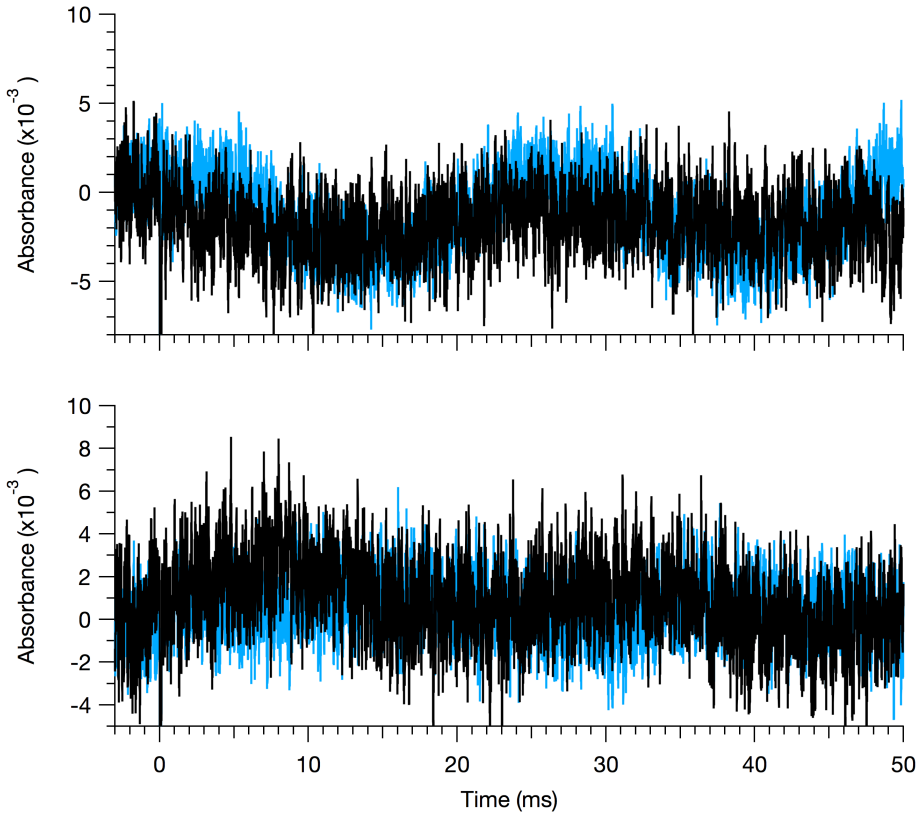

Figure 7.18: Time profiles at λ = 430 nm (black) and λ = 450 nm (light blue) from control experiments with $[Cl_2]$ = 0, $[CH_3C(O)CH_3] = 3.0 \times 10^{16}$ molecule cm^{-3} (top panel) and with $[Cl_2] = 6.8 \times 10^{15}$ molecule cm^{-3}, $[CH_3C(O)CH_3]$ = 0 (bottom panel). T = 298 K; P = 100 Torr.

These results call into question whether the observed absorbance signals in Figure 7.15 were from absorbance by $CH_3C(O)CHO$ at all. It is possible that this mystery absorber also absorbs at ~300 nm, where $CH_3C(O)CH_2O_2$ absorbs. However, compared to the typical peak absorbance of ~4% by $CH_3C(O)CH_2O_2$, contribution to the total absorbance by the mystery absorber is small, assuming that the absorber maintains a constant absorbance of ~0.6% across all wavelengths. Thus, although the nature of these absorbance signals could not be determined, the kinetics of $CH_3C(O)CH_2O_2$ determined from the UV absorbance signals at 300 nm should not be significantly affected.

7.4 Conclusion

This work investigated the kinetics of R4 and R5 at room temperature and P = 100 Torr using simultaneous IR and UV absorption spectroscopy. $\sigma_{CH_3C(O)CH_2O_2}$ was also measured over the spectral range of λ = 300 - 315 nm, which was isolated

from absorption by other peroxy radicals. At 300 nm, the measured absorption cross-section was $\sigma_{CH_3C(O)CH_2O_2} = (2.11 \pm 0.35) \times 10^{-18}$ cm^2 molecule^{-1}. The values measured in this work were almost a factor of 2 times higher than those in the JPL data evaluation.

Selective detection of HO_2 in the NIR enabled the identification and characterization of the rate enhancement to R27 by $CH_3C(O)CH_3$, which was found to have a significant impact on the overall kinetics of R5, even at room temperature. The measured values of $k_4 = (5.44 \pm 0.07) \times 10^{-12}$ cm^3 molecule^{-1} s^{-1} and $k_5 = (2.98 \pm 0.14) \times 10^{-12}$ cm^3 molecule^{-1} s^{-1} were a factor of ~1.5 and ~3 times slower than the values in the current JPL data evaluation, respectively. Future publication of this work will report the results from experiments conducted at lower temperatures, over the temperature range T = 220 - 300 K.

Work was also carried out to determine the yield of $CH_3C(O)CHO$ from R4 using absorption spectroscopy at λ = 420 nm; however, due to the presence of an unknown absorber, the product yield could not be determined. The unknown absorber appeared to have a constant absorbance signal of ~0.6% across the range λ = 420 - 550 nm and was only present with active $CH_3C(O)CH_2O_2$ chemistry. The identification of the absorber was beyond the scope of this work, and further investigation in the future may be warranted.

This chapter summarizes work carried out prior to implementation of the MIR laser, which was designed for direct detection of OH for the work described in Chapter 4. Therefore, information about the OH yield from R5b was not determined. Future work on the HO_2 + $CH_3C(O)CH_2O_2$ reaction with the updated IRKS apparatus would reveal valuable information about the importance of OH recycling on the overall kinetics.

Table 7.9: Full list of reactions and rate constants used in the kinetics model.

	Reaction			Rate constant (cm^3 $molecule^{-1}$ s^{-1})	Ref
Methanol					
(R7)	$Cl + CH_3OH$	$\longrightarrow$	$CH_2OH + HCl$	5.5×10^{-11}	[9], this lab
(R32a)	$OH + CH_3OH$	$\longrightarrow$	$CH_2OH + H_2O$	$0.85 \times 2.90 \times 10^{-12}\exp(345/T)$	[9]
(R32b)		$\longrightarrow$	$CH_3O + H_2O$	$0.15 \times 2.90 \times 10^{-12}\exp(345/T)$	[9]
(R8)	$CH_2OH + O_2$	$\longrightarrow$	$HO_2 + CH_2O$	9.1×10^{-11}	[9]
Acetone					
(R9)	$Cl + CH_3C(O)CH_3$	$\longrightarrow$	$CH_3C(O)CH_2 + HCl$	$1.63 \times 10^{-11}\exp(-610/T)$	[9]
(R2a)	$OH + CH_3C(O)CH_3$	$\longrightarrow$	$CH_3C(O)CH_2 + H_2O$	$0.98 \times [1.33 \times 10^{-13}$ $+3.823 \times 10^{-11}\exp(-2000/T)]$	[9]
(R2b)		$\longrightarrow$	$CH_3 + CH_3C(O)OH$	$0.02 \times [1.33 \times 10^{-13}$	
			$+3.823 \times 10^{-11}\exp(-2000/T)]$		
(R3)	$CH_3C(O)CH_2 + O_2$	$\xrightarrow{M}$	$CH_3C(O)CH_2O_2$	$k_0 = 3.0 \times 10^{-29}$ $k_\infty = 1.0 \times 10^{-12}$	[9]
(R26)	$CH_3C(O)CH_2 + O_2$	$\longrightarrow$	HO_2 + products	~0.02 of k_3	see text
RO_2 reactions					
(R5a)	$HO_2 + CH_3C(O)CH_2O_2$	$\longrightarrow$	$CH_3C(O)CH_2OOH + O_2$	$0.85 \times k_5$	branching ratios: [8]
(R5b)		$\longrightarrow$	$CH_3C(O)CH_2O + OH + O_2$	$0.15 \times k_5$	k_5: varied
(R4a)	$2\,CH_3C(O)CH_2O_2$	$\longrightarrow$	$CH_3C(O)CH_2OH$ $+ CH_3C(O)CHO + O_2$	$0.37 \times k_4$	branching ratios: [8]
(R4b)		$\longrightarrow$	$2\,CH_3C(O)CH_2O + O_2$	$0.63 \times k_4$	k_4: varied
(R15a)	$CH_3C(O)O_2 + CH_3C(O)CH_2O_2$	$\longrightarrow$	$CH_3C(O)OH$ $+ CH_3C(O)CHO + O_2$	$0.5 \times k_{15}$	[8]
(R15b)		$\longrightarrow$	$CH_3C(O)O$ $+ CH_3C(O)CH_2O + O_2$	$0.5 \times k_{15}$	

	Reaction			Rate constant (cm^3 $molecule^{-1}$ s^{-1})	Ref
(R18a)	$CH_3O_2 + CH_3C(O)CH_2O_2$	$\longrightarrow$	$CH_3OH + CH_3C(O)CHO + O_2$	$0.5 \times k_{18}$	
(R18b)		$\longrightarrow$	$CH_2O + CH_3C(O)CH_2OH + O_2$	$0.2 \times k_{18}$	[8]
(R18c)		$\longrightarrow$	$CH_3O + CH_3C(O)CH_2O + O_2$	$0.3 \times k_{18}$	
(R10)	$CH_3C(O)CH_2O$	$\xrightarrow{M}$	$CH_3C(O) + CH_2O$		Assumed instantaneous
(R11)	$CH_3C(O)CH_2O + O_2$	$\longrightarrow$	$CH_3C(O)CHO + HO_2$		
(R12)	$CH_3C(O) + O_2$	$\xrightarrow{M}$	$CH_3C(O)O_2$	$(1 - \alpha_{12b} - \alpha_{12c}) \times 5.1 \times 10^{-12}$	overall rate constant: [22]
(R12b)		$\longrightarrow$	OH + products	$\alpha_{12b} \times 5.1 \times 10^{-12}$	branching ratios
(R12c)		$\longrightarrow$	HO_2 + products	$\alpha_{12c} \times 5.1 \times 10^{-12}$	from this lab
(R14a)	$HO_2 + CH_3C(O)O_2$	$\longrightarrow$	$CH_3C(O)OOH + O_2$	$(1 - \alpha_{14b} - \alpha_{14c}) \times k_{14}$	this lab
(R14b)		$\longrightarrow$	$CH_3C(O)OH + O_3$	$\alpha_{14b} \times k_{14}$	this lab
(R14c)		$\longrightarrow$	$OH + CH_3C(O)O + O_2$	$\alpha_{14c} \times k_{14}$	this lab
(R20a)	$HO_2 + CH_3O_2$	$\longrightarrow$	$CH_3OOH + O_2$	$\{1 - 1/[1 + 498\exp(-1160/T)]\}$ $\times 3.8 \times 10^{-13}\exp(780/T)$	[9]
(R20b)		$\longrightarrow$	$CH_2O + H_2O + O_2$	$\{1/[1 + 498\exp(-1160/T)]\}$ $\times 3.8 \times 10^{-13}\exp(780/T)$	
(R13)	$2\,CH_3C(O)O_2$	$\longrightarrow$	$2\,CH_3C(O)O + O_2$	k_{13}	[9]
(R19a)	$CH_3O_2 + CH_3C(O)O_2$	$\longrightarrow$	$CH_3C(O)O + CH_3O + O_2$	$\alpha_{19a} \times k_{19}$	[9]
(R19b)		$\longrightarrow$	$CH_3C(O)OH + CH_2O + O_2$	$(1\text{-}\alpha_{19a}) \times k_{19}$	[9]
(R17a)	$CH_3O_2 + CH_3O_2$	$\longrightarrow$	$2\,CH_3O + O_2$	$\{1 - 1/[1 + 26.2\exp(-1130/T)]\}$ $\times 9.5 \times 10^{-14}\exp(390/T)$	[9]
(R17b)		$\longrightarrow$	$CH_3OH + CH_2O + O_2$	$\{1/[1 + 26.2\exp(-1130/T)]\}$ $\times 9.5 \times 10^{-14}\exp(390/T)$	
(R21)	$CH_3O + O_2$	$\longrightarrow$	$CH_2O + HO_2$	$3.9 \times 10^{-14}\exp(-900/\mathrm{T})$	[9]
(R33)	$CH_3C(O)O$	$\longrightarrow$	$CH_3 + CO_2$	Assumed instantaneous	[9]
(R16)	$CH_3 + O_2$	$\xrightarrow{M}$	CH_3O_2	$k_0 = 4.0 \times 10^{-31}(300/T)^{-3.6}$ $k_\infty = 1.2 \times 10^{-12}(300/T)^{1.1}$	[9]

HO_x reactions

	Reaction			Rate constant (cm^3 $molecule^{-1}$ s^{-1})	Ref
(R27)	$HO_2 + HO_2$	$\xrightarrow{M}$	$H_2O_2 + O_2$	k_{27}	varied, see text
(R34)	$OH + HO_2$	$\longrightarrow$	$H_2O + O_2$	$4.8 \times 10^{-11}\,\exp(250/T)$	[9]
(R35a)	$OH + OH$	$\longrightarrow$	$H_2O + O$	1.8×10^{-12}	[9]
(R35b)	$OH + OH$	$\xrightarrow{M}$	H_2O_2	$k_0 = 6.9 \times 10^{-31}(300/T)^{-1.0}$ $k_\infty = 2.6 \times 10^{-11}$	[9] [9]
(R36)	$OH + H_2O_2$	$\longrightarrow$	$H_2O + HO_2$	1.8×10^{-12}	[9]
(R37)	$OH + CH_2O$	$\longrightarrow$	$H_2O + HCO$	$5.5 \times 10^{-12}\,\exp(125/T)$	[9]
(R38)	$HCO + O_2$	$\longrightarrow$	$HO_2 + CO$	5.2×10^{-12}	[9]
(R39)	$O + OH$	$\longrightarrow$	$O_2 + H$	$1.8 \times 10^{-11}\,\exp(180/T)$	[9]
(R40)	$O + HO_2$	$\longrightarrow$	$O_2 + OH$	$3.0 \times 10^{-11}\,\exp(200/T)$	[9]
(R41)	$H + O_2$	$\xrightarrow{M}$	HO_2	$k_0 = 4.4 \times 10^{-32}(300/T)^{-1.3}$ $k_\infty = 7.5 \times 10^{-11}(300/T)^{0.2}$	
(R42)	$OH + O_3$	$\longrightarrow$	$HO_2 + O_2$	$1.7 \times 10^{-12}\,\exp(-940/T)$	[9]
(R43)	$HO_2 + O_3$	$\longrightarrow$	$OH + 2\,O_2$	$1.0 \times 10^{-14}\,\exp(-490/T)$	[9]

References

[1] Orlando, J. J.; Tyndall, G. S.; Vereecken, L.; Peeters, J. The Atmospheric Chemistry of the Acetonoxy Radical. *The Journal of Physical Chemistry A* **2000**, *104*, 11578–11588.

[2] Hasson, A. S.; Tyndall, G. S.; Orlando, J. J. A Product Yield Study of the Reaction of HO2 Radicals with Ethyl Peroxy (C2H5O2), Acetyl Peroxy (CH3C(O)O2), and Acetonyl Peroxy (CH3C(O)CH2O2) Radicals. *The Journal of Physical Chemistry A* **2004**, *108*, 5979–5989.

[3] Jenkin, M. E.; Hurley, M. D.; Wallington, T. J. Investigation of the Radical Product Channel of the CH3C(O)CH2O2 + HO2 Reaction in the Gas Phase. *Physical Chemistry Chemical Physics* **2008**, *10*, 4274–4280.

[4] Dillon, T. J.; Crowley, J. N. Direct Detection of OH Formation in the Reactions of HO2 with CH3C(O)O2 and Other Substituted Peroxy Radicals. *Atmospheric Chemistry and Physics* **2008**, *8*, 4877–4889.

[5] Hasson, A. S.; Tyndall, G. S.; Orlando, J. J.; Singh, S.; Hernandez, S. Q.; Campbell, S.; Ibarra, Y. Branching Ratios for the Reaction of Selected Carbonyl-Containing Peroxy Radicals with Hydroperoxy Radicals. *The Journal of Physical Chemistry A* **2012**, *116*, 6264–6281.

[6] Bridier, I.; Veyret, B.; Lesclaux, R.; Jenkin, M. E. Flash Photolysis Study of the UV Spectrum and Kinetics of Reactions of the Acetonylperoxy Radical. *J. Chem. Soc., Faraday Trans.* **1993**, *89*, 2993–2997.

[7] Cox, R. A.; Munk, J.; Nielsen, O. J.; Pagsberg, P.; Ratajczak, E. Ultraviolet Absorption Spectra and Kinetics of Acetonyl and Acetonylperoxy Radicals. *Chemical Physics Letters* **1990**, *173*, 206–210.

[8] Atkinson, R.; Baulch, D. L.; Cox, R. A.; Hampson, R. F.; Kerr, J. A.; Troe, J. Evaluated Kinetic and Photochemical Data for Atmospheric Chemistry: Supplement IV. IUPAC Subcommittee on Gas Kinetic Data Evaluation for Atmospheric Chemistry. *Journal of Physical and Chemical Reference Data* **1992**, *21*, 1125–1568.

[9] Sander, S. P.; Abbat, J.; Barker, J.R.; Burkholder, J.B.; Huie, R.E.; Kolb, C.E.; Kurylo, M.J.; Wilmouth, D.M.; Orkin, V.L.; Wine, P.H. *Chemical Kinetics and Photochemical Data for Use in Atmospheric Studies, Evaluation No. 18*; Jet Propulsion Laboratory, Pasadena: JPL Publication 15-10, 2015.

[10] Tyndall, G. S.; Cox, R. A.; Granier, C.; Lesclaux, R.; Moortgat, G. K.; Pilling, M. J.; Ravishankara, A. R.; Wallington, T. J. Atmospheric Chemistry of Small Organic Peroxy Radicals. *Journal of Geophysical Research: Atmospheres* **2001**, *106*, 12157–12182.

[11] Emrich, M.; Warneck, P. Branching Ratio for the Self-Reaction of Acetonyl Peroxy Radicals. *Zeitschrift Fur Naturforschung A* **2003**, *58*, 429–433.

[12] *FACSIMILE* version 4.1.41 [computer software]; Faringdon, Oxon, UK, 2003.

[13] Jenkin, M. E.; Cox, R. A.; Emrich, M.; Moortgat, G. K. Mechanisms of the Cl-Atom-Initiated Oxidation of Acetone and Hydroxyacetone in Air. *Journal of the Chemical Society, Faraday Transactions* **1993**, *89*, 2983–2991.

[14] Nielsen, O. J.; Johnson, M. S.; Wallington, T. J.; Christensen, L. K.; Platz, J. UV Absorption Spectra of HO2, CH3O2, C2H5O2, and CH3C(O)CH2O2 Radicals and Mechanism of the Reactions of F and Cl Atoms with CH3C(O)CH3. **2001**, DOI: 10.1002/kin.10037.

[15] Keller-Rudek, H.; Moortgat, G. K.; Sander, R.; Sörensen, R. The MPI-Mainz UV/VIS Spectral Atlas of Gaseous Molecules of Atmospheric Interest. *Earth System Science Data* **2013**, *5*, 365–373.

[16] Christensen, L. E.; Okumura, M.; Hansen, J. C.; Sander, S. P.; Francisco, J. S. Experimental and Ab Initio Study of the HO2CH3OH Complex: Thermodynamics and Kinetics of Formation. *J. Phys. Chem. A* **2006**, *110*, 6948–6959.

[17] Grieman, F. J.; Noell, A. C.; Davis-Van Atta, C.; Okumura, M.; Sander, S. P. Determination of Equilibrium Constants for the Reaction Between Acetone and HO2 Using Infrared Kinetic Spectroscopy. *The Journal of Physical Chemistry A* **2011**, *115*, 10527–10538.

[18] Plum, C. N.; Sanhueza, E.; Atkinson, R.; Carter, W. P. L.; Pitts, J. N. Hydroxyl Radical Rate Constants and Photolysis Rates of .Alpha.-Dicarbonyls. *Environmental Science & Technology* **1983**, *17*, 479–484.

[19] Meller, R.; Raber, W.; Crowley, J. N.; Jenkin, M. E.; Moortgat, G. K. The UV-Visible Absorption Spectrum of Methylglyoxal. *Journal of Photochemistry and Photobiology A: Chemistry* **1991**, *62*, 163–171.

[20] Chen, Y.; Wang, W.; Zhu, L. Wavelength-Dependent Photolysis of Methylglyoxal in the 290-440 Nm Region. *The Journal of Physical Chemistry A* **2000**, *104*, 11126–11131.

[21] Staffelbach, T. A.; Orlando, J. J.; Tyndall, G. S.; Calvert, J. G. The UV-Visible Absorption Spectrum and Photolysis Quantum Yields of Methylglyoxal. *Journal of Geophysical Research: Atmospheres* **1995**, *100*, 14189–14198.

[22] Atkinson, R.; Baulch, D. L.; Cox, R. A.; Crowley, J. N.; Hampson, R. F.; Hynes, R. G.; Jenkin, M. E.; Rossi, M. J.; Troe, J.; IUPAC Subcommittee Evaluated Kinetic and Photochemical Data for Atmospheric Chemistry: Volume II – Gas Phase Reactions of Organic Species. *Atmos. Chem. Phys.* **2006**, *6*, 3625–4055.